UNIVERSITÉ DE LORRAINE | BIBLIOTHÈQUES UNIVERSITAIRES

AVERTISSEMENT
DROIT D'AUTEUR

Ce document est le fruit d'un long travail approuvé par le jury de soutenance et mis à disposition de l'ensemble de la communauté universitaire élargie.

Il est soumis à la propriété intellectuelle de l'auteur. Ceci implique une obligation de citation et de référencement lors de l'utilisation de ce document. Toute contrefaçon, plagiat ou reproduction illicite encourt une poursuite pénale.

Contact bibliothèque : ddoc-theses-contact@univ-lorraine.fr
(Cette adresse ne permet pas de contacter les auteurs)

Code de la Propriété Intellectuelle. articles L 122. 4
Code de la Propriété Intellectuelle. articles L 335.2- L 335.10

UNIVERSITÉ DE LORRAINE
34 COURS LÉOPOLD — CS 25233
54052 NANCY CEDEX
TÉL : 03 54 50 54 00
CONTACT@UNIV-LORRAINE.FR
WWW.UNIV-LORRAINE.FR

C2MP (Chimie - Mécanique - Matériaux - Physique)

LCPME (Laboratoire de Chimie Physique et Microbiologie pour les Matériaux et l'Environnement)

Thèse

Présentée et soutenue publiquement pour l'obtention du titre de

DOCTEUR DE l'UNIVERSITE DE LORRAINE

Mention : Chimie

par **Rayan Kanaan**

Synthèse de métallopolymères par électropolymérisation pour des applications en électrochromisme

Synthesis of Metallopolymers via Electropolymerization for Electrochromic Applications

18 Décembre 2025

Membres du jury :

Rapporteurs :	**M. Boris LAKARD**	**Professeur, Institut UTINAM, Université de Franche Comté, Besançon**
	Mme Xiaonan SUN	**Chargée de Recherche CNRS, ITODYS, Université Paris Cité, Paris**
Examinateurs :	**M. Jérôme CHAUVIN**	**Professeur, DCM, Université de Grenoble Alpes, Grenoble**
	Mme Silvia MENA	**Maitre de Conférence, Universitat Autònoma de Barcelona, Barcelona**
Président de Jury :	**M. Sébastien PILLET**	**Directeur de Recherche CNRS, CRM2, Université de Lorraine, Nancy**
Directeur(s) de thèse :	**Mme Neus VILA CUSCO**	**Professeure, Universitat Autònoma de Barcelona, Barcelona**
	M. Alain WALCARIUS	**Directeur de Recherche CNRS, LCPME, Université de Lorraine, Nancy**

Acknowledgments:

First and foremost, I would like to express my deepest gratitude to my supervisor, Neus Vilà. I feel incredibly fortunate to have had the chance to work under your guidance. Thank you for your patience in answering my never-ending questions, for your encouragement when things weren't working, and for celebrating the small victories along the way. I have learned so much from your sharp scientific intuition, but also from your kindness, generosity, and sense of humor, which made even the most stressful moments lighter. I am especially grateful for the freedom you gave me to pursue my ideas, and for always being there to provide clarity when I got lost in them. Your trust and steady support carried me through this PhD more than you know.

I would also like to warmly thank Alain Walcarius, the head of the ELAN team. Our monthly meetings were always a valuable opportunity for me to step back, reflect, and receive your thoughtful suggestions. Your guidance, perspective, and encouragement provided an additional layer of support that made a real difference in the development of this work. I am grateful for the time you dedicated to following my progress and for the constructive advice that helped me move forward at critical moments.

I would also like to sincerely thank the members of my jury, Dr. Xiaonan Sun, Pr. Boris Lakard, Pr. Jérôme Chauvin, Dr. Silvia Mena, and Dr. Sébastien Pillet. I am deeply grateful that you accepted to evaluate my work and dedicate your time and expertise to this thesis. It is an honor to have such distinguished scholars take part in this important milestone of my journey. I also wish to thank the CSI members Almudena Marti Morant and Jérôme Chauvin for accompanying me during the early stages of my PhD. The yearly presentations were important moments to share my progress, receive your questions, and benefit from your guidance.

I also deeply acknowledge the other members of the ELAN group, Mariela Brites-Helu, Dr. Christelle Despas, Dr. Mathieu Etienne, Dr. Liang Liu, and Prof. Marc Hébrant for their insightful contributions and questions during the group meetings. Also, I would like to thank Gérard Paquot for his help in the construction of the electrochemical cells I used during my PhD and having his door open to help with any issues I faced and Claire Genois for technical support.

To my colleagues and fellow researchers in the lab: thank you for the stimulating discussions, the collaborations, and the countless moments that made the long days (and nights) in the lab far more enjoyable. I would like to give special thanks to Mahmoud Rahal, Odilon Wamba Tchio, and Abdelhak Fezraouio for sharing countless discussions during breaks and the constant support. Your generosity with your time, knowledge, and encouragement made a huge difference in my PhD experience, and I am truly grateful to have had such supportive colleagues by my side. To my lab friends, Nour, Claire, Emily, Sara, and Harpreet, thank you for the coffee breaks, laughter, and the occasional therapeutic rants. You made the lab feel less like a workplace and more like a community.

Beyond the lab, I am grateful to my friends Nour, Sara, Reem, Tamara, Lana, Ghenwa, and Israa who reminded me there is life beyond experiments and deadlines. Your support and good humor kept me joyful and sane.

Finally, none of this would have been possible without my family. Thank you for your unwavering love, patience, and belief in me, even when I doubted myself. Living far from home during these years was not always easy, but your constant support closed the distance. To my parents, Mohammad and Rola, thank you for teaching me perseverance and for always reminding me that no matter how far I am, I am never alone. Your encouragement whether through long calls, short texts, or simply knowing you were there carried me through the hardest moments. To my siblings Sara, Nour, and Hussein, thank you for keeping me grounded, for making me laugh at the right times, and for never letting me get too serious about myself or my work, also for planning the best adventures when I was back home. To my grandparents and my family as a whole: thank you for cheering me on in your own unique ways, whether by proudly telling everyone I was “still studying” (without ever being quite sure what), or by reminding me to eat properly and take care of myself whenever we spoke. Even from afar, your affection and encouragement were a constant source of strength, and your pride gave me that extra push when I needed it most.

Abbreviation list

- **AAO:** Anodic Aluminum Oxide
- **ACN:** Acetonitrile
- **Ag/AgCl:** Silver/Silver Chloride (Reference Electrode)
- **bpy:** 2,2'-Bipyridine / Bipyridine
- **$CDCl_3$:** Deuterated Chloroform
- **CD_3CN:** Deuterated Acetonitrile
- **CTAB (C16TAB):** Cetyltrimethylammonium Bromide
- **C20TAB:** Eicosyltrimethylammonium Bromide
- **DMA:** N,N-Dimethylacrylamide
- **DMF:** Dimethylformamide
- **DMSO:** Dimethyl Sulfoxide
- **$Fc(MeOH)_2$:** 1,1′-Ferrocenedimethanol
- **FTO:** Fluorine-Doped Tin Oxide
- **$HClO_4$:** Perchloric Acid
- **ITO:** Indium Tin Oxide
- **KPS:** Potassium Peroxodisulfate
- **$LiClO_4$:** Lithium Perchlorate
- **MBA:** N,N′-Methylenebisacrylamide
- **MoO_3:** Molybdenum Trioxide
- **MWCNT:** Multi-Walled Carbon Nanotube
- **$NaBH_4$:** Sodium Borohydride
- **$NaClO_4$:** Sodium Perchlorate
- **$NaNO_2$:** Sodium Nitrite
- **Na_2SO_4:** Sodium Sulfate
- **NiO:** Nickel Oxide
- **P3HT:** Poly(3-hexylthiophene)
- **PA:** Polyacetylene
- **PAMPS:** Poly(2-acrylamido-2-methylpropanesulfonic acid)

- **PANI:** Polyaniline
- **PAz:** Polyazulene
- **PB:** Prussian Blue
- **PCz:** Polycarbazole
- **PEDOT:** Poly(3,4-ethylenedioxythiophene)
- **PEO:** Poly(ethylene oxide)
- **PET:** Polyethylene Terephthalate
- **PFu:** Polyfuran
- **PFO:** Polyfluorene
- **PIF:** Polyindenofluorene
- **PIn:** Polyindole
- **PITN:** Polyisothianaphthene
- **PMMA:** Poly(methyl methacrylate)
- **PPE:** Poly(phenylene ethynylene)
- **PPP:** Poly(p-phenylene)
- **PPS:** Poly(p-phenylene sulfide)
- **PPV:** Poly(p-phenylene vinylene)
- **PPy / PPY:** Polypyrrole
- **PSS:** Polystyrene Sulfonate
- **PTh:** Polythiophene
- **PVA:** Poly(vinyl alcohol)
- **TBAClO_4:** Tetrabutylammonium Perchlorate
- **TBAPF_6:** Tetrabutylammonium Hexafluorophosphate
- **TEAClO_4:** Tetraethylammonium Perchlorate
- **TEOS:** Tetraethoxysilane / Tetraethyl Orthosilicate
- **TMOS:** Tetramethoxysilane
- **tppz:** Tetra-2-pyridinylpyrazine
- **tpy:** 2,2':6',2''-Terpyridine / Terpyridine
- **WO_3:** Tungsten Trioxide
- **--N=N--:** Azo bond/linkage

- **--NH-NH--:** Hydrazo bond/linkage
- **$[Co(tpy\text{-}Ph\text{-}NH_2)_2]^{2+}$:** Cobalt bis(terpyridine-phenyl-amine) complex (Compound 6)
- **$[Fe(CN)_6]^{4-}$:** Hexacyanoferrate(II) Anion
- **$[Fe(tpy\text{-}Ph)_2]^{2+}$:** Iron bis(terpyridine-phenyl) complex (Compound 1)
- **$[Fe(tpy\text{-}Ph\text{-}NH_2)_2]^{2+}$:** Iron bis(terpyridine-phenyl-amine) complex (Compound 2)
- **$[Ru(NH_3)_6]^{3+}$:** Hexaammineruthenium(III) Cation
- **$[Ru(tpy\text{-}Ph)_2]^{2+}$:** Ruthenium bis(terpyridine-phenyl) complex (Compound 3)
- **$[Ru(tpy\text{-}Ph\text{-}NH_2)_2]^{2+}$:** Ruthenium bis(terpyridine-phenyl-amine) complex (Compound 4)
- **$[Zn(tpy\text{-}Ph\text{-}NH_2)_2]^{2+}$:** Zinc bis(terpyridine-phenyl-amine) complex (Compound 5)
- **poly$[Fe(tpy\text{-}Ph\text{-}NH_2)_2]^{2+}$:** Electropolymerized film of the Iron-amine complex
- **poly$[Ru(tpy\text{-}Ph\text{-}NH_2)_2]^{2+}$:** Electropolymerized film of the Ruthenium-amine complex
- **CA:** Chronoamperometry
- **CE:** Counter Electrode (in electrochemistry)
- **CV:** Cyclic Voltammetry
- **EASA:** Electrochemically Assisted Self-Assembly
- **Ef:** Final Potential
- **Ei:** Initial Potential
- **Epa:** Anodic Peak Potential
- **Epc:** Cathodic Peak Potential
- **Es:** Switching Potential
- **Ipa:** Anodic Peak Current
- **Ipc:** Cathodic Peak Current
- **PRE:** Pseudo-Reference Electrode
- **RE:** Reference Electrode
- **SHE:** Standard Hydrogen Electrode
- **WE:** Working Electrode
- **ΔEp:** Peak-to-Peak Separation
- **Eb:** Electron Binding Energy (in XPS)
- **EK:** Electron Kinetic Energy (in XPS)
- **FTIR:** Fourier Transform Infrared Spectroscopy

- **GISAXS:** Grazing-Incidence Small-Angle X-ray Scattering
- **IR:** Infrared
- **NMR:** Nuclear Magnetic Resonance
- **SAXS:** Small-Angle X-ray Scattering
- **TEM:** Transmission Electron Microscopy
- **UV-Vis:** Ultraviolet-Visible (Spectroscopy)
- **XPS:** X-ray Photoelectron Spectroscopy
- **CE:** Coloration Efficiency (in electrochromism)
- **CR:** Contrast Ratio
- **EC:** Electrochromic / Electrochromism
- **ECD:** Electrochromic Device
- **ΔT%:** Transmittance Change
- **A:** Electrode Area
- **C:** Concentration
- **D:** Diffusion Coefficient
- **F:** Faraday Constant
- **I:** Current / Transmitted Light Intensity
- **I_0:** Incident Light Intensity
- **l:** Path Length (in spectroscopy)
- **n:** Number of Electrons
- **Φ (Phi):** Work Function (in XPS)
- **HOMO:** Highest Occupied Molecular Orbital
- **LC:** Ligand-Centered (transition)
- **LMCT:** Ligand-to-Metal Charge Transfer
- **LUMO:** Lowest Unoccupied Molecular Orbital
- **MC:** Metal-Centered (transition)
- **MLCT:** Metal-to-Ligand Charge Transfer
- **MO:** Molecular Orbital
- **CMPs:** Conducting Metallopolymers
- **CPs:** Conducting Polymers

- **PLEDs:** Polymer Light-Emitting Diodes
- **SDAs:** Structure-Directing Agents
- **TMOs:** Transition Metal Oxides
- **CVD:** Chemical Vapor Deposition
- **EISA:** Evaporation-Induced Self-Assembly
- **LbL:** Layer-by-Layer
- **LB:** Langmuir-Blodgett
- **TLCT:** True Liquid Crystal Templating
- **1D:** One-Dimensional
- **2D:** Two-Dimensional
- **hv:** Photon Energy (in XPS)
- **NH_2:** Amino group
- **Ph:** Phenyl

Table of Contents

Table of Contents

Resume: ... 1

1. Introduction and Bibliography ... 13

1.1. Conjugated Polymers: Structure, Properties, and Applications ... 14

1.1.1. Polythiophenes and Their Derivatives ... 17

1.1.2. Poly(p-phenylene)s: Doping and Stability ... 17

1.1.3. Polypyrrole: From Chemical Oxidation to Electrochemical Polymerization ... 18

1.1.4. Polyaniline: A Versatile Conducting Polymer ... 19

1.2. Metallopolymers: Background Discovery and Synthesis ... 21

1.2.1. Metallopolymers formed using Electropolymerization ... 24

1.2.2. Polymers Containing Polypyridyl Complexes ... 25

1.2.3. Bipyridine Complexes vs Terpyridine Complexes ... 31

1.3. Methods to Functionalize Electrode Surfaces ... 32

1.3.1 Coating-Based Methods ... 32

1.3.2. Layer-by-Layer Assembly ... 34

1.3.3. Electropolmyerization on Electrode Surfaces ... 35

1.4. Electrografting of Organic Groups ... 36

1.5. Introduction to Electrochromism ... 38

1.5.1. Electrochromic Materials ... 39

1.5.2. Typical Organic EC Materials ... 40

1.5.3. Other EC Materials ... 45

1.6. Electrochromic Devices ... 46

1.6.1. Configuration of ECDs ... 47

1.6.2. Electrochromic Key Performance Paremeters ... 50

1.7. One Dimensional Nanostructures ... 52

1.8. Mesoporous Silica Materials: Template-Based Synthesis ... 53

1.9. Mesoporous Silica Films on Solid Substrates ... 55

1.9.1. Vertically Aligned and Ordered Mesoporous Silica Films on Solid Surfaces ... 56

1.9.2. Electrochemically Assisted Self-Assembly Method ... 56

1.9.3. Applications of the Ordered Mesoporous Silica Films covered Electrodes ... 58

2. Experimental Part ... 64

2.1. List of Chemicals and Solvents used ... 64

2.2. Electrochemical apparatus and methods ... 65

2.2.1. Electrochemical cell 65
2.2.2. Spectroelectrochemical cell 66
2.2.3. Electrodes 67
2.2.4. Potentiostat 68
2.2.4. Electrochemical techniques 68
2.2.5. Spectroscopic Methods 71
2.2.6. Grazing-Incidence Small-Angle X-ray Scattering 74
2.3. Synthesis and Electrode Modification Protocols 74
2.3.1. Synthesis of $[Fe(tpy\text{-}Ph\text{-}NH_2)_2][PF_6]_2$, (1): 74
2.3.2. Synthesis of $[Ru(tpy\text{-}Ph\text{-}NH_2)_2][PF_6]_2$, (2): 75
2.3.3. Synthesis of $[Zn(tpy\text{-}Ph\text{-}NH_2)_2][PF_6]_2$, (3): 76
2.3.4. Synthesis of $[Co(tpy\text{-}Ph\text{-}NH_2)_2][PF_6]_2$, (4): 77
2.3.5. Synthesis of $[Fe(tpy)_2][PF_6]_2$: 78
2.3.6. Synthesis of $[Ru(tpy\text{-}Ph)_2][PF_6]_2$: 78
2.3.7. Synthesis of Eicosyltrimethylammonium Bromide (C_{20}TAB) 79
2.3.8. Synthesis of the Conductive Gel for Spectroelectrochemical Experiments 80
2.3.9. Electrografting of Bis (aminophenyl terpyridine) based Complexes and Compounds on Electrode Surface 81
2.3.10. Electropolymerization of Bis(aminophenyl terpyridine) complexes: 81
2.3.11. Electrochemical Characterization of the modified films 82
2.3.12. Synthesis of the Vertically Oriented Mesoporous Silica Films 83
3. Chapter 3: Electropolymerization of Aminophenyl-Substituted Bis(terpyridine) Metal Complexes and Electrochromic Properties of the Obtained Metallopolymers 87
3.1. Introduction 87
3.2. Results and Discussion 89
3.2.1. Electrochemical Behavior of $[Fe(tpy\text{-}Ph\text{-}NH_2)_2]^{2+}$ on Electrode Surfaces 89
3.2.2. Comparison to the electropolymerization of aniline-based monomers. 103
3.2.3. Electrografting of the in situ monodiazonium cation of the complexes: 104
3.2.4. Electropolymerization of 2 after grafting: 106
3.2.5. Characterization of the Electropolymerized Films 108
3.2.6. Electrochromic response of the films 118
3.2.7. Electrochemical behavior of $[Ru(tpy\text{-}Ph\text{-}NH_2)_2]^{2+}$ on Electrode Surfaces 121
3.2.8. Electrografting of 4 on ITO electrodes 127
3.2.9. ELectropolymerization of 4 after grafting 128

3.2.10. Characterization of the Electropolymerized Films 129
3.2.11. Electrochromic response of the films 133
3.2.12. Effect of Changing the Concentration of the Electroactive species on the Electropolymerization of the metallopolymers 136
3.2.13. Optical and Profilometric Analysis of Electropolymerized Films 139
3.2.14. Electrochemical Behavior of $[Zn(tpy\text{-}Ph\text{-}NH_2)_2]^{2+}$ and $[Co(tpy\text{-}Ph\text{-}NH_2)_2]^{2+}$ on Electrode Surfaces 141
3.2.15. Electrografting of 5 and 6 on ITO followed by electropolymerization and electrochemical characterization 145
3.3. Conclusions and Perspectives 148
4. Chapter 4: Confinement Effects of Vertically Oriented Mesoporous Silica Films on the Optical and Electrochemical Properties of Conducting Polymer Films 152
4.1. Introduction 152
4.2. Results and Discussion 155
4.2.1. Charge selectivity for the transport of redox probes through the vertically oriented mesoporous silica films 155
4.2.2. Structural Characterization of the Ordered Mesoporous Silica Films 157
4.2.3. Electrochemical Polymerization inside Mesoporous Silica Films with Different Pore Sizes 160
4.2.4. Electrochemical Characterization of the Obtained Fe Metallopolymers inside Silica Films 165
4.2.5. Optical Characterization of Fe-based Polymers using UV-VIS 166
4.2.6. Electrochromic Response of the Metallopolymer inside Mesoporous Silica Films 167
4.2.7. Electropolymerization of the Ruthenium Complex (4) Inside The Silica Films 170
4.2.8. Electrochemical Characterization of the Obtained Ru Metallopolymers inside Silica Films 172
4.2.9. Optical Characterization of Ru-based Polymers using UV-VIS 173
4.2.10. Electrochromic Response of the Metallopolymer inside Mesoporous Silica Films 174
4.3. Conclusion 176
5. General Conclusion and Perspectives 178
6. References 181

Resume:

Les polymères conducteurs (PC) tels que la polyaniline (PANI), le polypyrrole (PPy) et le polythiophène (PTh) suscitent un intérêt soutenu en raison de leur combinaison unique de conductivité électronique, de polyvalence chimique et de coûts de synthèse relativement faibles. À la différence des polymères massifs classiques, les PC possèdent des squelettes π-conjugués qui permettent la délocalisation de charge, conférant un comportement semi-conducteur voire métallique après dopage approprié. Leur organisation à l'échelle nanométrique en structures unidimensionnelles (nanofils, nanotubes) améliore encore le transport de charge, l'accessibilité de surface et la flexibilité mécanique. Ces caractéristiques rendent les PC attractifs pour de nombreuses applications, notamment les supercondensateurs, capteurs chimiques et dispositifs électrochromes.

Une extension particulièrement puissante de la chimie des PC consiste à incorporer des complexes métal-ligand dans l'ossature polymère, donnant naissance aux métallopolymères. Parmi les plus étudiés figurent les complexes basés sur la 2,2′:6′,2″-terpyridine (tpy), qui chélate fortement des métaux de transition tels que Fe(II) et Ru(II). Ces complexes bis(terpyridine) présentent des états redox multiples, une communication électronique efficace et des propriétés optiques riches. Soumis à l'électropolymérisation, des complexes terpyridine fonctionnalisés par des groupes amino forment des réseaux étendus ancrés directement à la surface des électrodes. Le groupe NH_2 joue un rôle central en permettant la polymérisation oxydante via couplage radicalaire, conduisant à des films de métallopolymères stables et robustes. Les matériaux obtenus sont électrochromes, c'est-à-dire capables de changer réversiblement de couleur sous potentiel appliqué propriété d'un grand intérêt pour les vitrages intelligents, afficheurs et dispositifs optoélectroniques.

Malgré ces atouts, les métallopolymères électropolymérisés souffrent parfois de limitations liées à la morphologie du film, à l'adhérence et à l'accessibilité des sites électroactifs. Une croissance non contrôlée peut mener à des dépôts épais ou inhomogènes, tandis qu'un ordre structurel insuffisant peut freiner le transport des contre-ions et dégrader les performances optiques de commutation. Pour y remédier, des stratégies de confinement de la croissance dans des nanostructures définies sont nécessaires.

Dans ce contexte, les films minces de silice mésoporeuse émergent comme matrices hôtes très polyvalentes. Ils peuvent être fabriqués par des méthodes de gabarit, en particulier l'auto-assemblage assisté électrochimiquement (EASA), qui produit des canaux mésoporeux orientés verticalement, déposés directement sur des substrats conducteurs tels que l'ITO. Par rapport à l'auto-assemblage induit par évaporation (EISA), qui génère souvent des pores parallèles au substrat, EASA confère une orientation verticale, offrant des voies directes pour le transport ionique entre l'électrolyte et la surface de l'électrode. Les parois riches en silanols portent une charge négative à pH neutre, induisant un transport sélectif en charge: les espèces cationiques sont pré-concentrées, les anions repoussés et les neutres diffusent principalement selon des effets stériques. Ces propriétés rendent les films de silice mésoporeuse attractifs non seulement comme couches tamisantes/antifouling, mais aussi comme hôtes nanostructurés pour la croissance confinée de polymères conducteurs et électrochromes.

En combinant l'activité électronique et optique des polymères métal-terpyridine avec le contrôle structurel de films de silice à canaux verticaux, il devient possible de concevoir des matériaux hybrides dotés d'une meilleure stabilité électrochimique, d'une morphologie réglable et de performances électrochromes améliorées. La présente thèse se situe à cette interface et vise à exploiter les films minces de silice mésoporeuse comme plateformes nanostructurées pour l'électropolymérisation de métallopolymères à base de terpyridine et à étudier leurs propriétés électrochimiques et optiques.

L'objectif principal de la thèse est la formation et la caractérisation de films de métallopolymères stables et adhérents sur électrodes transparentes conductrices, en mettant l'accent sur leurs propriétés électrochromes. Ces matériaux reposent sur des métaux de transition tels que Fe, Ru et Co, choisis pour leurs états d'oxydation multiples, leur réversibilité redox et leur forte coordination avec les ligands terpyridine. L'intégration de ces complexes dans des ossatures polymères confère des propriétés électroniques et optiques singulières, issues des transitions transfert de charge métal-vers-ligand (MLCT) et ligand-vers-métal (LMCT), favorisant la délocalisation électronique et une modulation spectrale multistate. Les objectifs spécifiques sont résumés ci-après:

- Synthèse de films électroactifs de complexes bis(terpyridine) (Fe, Ru, Co) directement sur ITO par polymérisation oxydante de complexes terpyridine fonctionnalisés par des groupes

aminophényles (–NH_2), indispensables pour initier la croissance. Cette approche assure un contact intime polymère/substrat propice aux investigations électrochimiques et spectro-électrochimiques.

- Contrairement à l'aniline où le couplage s'effectue classiquement en para, la substitution par la terpyridine bloque ce site et empêche la voie conventionnelle. Des liaisons alternatives — C–C ortho-ortho, –NH–NH– ou –N=N– ont donc été envisagées. La combinaison CV/UV-Vis/XPS a démontré la formation dominante de liaisons azo, apportant un éclairage fondamental sur le mécanisme de croissance.

- Dépôt de poly[$Fe(tpy\text{-}Ph\text{-}NH_2)_2]^{2+}$ et poly[$Ru(tpy\text{-}Ph\text{-}NH_2)_2]^{2+}$ sur ITO, puis étude de la réponse optique in situ par spectro-électrochimie sous potentiel appliqué. Détermination du contraste, de l'efficacité de coloration et des temps de commutation pour évaluer la pertinence en vitrages intelligents et optoélectronique.

- Utilisation de films VMSF, à pores verticaux de 2 à 4,3 nm (méthode EASA), comme hôtes pour la croissance confinée des métallopolymères en nanofils, et comparaison systématique avec les films non confinés.

- Évaluation des bénéfices du confinement sur l'ordre structural, la stabilité électrochimique et l'efficacité de commutation électrochrome par rapport aux dépôts sur ITO nu.

Les complexes bis(terpyridine) aminophénylés de Fe(II) et Ru(II) s'électropolymérisent avec succès sur ITO par voltammétrie cyclique, le groupe –NH_2 s'avérant essentiel: les complexes dépourvus de cette fonction ne forment pas de films adhérents. À la différence de la polymérisation de l'aniline (couplage para–para), l'encombrement par la terpyridine bloque cette voie et favorise des liaisons alternatives, en particulier de type azo, comme l'attestent UV-Vis et XPS. L'efficacité de croissance dépend de la structure du complexe et de l'électrolyte de support: les milieux perchlorate se sont révélés idéaux, contrairement, par exemple, aux sulfates. Les films présentent des couples redox bien définis et réversibles (Fe^{3+}/Fe^{2+} et Ru^{3+}/Ru^{2+}), une forte adhérence et une bonne stabilité au cyclage, avec toutefois des limitations diffusives pour les dépôts épais.

Les mesures spectro-électrochimiques confirment l'électrochromisme: sous commutation de potentiel, des changements de couleur nets et réversibles, associés aux transitions MLCT, sont observés. Les systèmes Fe et Ru montrent des commutations rapides (quelques secondes), de fortes efficacités de coloration et des contrastes marqués, établissant ces métallopolymères électropolymérisés comme candidats prometteurs pour l'électrochromisme.

Pour améliorer le contrôle structurel et la stabilité, la croissance a été confinée dans des films VMSF synthétisés par EASA sur ITO. Ces films, constitués de canaux hexagonaux verticaux (2 à 4,3 nm), ont été validés électrochimiquement par des sondes standards: $Ru(NH_3)_6^{3+}$, $Fe(CN)_6^{3-}$ et FcMeOH. Le confinement révèle une forte dépendance au diamètre de canal: à 2 nm, la polymérisation est inefficace; à 3 nm, les courants initiaux augmentent mais la réponse demeure instable au cyclage; à 4,3 nm, la croissance est optimale, avec des pics nets et stables qui augmentent avec le nombre de scans. Les films restent intacts après rinçage, attestant une incorporation robuste du polymère dans les canaux.

La spectro-électrochimie montre que les métallopolymères confinés conservent leur électrochromisme intrinsèque, les films de 4,3 nm se distinguant par une reproductibilité et une stabilité accrues. L'alignement vertical des mésopores facilite le transport ionique et limite la sur-croissance, procurant de bonnes réponses redox et une commutation optique régulière.

Cette thèse démontre donc la synthèse et la caractérisation réussies de films électrochromes à base de complexes bis(terpyridine) aminophénylés de Fe(II) et Ru(II), à la fois sur ITO nu et dans des films de silice mésoporeuse orientés verticalement. Sur ITO, la polymérisation progresse efficacement via les substituants amino, selon un mécanisme distinct de la PANI et dominé par des liaisons azo (confirmé par spectroscopies). Les films présentent une activité redox nette, une bonne adhérence et un électrochromisme réversible avec commutation rapide et forte efficacité de coloration. L'électrolyte de support influence sensiblement la cinétique de polymérisation et la stabilité des films. En confinement mésoporeux, le comportement dépend fortement de la taille de pore: inefficacité à 2 nm, instabilité à 3 nm, et performances optimales à 4,3 nm, avec des réponses redox robustes. Les films confinés conservent leurs propriétés électrochromes, illustrant l'intérêt de la silice mésoporeuse comme gabarit nanostructuré pour améliorer le contrôle morphologique, le transport de masse et la durabilité.

Dans l'ensemble, ce travail établit les films VMSF comme d'excellents gabarits pour la fabrication de nanofils de métallopolymères ordonnés, aux propriétés électrochimiques et optiques ajustables. Les enseignements tirés des mécanismes de polymérisation, des effets de l'électrolyte et des phénomènes de confinement ouvrent de nouvelles perspectives pour la conception rationnelle de matériaux hybrides à l'interface de la chimie de coordination, de la science des polymères et des matériaux nanostructurés.

Des recherches futures pourront étendre cette approche à d'autres métaux de transition et familles de ligands afin de diversifier les réponses électrochromes. L'optimisation complémentaire de la taille des pores, de l'épaisseur de film et des stratégies de fonctionnalisation devrait permettre d'affiner les cinétiques de commutation et la stabilité. Au-delà de l'électrochromisme, ces métallopolymères confinés présentent un potentiel pour le stockage d'énergie, la détection et la catalyse, domaines où le transport de charge contrôlé et l'organisation à l'échelle nanométrique sont essentiels.

Electrochemistry, the study of chemical phenomena driven by the movement of electrons across interfaces, has evolved from its early roots in the 18th and 19th centuries into a model for modern material science. The pioneering work of Volta, Faraday, and Ostwald established the fundamental principles of electrode potentials, redox reactions, and interfacial processes that remain the foundation of the field today [1]. With the interesting electroanalytical methods and controlled electrodeposition techniques, electrochemistry has transitioned from a primarily analytical discipline to a powerful synthetic tool for designing functional materials [2]. One of the most significant milestones in this evolution was the incorporation of the electrochemical methods into the synthesis of conducting polymers. Specifically, electropolymerization is a versatile technique used to synthesize conducting polymers as thin and uniform films directly on working electrode's surfaces. The electropolymerization mechanism is readily described in literature for well-known organic monomers such as aniline where polyaniline served as a model system in the domain of conducting polymers. Also the scale of electropolymerization exceeds beyond only aniline-based systems, where this technique has been shown to be useful and successful in the formation of metallopolymers.

This is where the thesis objectives lie, where the main goal of this thesis is to form stable and adherent metallopolymer films on transparent conducting electrodes to study their electrochromic properties. These films are based on a d-transition metal center such as Fe, Ru, and Co since they have multiple oxidation states and can undergoe reversible redox processes and most importantly they form stable bonds with the donor ligands. This allows for controlled integration of the metal centers into the polymer backbone. Finally, the transition metal complexes have characteristic MLCT and LMCT transitions leading to unique optical properties and enhanced electron delocalization along the polymer chain. With respect to the desired ligand, terpyridine-based ligands are that of interest due to their planar geometry and effective conjugation to with the metal ions. Furthermore, it is known as a non-innocent ligand capable of stabilizing the low-valency metals and form octahedral complexes. This hybrid nature of complexes makes them especially attractive for electrochromic applications, where multistate redox activity and precise spectral modulation are present. In this case to have a successful polymerization process, these complexes must bear aminophenyl groups to undergoe oxidative polymerization such as aniline where oxidation leads to nitrogen-centered radicals that usually couple at the para position to form extended conjugated chains through C–N or C–C linkages.

Here lies another objective which is to study and unravel the polymerization mechanism for these aminophenyl-substituted Bis(terpyridine) metal complexes since when compared to the simple monomer units as aniline, the para position is already occupied with a terpyridine substituent that effectively blocks the conventional coupling so alternative pathways such as ortho–ortho (C–C), NH–NH, or N=N couplings may dominate. This was studied and evaluated to prove that in this case, the azo bond was formed between the monomer units which was performed using CV and UV-VIS and XPS to study the properties of the formed films. We aim to expand understanding of such metallopolymer formation by electro-assisted polymerization. Through a combination of spectroscopic and electrochemical characterization, this study provides new insight into the structure and growth mechanism of electrochemically generated films. As these films present electrochromic properties, they are deposited on transparent electrodes which are ITO electrodes and spectroelectrochemical tests are performed to study the properties of both Iron and Ruthenium based metallopolymers by applying specific potentials and recording the UV spectra simultaneously.

Another objective in alignment with the previous goal, is to form the metallopolymers in the same manner that is previously mentioned inside vertically oriented mesoporous silica films that are depositied on ITO electrodes. This originates from the combination of organic semiconductors with low dimensionality to have improved transport properties compared to its usual bulky counterpart. This is previously described in literature where it shows 1D nanostructured conducting polymers that are produced using hard or soft template approaches. With the different templates that can be used, the focus lies on obtaining uniform films that are perpendicular to the electrode surface such as the PANI nanowires obtained on ITO electrodes using vertically oriented mesoporous silica template. Therefore, we have extended this approach to generate also metallopolymer nanowires such as poly[$Fe(tpy\text{-}Ph\text{-}NH_2)_2]^{2+}$ and poly[$Ru(tpy\text{-}Ph\text{-}NH_2)_2]^{2+}$ films using the mesoporous silica templates (with pore size ranging between 2-4.3 nm). Then we evaluate their respective electrochemical behavior and spectroelectrochemical response and by that we can study the effect of the confinement of these wires inside insulating films compared to the non-confined wires formed.

In the following sections of this chapter, we introduce the conducting polymers and explain about their history, then move over to talk about metallopolymers and how they are synthesized and

present some examples. Then an expalantion about techniques to functionalize electrodes is presented, followed by an introduction on electrochromism and detailed explanation on the material and properties. Finally, a section on mesoporous films is presented and focusing on ordered mesoporous silica films.

The following chapter is the experimental part where all chemicals and solvents used during the thesis are presented and a detailed explanation of all the machines used and the different set-ups. Then a presentation of different complexes synthesized is shown where the protocol is mentioned along with some NMR data. Finally, a detailed explanation is found that describes the solutions that were used in the electropolymerization and characterization processes.

Then chapter 3, which is the main part of the thesis includes the polymerization principle of the metal complexes to form poly[$Fe(tpy\text{-}Ph\text{-}NH_2)_2]^{2+}$ films through the amino group and comparing it to complexes without amino-end groups. The polymerization was also tested using different electrolytes to see the effect of changing the supporting species on the polymerization kinetics. Furthermore, different number of scans were applied to form metallopolymers with different chain lengths that are characterized electrochemically and optically. These modified electrodes are also characterized using XPS, Raman, and IR to confirm the nature of the link between the monomer units. Then the electrochromic properties of these polymers are studied using spectroelectrochemistry which is studying the change in the optical properties in response to an applied potential. Poly[$Ru(tpy\text{-}Ph\text{-}NH_2)_2]^{2+}$ films were also described in this chapter in order to show the electrochemical and optical properties where the films were prepared in the same way as the iron ones, so the same procedures were performed while only changing the electroactive species.

Finally, a small chapter introduces the idea of forming these metallopolymers that were shown in the previous chapter but in this case they are confined inside ordered mesoporous silica films. The idea arises from the goal of forming 1D metallopolymers that are ordered and uniform, so in order to achieve that either soft or hard template approaches are used to assist. In this case we synthesize vertically oriented mesoporous silica films electrochemically using different surfactants to obtain varying pore sizes. Then, electropolymerization is performed inside these pores and characterized to see the effect of confining these wires inside insulating films.

Chapter I: General Introduction

1. Introduction and Bibliography

Polymers have traditionally been regarded as insulating materials. However, around four decades ago, reports began to emerge describing polymers that exhibited electrical conductivity [3]. This discovery marked a major breakthrough, as conductive behavior had previously been associated almost exclusively with inorganic materials such as metals. The possibility of combining the mechanical flexibility and processability of polymers with the electrical conductivity of metals generated significant interest in both academic research and industrial applications as shown in **Figure 1**. For this unique class of materials, the term "synthetic metals" was introduced, referring to non-metallic substances that are capable of conducting electricity through the presence of mobile charge carriers [4].

The general term "conductive polymers (CPs)" encompasses a broad category of materials that can be classified based on their mechanism of charge transport: ionic conductors and electronic conductors [5]. In the case of ionic conductivity, the polymer must undergo reversible oxidation and reduction, which permits counter-ions to move within the polymer matrix. Depending on the redox state of the polymer, either anionic or cationic conductivity may occur. When the polymer is oxidized, the backbone becomes positively charged (polycationic), enabling small anions such as chloride (Cl^-) to migrate under an applied potential. Conversely, when the polymer is reduced, the backbone carries negative charges (polyanionic), thereby allowing cations to serve as the mobile species [6].

In contrast, electronic conductivity in polymers arises from the presence of a conjugated π-electron backbone, which allows charge carriers such as electrons or holes to delocalize and move through the material [7], [8]. Unlike ionic conductors, the charge transport here does not rely on the mobility of external ions but instead on the extended π-system within the polymer chain. Upon doping which is either by oxidation or reduction, these polymers exhibit significantly enhanced conductivity as the injected charges create delocalized states that facilitate electron transport. Research on conducting polymers began to move forward in the 1970s and reached a major milestone when the Nobel Prize in Chemistry was awarded in 2000 for pioneering work in this field [9], [10]. Since then, a wide variety of conducting polymers have been developed. Early studies focused on materials such as polyaniline (PANI) and polyacetylene (PA), while subsequent

efforts expanded to include polythiophene (PTh), polypyrrole (PPy), and poly(3,4-ethylenedioxythiophene) (PEDOT), which have become some of the most widely studied systems today (see **Figure 2**) [11], [12], [13], [14], [15].

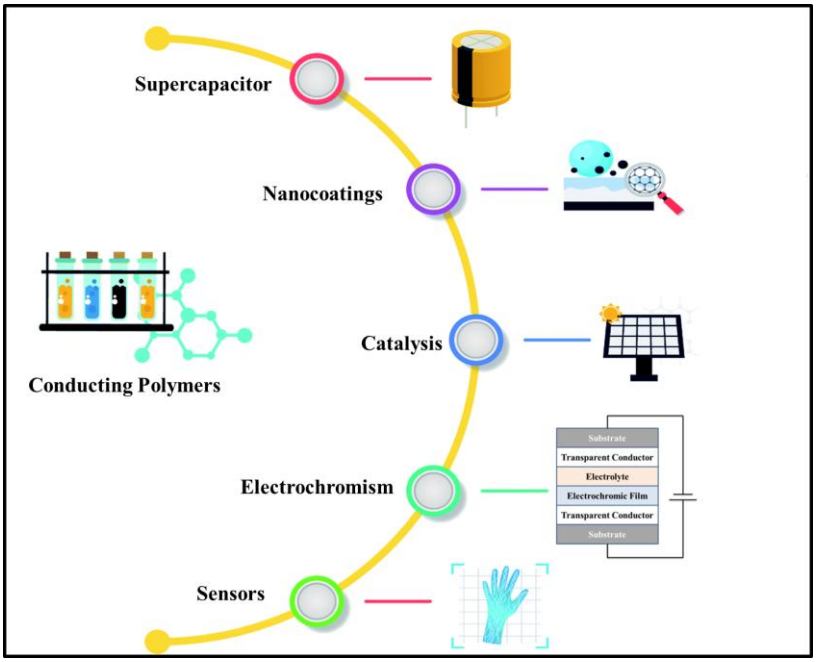

Figure 1: Schematic illustration of the different applications of conducting polymers.

1.1. Conjugated Polymers: Structure, Properties, and Applications

Redox-active polymers with conjugated backbones have played a major role in establishing the field of electrically active macromolecules. Conjugated polymers (also referred to as intrinsically conductive polymers) are defined as macromolecules that contain continuous sequences of alternating single and double bonds along their chains, creating a fully conjugated π-electron system [16]. The modern history of conducting polymers began in 1976, when Alan MacDiarmid, Hideki Shirakawa, and Alan J. Heeger reported that the conductivity of *trans*-polyacetylene could be increased by up to seven orders of magnitude through halogen doping [7]. This landmark discovery revolutionized the understanding of polymeric materials, ultimately earning the three scientists the Nobel Prize mentioned above [17]. Despite its significance, polyacetylene itself proved to be chemically unstable and therefore unsuitable for practical applications [18]. Nevertheless, its discovery created extensive efforts to identify other conjugated polymers with

greater stability and comparable electronic properties. As a result, a wide range of conjugated polymers were developed, many of which are now considered fundamental to the field.

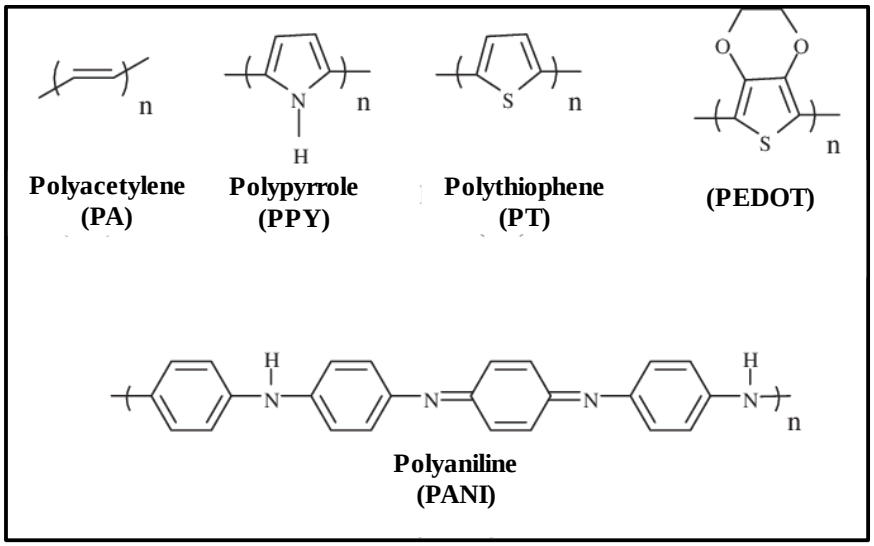

Figure 2: Chemical structures of the most common conjugated polymers, which have been exploited readily or as the building block for synthesis of more sophisticated redox active polymers.

These materials exhibit a broad spectrum of electrical behavior, ranging from insulating to metallic, with most reported conductivities falling between 10^{-5} and 10^{3} $S \cdot cm^{-1}$ typically within the semiconducting regime [19]. Importantly, they uniquely combine the electronic properties of metals with the mechanical flexibility of polymers, which has driven sustained research efforts since the 1980s. From a structural perspective, the conjugated frameworks in these polymers consist of carbon atoms bonded via σ-bonds that provide structural integrity, alongside orthogonal π-bonds that are delocalized and enable electron mobility along the polymer backbone (intramolecular charge transfer) [20]. Additionally, inter-chain electron hopping contributes significantly to the overall conductivity of conjugated polymers. Fundamentally, depending on the electronic band structure, such materials can be classified as insulators, semiconductors, or conductors. Along the years, many compounds were studied and interesting conducting polymers were discovered which are summarized in the table below (**Table 1**) where the main classes of conducting polymers are listed, with particular emphasis on well-established systems and selected derivatives that illustrate their structural diversity and functional versatility.

Table 1:Chronological Overview of Conducting Polymers, Their Discovery, and Main Synthetic Routes where 1 is electrochemical polymerization and 2 is chemical polymerization.

Polymer	**Year of Discovery**	**References**	**Main Synthesis Route**
Polypyrrole (PPY)	1963 then (1979-1980)	[21]	1
Polyacetylene (PA)	1977	[7]	2
Poly(p-phenylene sulfide) (PPS)	Late 1970s	[22]	2
Polyaniline (PANI)	1980-1986	[23], [24], [25]	1
Polyazulene (PAz)	1980s	[26]	2
Polycarbazole (PCz)	1981-1983	[27]	1
Polythiophene (PTh)	1982	[28], [29]	1
Polyfuran (PFu)	1982	[30]	1
Polyisothianaphthene (PITN)	1984	[31]	1
Polyindole (PIn)	Mid-1980s	[32]	1
Poly(p-phenylene) (PPP)	Mid-1980s	[33]	2
Poly(p-phenylene vinylene) (PPV)	1987-1990	[34]	2
PEDOT [Poly(3,4-ethylenedioxythiophene)]	1988-1992	[35]	1
Poly(3-hexylthiophene) (P3HT)	1992	[36]	2
Poly(phenylene ethynylene) (PPE)	Mid-1990s	[37]	2
Polyfluorene (PFO)	Late 1990s	[38]	2
Polyindenofluorene (PIF)	Early 2000s	[39]	2

Regarding their synthesis route**,** there are two major approaches: chemical polymerization and electrochemical polymerization [40]. In chemical polymerization, the monomers are oxidized in the presence of an oxidizing agent, typically in an acidic medium [41]. By contrast, electrochemical polymerization involves the growth and deposition of polymer films directly onto a conducting substrate from a monomer-containing electrolyte solution, where the applied potential or current drives the oxidation of monomers at the electrode–solution interface. The choice between these methods largely depends on the intended application and the specific

material requirements [42]. In recent years, growing interest in nanoscale science and technology has driven the development of CPs with precisely controlled shapes and morphologies. Consequently, a wide variety of nanostructured CPs such as nanofibers, nanotubes, and thin films have been engineered through diverse synthetic strategies to tailor their properties for advanced applications.

1.1.1. Polythiophenes and Their Derivatives

Polythiophene and its derivatives have garnered attention due to their superior environmental and thermal stability, as well as their excellent optical properties compared to other conducting polymers. They have been widely applied in nonlinear optical devices, photochromic modules, polymer LEDs, anticorrosion coatings, and energy storage systems as their electronic and optical behavior can be tuned through chemical modifications or doping strategies. Among the derivatives, poly(3,4-ethylenedioxythiophene) (PEDOT) is particularly important owing to its high electrical conductivity and electro-optical performance. However, it suffers from poor water solubility, which was addressed by incorporating polystyrene sulfonate (PSS) [43]. In the PEDOT:PSS complex, PSS functions both as a dopant and as a stabilizer, yielding materials with enhanced conductivity, mechanical flexibility, and long-term thermal stability by performing solvent treatments, surfactant addition, or optimization of PSS concentration. Polythiophenes have been synthesized through a variety of methods, including the early Yamamoto and Lin–Dudek chemical routes, as well as oxidative polymerization, organometallic coupling and template-assisted or solvothermal techniques [44].

1.1.2. Poly(p-phenylene)s: Doping and Stability

Poly(p-phenylene) (PPP) is a conjugated macromolecule consisting of benzenoid aromatic units linked through C–C bonds. It is known for having exceptional thermal and environmental stability, mechanical rigidity, tunable electronic and optical properties, and ease of doping. PPP can undergo both p-type and n-type doping [45], with conductivity strongly dependent on dopant type and exposure time. Its high modulus and tensile strength, which exceed those of engineering polymers such as polyimides, together with its conjugated backbone, makes PPP valuable not only in optoelectronics (blue-emitting organic LEDs) but also in high-performance structural applications. The intrinsic solubility of PPP is poor; however, it can be improved by attaching flexible side

chains. Its structure and band gap are tunable by doping or chemical modification, and undergoes structural changes depending on the temperature. Several synthetic approaches have been explored to obtain PPP. Early methods included the Wurtz–Fittig and Ullmann coupling reactions, though these routes often gave low molecular weight polymers with irregular structures [46]. More advanced strategies involve oxidative coupling of benzene using Lewis acid/oxidant systems ($FeCl_3$ alone, or $AuCl_3/CuCl_2$ combinations) as well as precursor routes developed by Marvel, Grubbs, and ICI, which allow polymer formation from soluble intermediates. Additional techniques such as reductive polymerization have also been employed.

1.1.3. Polypyrrole: From Chemical Oxidation to Electrochemical Polymerization

Polypyrrole is a very well-known conducting polymer due to its exceptional stability, high conductivity, and ease of polymerization, both as a homopolymer and in composite forms. Initially synthesized through the chemical oxidation of pyrrole monomers using hydrogen peroxide, PPy typically presents as a black, powdery material. In its undoped state, PPy exhibits insulating properties, but upon doping with halogen-based electron acceptors such as bromine or iodine, its conductivity increases significantly which earns it the title of a conductive polymer. Electrochemically synthesized PPy films, demonstrate enhanced stability under ambient conditions and maintain thermal stability up to 300°C [47]. Electrochemical synthesis is the preferred method for producing highly conductive PPy (**Figure 3**), as it allows precise control over film thickness and morphology by adjusting electrochemical parameters.

Despite its advantages, this method is limited by lower yields due to the constrained size of the anode. The polymerization mechanism involves the formation of a radical cation through deprotonation, which subsequently reacts with neutral monomer units. Chain propagation proceeds via reoxidation and further proton loss, with experimental evidence confirming proton release during pyrrole oxidation. Early synthetic routes involved oxidizing pyrrole with hydrogen peroxide, yielding an amorphous, insoluble black powder known as "pyrrole black," which exhibited low conductivity were able to be improved through halogen doping or the use of oxidants such as $FeCl_3$ or Cu(II) salts [48].

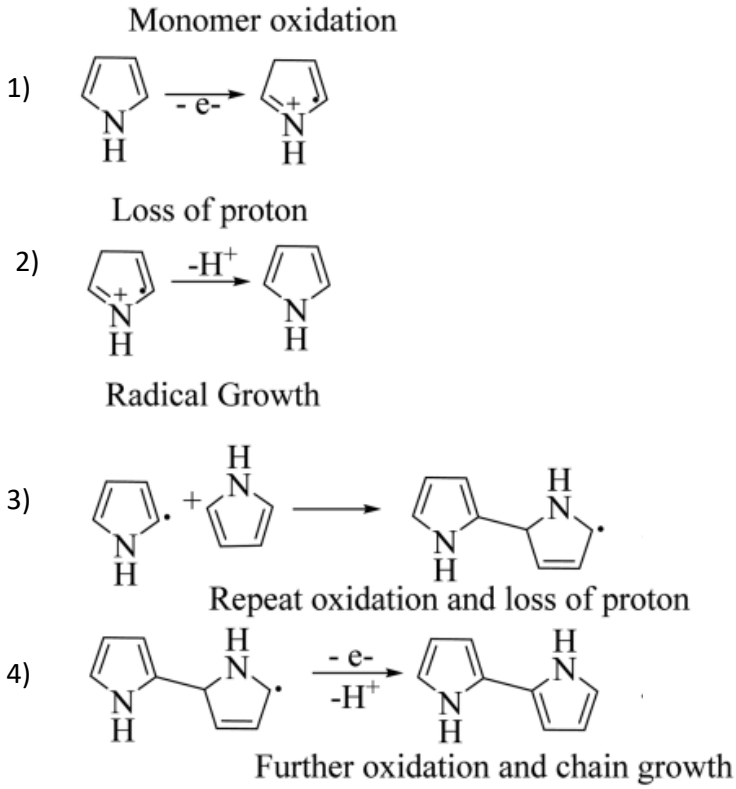

Figure 3: Mechanism of electrochemical synthesis of polypyrrole.

1.1.4. Polyaniline: A Versatile Conducting Polymer

Among the different conducting polymers (CPs), polyaniline **(**PANI**)** is one of the most widely investigated due to its versatility and pronounced redox activity. Its monomer, aniline, is inexpensive and readily available, making PANI highly attractive for large-scale use. The polymer has been known for over a century originally observed as aniline black when aniline was oxidized to form a dark material. However, its significance as a conducting polymer emerged much later. Following the discovery of conductivity in polyacetylene, MacDiarmid and co-workers demonstrated that the emeraldine base (**Figure 4**) form of PANI could be converted into a semiconducting state upon treatment with dilute HCl, a process termed protonic acid doping. This was the first report of proton doping in a polymeric system. Since then, PANI has been synthesized by various chemical and electrochemical methods, doped with a wide range of protonic acids, and studied extensively for numerous applications. Compared with other CPs, PANI stands out due to its straightforward synthesis, low production cost, excellent electrochemical reversibility, high thermal and environmental stability, and well-defined doping/de-doping chemistry [49].

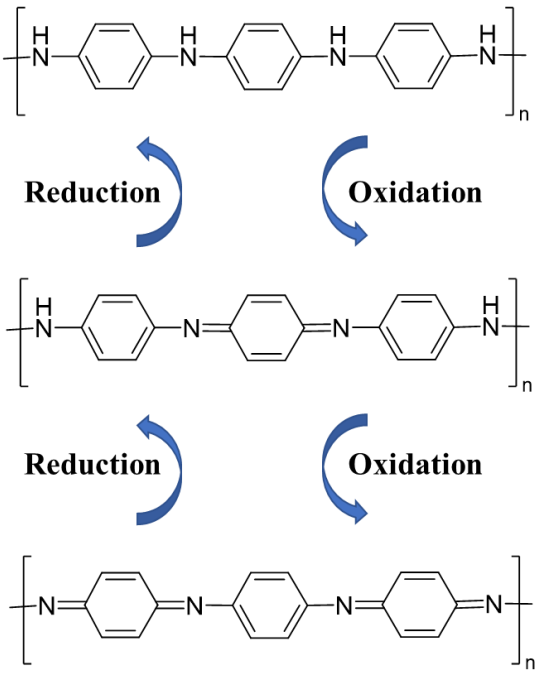

Figure 4: Structural illustration of different forms of polyaniline.

As it is known that electrical conductivity arises only after the generation of internal charge carriers within the polymer backbone. In this case while its structure contains conjugated single and double bonds along with amine lone pairs, it remains insulating until externally doped through partial oxidation or reduction. Doping of PANI can occur through chemical**,** electrochemical**,** photo- or self-doping, with the most common route being protonic acid doping. In this case, the emeraldine base (partially oxidized) is treated with strong acids such as HCl or H_2SO_4. Protonation of the imine nitrogen functions, accompanied by the insertion of counter-anions (Cl^-, HSO_4^-), produces positively charged bipolaron segments that delocalize into polarons, forming a stable polaron lattice and the conductive emeraldine salt. The fully reduced leucoemeraldine form can also be converted into a conducting state via oxidative doping. Chemical oxidants such as halogens, H_2O_2, $FeCl_3$, or $SnCl_3$ are commonly used, though they often lead to side reactions and poor control of doping level. In contrast, electrochemical doping offers precise control, as oxidation occurs directly at an electrode in an acidic electrolyte, with accompanying ion diffusion creating mobile charge carriers (polarons and bipolarons) within the polymer chain [50].

Several synthetic approaches have been developed for PANI, with chemical oxidative polymerization being the most straightforward and widely adopted in the past. In this method, aniline monomers are polymerized in the presence of an oxidizing agent and a dopant acid under ambient conditions. Common oxidants include ammonium persulfate, ceric nitrate, ceric sulfate, and potassium dichromate. A characteristic green color appears during the reaction, signaling the formation of the emeraldine salt form. The same approach can also be used to fabricate composites by introducing additional fillers during polymerization. Other methods have also been applied. Interfacial polymerization is performed at the boundary between an aqueous oxidant/dopant solution and an organic monomer phase (toluene) [51], while microemulsion polymerization employs surfactants to create polymerization sites at the interface of immiscible liquids [52].

Electropolymerization offers another versatile route, producing films directly on electrode surfaces without requiring an external oxidant that leads to the formation of thin films. Furthermore, electrospinning has been utilized to obtain fibrous PANI morphologies with micro- to nanoscale diameters. This method involves applying a strong electric field to polymer droplets, which stretch under electrostatic forces to form fibers deposited on a counter electrode. Electrospinning enables the preparation of bulk fibrous structures of PANI and its composites, including PANI blends with polyethylene oxide or carbon nanotubes. Overall, the wide range of synthetic strategies available for PANI, combined with its tunable conductivity and stability, have made it one of the cornerstone materials in the field of conducting polymers that has applications in advanced technologies, including sensors and biosensors, corrosion inhibition, membrane technology, supercapacitors, fuel cells, lithium-ion batteries, electrocatalysis, and electrochromism [53].

1.2. Metallopolymers: Background Discovery and Synthesis

The development of π-conjugated conducting polymers (CPs) has advanced significantly over the past decades, establishing them as key semiconducting materials for use in optoelectronics as well as electronic devices as mentioned above. Significant progress has been achieved through synthetic innovations and structural modifications, not only by tailoring the polymeric backbone but also by introducing functional side groups to enhance material performance [8]. Among these modifications, the incorporation of metal complexes has proven particularly valuable due to their additional properties and diverse applications, including catalysis [54], sensing [55], and light

emission. The resulting conducting metallopolymers (CMPs) inherit characteristics from both the conjugated polymer framework and the metal moieties, while additional functionalities emerge from the interactions between these two components [56]. Because the metal centers are covalently integrated in the polymer backbone, electron and energy transfer processes can occur more efficiently than in simple blends of conducting polymers and metal complexes, which often suffer from phase segregation and reduced stability.

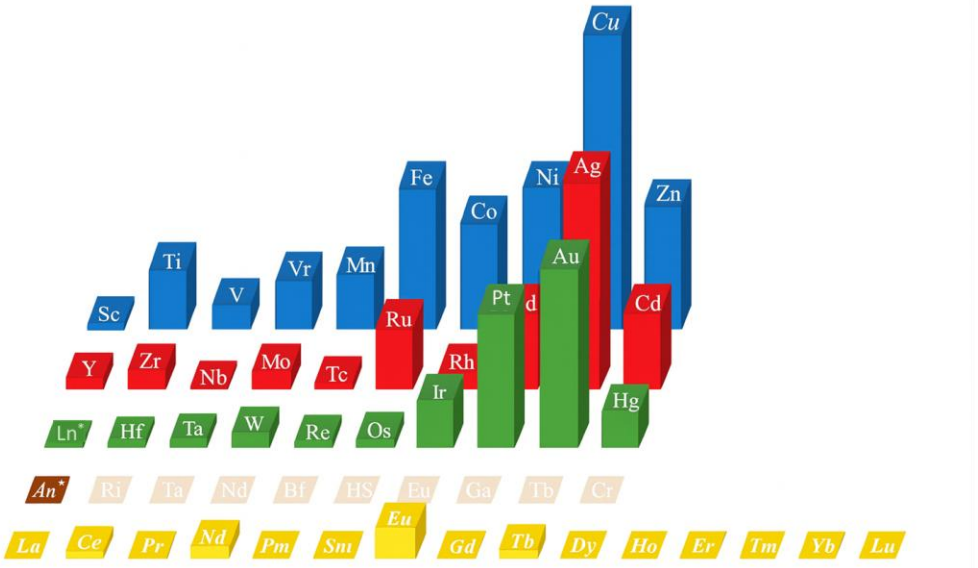

Figure 5: Schematic representation of the d- and f- metal group metals that were utilized in combination polymers together with their number of publications.

Such strong electronic communication enables unique properties, including enhanced redox activity [56], selective small-molecule interactions [57], and direct charge transfer in hybrid semiconductors [58]. These effects highlight the potential of CMPs as multifunctional materials that combine the advantages of both organic CPs and metal coordination complexes, expanding their application in next-generation electronic, optoelectronic, and catalytic systems. Numerous metallopolymers are accessable due to the variation of metal ions, ligands as well as the polymer matrix consisting of various monomers and their respective derivatives. Consequently, a large number of publications regarding metallopolymers, their syntheses and/or applications have been reported with a quantitative representation of the metals used as shown in **Figure 5**.

A well-known classification of CMPs was proposed by Wolf in the past **(Figure 6)**, which categorizes them according to how the metal centers are incorporated into the polymer backbone

[59], [60]. As the field has evolved, it has become evident that not only the point of attachment but also the coordination environment of the metal ions plays a crucial role in determining the structural and functional properties of CMPs [61]. In Wolf Type I CMPs, the metal centers are attached to the polymer backbone through insulating linkers typically flexible alkyl chains resulting in minimal or no direct electronic communication between the organic backbone and the metal sites. From a coordination perspective, the metal ions may bind to the polymer either via single or multiple organic linkers, with or without additional auxiliary ligands to stabilize the coordination sphere**.** In Wolf Type II CMPs, the metal centers are covalently bound directly to the conjugated backbone, leading to strong electronic coupling between the two components. When a conjugated unit is inserted between the polymer main chain and the metal center, the strength of the interaction can be moderated while still maintaining efficient electron and/or energy transfer. This provides flexibility in tuning the overall properties of the polymer. In Wolf Type III CMPs, the metal centers become integral components of backbone the conjugated itself. In this arrangement, the metals not only provide structural stability but also engage in strong electronic interactions with the organic bridges. As a result, the optical and electronic properties of these systems are highly sensitive to electronic changes within the polymer chain.

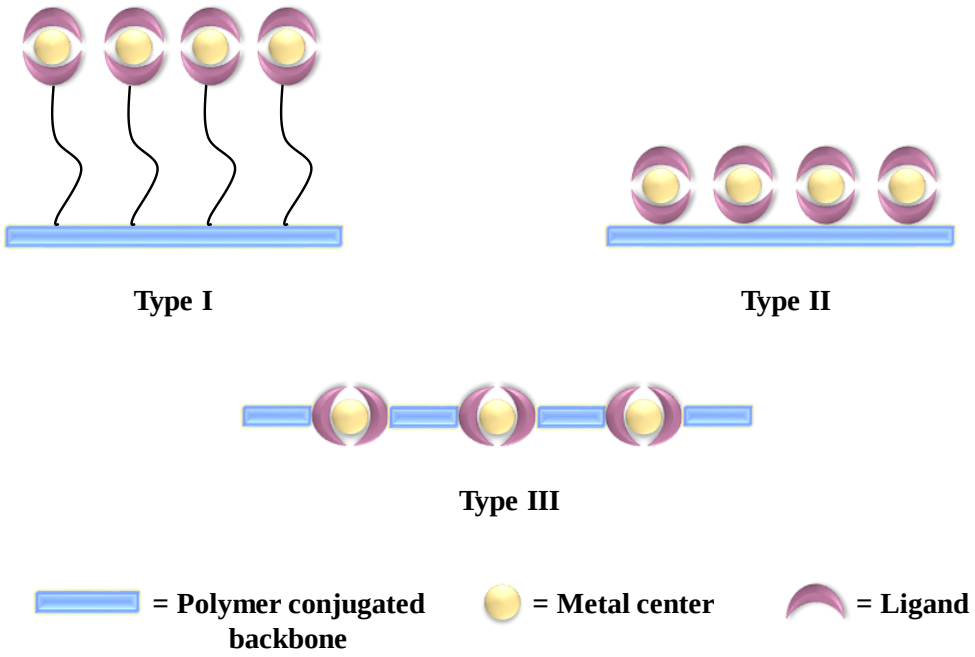

Figure 6: Possible arrangements of metal ions within metal-containing polymers (classification according to Wolf).

The overall properties depend strongly on the coordination geometry and number of coordination contacts around the metal. For example, a square-planar geometry often facilitates extension of the π-conjugation, whereas octahedral or other geometries may either extend or disrupt conjugation depending on the ligand arrangement. Because of their strong electronic communication and high tunability, Wolf Type III CMPs have received significant attention and are among the most widely investigated subclasses.

1.2.1. Metallopolymers formed using Electropolymerization

As mentioned above, conducting polymers such as PANI and PPY were formed using electropolymerization and this technique has expanded beyond only aniline-based systems where it reached the incorporation of this strategy to form metallopolymers. A variety of electrochemical techniques can be employed for electropolymerization, most commonly potentiostatic and galvanostatic methods, where the potential or current is held constant, and potentiodynamic approaches, where these parameters are varied. Although the fundamental polymerization mechanism is essentially independent of the selected method, the resulting film morphology in the

solid state is strongly influenced by the applied technique. The choice between static and dynamic modes often determines film characteristics such as homogeneity and adhesion to the substrate, though the optimal conditions are largely system-dependent [62].

The selection of electrode material is similarly dictated by the intended purpose of the electropolymerized film. For routine electrochemical characterization or proof-of-concept experiments, conventional working electrodes such as glassy carbon, platinum, or gold are typically employed. In contrast, when spectroscopic analyses are required or when the films are designed for optoelectronic applications (polymer light-emitting diodes, photovoltaic devices, or electrochromic components), transparent conductive substrates such as indium tin oxide (ITO) or fluorine-doped tin oxide (FTO) are preferred [63].

1.2.2. Polymers Containing Polypyridyl Complexes

In 1932, Morgan and Burstall reported the synthesis of 2,2':6',2''-terpyridine (tpy) [64] which contains three coordination sites belonging to N-heteroaromatic rings which is presented in **Figure 7** [65]. In the recent decades this ligand has been gaining a lot of attention due to its various applications in different fields. For example, complexes of terpyridine played an important role in the biological field where it was discovered that they can bind to DNA through intercalation in the 1970s [66]. Furthermore, these compounds have been used in many chemistry related fields such as electrocatalysts for proton and CO_2 reduction, as catalysts for C-C bond formation [67], as photosensitizers [68], supramolecular chemistry [69] and as redox shuttles for dye-sensitized solar cells [70].

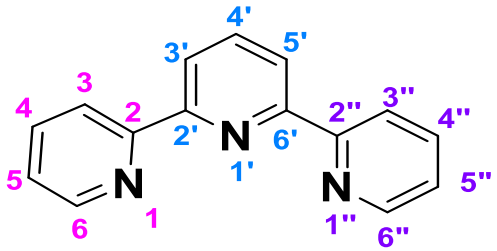

Figure 7: Structural representation of the terpyridine framework.

As the terpyridine molecule behaves as a tridentate ligand [65], there are two possible complexes, the mono-tpy and the bis-tpy complexes that are presented in **Figure 8**, where the ligand is

bounded to the metal, M, in a nearly planar geometry [71]. The stability of the bis-tpy complexes is directly related to the metal cations in the complex, and the binding affinity towards the transition metals is as follows: $Cd^{2+} < Zn^{2+} < Fe^{2+} < Os^{2+} < Ru^{2+}$ [72]. Recently, different complexes using different metal centers have been synthesized and characterized such as Fe [64], Ni [73], Os [73], Ru [74], Pt [75], and Zn [76] based complexes. This is the reason why tpy nowadays is considered an excellent ligand in coordination chemistry.

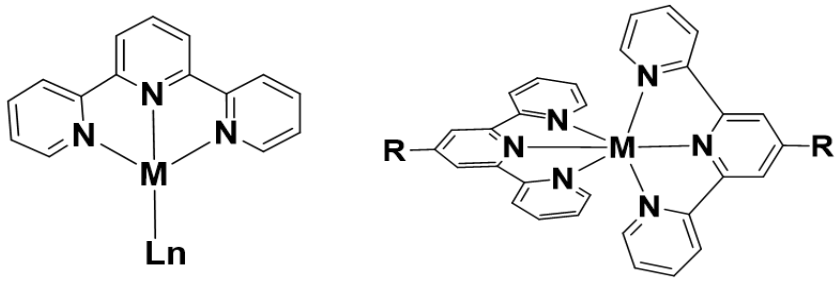

Figure 8: Two possible complex structures of the tpy-based metal complexes where Ln is any ligand set bound to M.

At the C4' position, a lot of functional groups can be added such as hydroxyl groups [77] or methanesulfonyl groups [78] along with chloro or bromo substituents [79]. These ligands are also redox-active that can be reduced several times. Therefore, the metal complexes based on this ligand present interesting electrochemical properties [80]. Furthermore, the ligand has one important advantage over the bidentate ligand which is 2,2'-bipyridine (bpy), where the terpyridine complexes $[M(tpy)_2]^{n+}$ unlike the bypridine complexes $[M(bpy)_3]^{n+}$, are achiral which is important in the case of multinuclear systems [81], [82] that is explained later.

In the case of Type III metallopolymers, substituted terpyridines, bipyridines, phenanthrolines, and pyridines have been employed as polymerizable ligands to incorporate Fe(II), Ru(II), and Os(II) centers directly into the polymer backbone [83], [84]. Constable, Forster, and co-workers systematically investigated the effect of monomer size on the reactivity and conductivity of Ru(II) and Os(II) terpyridine complexes bearing thienyl, bithienyl, or terthienyl substituents [85]. While monothienyl complexes such as $[Ru(tpy)_2]^{2+}$ and $[Os(tpy)_2]^{2+}$ generated highly reactive radical cations during oxidative polymerization, requiring rigorously anhydrous conditions and $BF_3 \cdot OEt_2$ as solvent, the corresponding bi- and terthienyl analogues could be electropolymerized under milder conditions. In situ conductivity measurements revealed that charge transport was significantly enhanced when the redox potentials of the metal center and the bridging unit were

closely matched. Alternative synthetic strategies were also explored by Forster and Meyer, who demonstrated polymerization of aminophenanthroline and vinylbipyridine complexes in unconventional media such as ionic liquids [86] and SiO_2 sol–gel films [87]. Type II metallopolymers were obtained from heteroleptic polypyridyl complexes carrying two polymerizable substituents on a single ligand, ensuring their incorporation into the main chain. Systems based on Ru(II), Ir(III), and Eu(III) complexes were reported. Notably, Holliday and co-workers introduced an emissive Ir(III) complex into a conjugated polymer with the aim of generating polymer light-emitting diodes (PLEDs); however, the resulting materials were non-emissive due to stabilization of a ligand-centered triplet state that suppressed metal-to-ligand charge transfer (MLCT) [88].In contrast, Eu(III)-based polymers displayed strong, purely metal-centered photoluminescence, making them promising candidates for optoelectronic applications [89]. Type I metallopolymers, featuring pendant metal complexes attached via insulating linkers, were also widely studied. These included Ru(II) systems [90], as well as Co(II) [91] and Cu(II) [92] derivatives. Cosnier and co-workers demonstrated that electropolymerization of pyrrole-functionalized $[Ru(bpy)_3]^{2+}$ complexes on carbon nanotube (MWCNT) electrodes yielded films with higher polymerization efficiency and enhanced electroactivity compared to those grown on platinum substrates [90]. Fujihara and colleagues further extended this concept by functionalizing gold nanoparticles with both $[Ru(tpy)_2]^{2+}$ complexes and electropolymerizable pyrrole units, enabling the fabrication of metal–polymer nanocomposite films [93].

In addition, metallopolymers with metal centers incorporated into the backbone and laterally attached 2,2′-bipyridine ligands have been synthesized from Ru(II), Re(II), and Os(II) precursors [94], [95], [96]. Wasberg and co-workers investigated the electropolymerization mechanism of $[Ru(bpy)(CO)_2Cl_2]$ complexes, which afforded Ru(0)-based metallopolymer films capable of catalyzing CO_2 reduction [97], [98]. Partial oxidation of such metal–backbone polymers resulted in conductivities as high as 0.3 $S \cdot cm^{-1}$ [99]. A related approach was developed by Chardon-Noblat, Deronzier, and co-workers, who synthesized a $[Ru(bpy)(CO)_2(CH_3CN)]_2^{2+}$ dimer bearing an electropolymerizable pyrrole group covalently attached to the bipyridine unit. This design enabled two distinct anodic and cathodic electropolymerization pathways, leading to the controlled formation of cross-linked metallopolymer networks suitable for electrocatalytic CO_2 reduction.

These complexes usually are multielectron systems so the electronic Schrödinger equation cannot be solved in this case. Therefore, electronic wavefunctions of a molecular system can be expressed as products of one electron wavefunctions, where each consist of an orbital and a spin part.

$$\Psi = \Phi S = \prod \varphi_i \, s_i$$

The φ_i are the molecular orbitals (MO) and the s_i is one of the two possible spin states. Normally, the orbital part of this multielectron wavefunction defines the electronic configuration to which the electronic state belongs to. Many inorganic molecules of electrochemical interest are coordination compounds of transition metals which have an octahedral geometry. The molecular orbitals are classified to their predominant atomic orbital contribution such as:

1. Strongly bonding, ligand centered σ_L orbitals.
2. Bonding, ligand centered π_L orbitals.
3. Non-bonding π_M (t_{2g}) metal centered, d orbitals.
4. Antibonding σ_M^* (e_g) metal centered, d orbitals.
5. Ligand centered antibonding π_L^* orbitals.
6. Antibonding, metal centered σ_M^* orbitals.

Usually, for an octahedral complex with a d^n metal ion, regarding the electronic configuration of the ground state, the orbitals 1 & 2 are completely filled whereas in orbitals 3 and 4 only n electrons occupy these orbitals. Therefore, excited configurations are achievable starting from ground state configurations by promoting the excitation of one electron from an occupied MO to a vacant MO as presented in **Figure 9**.

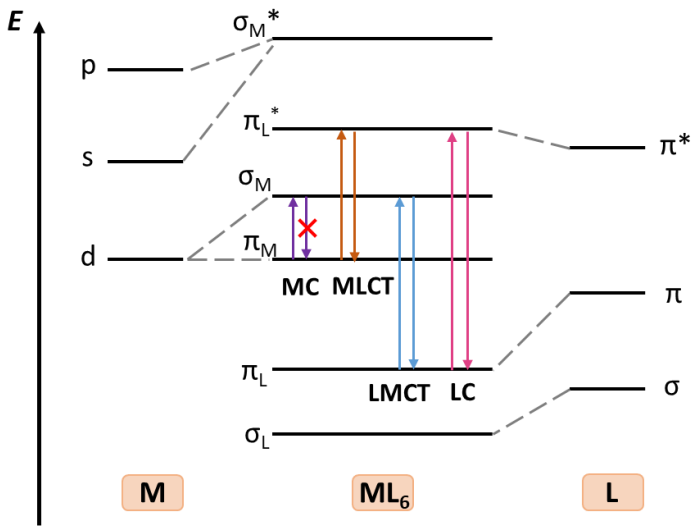

Figure 9: Molecular orbital diagram for an octahedral metal complex, the arrows indicate the types of transitions based on MO configuration.

Therefore, at low energy it is possible to find different electronic transitions such as:

Metal centered, MC, transitions from orbitals of type 3 to orbitals of type 4.

1. Ligand centered, LC, transitions from 2 to 5.
2. Ligand to metal charge transfer, LMCT, from 3 to 5.
3. Metal to ligand charge transfer, MLCT, from 2 to 3

The relative energy ordering of these types of configurations in any specific complex very much depends on the nature of the metal and the ligands, as seen in commonly used coordination complexes such as $[Ru(bpy)_3]^{2+}$ and $[Fe(bpy)_3]^{2+}$.

1.2.2.1. Ruthenium Polypyridine Complexes

Over the past two decades, Ru (II)-polypyridine complexes have garnered significant interest due to their distinctive combination of ground and excited state Properties [100]. A typical example is the well-known tris(2,2′-bipyridine) ruthenium(II) complex, $[Ru(bpy)_3]^{2+}$, which has found widespread application as a photoluminescent compound and as an excited-state reactant in energy and electron transfer processes. Originally reported as a luminescent species in fluid solution by Paris and Brandt in 1959 [101], $[Ru(bpy)_3]^{2+}$ has since become the prototype for the design and development of increasingly complex photoactive molecules. The absorption spectrum of ruthenium bipyridine complexes is dominated by a strong metal-to-ligand charge transfer (MLCT)

band in the visible region. Specifically, $[Ru(bpy)_3]^{2+}$ exhibits a prominent MLCT absorption maximum around 450 nm, as shown in **Figure 10**. In contrast, ligand-centered (π–π^*) transitions occur at higher energies (typically near 185 and 285 nm), display high molar extinction coefficients, and are primarily associated with the electronic structure of the ligands. Additionally, weak spin-forbidden d–d (metal-centered) transitions can also be observed at longer wavelengths (e.g, 322 and 344 nm), corresponding to electronic excitation from t_2g to eg orbitals [102]. The oxidation of $[Ru(bpy)_3]^{2+}$ complexes typically involves electron removal from a metal-centered orbital, leading to the formation of Ru(III) species. These oxidized Ru(III) centers exhibit considerable inertness toward ligand substitution. The oxidation potential for $[Ru(bpy)_3]^{2+}$ generally lies within a narrow range around +1.25 V versus NHE. However, this potential can be significantly altered by substituting one or more bipyridine ligands with structurally related ones. On the other hand, reduction of the $[Ru(bpy)_3]^{2+}$ complex occurs at the ligand's π^* orbital, at approximately –1.46 V, which is typically the same orbital involved in metal-to-ligand charge transfer (MLCT) transitions. Notably, the photo-excited state of $[Ru(bpy)_3]^{2+}$ possesses higher energy than the ground state, rendering it both a stronger oxidizing and reducing agent.

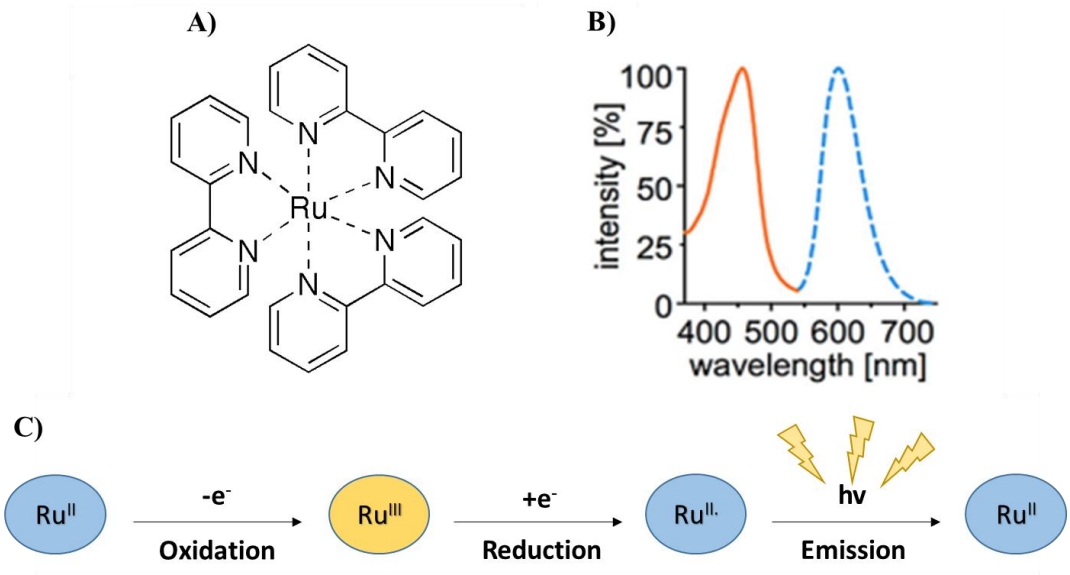

Figure 10: (a) Structure of the complex, (b) absorbance and emission spectrum of $[Ru(bpy)_3]^{2+}$, (c) Reactivity of $[Ru(bpy)_3]^{2+}$. Originally the complex has Ru^{II}, which can be oxidized with $(NH_3)_2Ce(NO_3)_6$ to Ru^{III}, which can also be reduced to Ru^{II}*, an excited-state metal complex that emits a photon upon decay trough a normal fluorescence. [103]

1.2.3. Bipyridine Complexes vs Terpyridine Complexes

From the perspective of excited-state properties, bipyridyl ligands are better than terpyridine ligands for complexation with ruthenium(II) centers. A well-known example is the $[Ru(bpy)_3]^{2+}$ complex, which, at room temperature in fluid solution, exhibits strong and long-lived luminescence originating from its triplet metal-to-ligand charge transfer (^{3}MLCT) state. The ^{3}MLCT lifetime typically reaches around 1000 nanoseconds. In contrast, $[Ru(tpy)_2]^{2+}$ displays negligible luminescence under similar conditions, with a considerably shorter ^{3}MLCT lifetime of approximately 250 picoseconds. This difference arises from differences in non-radiative deactivation pathways. In both cases, the primary quenching mechanism at room temperature involves thermally activated crossing from the ^{3}MLCT state to a higher-lying, distorted triplet metal-centered (^{3}MC) excited state.

Terpyridine, due to its unfavorable bite angle for octahedral coordination, generates a weaker ligand field compared to bipyridyl ligands. As a result, the energy gap between the ^{3}MLCT and ^{3}MC states is smaller in tpy complexes, promoting faster non-radiative decay via the ^{3}MC pathway. From a structural standpoint, terpyridine (tpy)-based bridging ligands offer notable advantages over their bidentate counterparts, particularly in the design of metal complexes. One significant reason lies in the differing coordination geometries and the resulting stereochemical implications. As illustrated in **Figure 11**, complexes formed with bidentate ligands, such as 2,2'-bipyridine (bpy), can exhibit stereoisomerism due to the nature of six-coordinate metal centers. For instance, the homoleptic complex $[Ru(bpy)_3]^{2+}$ exists in two enantiomeric forms (Λ and Δ). When the two donor nitrogen atoms are chemically non-equivalent, as in mono-substituted bipyridines, both geometrical (facial and meridional) and optical isomers can arise, further complicating the stereochemistry.

In contrast, ruthenium complexes coordinated with two tridentate terpyridine ligands such as $[Ru(tpy)_2]^{2+}$ form structurally simpler, achiral species. The octahedral coordination of the metal center by the two rigid, planar tpy ligands results in a well-defined geometry without the formation of stereoisomers. Even upon introducing substituents at the 4'-position of each tpy unit, the global symmetry of the complex is largely retained, and no additional geometric isomers are generated.

This structural rigidity and simplicity make terpyridine-based ligands highly appealing for applications requiring uniformity and predictability in metal coordination environments [104].

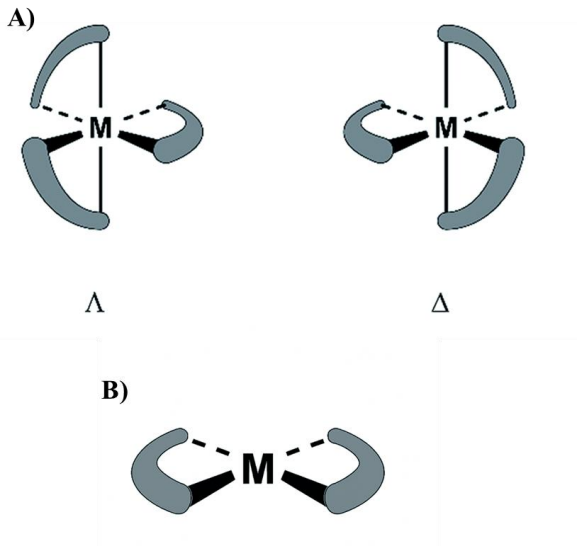

Figure 11: (a) Schematic representations of the two chiral isomers of $[Ru(bpy)_3]^{2+}$complex, (b) unique form of $[Ru(tpy)_2]^{2+}$.

1.3. Methods to Functionalize Electrode Surfaces

In recent years**,** significant advancements have been made in electrode surface modification techniques, driven by a broad range of applications including solar energy harvesting and storage, targeted electroorganic synthesis, molecular electronics, and electrochromic display technologies [105], [106]**.** These modification strategies have evolved over the years, as the interest in forming uniform thin films on conductive electrodes has rised as each strategy targets specific compounds for their unique applications. Some well-known procedures used are spin-coating, ink-jet printing, doctor blading, drop-casting, and electropolymerization which are explained below.

1.3.1 Coating-Based Methods

A lot of coating methods are pretty well known in facilitating the functionalization of electrode surfaces with different compounds and molecules. In general, there are four different coating methods to deposit on the electrode surface which are: Dip coating, Spin coating, Spray coating, and Drop coating which are presented in **Figure 12**.

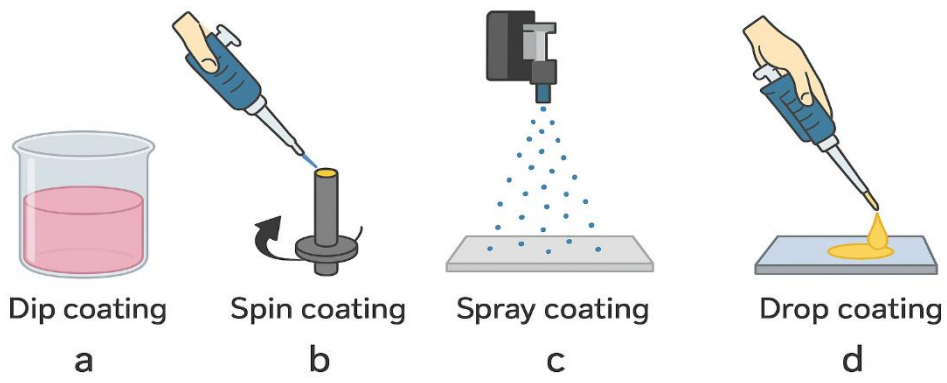

Figure 12: Schematic representation of the four coating methods for the deposition on the electrode surfaces.

1.3.1.1. Dip Coating

It is a straightforward technique for electrode surface modification [107] involves immersing the electrode in a polymer suspension for a defined duration, allowing a polymer film to adsorb onto the surface (Fig. 12a). The thickness of the resulting film can be adjusted by tuning parameters such as incubation time, polymer concentration in the suspension, and mass transfer dynamics. Although this dip-coating method is cost-effective and consumes minimal material, it is limited by a relatively slow deposition process and often results in partial or uneven coverage of the electrode surface. To address these limitations, spin coating is commonly employed as an alternative, offering improved uniformity.

1.3.1.2. Spray Coating

Spray coating is another widely used technique for depositing thin and uniform films onto electrode surfaces, offering the advantage of a large electrochemically active area (Fig. 12c) [108]. In this method, a suspension containing the modifying material is atomized and directed onto the electrode surface using a nozzle or a carrier gas system. As the spray contacts the surface, the solvent evaporates, leaving behind a homogeneous film. The uniformity and reproducibility of the deposited layer can be finely tuned by adjusting parameters such as the spray distance, droplet size, and flow rate. Despite its advantages in producing consistent and scalable coatings, spray coating often requires significant material consumption and relies on costly specialized equipment.

1.3.1.3. Spin Coating

Spin coating is a technique that produces smooth, laterally uniform films on electrode surfaces (Fig. 12b). A microlitre-scale of the catalyst–polymer composite is dispensed onto the substrate, which is then accelerated to a set rotational speed (typically ~2000 rpm), held for a defined time, and gradually decelerated while the solvent evaporates. Film thickness is governed by the properties of the deposited phase (e.g., viscosity, concentration, solvent volatility) and by processing parameters such as dispensed volume, acceleration profile, angular velocity, and spin time, yielding layers from several nanometres to several micrometres [109]. Spin coating is well suited to screen-printed electrodes and offers excellent uniformity and reproducibility, but it requires dedicated, relatively expensive equipment to be used.

1.3.1.4. Drop Coating

This simple, widely used method prepares chemically modified electrodes by dispensing a defined volume of a modifier-containing solution or suspension onto the substrate and allowing it to dry under UV irradiation, under a nitrogen stream, or at ambient conditions (Fig. 12d) [110]. Deposition is rapid (on the order of ~1 min) and straightforward, and the same stock suspension can be reused. The deposited mass scales with droplet volume and solute concentration, allowing an approximate estimate of the number of monolayers formed over the coated area. Principal limitations include particle agglomeration, spatial non-uniformity, and drying artifacts such as the "coffee-ring" effect, in which capillary flows drive material to the droplet edge and leave a ring-like residue. Despite these drawbacks, drop coating remains attractive for quick fabrication and screening of modified electrodes.

1.3.2. Layer-by-Layer Assembly

Layer-by-layer (LbL) self-assembly is a well-established technique for fabricating ultrathin films on solid substrates through the sequential adsorption of oppositely charged species. This process, often described as an alternating deposition method, involves the alternate exposure of the substrate to positively and negatively charged materials, resulting in the immediate formation of layers via electrostatic interactions. Since the early development of the Langmuir-Blodgett (LB) method, which enabled the deposition of charged species in thin film form, the assembly has become a widely adopted strategy for constructing multilayered architectures with precise control over film thickness and composition. Layer-by-layer technique, as a bottom-up approach, offers

the advantage of enabling the design and fabrication of tailor-made molecular systems with precise control over structure and composition as shown in **Figure 13**.

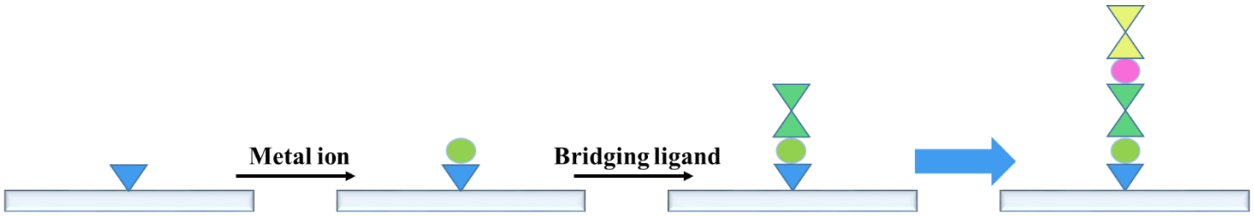

Figure 13: Layer-by-Layer assembly on electrode surface.

The resulting multilayers typically exhibit highly ordered nanoscale features, with structural properties influenced by the nature of the organic or inorganic materials employed. Subsequent innovations in the field have led to the development of methods for assembling oppositely charged colloidal particles and sequentially layering metal ions to produce polycrystalline coatings on various substrates, including glass. In addition to its structural versatility, it is valued for its simplicity, robustness, and minimal equipment requirements. The technique relies on straightforward physicochemical principles and can be readily optimized through control of stoichiometric ratios, without the need for complex chemical synthesis or reactions.

1.3.3. Electropolmyerization on Electrode Surfaces

Electropolymerization is a highly effective method for modifying electrode surfaces due to its precision, scalability, and ability to produce uniform, adherent polymer films under mild conditions. Unlike spin coating or layer-by-layer assembly, electropolymerization allows for direct control over film thickness and morphology by adjusting electrochemical parameters such as potential, current, and deposition time [111] while also providing simultaneous polymer formation and film deposition. This method is particularly advantageous for creating conducting polymer films such as polyaniline because it enables the formation of π-conjugated systems with tunable electronic and optical properties [112]. The process involves oxidizing monomers at the electrode surface, leading to polymerization and deposition, which results in films with strong adhesion and stability [111]. Additionally, electropolymerization facilitates the incorporation of functional groups or dopants during film growth, enhancing the electrochemical activity and selectivity of the modified electrodes [113]. This technique is widely used in applications such as organic

electronics, biosensors, and energy storage, where tailored interfacial properties are critical [113]. It encompasses both oxidative and reductive electropolymerization.

The most widely employed electrochemical approach for synthesizing the conducting polymers is the anodic oxidation of suitably functionalized monomers. In contrast, cathodic electropolymerization is far less commonly utilized. During anodic polymerization, both the formation of the polymer film and the simultaneous incorporation of counterions (doping) occur as a direct result of monomer oxidation. Typically**,** the oxidation potential required to initiate monomer polymerization is significantly higher than that needed for the subsequent charging of the oligomeric intermediates or the resulting polymeric film. Although this technique is well established, the underlying mechanism of electropolymerization remains only partially understood and has been described through several differing models and interpretations in the literature [114], [115].

1.4. Electrografting of Organic Groups

An important method for adhering organic layers onto substrate surfaces is electrografting. This term specifically refers to the covalent attachment of organic molecules to solid conducting substrates through electrochemical reactions, thereby modifying the surface properties. The covalent bonding achieved in electrografting is often described as chemisorption, which is considerably stronger than physisorption [116]. The general mechanism of electrografting involves the electrochemical generation of radical species either through oxidation or reduction of the organic precursors, followed by their subsequent chemisorption onto the electrode surface. A wide range of reagents, including amines, alcohols, carboxylates, Grignard reagents, vinylic compounds, and diazonium salts, can be employed for this purpose. Among these, reductive strategies are particularly common for the electrografting of vinylic and diazonium salts on conductive substrates, while amino-bearing compounds have also been widely applied.

The molecular layers formed by electrografting are typically thin and are characterized using electrochemical methods in combination with spectroscopic techniques such as infrared spectroscopy (IR), X-ray photoelectron spectroscopy (XPS), and atomic force microscopy (AFM). These modified surfaces find applications in diverse fields including chemical sensing, molecular electronics, corrosion inhibition, energy conversion, and the fabrication of composite materials [117]. Furthermore, the grafted molecules, when functionalized with specific moieties, provide

reactive platforms that can be exploited for the adhesion of additional materials, such as polymers, to electrode surfaces [118].

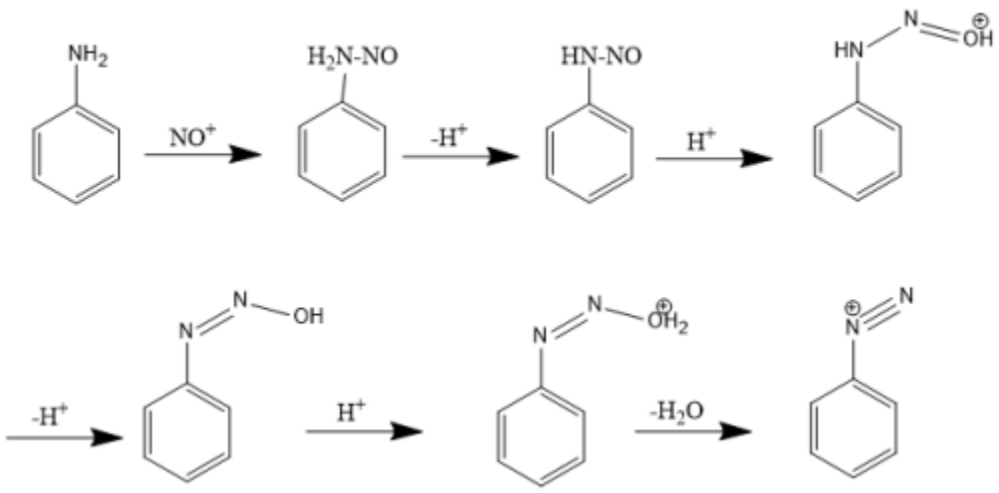

Figure 14: Reaction mechanism of diazonium salt formation in acidic aqueous solution.

Aromatic diazonium salts ($ArN_2^+ X^-$) have been well known for decades and are widely used in the synthesis of azo dyes [119]. A key feature of these salts is their ability to undergo dediazonation, i.e., the loss of molecular nitrogen (N_2), which can yield either aryl radicals or aryl cations. In the context of electrografting, the homolytic dediazonation pathway is preferred, as it generates aryl radicals capable of covalently binding to the electrode surface. Diazonium salts exhibit good stability in strongly acidic media (pH ~2–3), whereas under neutral or alkaline conditions they readily convert into diazohydroxides and diazoates, respectively [116]. They are typically synthesized in a straightforward manner from aromatic amines. The conventional route involves the reaction of an aromatic amine with sodium nitrite in an aqueous acidic solution at low temperature. Upon completion of the reaction, the resulting diazonium salt is isolated by filtration and washing. The mechanism of diazonium cation formation is illustrated in **Figure 14** [120]. Alternatively, diazonium salts can be generated *in situ*. This is achieved by introducing the precursor species namely, an aromatic amine and sodium nitrite, into an aqueous acidic solution, thereby producing the diazonium cation directly in the electrolyte. The freshly formed species can then undergo electrochemical reduction and be grafted immediately onto the electrode surface [121].

1.5. Introduction to Electrochromism

The term electrochromism was first introduced by Platt in 1961 that describes the visible color changes that is induced by an external electric stimulus that gives rise to reversible oxidation-reduction reactions [122], [123]. These materials typically transition between colored and bleached (colorless) states in response to electrochemical stimuli [123]. When a material exhibits multiple distinct colored states across different redox levels, the phenomenon is referred to as multielectrochromism or polyelectrochromism [124]. However, the foundational observations of color changes driven by redox reactions trace back much earlier. In 1815, the chemist Jöns Jacob Berzelius documented the reduction-induced transformation of tungsten trioxide (WO_3) from pale yellow to deep blue [125]. Similarly, during the 1840s, the advent of photography and the use of Prussian blue (PB) marked the early exploration of redox-based coloration through electron transfer processes [126].

The systematic investigation of electrochromic behavior advanced significantly in the 20th century. Early electrochromic devices (ECDs) utilizing materials such as iodine, silver, molybdenum trioxide (MoO_3), and tungsten trioxide (WO_3) were developed during this period. A key milestone was reached in 1969 when Deb proposed a comprehensive concept of electrochromic devices [127]. This was further substantiated by his 1973 report, which demonstrated a functional ECD comprising a WO_3 thin film immersed in an ion-containing electrolyte—widely regarded as the formal inception of electrochromic technology [128].



Figure 15: Electrochromic smart glass showing different states from SageGlass.com

Since then, the field has witnessed rapid growth, with extensive research dedicated to synthesizing and characterizing a wide array of electrochromic materials, including transition metal oxides, conjugated organic polymers, and hybrid systems. These efforts have aimed not only to improve the performance of electrochromic materials but also to elucidate their underlying coloration and bleaching mechanisms [129], [130]. Today, electrochromic materials and devices represent a dynamic area of research, attracting the attention of scientists and engineers alike. Significant advancements have been made toward improving their optical contrast, switching speed, durability, and energy efficiency. Applications are broad and impactful, encompassing smart windows as shown in **Figure 15**, flexible displays, and other adaptive optical systems [131], [132], [133].

1.5.1. Electrochromic Materials

The electrochromic materials are divided into 3 main categories which are inorganic, organic, and other materials such as metal complexes and polynuclear transition-metal hexacyanometallates. And nowadays, hybrid materials based on inorganic and organic EC materials are becoming more and more popular due to the synergistic effects obtained through hybridization [122].

A significant class of inorganic electrochromic (EC) materials consists of transition metal oxides (TMOs) that are stated in Table 2, which are widely studied due to their pronounced color contrast and high photochemical stability [134]. Electrochromic behavior has been observed in oxides of various transition metals, including chromium, cobalt, copper, iridium, iron, manganese, nickel, palladium, rhodium, ruthenium, titanium, tungsten, and vanadium. Among these, materials such as tungsten trioxide (WO_3), molybdenum trioxide (MoO_3), iridium dioxide (IrO_2), and nickel oxide (NiO) exhibit strong electrochromic responses, with the ability to switch between transparent and deeply colored states. Others undergo transitions from one vibrant color to another of lower intensity [125]. The electrochromic behavior in TMOs is primarily driven by redox reactions, which involve electron transfer accompanied by the insertion or extraction of counter ions (e.g., H^+, Li^+, Na^+). This process alters the material's electronic structure, leading to visible color changes. Specifically, coloration arises from intervalence charge transfer transitions electron movements within the valence band between different metal oxidation states. This optical intervalence charge transfer is considered the fundamental mechanism responsible for the color changes observed in TMOs [135].

Table 2: Electrochromic transition metal oxides and their EC properties

Insertion type	Ion insertion	Color oxidized state	Reduced state
Cathodically	MoO_3	Transparent	Blue
	V_2O_5	Yellow	Blue-Black
	Nb_2O_5	Yellow	Blue
	WO_3	Transparent	Blue
Anodically	$Ir(OH)_3$	Blue-black	Transparent
	$Ni(OH)_2$	Brown-bronze	Transparent or pale-green

Tungsten trioxide (WO_3) is among the most extensively studied electrochromic (EC) materials within the class of transition metal oxides and has already found use in a variety of commercial applications. In its oxidized state (W^{6+}), thin films of WO_3 are typically colorless or exhibit a pale yellow hue. Upon electrochemical reduction, the material undergoes a color change to deep blue. This transition is attributed to the partial reduction of W^{6+} to W^{5+}, accompanied by the insertion of charge-balancing cations and electrons, where there are small cations such as H^+, Li^+, or Na^+ [136], [137]. The identity and size of the inserted cation play a crucial role in determining the reversibility, speed, and stability of the redox process. Among these, protons (H^+) and lithium ions (Li^+) are most commonly employed due to their small ionic radii, which facilitate faster diffusion and improved electrochemical reversibility [138]. Additionally, the electrochromic performance of WO_3 is highly dependent on its morphology and structural characteristics. Variations in crystal phase, porosity, particle size, and surface area can significantly influence coloration efficiency, switching speed, and cycling stability. Tailoring the nanostructure of WO_3 such as using nanorods, nanoparticles, or mesoporous films has been shown to enhance its EC response by improving ion transport pathways and surface reactivity [139], [140].

1.5.2. Typical Organic EC Materials

In organic EC materials, conjugated polymers and small molecular materials exhibit interesting electrochromic properties.

1.5.2.1. Conjugated Polymers

Conjugated polymers (CPs), also referred to as conducting polymers that were described previosly, are a class of organic materials capable of conducting electricity. Their electrical conductivity arises from a backbone structure consisting of alternating single and double bonds. This conjugation imparts unique and tunable optical and electronic properties, making CPs highly attractive for electrochromic applications. These polymers are typically synthesized through the polymerization of aromatic monomers such as pyrrole, aniline, thiophene, furan, carbazole, azulene, and indole [141]. Like transition metal oxides (TMOs), CPs exhibit electrochromism through the insertion and extraction of electrons and ions during redox processes. These changes in electronic structure are directly responsible for the observed color transitions. The color displayed by a conjugated polymer is determined by its band gap, which is the energy difference between the highest occupied molecular orbital (HOMO, often referred to as the valence band) and the lowest unoccupied molecular orbital (LUMO, or conduction band). During redox switching, the introduction of charge carriers (e.g., polarons or bipolarons) can generate new electronic states within the band gap, thereby altering the material's optical absorption and leading to a visible change in color [141], [142]. Due to their structural versatility and tunable electronic properties, conjugated polymers are key materials in the development of flexible, lightweight, and multi-color electrochromic devices.

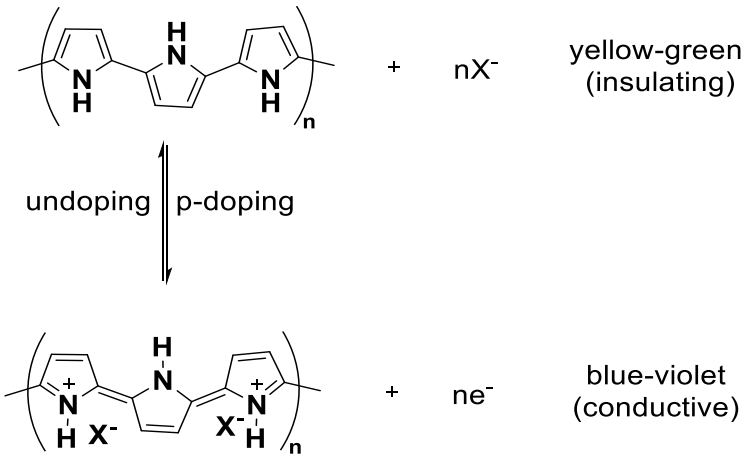

Figure 16: The p-doping and undoping process of poly(pyrrole) thin films.

The insertion of charge carriers into conjugated polymers (CPs), commonly referred to as doping, is a fundamental process that enables their electrochromic behavior. Doping can be classified into two main types: p-doping and n-doping. P-doping involves the oxidation of the polymer backbone, during which anions are incorporated into the polymer matrix to maintain charge neutrality [141], [142], [143]. This process results in the formation of delocalized charge carriers typically polarons and bipolarons which significantly alter the polymer's electronic structure and induce a color change. Conjugated polymers that undergo optical transitions upon oxidation are referred to as anodically coloring electrochromic materials [143]. The reverse process, often called undoping, involves reduction of the polymer, during which the anions are expelled, and the polymer returns to its neutral (non-conductive) state [144]. A typical example of this behavior is illustrated in **Figure 16**, which shows the p-doping and undoping processes in poly(pyrrole). Conversely, n-doping entails the reduction of the polymer, leading to the insertion of cations into the polymer structure. This process causes cathodic coloration, where the material exhibits color change upon gaining electrons. During the reverse oxidation step, cations are released, and the polymer reverts to its neutral form [145]. Although both p-doping and n-doping mechanisms are theoretically viable, the vast majority of electrochromic conjugated polymers explored to date are p-doped systems. This is largely due to the higher chemical and electrochemical stability of p-doped states, whereas n-doped polymers often suffer from degradation and instability in ambient or oxidative environments. Also, the intrinsic color exhibited by the materials is directly related to the band gap. The larger the band gap, the more visible light will transmit through; while the lower the band gap, the more light is absorbed by the materials.

Conjugated polymers (CPs) have garnered significant interest over the past few decades due to their promising electrochromic (EC) properties. These materials offer several key advantages, including fast switching response, high optical contrast, low production cost, ease of fabrication, and a high degree of color tunability. Such characteristics make CPs strong candidates for applications in flexible displays, smart windows, and wearable electronics.

However, despite their benefits, CPs also face several limitations. A major drawback is their limited chemical and thermal stability, which can compromise long-term device performance. Over-extended operation, polymer degradation may occur either through environmental exposure or repeated redox cycling resulting in diminished EC efficiency and durability [146].

Polythiophene is among the most extensively studied conjugated polymers, primarily due to its favorable electrochromic properties and straightforward synthesis. A wide variety of polythiophene derivatives with specific substituents have been developed to tailor color transitions and optimize electrochromic performance [145], [147], [148]. These chemical modifications enable precise control over the polymer's band gap, solubility, film-forming ability, and switching behavior, making polythiophenes highly versatile for electrochromic device applications.

Poly(3,4-ethylenedioxythiophene) (PEDOT) is one of the most widely utilized electrochromic (EC) materials due to its high optical contrast, rapid switching speed, and moderate band gap [149]. The spectroelectrochemical behavior of PEDOT thin films is illustrated in **Figure 17** , showing the distinct color changes associated with its different redox states [150].

To enhance its processability and environmental stability, poly(styrene sulfonate) (PSS) is often introduced to form a macromolecular salt, PEDOT:PSS. This composite exhibits improved chemical stability, film-forming capability, and aqueous solubility, making it suitable for a variety of device fabrication methods. PEDOT:PSS films can be prepared through multiple techniques, including electropolymerization, dip coating, spin coating, and others.

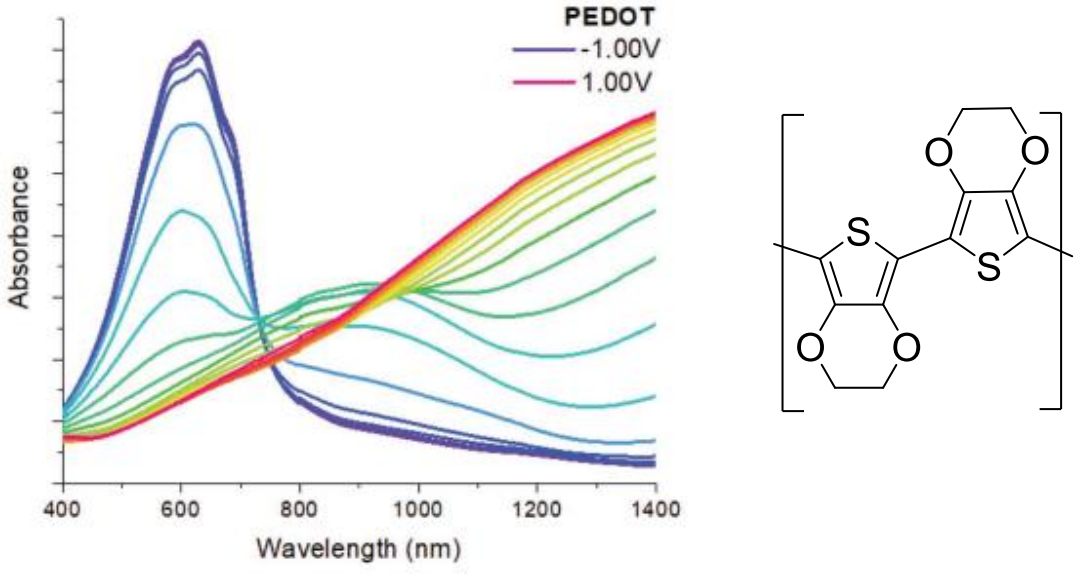

Figure 17: Spectroelectrochemistry for a PEDOT film on an ITO glass substrate [151]**.**

Polyaniline (PANI) is a versatile multicolored electrochromic (EC) material capable of switching among various color states, including transparent, yellow, green, dark blue, and black. The observed color changes are highly dependent on both the oxidation state of the polymer and the pH of the surrounding electrolyte solution [152]. The electrochemical switching of PANI involves a series of complex redox processes that include the insertion and removal of protons (H^+) and/or anions, depending on the environmental conditions and applied potential. [153]. In cyclic voltammetry (CV), the oxidation states of polyaniline (PANI) can be clearly identified through its characteristic redox peaks. Two prominent oxidation peaks are typically observed around 0.2 V and 0.6 V, with their corresponding reduction peaks appearing at approximately 0.1 V and 0.45 V, respectively [153]. During the anodic sweep (oxidation process), PANI exhibits a gradual shift in its absorption band from approximately 430 nm to 810 nm reflecting a series of intermediate color transitions linked to changes in its electronic structure. Among the various fabrication methods available, electropolymerization and spin coating are the most widely employed techniques for the preparation of PANI thin films [154], [155]. These methods allow precise control over film thickness and morphology, which are critical factors influencing electrochromic performance.

Poly(pyrrole) (Ppy) is a representative p-type conducting polymer (CP). In its oxidized form, Ppy displays a blue-violet color (λ = 670 nm), which shifts to yellow-green (λ = 420 nm) upon reduction. When undoped, the film exhibits a pale-yellow appearance. From an electrochromic perspective, Ppy films are known for their rapid switching behavior and pronounced optical contrast, particularly in the case of poly(3,4-disubstituted pyrrole) derivatives. Despite these favorable properties, the long-term durability of Ppy is limited, primarily due to polymer degradation during repeated redox cycling. Ppy films can be conveniently synthesized via electropolymerization from pyrrole monomers [156], [157].

1.5.2.2. Organic Small Molecules

Viologens (4,4‟-dipyridinium compounds), that can be reduced to deep blue-purple color, are typical organic small molecular EC materials. **Figure 18** shows the common redox states of viologens, which may experience one-electron and two-electron reductions. The first electron

reduction is reversible and exhibit electrochromic properties; while the second electron reduction process is electrochemically nonreversible [158].

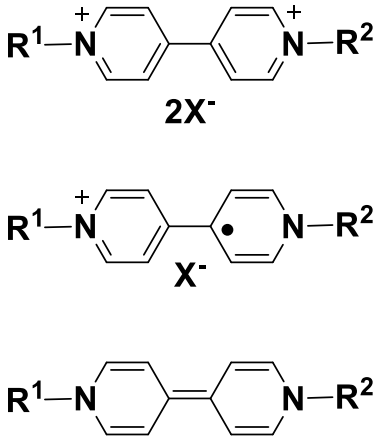

Figure 18: Common redox states of viologens with attached group R1 and R2 . X refers to charged anion.

1.5.3. Other EC Materials

1.5.3.1. Metal Coordination Complexes

These are coordination complexes that consist of a metallic center and surrounding ligands as explained before [159]. Their electrochromic behavior arises from redox-induced charge transfer processes that occur either at the metal center or within the ligands themselves. A representative example is the ferroin complex, $[Fe(phen)_3]^{2+}$ (where phen = 1,10-phenanthroline), which undergoes a visible color change from red to pale blue upon oxidation of Fe^{2+} to Fe^{3+} [160]. In many cases, both metal-centered and ligand-centered redox processes contribute to the electrochromic switching, and the overall color change can be influenced or fine-tuned by modifying the ligand environment. A notable case was presented in 1985 [161] which showed that using a modified bipyridine ligand can exhibit seven color states in the various redox reactions.

Furthermore, recent developments in electrochromic materials have highlighted the potential of Fe(II) and Ru(II) bis(terpyridine)-based complexes with N',N'-disubstituted aminophenyl side chains, which can be electropolymerized to form conducting metallopolymer films that change color under applied voltage [162]. However, these early systems suffer from several limitations, including long response times, fabrication difficulties, low coloration efficiency, and poor long-term stability [141].

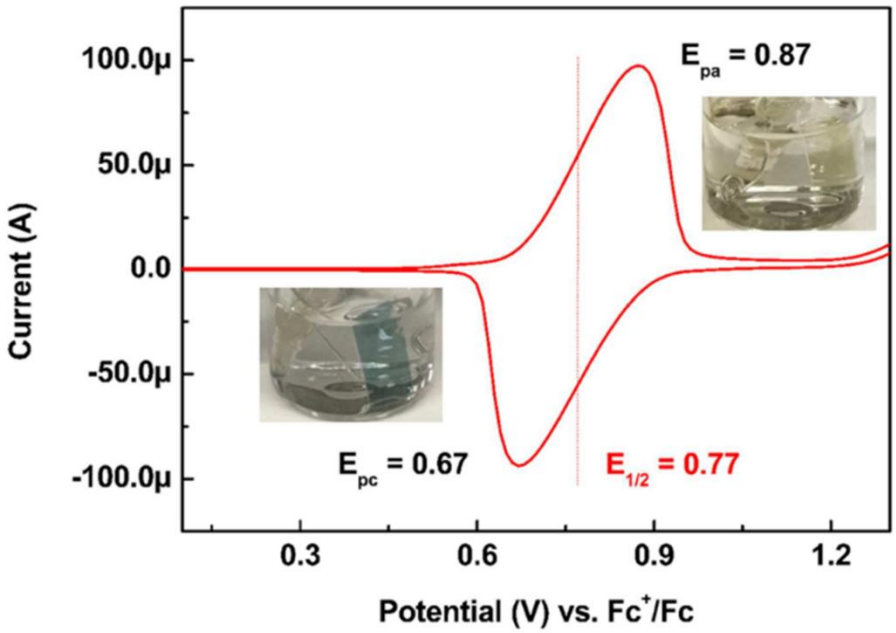

Figure 19: Cyclic Voltammetry of poly-Fe(4'-(2,2'-bithiophen-5-yl)-2,2':6',2''-terpyridine)$_2$ on ITO in a monomer-free acetonitrile solution with 0.1 M TBAPF6 as supporting electrolyte showing the effect of the applied potential on the color of the polymer film.

To overcome these challenges, attention has turned to thiophene-containing Fe(II) bis(terpyridine) complexes. The Fe(II) bis(terpyridine) core is promising due to its rigid, linear structure that enhances polymer stability and enables efficient electron delocalization [163]. Additionally, thiophene and its derivatives are well-known for their excellent electropolymerization behavior and favorable electrochromic (EC) properties as shown in **Figure 19** [164]. Importantly, introducing thiophene units into Fe(II) bis(terpyridine) complexes offers an effective route to create the metallopolymers with improved processability, faster redox activity, and tunable optical properties [165]. Therefore, combining the structural advantages of terpyridine-based coordination complexes with the electrochemical versatility of thiophene units offers a promising strategy for designing electrochromic materials with enhanced performance and practical applicability.

1.6. Electrochromic Devices

Electrochromic devices (ECDs) are a class of electrochemical systems capable of reversibly modulating their optical properties such as transmittance and reflectance in response to an externally applied potential [135]. Structurally, an ECD consists of three primary components: a

working electrode, a counter electrode, and an electrolyte, typically arranged in a sandwich configuration, where the electrolyte is positioned between the two electrodes. Depending on their optical behavior, ECDs are generally classified into two types: transmissive ECDs and reflective ECDs. Transmissive devices operate by reversibly altering light transmission in the visible spectrum and are commonly employed in applications such as smart windows and automotive rearview mirrors. In contrast, reflective ECDs are typically designed to function in the infrared (IR) region, where they modulate reflectivity for thermal management purposes [166]. This thesis will primarily focus on transmissive ECDs due to their widespread use and commercial relevance in energy-efficient architectural glazing and adaptive optical technologies.

1.6.1. Configuration of ECDs

As previously described, an electrochromic device (ECD) consists of multiple functional layers, including a working electrode, a counter electrode, and an electrolyte sandwiched between them. In transmissive ECDs, two primary configurations are commonly employed: the single-layer ECD and the complementary ECD, as illustrated in **Figure 20**. A rigid or flexible substrate serves as the mechanical support for the entire device assembly. The electrodes are typically fabricated from transparent conductive materials such as indium tin oxide (ITO) or fluorine-doped tin oxide (FTO) which permit visible light transmission while enabling electron flow. The electrolyte, situated between the electrodes, facilitates ion transport and must possess high ionic conductivity to ensure efficient redox switching. In the single-layer configuration, only the working electrode is coated with an electrochromic (EC) material, while the counter electrode remains passive. Conversely, in the complementary ECD design, both electrodes are coated with electrochromic materials that exhibit complementary optical and electrochemical behaviors. This dual-active-layer structure enhances device performance by enabling more balanced charge compensation and improving optical contrast.

The single-layer electrochromic device (ECD) provides a fundamental platform for evaluating the intrinsic electrochromic properties of active materials. It is commonly employed in laboratory settings to assess parameters such as coloration efficiency, switching kinetics, and stability. In contrast, the complementary ECD incorporates an additional electrochromic layer referred to as the complementary EC layer on the counter electrode. In this configuration, both EC layers

undergo simultaneous redox switching, thereby significantly enhancing the optical contrast of the device. The complementary EC layer is typically designed to undergo a coloration transition opposite in polarity to that of the primary EC layer. For instance, when the primary EC material is cathodically coloring, the complementary layer should be anodically coloring to ensure synchronized optical modulation [152]. Moreover, it is essential that the color hues and switching potential windows of both EC layers are compatible to achieve effective contrast and reversibility. In addition to optical enhancement, this complementary architecture offers improved electrochemical charge balance, as the redox processes on both electrodes are mutually compensating. This leads to greater cycling stability and longevity of the device, offering a distinct advantage over the single-layer configuration.

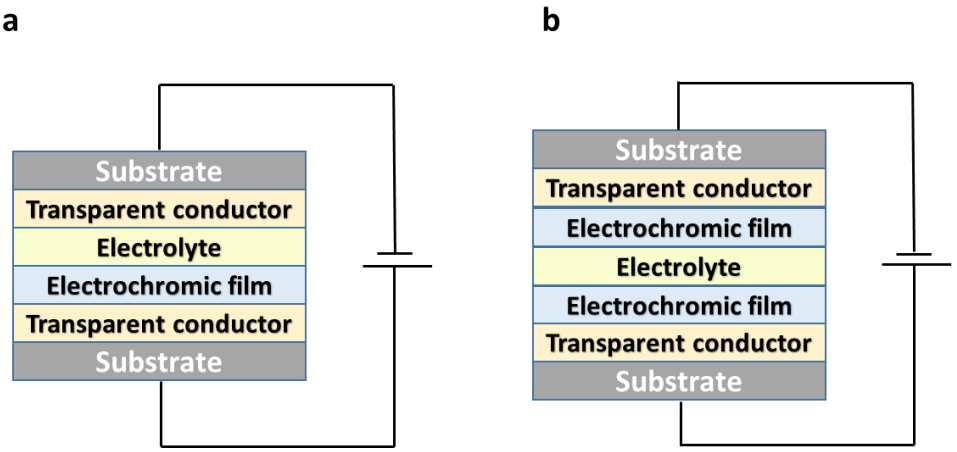

Figure 20: Schematic illustration of (a) single-component and (b) complementary electrochromic devices.

1.6.1.1. Components of The Transmission ECDs

According to the configuration of the electrochromic devices, the components that form the device are explained in the following sections which are the transparent conductors, electrolytes, and EC material.

In transmission-type electrochromic devices (ECDs), the transparency of the electrodes is a critical parameter, as it directly impacts the ability of light to pass through the device. These electrodes are typically fabricated by depositing transparent conductive materials such as indium tin oxide (ITO), fluorine-doped tin oxide (FTO), or silver nanowire grids onto transparent substrates. The substrates themselves are non-conductive and serve primarily as mechanical support; common

materials include glass and flexible polymers like polyethylene terephthalate (PET). The transparent conductive electrodes perform dual roles: they function as both current collectors and charge-balancing layers within the ECD structure. In a single-layer ECD, the working electrode delivers electrons to or from the electrochromic layer, while the counter electrode acts as a passive balancing component. In complementary (dual-layer) ECDs, a second electrochromic layer is also deposited onto the counter electrode, allowing for synchronized redox activity between the two electrodes. To ensure optimal device performance, these transparent conductors must exhibit high optical transmittance, especially in the visible range, while maintaining sufficient electrical conductivity to facilitate efficient charge transport during redox switching.

The electrolyte layer in these devices separate the electrodes and provides a pathway for the ion transfer between the electrodes. It is known that it is an electronic insulator to prevent the short circuit of the device, which exhibits high ionic conductivity for ion transfer. The commonly used electrolytes in ECDs are gel and liquid electrolytes. The most applied one is the gel electrolyte, which is divided into polymer electrolytes and polyelectrolytes. Polymer electrolytes include neutral macromolecules that are dissolved in the solvent to increase the viscosity. Some common polymers used in the electrolyte layers are poly (vinyl alcohol) (PVA), poly (ethylene oxide) (PEO), and poly (methyl methacrylate) (PMMA). Similar to liquid electrolytes, gel electrolytes incorporate dissolved salts or acids within a solvent to facilitate ionic conductivity. In contrast**,** polyelectrolytes also referred to as polysalts are polymers containing ionizable functional groups, enabling them to exhibit both polymeric and ionic properties. For instance, poly(2-acrylamido-2-methylpropanesulfonic acid) (PAMPS) is a well-known strong anionic polyelectrolyte that can form a crosslinked gel network. Such gel-based electrolytes offer the added advantage of acting as an adhesive layer, effectively binding the two electrodes together and thus simplifying the assembly process of electrochromic devices (ECDs). However, limitations such as relatively low ionic conductivity and poor thermal stability continue to present challenges for their broader application in high-performance ECDs [167].

The electrochromic (EC) layers serve as the active components in electrochromic devices, responsible for undergoing optical changes in response to applied electrical potentials. These layers are composed of electrochromic materials and are fabricated using a variety of techniques and methods, including electropolymerization**,** layer-by-layer assembly**,** spray coating, among

others. Detailed descriptions of the synthesis and fabrication methods for these EC layers will be presented in Chapter 3.

1.6.2. Electrochromic Key Performance Paremeters

The performance of transmissive electrochromic (EC) materials and devices is typically assessed through several critical parameters, including optical contrast**,** switching speed**,** electrochemical stability**,** cycling durability**,** and optical memory effects. These characteristics provide comprehensive insight into the functionality and reliability of EC systems. The most commonly used performance indicators for evaluating EC behavior are outlined below.

1.6.2.1. Optical Contrast

Optical contrast is a fundamental parameter that characterizes the optical responsiveness of electrochromic (EC) materials. It is defined as the change in optical transmittance (Δ%T) between the bleached (high transmittance) and colored (low transmittance) states at a specific wavelength, typically the wavelength of maximum contrast (λmax), as expressed in the equation below. This measurement is commonly performed using UV–Vis spectroscopy across the visible spectrum to identify the wavelength where the transmittance difference is most pronounced [168].

An additional related metric is the contrast ratio (CR), is presented. This ratio quantifies the proportion of transmitted light in the colored state relative to that in the bleached state at λmax, offering an alternative perspective on the visual effectiveness of the EC material [155].

$$\Delta\%T = \%T\{bleach\} - \%T\{color\}$$

$$CR = \left\{\%T_{\{color\}}\right\}/\left\{\%T_{\{bleach\}}\right\}$$

1.6.2.2. Switching Response

Switching response is a critical aspect of electrochromic (EC) performance, encompassing parameters such as coloration efficiency (CE), coloration time, and bleaching time. Among these, coloration efficiency serves as a key metric for assessing the electro-optical performance of EC materials. Coloration efficiency (CE) is defined as the change in optical absorbance (ΔA) at a specific wavelength (λ) per unit charge (Q) inserted per unit area. It is expressed mathematically

in the equation below. The absorbance change (ΔA) is derived from the transmittance values of the bleached (%T bleach) and colored (%T color) states, as shown in the equation below [123], [147], [169]. This parameter quantitatively reflects the relationship between optical modulation and the charge density required to achieve it, thereby offering insight into the efficiency of the material's redox-driven color change. Typically, organic EC materials demonstrate higher coloration efficiency than their inorganic counterparts, attributed to their greater molar absorption coefficients.

$$CE(\lambda) = \Delta A / Q \quad (cm^2/C)$$

$$\Delta A = Log_{10}[\%T\{bleach\}/\%T\{color\}]$$

Switching time, also referred to as coloration time, is defined as the duration required for an electrochromic material to transition from its bleached state to 90% of its fully colored state. Conversely, bleaching time refers to the period needed for the material to revert from the colored state back to the bleached state. The kinetics of this switching process can be influenced by several factors, including ion diffusion rates within the electrochromic film, the magnitude of the applied potential or current, film thickness, surface morphology, and material composition. Typically, organic electrochromic materials exhibit faster switching times compared to their inorganic counterparts due to their higher charge mobility and different structural characteristics [123], [170].

1.6.2.3. Stability and Cycle Life

During repeated redox cycling, the electrochromic (EC) performance of materials tends to deteriorate over time. Electrochemical stability refers to the number of switching cycles an EC material can undergo without experiencing significant loss in its optical or electrochemical properties. Performance degradation is commonly attributed to factors such as over-oxidation or over-reduction due to high applied potentials, a decrease in the ionic conductivity of the electrodes or electrolyte, and the occurrence of undesirable side reactions. Additionally, irreversible reactions involving oxygen or moisture can also contribute to the long-term instability of electrochromic systems [123].

1.6.2.4. Optical Memory

Optical memory, also referred to as open-circuit memory, describes the ability of electrochromic (EC) materials to retain their colored or bleached state even after the external electrical potential or current has been removed. The duration for which an EC material maintains its optical state without a continuous power supply is termed its optical memory [123]. This characteristic varies significantly among different materials. For example, viologens and polypyridyl complexes typically lose their coloration almost immediately once the electric field is discontinued. In contrast, inorganic transition metal oxides, such as WO_3, are capable of maintaining their colored states for extended periods, ranging from several days to even weeks. This disparity is primarily attributed to the differences in ion diffusion kinetics after the cessation of the electrical stimulus.

1.7. One Dimensional Nanostructures

One-dimensional (1D) nanomaterials are defined as nanostructures in which two of the three spatial dimensions fall within the 1–100 nm range where it includes nanotubes, nanowires or nanofibers, nanorods, and nanoribbons. Owing to their high aspect ratio and mechanical flexibility, 1D nanostructures exhibit remarkable electronic, optical, and magnetic properties, making them highly attractive for advanced functional applications [171]. In recent years, they have emerged as a dynamic research focus in materials chemistry and physics, with demonstrated potential in catalysis, optoelectronics, biosciences, sensing, and energy harvesting [172]. Although 1D nanostructures share certain features with zero-dimensional nanoparticles and two-dimensional thin films or sheets such as quantum confinement and large surface area, their geometry imparts unique characteristics. In particular, confined electron and photon transport along one dimension, combined with favorable mechanical properties, enables functionalities that are difficult to achieve with other nanomaterial classes. Furthermore, their ability to be integrated and patterned over large areas makes them promising for flexible electronic and optoelectronic devices. While much research has traditionally centered on inorganic metals, metal oxides, and carbon-based nanostructures, the past two decades have also seen a surge of interest in π-conjugated organic semiconductors. This has significantly expanded the understanding of their diverse photonic, electronic, and optoelectronic properties and opened new pathways toward exciting technological applications [173].

Several strategies have been developed for the preparation of inorganic and organic one-dimensional (1D) nanostructures, including template-assisted methods, nanolithography, electrospinning, and supramolecular self-assembly in solution or at interfaces [174]. The choice of synthesis approach plays a crucial role, as it directly influences the morphology and dimensionality of the resulting nanomaterials. Among these techniques, template-based synthesis offers a particularly straightforward route to achieve 1D nanostructuration. In this approach, the template acts as a scaffold, guiding the in situ formation of the material and confining it into a morphology complementary to that of the template [175]. This strategy has been widely employed to fabricate nanotubes, nanowires, and nanorods from metallic, inorganic, and organic precursors [176]. A variety of both hard and soft templates have been utilized, including track-etched membranes, anodic aluminum oxide (AAO), porous silica membranes, block copolymers, surfactants, molecular aggregates, and liquid crystals.

1.8. Mesoporous Silica Materials: Template-Based Synthesis

Mesoporous silica films have emerged as indispensable scaffolds for the preparation of one-dimensional (1D) nanomaterials due to their highly ordered pore geometry, large specific surface area, and tunable pore size distribution [177], [178]. Their intrinsic properties allow them to function as robust hard templates in which the confined growth of precursors leads to well-defined films with uniform dimensions and reproducible morphologies [179], [180]. This templating strategy is particularly attractive because silica is chemically inert, mechanically stable, and thermally resistant, ensuring that the synthesis process is both controllable and repeatable. Another advantage of mesoporous silica lies in the versatility of its preparation: sol–gel routes combined with surfactant- or block copolymer–directed self-assembly allow fine-tuning of pore diameter, pore connectivity, and wall thickness [181]. Depending on surfactant concentration and reaction conditions, different structural motifs—hexagonal (MCM-41, SBA-15), cubic (MCM-48, SBA-16), or lamellar (MCM-50)—can be obtained, enabling researchers to select pore architectures best suited for targeted applications [182], [183], [184]. The combination of large pore volume (>0.7 $cm^3\ g^{-1}$) and high surface area (500–1500 $m^2\ g^{-1}$) provides abundant space for infiltration of metals, oxides, polymers, and biomolecules, which can subsequently be converted into ordered 1D nanostructures after template removal.

The synthesis of ordered mesoporous silica is most commonly achieved via the sol–gel method, in which silica precursors such as tetraethoxysilane (TEOS) or tetramethoxysilane (TMOS) undergo hydrolysis and condensation in the presence of supramolecular assemblies that act as structure-directing agents (SDAs). These SDAs, typically composed of ionic or non-ionic surfactants or amphiphilic polymers, promote cooperative self-assembly, generating a soft template that guides the in situ organization of the silica framework. This approach enables the preparation of mesoporous structures with highly uniform pore sizes, generally in the range of 2–10 nm.

Two primary mechanisms have been proposed to explain mesoporous silica formation. The first, referred to as the true liquid crystal templating (TLCT) mechanism, requires high surfactant concentrations under controlled temperature and pH. In this pathway, a lyotropic liquid crystalline phase forms prior to the introduction of the silica precursor, which subsequently condenses around the pre-organized surfactant scaffold (**Figure 21**). In contrast, the cooperative self-assembly mechanism involves simultaneous organization of the surfactant micelles and silica species. Here, the inorganic precursor interacts directly with the surfactant head groups, resulting in a co-assembled hybrid structure in which silica condensation and template ordering proceed concurrently [181].

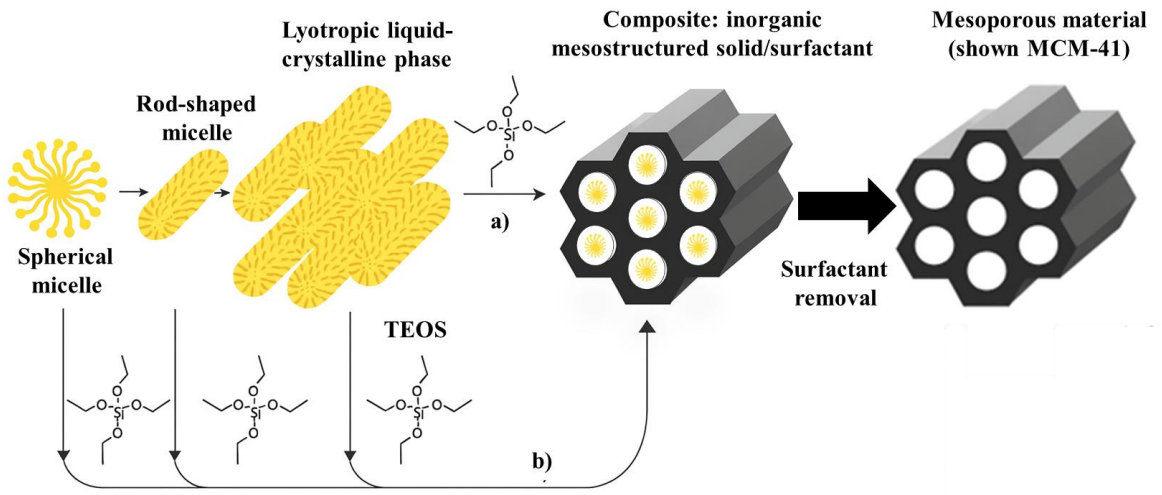

Figure 21: Proposed mechanisms for mesoporous silica formation (a) the TLCT approach and (b) cooperative liquid crystal template path.

1.9. Mesoporous Silica Films on Solid Substrates

A key feature of mesoporous silica is its ability to be fabricated as thin films, which are highly attractive for applications in catalysis, sensing, and as insulating layers. Because bulk mesoporous silica is rigid and difficult to transform post-synthesis, dedicated deposition strategies have been developed and studied such as reducing the film thickness by wet etching [185], [186]. Supported films are typically obtained by dip-coating, spin-coating, or drop-casting a sol containing silica precursors and surfactants, followed by micellization and polycondensation during solvent evaporation. The most established method is evaporation-induced self-assembly (EISA), in which film formation occurs from a diluted sol as solvent evaporation drives surfactant templating and silica condensation [187], [188]. By adjusting sol composition, surfactant type, and post-treatment conditions, ordered mesostructures with hexagonal, cubic, rhombohedral, or gyroid symmetries can be achieved on substrates such as Au, Pt, ITO, FTO, alumina, silicon, and carbon. Despite its versatility, the EISA method faces challenges for electrochemical applications. Thermal treatments often induce film cracking and shrinkage, while the parallel alignment of mesopore channels to the substrate restricts mass transport across the film, limiting accessibility to the electrode surface. To address these limitations, efforts have focused on controlling pore orientation, with particular

emphasis on achieving perpendicular channel alignment to enhance ion and molecule transport and thus optimize electrochemical performance [189].

1.9.1. Vertically Aligned and Ordered Mesoporous Silica Films on Solid Surfaces

A major limitation of supported mesoporous materials mentioned above lies in the restricted accessibility of the underlying substrate, as pore channels in EISA-derived thin films are typically oriented parallel to the electrode surface, thereby limiting mass transport and practical applicability. To address this issue, Zhao *et al.* [189] reported the first continuous nanoporous silica thin film with a three-dimensionally accessible pore network. Using dip-coating of an acidic sol containing a cationic surfactant such as CTAB onto polished silicon wafers and glass, they achieved uniform films of ~300 nm thickness with pore diameters between 18 and 25 Å, depending on the surfactant employed. Further progress was made with the deposition of mesoporous silica thin films from Stöber solutions, where hydrolyzed silica precursors, surfactants, and ethanol were cross-linked using ammonia as a catalyst. This approach yielded continuous two-dimensional architectures with channels aligned perpendicularly to the substrate surface [190]. Other methods to induce vertical alignment have included epitaxial growth on patterned substrates, application of external stimuli such as magnetic or radiofrequency fields, and scanning electrochemical microscopy-assisted deposition [191]. Despite these advances, many of these approaches remain limited by their complexity, multi-step substrate pretreatment requirements, restricted substrate compatibility, and poor control over pore diameter (often above 5–6 nm). This challenge was eventually addressed in 2007, where a new method was introduced: the Electrochemically Assisted Self-Assembly (EASA) method, a versatile and comparatively straightforward strategy to produce mesoporous silica films with vertically aligned channels directly on conductive substrates [192].

1.9.2. Electrochemically Assisted Self-Assembly Method

The Electrochemically Assisted Self-Assembly (EASA) method shown in **Figure 22**, first reported in 2007 [192], provides a fast and versatile route to vertically aligned mesoporous silica films. The resulting membranes exhibit orthogonal channel orientation with pore diameters of 2–3 nm or even higher (depending on the surfactant used) and can be deposited on various conductive substrates, including ITO, FTO, Au, Pt, and glassy carbon [193], [194]. Unlike conventional sol–gel

approaches, EASA operates under kinetic control, similar to Stöber growth, but enables film formation within only 5–30 s at room temperature [185]. The process is carried out in a three-electrode cell by applying either a reductive potential (potentiostatic) or a negative current (galvanostatic) in a hydrolyzed sol containing a silica precursor (typically TEOS) and a cationic surfactant such as CTAB. The applied bias drives self-assembly of the surfactant species at the electrode surface while simultaneously generating hydroxide ions, which locally increase the pH and catalyze silica condensation around the pre-organized micelles. This electrochemically driven cooperative self-assembly produces silica films with hexagonally packed mesopores oriented perpendicular to the substrate [195]. The EASA method reliably yields homogeneous, crack-free thin films over wide areas and is also suitable for non-flat surfaces. Film thickness (typically 50–200 nm) can be tuned by varying deposition time or precursor concentration [196]. Importantly, the CTAB/TEOS ratio critically governs mesostructure orientation: at low ratios (≈0.16), amorphous films are obtained, while higher ratios (up to ≈0.64) yield partially ordered or fully hexagonally oriented channels [194]. Likewise, systematic control of TEOS concentration (50–350 mM) at fixed potential (–1.3 V) and deposition time (around 20 s) allows precise adjustment of film thickness within the 50–200 nm range.

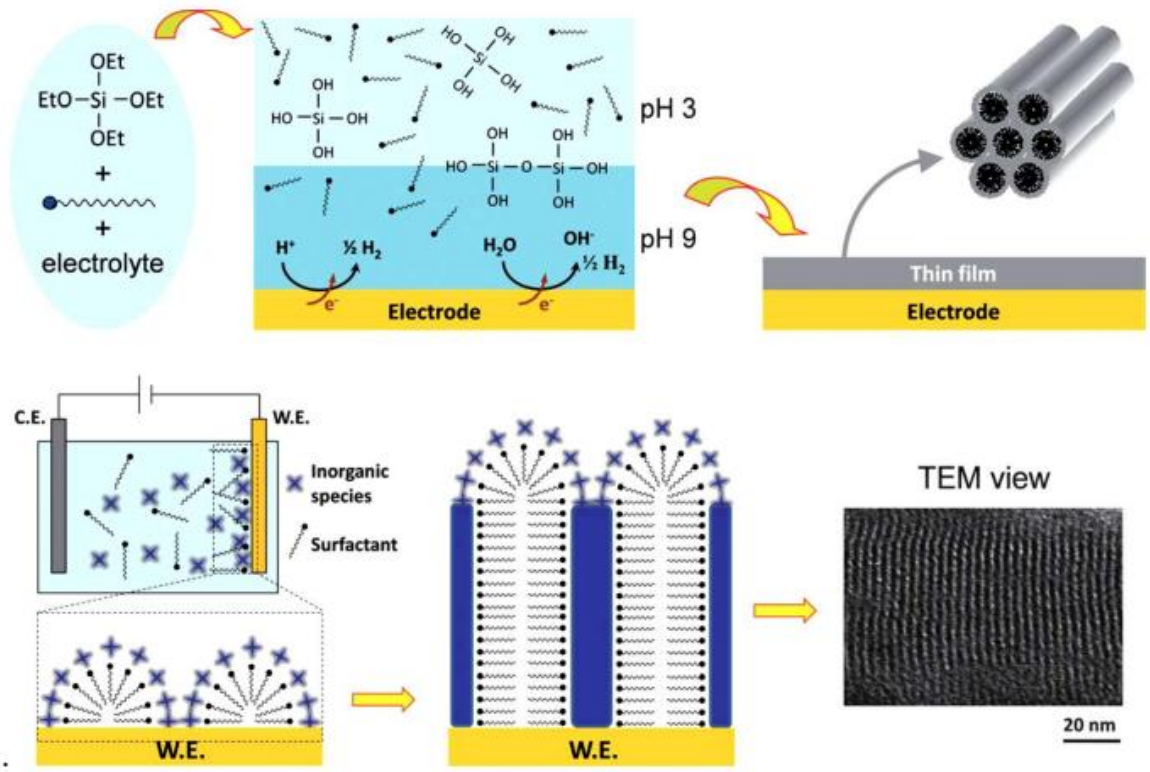

Figure 22: Schematic illustration of the EASA method used to generate ordered and oriented mesoporous silica thin films via sol gel self-assembly using electrochemistry **[195]**.

1.9.3. Applications of the Ordered Mesoporous Silica Films covered Electrodes

Although silica is intrinsically insulating and electrochemically inactive, silica-based materials can nevertheless play an important role in electrochemistry. When used as electrode modifiers, mesoporous silica films provide highly ordered porous networks that facilitate rapid mass transport, can be functionalized with organic molecules, and offer molecular- and nanoscale hosting capabilities [197]. Their large surface area, uniform and accessible mesopore channels, and excellent thermal and mechanical stability make them well-suited for device integration. In particular, ordered mesoporous silica thin films on electrode surfaces have attracted attention in electrochemical sensing due to their selectivity for small redox-active species. Applications have included the detection of drugs, pesticides, explosives, biomolecules, and heavy metals [198]. The versatility of mesoporous silica is further enhanced by its ability to be functionalized with organic groups or redox-active moieties. Strategies include post-synthesis grafting, where organic molecules react with surface silanol groups (e.g., ferrocene, hydroquinone, ammonium); co-

condensation, where organosilanes are incorporated directly during silica network formation (e.g., thiol, amine, alkoxyamine, alkyl, hexadecyl, azide); and combined approaches, where pre-functionalized silica undergoes further post-modification [199]. More recently, advanced chemistries such as Huisgen coupling and "click" reactions have enabled efficient dual-step functionalization. Our group in LCPME has demonstrated this strategy previously by attaching ferrocene and tetrazine units to azido-functionalized silica films [200]. Such functionalized mesoporous silica has been exploited in diverse applications such as in sensitive hydrogen peroxide detection [201], amylase-functionalized films for catalytic starch degradation under extreme temperature and pH conditions [202], and transparent ITO-supported silica films bearing cobaltocenium groups for electrochemical energy storage [203]. Furthermore, vertically oriented mesoporous silica films on conductive supports can act as robust hard templates for the incorporation of guest species, either chemically or electrochemically.

It is well-known that hard templates such as anodized aluminum oxide (AAO), polycarbonate, poly(methyl methacrylate) (PMMA) and the mesoporous silica films are used for material synthesis at the nanoscale such as nanowires [204]. Also, knowing that these mesoporous silica thin films range between 2 to 30 nm, depending on the surfactant used during the preparation process, with this information in mind the nanostructures that would be confined inside these channels will retain the diameter size of the pore. For instance, metal nanowires can be fabricated by chemical reduction of metal complexes or by chemical vapor deposition within the channels of mesoporous silica templates [205]. Electrodeposition represents another widely used technique for producing metallic as well as organic films and nanostructures [206]. This method is particularly interesting as it is straightforward, clean, and rapid, while also allowing precise control over nanostructure growth by adjusting parameters such as current density and deposition time. For example, PANI nanostructures can be synthesized by the template approach and it is a particularly well-established and straightforward way to synthesize PANI in 1D configuration [207]. This can be accomplished either using hard templates such as anodic alumina oxide (AAO), polycarbonate track-etched membrane and silica-based template. In our group, polyaniline wires were successfully incorporated inside vertically oriented mesoporous silica films that were deposited on ITO using EASA, where the pore size ranged between 2 and 3 nm, depending on the surfactant used. Where the polymer chain was synthesized using Electropolymerization using an acidic

solution [208]. This sparked the interest in testing the formation of uniform 1D metallopolymers inside the mesoporous silica films which was one of the objectives of this thesis.

Chapter II: Experimental Part

2. Experimental Part

In this chapter, the experimental methodology describes the materials synthesis as well as a detailed list of chemicals used, thin films fabrication, characterization methods, and the preparation process for the development of the electrochromic devices. Chemical composition and structure were verified by XPS, Raman and FTIR spectroscopy, TEM, and GISAXS. Electrochemical analysis such as cyclic voltammetry was applied to follow the electrochemical behavior of the sample materials. Furthermore, the spectroelectrochemistry and electrochromic behavior of the sample materials was studied as well in special electrochemical cells.

2.1. List of Chemicals and Solvents used

Compound	Molecular Formula	Molecular Weight (g/mol)	Purity (%)	Supplier
Perchloric acid	$HClO_4$	100.46	70	Sigma-Aldrich
Lithium perchlorate	$LiClO_4$	106.39	98	Sigma-Aldrich
Sodium nitrite	$NaNO_2$	68.99	97	Sigma-Aldrich
Sodium nitrate	$NaNO_3$	84.99	99.99	Thermoscientific
4-([2,2':6',2''-Terpyridin]-4'-yl)aniline	$C_{17}H_{13}N_4$	273.31	97	BLD Pharm
Iron (II) Chloride tetrahydrate	$FeCl_2 \cdot 4H_2O$	198.81	99	Sigma-Aldrich
Ruthenium(III) chloride trihydrate	$RuCl_3 \cdot 3H_2O$	261.47	99.9	BLD Pharm
N-ethylmorpholine	$C_6H_{13}NO$	115.17	97	Sigma-Aldrich
Ammonium hexafluorophosphate	NH_4PF_6	145	98	Sigma-Aldrich
Tetraethoxysilane	$C_8H_{20}O_4Si$	208.33	98	ALFA-AESAR
Cetyltrimethylammonium bromide	$C_{19}H_{42}BrN$	364.46	99	FLUKA
Trimethyloctadecylammonium bromide	$C_{21}H_{46}BrN$	392.50	98	Aldrich
Tetrabutylammonium tetrafluoroborate	$C_{16}H_{36}BF_4N$	321.28		Aldrich
Hexaammineruthenium(III) chloride	$[Ru(NH_3)_6]Cl_3$	307.65	98	Aldrich
Potassium hexacyanoferrate(II) trihydrate	$K_4[Fe(CN)_6] \cdot 3H_2O$	422.39	99.5	Sigma-Aldrich
1,1′-Ferrocenedimethanol	$C_{12}H_{14}FeO_2$	246.08	98	Aldrich
Zinc acetate dihydrate	$C_4H_{10}O_6Zn$	219.50	99	Sigma-Aldrich

1-Bromoeicosane	$C_{20}H_{41}Br$	345.46	97	Sigma-Aldrich
4-Aminoazobenzene	$C_{12}H_{11}N_3$	197.24		Sigma-Aldrich
4,4'-Diaminoazobenzene	$C_{12}H_{12}N_4$	212.25	95	Thermoscientific
N,N-Dimethylacrylamide	C_5H_9NO	99.13		FLUKA
N,N′-Methylenebisacrylamide	$C_7H_{10}N_2O_2$	154.17	99.5	Sigma
Potassium peroxodisulfate	$K_2S_2O_8$	270.32	98	MERCK
Lithium chloride	LiCl	42.39	99	Sigma-Aldrich
Cobalt (II) chloride hexahydrate	$CoCl_2 \cdot 6H_2O$	237.93	98	Sigma-Aldrich
2,2':6',2''-Terpyridine	$C_{15}H_{11}N_3$	233.27	97	BLD Pharma
4'phenyl-2,2':6',2''-terpyridine	$C_{21}H_{15}N_3$	309.36	98	BLD Pharma
Tetrabutylammonium hexafluorophosphate	$C_{16}H_{36}F_6NP$	387.43		FLUKA
Sodium perchlorate monohydrate	$NaClO_4 \cdot H_2O$	140.49	98	MERCK
tetrabutylammonium perchlorate	$C_{16}H_{36}ClNO_4$	337.91		FLUKA
Sodium sulfate	Na_2SO_4	142.04	98	BILLAULT
Tetraethylammonium perchlorate	$C_8H_{20}ClNO_4$	229.71		EASTMAN
Ethanol	C_2H_5OH	58.08	99.9	Sigma-Aldrich
Acetone	CH_3COCH_3	58.08	99.5	Sigma-Aldrich
Sulfuric Acid	H_2SO_4	98.08	100	Aldrich
Acetonitrile	CH_3CN	41.05	99.9	Sigma-Aldrich
Diethyl ether	$C_4H_{10}O$	74.12	99.8	VWR Chemicals
Trimethylamine	C_3H_9N	59.11	45	Sigma-Aldrich
Acetonitrile-d3	CD_3CN	44.07		Sigma-Aldrich
Chloroform-d	$CDCl_3$	120.37	99.8	Aldrich

2.2. Electrochemical apparatus and methods

2.2.1. Electrochemical cell

In this thesis, the main focus was centered around synthesizing conductive metallopolymers on electrode surfaces and electrochemically characterizing these polymers. Therefore, a principal cell was used throughout this research, where this electrochemical cell was designed and fabricated in our laboratory and it is shown in the **Figure 23**.

There are 2 main parts in this cell: the bottom plate and the solution chamber. The bottom plate with its supporting rods is made up of stainless steel and the other part which is made up of Teflon material with a small hole at the bottom with a specific diameter of 0.6 cm and it has an O-ring

inside it, and this cell has a solution capacity of around 25 ml. In this case, the working electrode (which is normally an ITO plate) is placed on the O-ring space that provides the necessary contact between the electrode solution and the electrode.

To make sure that the electrode doesn't move and retains its position, it is sealed with Scotch tape and then closed with the bottom plate to prevent the leakage of the solution. A copper wire or silver tape is used as the connection to the working electrode. The counter and reference electrodes are inserted in the cell with the help of a holder to keep them in place.

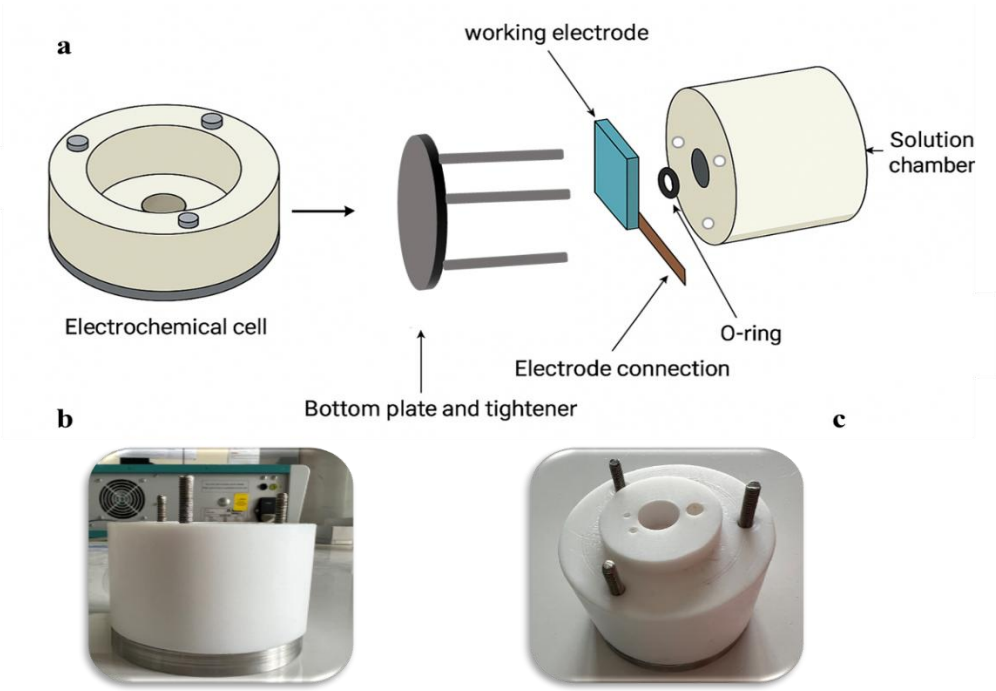

Figure 23: Schematic Representation of the Custom Three-Electrode Electrochemical Cell: (a) Conceptual Sketch, (b) Side View, and (c) Top View.

2.2.2. Spectroelectrochemical cell

The spectroelectrochemical experiments were done using a two electrode system where the modified ITO was used as the working electrode and a blank ITO was used as the counter electrode. A spacer was added between the two electrodes to create a space and prevent the contact between the two electrodes. A conductive gel was used where it was introduced between the two electrodes and then this sandwich-like setup was firm and didn't move by screwing and tightening the base which created a stable electrochromic device as shown in **Figure 24**.

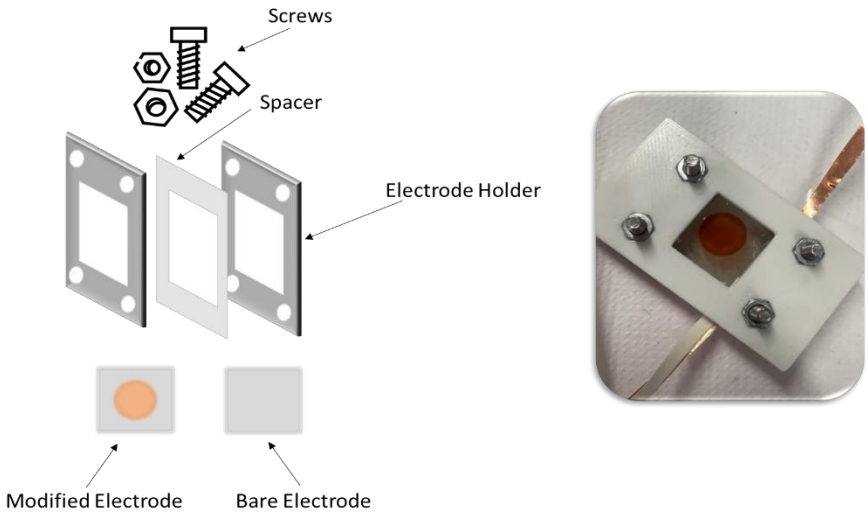

Figure 24: Schematic representation of the spectroelectrochemical cell using a two electrode system.

2.2.3. Electrodes

Electrodes are key components in electrochemical systems, where they serve as sites for electron transfer reactions that occur under the control of an external power source typically a potentiostat [209]. Electrochemical setups may involve two, three, or even four electrodes, but the three-electrode configuration is the most widely adopted due to its enhanced precision and control. This configuration enables independent measurement and control of the working electrode's (WE) potential and current, without interference from changes at the counter electrode (CE).

In this system, the working electrode, where the target electrochemical reaction occurs, is chosen for its stability, corrosion resistance, and high surface activity. Common materials include platinum (Pt), gold (Au), and glassy carbon. The reference electrode (RE) provides a stable and known potential against which the WE potential is controlled and measured. Ideal REs, such as the standard hydrogen electrode (SHE), saturated calomel electrode (SCE), and silver/silver chloride (Ag/AgCl) electrode, are designed to pass negligible current to ensure constant potential. In some cases, metallic wires (e.g., Ag, Au, or Pt) are used as reference points and are termed pseudo-reference electrodes (PREs) due to their undefined and variable thermodynamic potentials.

The counter electrode, made from inert materials like Pt, Au, nickel, or stainless steel, serves to complete the electrical circuit by balancing the electron flow generated by reactions at the WE [210], [211].

In the experiments done during the thesis, we used Ag/AgCl and sometimes Ag as the reference electrode. For the working electrode, we use most of the time ITO and in some cases a carbon electrode. And finally for the counter electrode we use stainless steel.

2.2.4. Potentiostat

A potentiostat is an essential electronic instrument in electrochemical systems, designed to precisely regulate the potential difference between the (WE) and the (RE) within an electrolyte-containing cell. It achieves this by directing current through the (CE), thereby maintaining a stable working potential. The current flowing as a result of electrochemical reactions is monitored between the WE and CE, enabling the analysis of reaction kinetics and mechanisms through graphical data output.

The device interfaces with a computer equipped with specialized software, which facilitates user-defined experimental control and real-time data acquisition. In this work, electrochemical measurements were conducted using one of the following potentiostat/galvanostat models from Metrohm Autolab which are Autolab PGSTAT 101 potentiostat/galvanostat and μAutolab type III.

2.2.4. Electrochemical techniques

Electrochemical techniques encompass a range of methods designed to investigate processes occurring within an electrochemical cell by tracking changes in either current (amperes) or potential (volts) as a function of time (seconds). These techniques are generally grouped into three main categories: potentiometry, coulometry, and voltammetry. Among these, voltammetric methods are the most widely utilized in contemporary electrochemical analysis due to their versatility and analytical power. Voltammetry offers both qualitative and quantitative insights, along with advantages such as high sensitivity**,** fast data acquisition**,** relatively simple instrumentation, and the ability to extract kinetic parameters. Its robust theoretical foundation also supports the reliable estimation of unknown variables in redox systems [212].

All voltammetric techniques share a core operational principle: an external potential is applied to the working electrode, and the resulting current is measured as it flows through the electrochemical cell [172]. Well-known examples of voltammetric methods include cyclic voltammetry (CV) and

chronoamperometry. These techniques are typically managed using a potentiostat**,** which is connected to a computer interface equipped with specialized software for experiment control and data processing.

2.2.4.1. Cyclic Voltammetry

Cyclic voltammetry (CV) is one of the most widely employed electrochemical techniques, valued for its broad applicability across various domains including electroanalysis**,** material characterization**,** electrosynthesis, and the study of reaction intermediates, redox processes, energy storage mechanisms, and material stability.

During this research, CV was used for electropolymerization and subsequent material deposition and followed by electrochemical characterization. Beyond electrochemistry, CV has found increasing relevance in interdisciplinary research involving chemistry, physics, and materials science [210], [213], [214].

The technique operates by linearly sweeping the applied potential between two values in a forward direction and then reversing it back at a defined scan rate (typically expressed in V/s), completing a full potential cycle. During this process, the current generated by oxidation and reduction of electroactive species is continuously measured

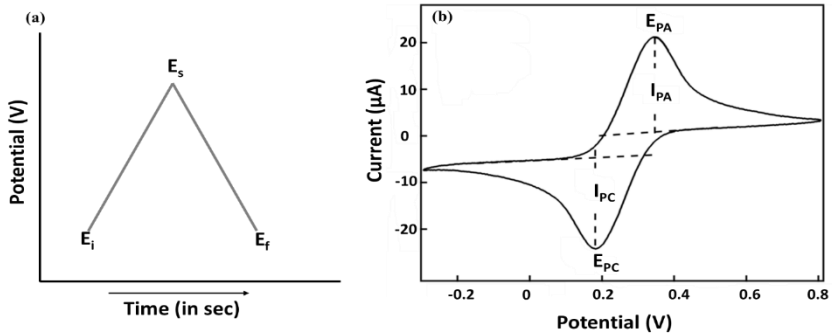

Figure 25: (a) Schematic representation of the potential excitation cycle over time, illustrating the initial potential (Ei), switching potential (Es), and final potential (Ef); (b) Representative cyclic voltammogram recorded in 1 mM $K_4[Fe(CN)_6]$ with 0.1 M $NaNO_3$ as the supporting electrolyte at a scan rate of 50 $mV{\cdot}s^{-1}$.

This produces a characteristic current–potential plot known as a voltammogram (I vs. E), from which key features such as the anodic and cathodic peak potentials (Epa and Epc) and the corresponding peak currents (Ipa and Ipc) can be extracted (as shown in **Figure 25**). These parameters provide valuable insights into the kinetics, mechanism, and concentration of the electrochemical reactions under investigation [214].

2.2.4.2. Chronoamperometry

Chronoamperometry is a straightforward yet powerful electrochemical technique used to monitor current as a function of time under a constant applied potential. Often referred to as a "potential step method," it is widely employed to investigate diffusion-controlled redox processes[215].

In a typical chronoamperometric experiment, the working electrode potential is rapidly stepped from its open circuit potential where no net electrochemical reaction occurs to a value at which the analyte undergoes oxidation or reduction, depending on the system conditions (**Figure 26**A). This potential is maintained for a predetermined period, allowing the redox process to proceed.

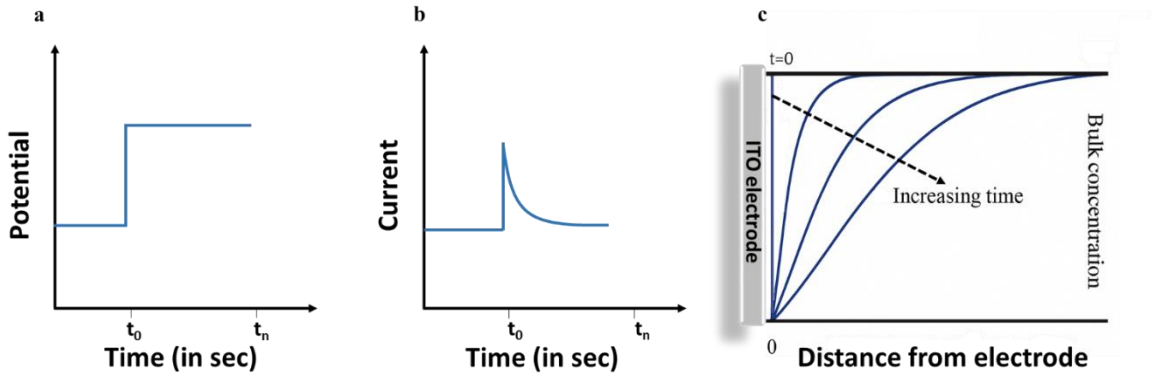

Figure 26: (a) Representative potential-time input profile; (b) the corresponding current-time transient response; and (c) the concentration profile of the analyte species as a function of time following the applied potential.

Immediately following the potential step, a sharp spike in current is observed. This transient response corresponds to the rapid consumption of electroactive species near the electrode surface. Over time, the current decays due to the formation of a diffusion layer, eventually reaching a quasi-steady-state (**Figure 26**B). During this period, a concentration gradient forms between the bulk

solution and the electrode surface (**Figure 26**C), and analyte molecules diffuse from the bulk to the electrode interface.

As time progresses, the diffusion layer continues to grow, the concentration gradient flattens, and the corresponding current decreases. The resulting chronoamperometric response referred to as a chronoamperogram can be mathematically described by the Cottrell equation (Equation 2.1), where the current is inversely proportional to the square root of time and directly proportional to the analyte concentration.

$$i_t = \frac{nFAC\sqrt{D}}{\sqrt{\pi t}}$$

Where n is the number of electrons transferred during the reaction, F is Farradays constant, A corresponds to the surface are, C represents the analyte concentration (in mol/L), D is the diffusion coefficient (cm^2/s), and t is time in sec.

2.2.5. Spectroscopic Methods

The modified electrodes after grafting and electropolymerization were characterized by different spectroscopic techniques.

2.2.5.1. UV-Vis Spectroscopy

UV-Visible spectroscopy is an analytical technique that relies on the absorption of ultraviolet and/or visible light (wavelength range: 200–800 nm) of compounds in liquid or solid state and it gives quantitative and qualitative information about the compounds and complexes. This method is governed by the Beer-Lambert law, which describes the attenuation of a monochromatic light beam as it passes through an absorbing medium (**Figure 27**). Specifically, when light of initial intensity (**I_0**) passes through a solution of thickness (**l**) and concentration (**C**), a portion of the light is absorbed, and the remaining intensity (**I**) is transmitted. The decrease in light intensity follows an exponential decay pattern, described by:

$$I = I_0 \times e^{-KlC}$$

I: transmitted light intensity

I_0: incident light intensity

l: path length (cm)

C: concentration of the absorbing species

k: absorption coefficient specific to the substance

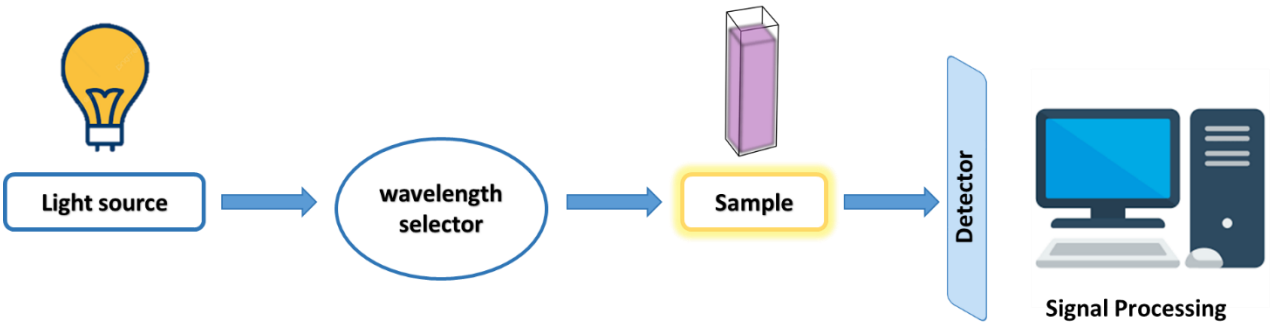

Figure 27: UV-VIS spectroscopy experimental set-up.

This relationship can be also expressed in terms of absorbance and transmittance, where using this approach one can determine the molar absorption coefficient of the absorbing material which is an intrinsic property that describes how strongly a chemical species absorbs light at a given wavelength [216].

The UV-Vis spectra were recorded on a Cary 60 spectrophotometer (Agilent Technologies). The absorbance was measured using a Cary WinUV-Scan software using different wavelength ranges between 200 and 800 nm. Preceding the characterization of the polymerized surfaces, blank measurements were done to compensate the background absorption of the ITO substrate, and in solution blank measurements were performed by preparing blank solutions consisting only of an organic solvent.

2.2.5.2. X-ray Photoelectron Spectroscopy

X-ray photoelectron spectroscopy (XPS) is a spectroscopic technique used to investigate thin film layers. In XPS the substrate is bombarded with X-rays with a well-defined energy. The X-rays interact with core electrons present around the nucleus of the different atoms present in the sample, and these electrons, if they escape the sample, is emitted at a well-defined kinetic energy, EK, given by:

$$Ek = hv - Eb - \Phi$$

Where hv is the X-ray photon energy, Eb is the electron binding energy, and Φ the work function that is the energy needed for the electron to free itself from the surface. Where all the values depend on the spectrometer and the substrate. In fact, the kinetic energy of the photoelectrons emanating from different types of atoms and orbitals, and even the same type of atom and orbital in different binding states, have different binding energies. Thus, by separating the electrons with different kinetic energy in an analyzer and displaying the results in a spectrum showing the photoelectron intensity, different types of atoms present on the surface and their abundance can be easily determined [217].

The samples were analyzed using KRATOS Axis Ultra X-ray photoelectron spectrometer equipped with the monochromatic Al Kα X-ray source (hν = 1486.6 eV, 150 W) (Kratos Analytical, Manchester, UK) in an analytical chamber that was maintained at low pressure (10−9 mbar). All the binding energies were calibrated using the C 1 s binding energy peak centered at 284.5 eV as a reference. Curve-fitting of the XPS data has been done by using Gaussian-Lorentzian functions with CasaXPS sotware.

2.2.5.3. Raman Spectroscopy

Raman spectroscopy is a non-destructive vibrational spectroscopic technique used to provide molecular-level information on the chemical composition, structure, and interactions within a material. The technique is based on inelastic scattering of monochromatic light, usually from a laser source, known as Raman scattering. When the incident light interacts with molecular vibrations, phonons, or other excitations in the system, a small fraction of the scattered light is shifted in energy, corresponding to the vibrational modes of the molecules. The energy difference between the incident and scattered photons (Raman shift) is characteristic of specific molecular bonds and functional groups, thus allowing for compound identification and structural elucidation [218].

In contrast to infrared (IR) spectroscopy, which relies on changes in dipole moment, Raman spectroscopy depends on changes in molecular polarizability, making it especially useful for studying symmetrical non-polar bonds and complex molecular structures. Raman spectra typically display sharp and well-resolved peaks, making the technique highly effective for detecting subtle changes in molecular environments.

A Renishaw inViaTM Qontor microspectrometer with an optical microscope in confocal mode, equipped with a long-frontal Olympus X50 objective with a numerical aperture of 0.55 and a slit opening aperture of 0.65 μm was used on the sample, the laser's (λ = 532 nm) power was about 10 mW. The spectra were acquired in 20 acquisitions of 5 s each with a spectral resolution of 3 cm^{-1}.

2.2.5.4. Fourier Transform Infrared Spectroscopy

Fourier Transform Infrared Spectroscopy (FTIR) is a spectroscopic technique used to characterize the functional groups present in organic molecules (such as OH, NH_2, acrylate, etc.). It is therefore used for identifying a compound or even determining the composition of a sample. This technique analyzes the infrared region of the electromagnetic spectrum, which corresponds to the energy difference between two vibrational states.

The principle of this technique is based on the interaction of infrared radiation with the material. It measures how much light is absorbed by the compounds at each wavelength, which causes the vibration of their chemical bonds. FTIR uses an interferometer to collect interferograms which are mathematically converted (using a Fourier transform) into an IR absorption spectrum. This resulting spectrum is a plot of absorbance or transmittance as a function of the wavelength (cm^{-1}).

2.2.6. Grazing-Incidence Small-Angle X-ray Scattering

Small Angle X ray scattering is a non-destructive and highly versatile method for analyzing non-structures and any type of material, spanning from inorganic materials to biological ones. X rays or neutron transmission geometry are very well established and normally used in micro-scale characterization with a high grade of precision [219]. In our case, it was used to characterize the mesoporous silica films with different pore size. This was done by collecting data on a "SAXSess mc^2" instrument (Anton Paar) equipped with Cu-Kα source (λ = 0.1542 nm) operating at 40 kV and 50 mA and a CCD detector (Princeton Instruments).

2.3. Synthesis and Electrode Modification Protocols

2.3.1. Synthesis of $[Fe(tpy\text{-}Ph\text{-}NH_2)_2][PF_6]_2$, (1):

The preparation of the complex involves preparing a solution of 250 mg (0.77 mmol) of the ligand 4-[(2,2':6',2''-terpyridine]-4'-yl)aniline and 48.79 mg (0.385 mmol) of ferrous chloride in 10 ml of ethanol. It is important to mention that other iron(ll) salts could also be used for the synthesis

of this complex. The color of the solution turns purple immediately; then we leave the solution stirring overnight.

The next day, we prepare another solution consisting of 100 mg of sodium hexafluorophosphate in 5 ml of water, then add this solution to the previous one and leave it for 10 minutes to precipitate 1. Then, we filtrate the powder and we dry the product by rinsing the filtrate with diethyl ether obtaining the complex at 79% yield. After preparing the complex, ^{1}H-NMR is performed to check using CD_3CN as a solvent. δ = 9.08 (s, 4H), 8.57 (d, 4H), 8.15 (d, 4H), 7.85 (td, 4H), 7.20 (d, 4H), 7.08 (t, 4H), 7 (d, 4H), 4.85 (s, -NH_2).

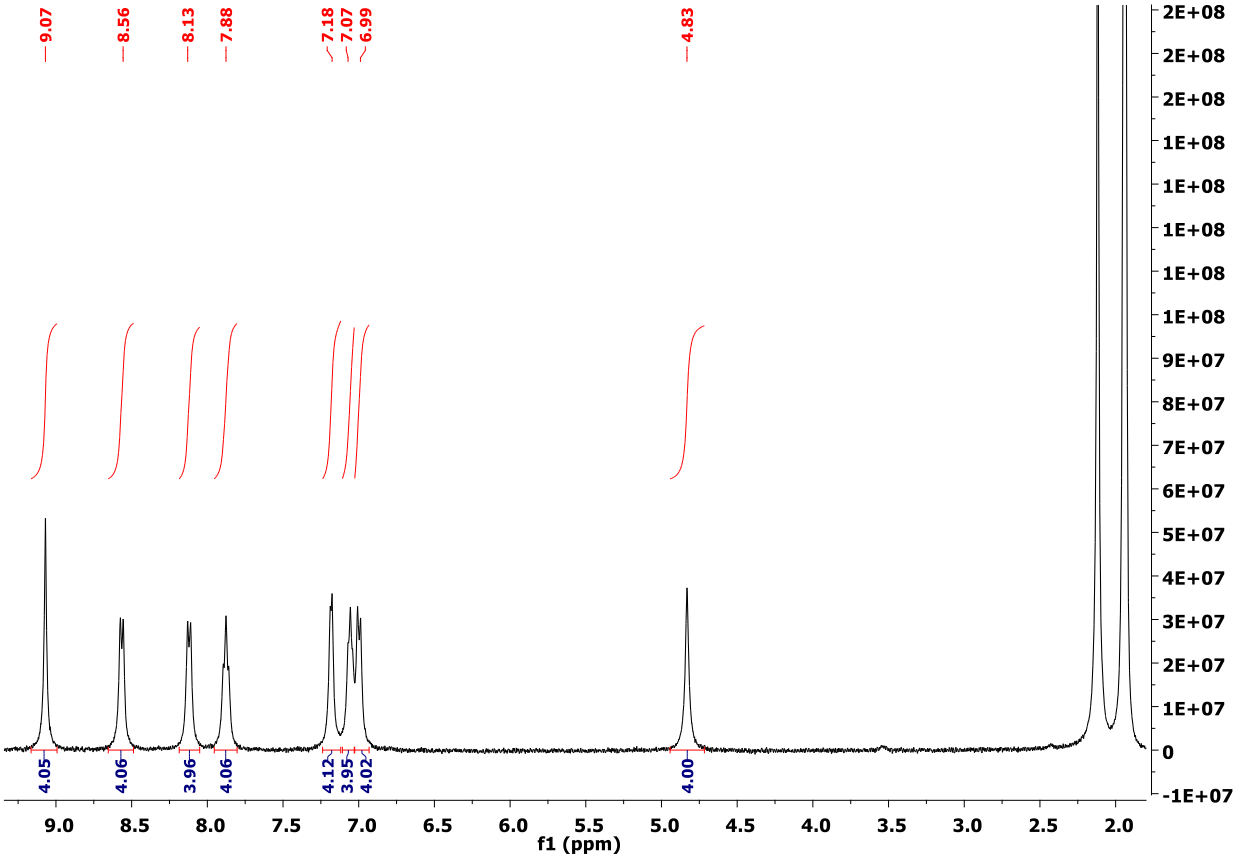

Figure 28: ^{1}H-NMR spectrum of (1) in CD_3CN.

2.3.2. Synthesis of [Ru(tpy-Ph-NH_2)$_2$][PF_6]$_2$, (2):

The preparation of the complex involves preparing a solution of 100 mg (0.382 mmol) of ruthenium (III)chloride trihydrate and 246.52 mg (0.76 mmol) of the ligand 4-[(2,2':6',2''-terpyridine]-4'-yl)aniline in 100 ml of ethanol and 4 drops of ethyl morpholine for reduction. This solution is refluxed at 95°C for 24 hours.

After filtration, the solution is concentrated and a mixture of H_2O with 200 mg of ammonium hexafluorophosphate is added to precipitate the complex. A red powder is obtained, washed with water, and dried to achieve a yield of 60%. After preparing the complex, ^{1}H-NMR is performed to check using CD_3CN as a solvent. δ = 8.9 (s, 4H), 8.6 (d, 4H), 8.1 (d, 4H), 7.9 (td, 4H), 7.4 (d, 4H), 7.2 (t, 4H), 7 (d, 4H), 4.77 (s, 4H).

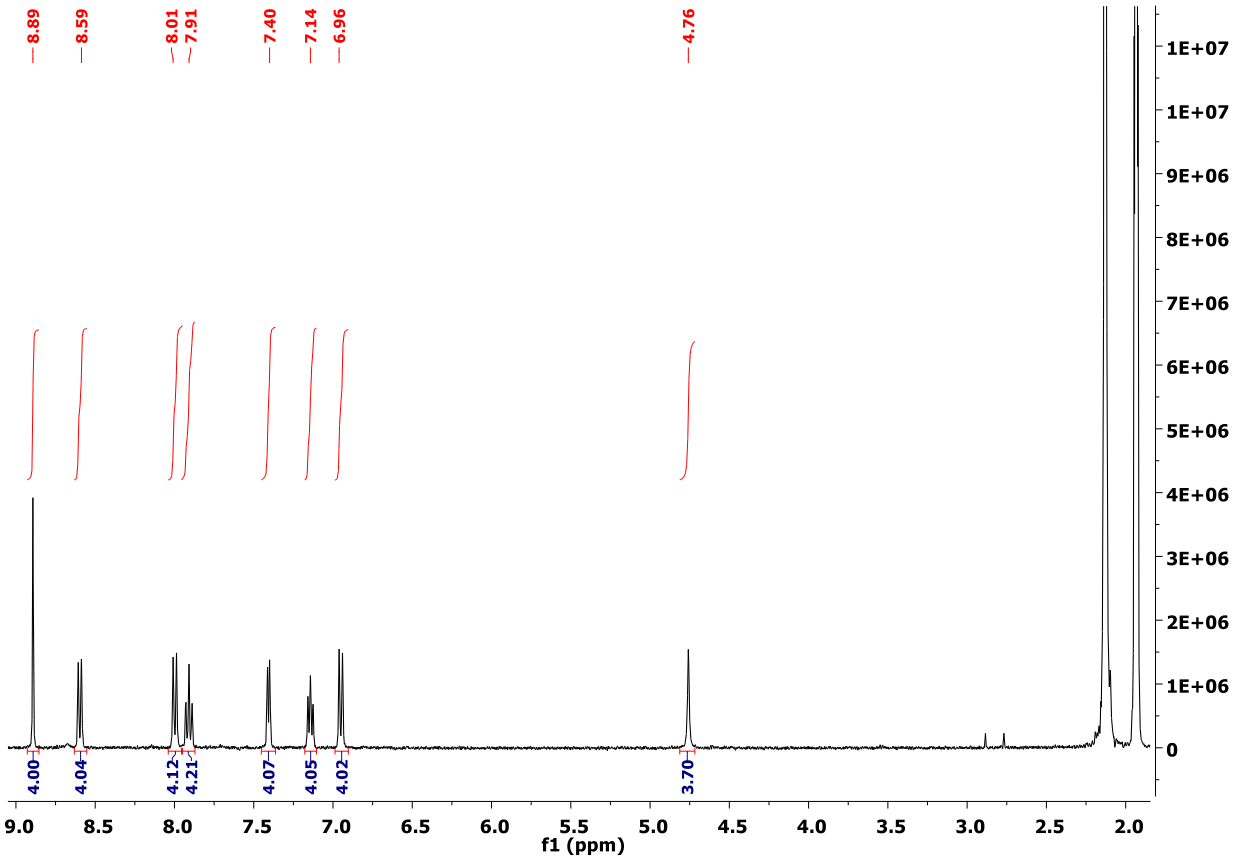

Figure 29: ^{1}H-NMR spectrum of (2) in CD_3CN.

2.3.3. Synthesis of $[Zn(tpy\text{-}Ph\text{-}NH_2)_2][PF_6]_2$, (3):

The preparation of this complex involves preparing a solution of 80 mg (0.355 mmol) of zinc acetate dehydrate and 230 mg (0.715 mmol) of the ligand 4-[(2,2':6',2''-terpyridine]-4'-yl)aniline in 80 ml of methanol. This solution is then refluxed at 80°C for 10 hours. After that, the solution is cooled to room temperature and concentrated, and a mixture of H_2O with 200 mg of ammonium hexafluorophosphate is added to precipitate the complex. A yellow powder is obtained which is washed with diethyl ether to dry the compound and we achieve a yield of 71%. If the compound was determined to be not pure by NMR it is recrystallized by preparing a solution of 9 ml of

methanol to 3 ml of acetonitrile., ^{1}H-NMR is performed to check using CD_3CN as a solvent. δ = 8.85 (s, 4H), 8.7 (d, 4H), 8.19 (td, 4H), 8.1 (d,4H), 7.8 (d, 4H), 7.4 (t, 4H), 6.99 (d, 4H), 4.7 (s, 4H).

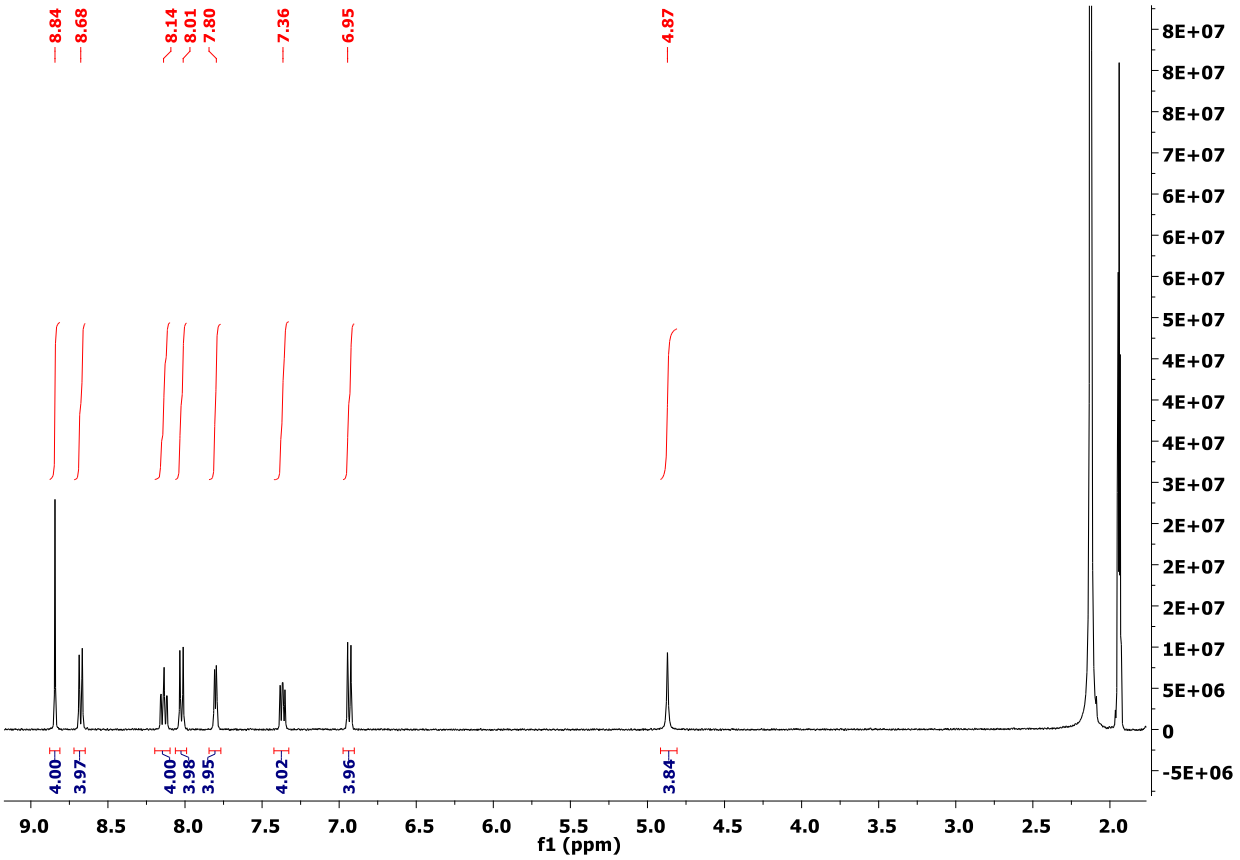

Figure 30: ^{1}H-NMR spectrum of (3) in CD_3CN.

2.3.4. Synthesis of $[Co(tpy\text{-}Ph\text{-}NH_2)_2][PF_6]_2$, (4):

The preparation of this complex involves preparing a solution of 183 mg (0.77 mmol) of cobalt (II) chloride hexahydrate and 500 mg (1.54 mmol) of the ligand 4-[(2,2':6',2''-terpyridin]-4'-yl)aniline in 80 ml of methanol. This solution is then refluxed at 80°C overnight. After that, the solution is cooled to room temperature and concentrated, and a mixture of H_2O with 200 mg of ammonium hexafluorophosphate is added to precipitate the complex. A brown-orange powder is obtained which is washed with diethyl ether to dry the compound and we achieve a yield of 75%. This compound doesn't show a good ^{1}H-NMR spectra since this complex is paramagnetic.

2.3.5. Synthesis of $[Fe(tpy)_2][PF_6]_2$:

The preparation of this complex is similar to that of (1) where the only difference is the ligand used which is 2,2′:6′,2″-terpyridine instead of 4-[(2,2’:6’,2’’-terpyridine]-4’-yl)aniline.

A solution of 180 mg (0.77 mmol) of the ligand 2,2′:6′,2″-terpyridine and 145 mg (0.385 mmol) of ferrous chloride in 10 ml of ethanol. The color of the solution turns purple immediately; then we leave the solution stirring overnight. The next day, we prepare another solution consisting of 100 mg of sodium hexafluorophosphate in 5 ml of water, then add this solution to the previous one to precipitate. After filtration, we obtain the complex which is also purple with a yield of 75 %. Then, ^{1}H-NMR is performed to check using CD_3CN as a solvent.

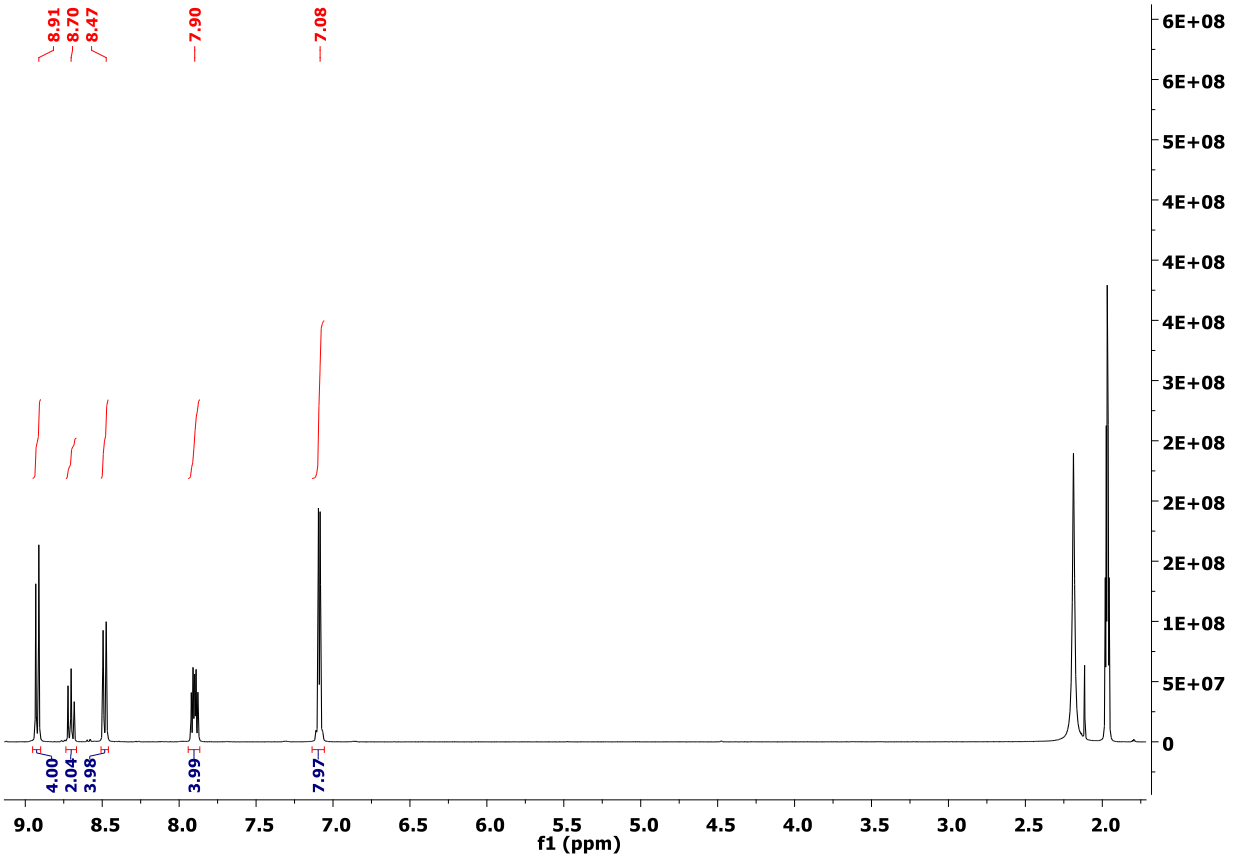

Figure 31: ^{1}H-NMR spectrum of the iron complex in CD_3CN.

2.3.6. Synthesis of $[Ru(tpy\text{-}Ph)_2][PF_6]_2$:

The preparation of the complex is similar to that of (2) where the only difference is also the ligand used which is 4'-phenyl-2,2':6',2"-terpyridine instead of the original ligand.

The preparation of the complex involves preparing a solution of 100 mg (0.382 mmol) of ruthenium (III)chloride trihydrate and 235 mg (0.76 mmol) of the ligand 4'-phenyl-2,2':6',2''-terpyridine in 100 ml of ethanol and 4 drops of ethyl morpholine for reduction. This solution is refluxed at 95°C for 24 hours. After filtration, the solution is concentrated and a mixture of H_2O with 200 mg of ammonium hexafluorophosphate is added to precipitate the complex. A red powder is obtained, washed with water, and dried to achieve a yield of 80%. After preparing the complex, ^{1}H-NMR is performed to check using CD_3CN as a solvent.

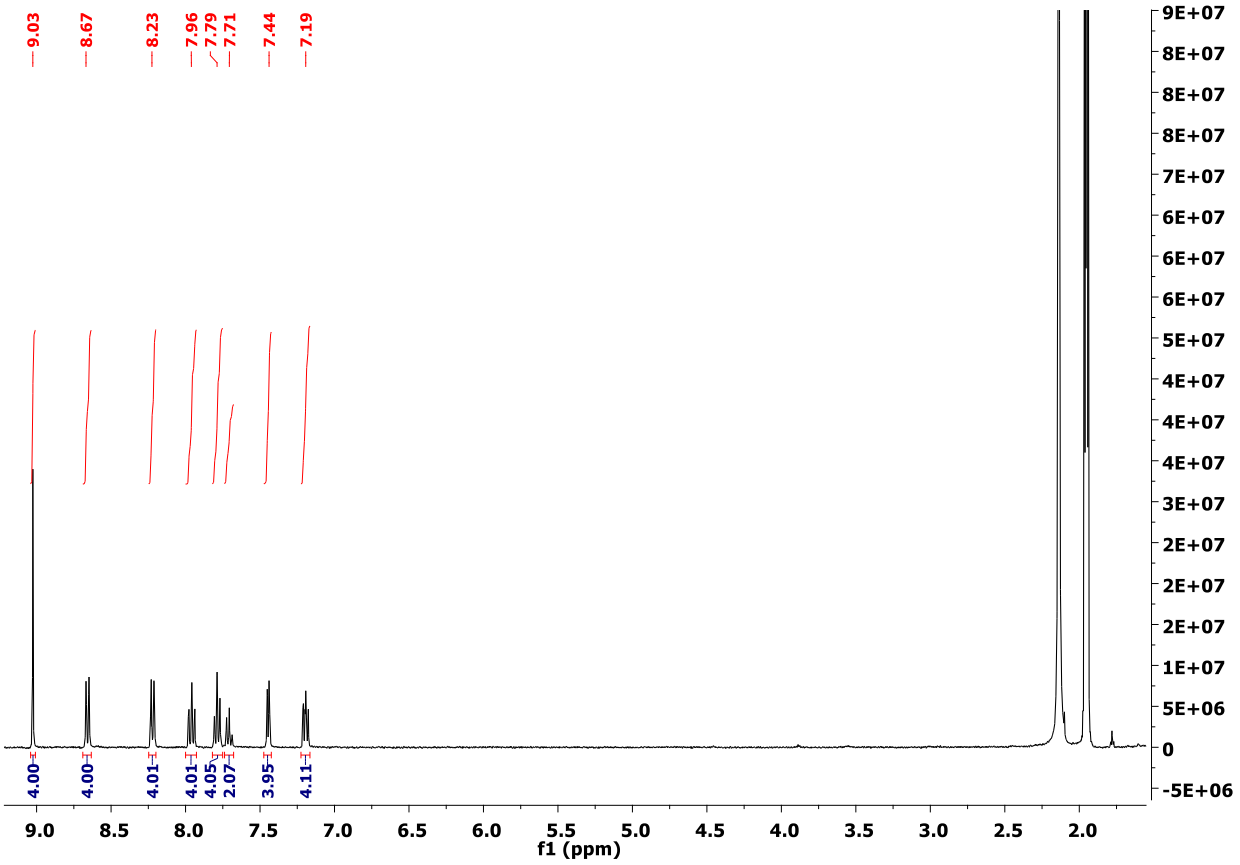

Figure 32: ^{1}H-NMR spectrum of ruthenium complex in CD_3CN.

2.3.7. Synthesis of Eicosyltrimethylammonium Bromide (C_{20}TAB)

A mixture of 5 g of 1-bromoeicosane (13.8 mmol) and 20 ml of trimethylamine was added to ethanol (25 ml) in a round-bottom flask equipped with a reflux condenser. The reaction mixture was heated under reflux at 80-100°C overnight (around 16 hours) under a nitrogen atmosphere.

After refluxing, the solution is filtrated and then placed in the refrigerator overnight to reduce the temperature and induce crystallization of the desired compound. Then the next day the solution is

filtrated and washed with cold ethanol to remove any non-reacted starting material and then dried using diethyl ether to obtain a white surfactant powder and a yield of around 82%. After preparing the surfactant, ^{1}H-NMR is performed to check using $CdCl_3$ as a solvent. δ = 3.47-3.56 (m, 2H), 3.41 (s, 9H), 1.63-1.77 (m,2H), 1.26-1.37 (m, 2H), 1.17 (brs, 32), 0.83 (t, 3H).

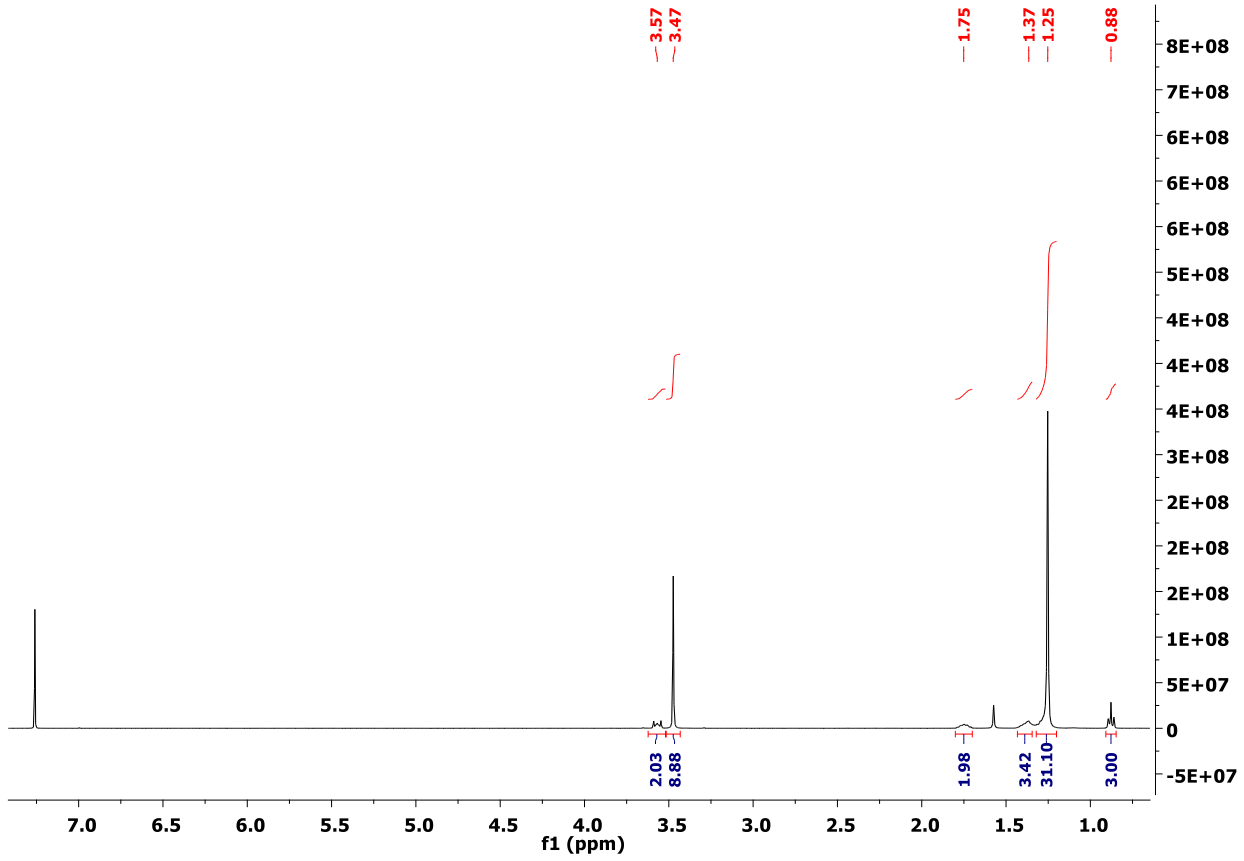

Figure 33: ^{1}H-NMR spectrum of C_{20}TAB in $CDCl_3$.

2.3.8. Synthesis of the Conductive Gel for Spectroelectrochemical Experiments

The hydrogel was prepared via free-radical polymerization of N,N-dimethylacrylamide (DMA), using N, N′-methylenebisacrylamide (MBA) as a crosslinker, and potassium peroxodisulfate (KPS) as the initiator. Lithium perchlorate ($LiClO_4$) was incorporated to enhance the gel's conductivity.

In a 50 mL beaker, 17.4 g of deionized water was added, followed by 2.6 g (26.2 mmol) of DMA and 2.5 g (23.5 mmol) of $LiClO_4$. The mixture was stirred at room temperature until the salt was fully dissolved. Subsequently, 2.6 mg of MBA (±0.2 mg) (0.0169 mmol) was added and stirring was continued for 2 hours to ensure homogeneity. After this pre-polymer solution was well mixed,

it was placed in an ice bath and cooled for 5–10 minutes. Once cooled, 6 mg (0.0222 mmol) of KPS was introduced as the thermal initiator. The solution was maintained under stirring in the ice bath for an additional 1.5–2 hours to initiate partial polymerization while preventing premature gelation.

Following the initiation phase, the solution was poured into a mold and transferred to an oven preheated to 60 °C. The polymerization was completed by thermal curing for 10 minutes, resulting in the formation of a transparent, flexible hydrogel weighing approximately 20 g.

2.3.9. Electrografting of Bis (aminophenyl terpyridine) based Complexes and Compounds on Electrode Surface

In order to graft the desired monomers / compounds on the electrode surface, we form diazonium salts in solution which eventually undergoe electrochemical reduction. An aqueous solution containing 1 mM of the desired grafted molecule containing an amino group and 1 mM sodium nitrite in 0.5 M HCl was prepared then left stirring for around 10 minutes to have the formation of the monodiazonium cations in solution. Then the in situ generated cations are then electrochemically reduced using cyclic voltammetry (at around -0.1 to -0.2 V) to obtain reactive aryl groups that eventually graft on either bare ITO electrode or ITO electrodes that are functionalized with vertically aligned mesoporous silica films.

This covalent link ensures that these compounds are stable and not easily removed from the electrode surface. Finally, these modified electrodes are then rinsed with water and ultrasonicated in ethanol solution to remove unreacted species.

2.3.10. Electropolymerization of Bis(aminophenyl terpyridine) complexes:

The principle of this process is to form molecular wires as mentioned in the chapter above. This process is detailed in the results section and it is based on the oxidative polymerization of the coordination complexes such as (1) and (2) to create polymer chains on the electrode surface. Different electrolyte solutions were used for the electropolymerization.

Initially, we used an acidic solution composed of H_2O/ACN with 0.1 M of perchloric acid and 1 mM of the complexes (1) and (2), studying the effect of changing the number of scans. Recently, along with changing the number of scans, we also changed the nature of the electrolyte used to study the effect on the efficinecy of the electropolymerization process. The electrolytes tested

included lithium perchlorate, tetrabutylammonium hexafluorophosphate ($TBAPF_6$), sodium perchlorate, sulfuric acid, tetrabutylammonium perchlorate, sodium sulfate, and tetraethylammonium perchlorate.

Furthermore, in order to form these polymers, the electropolymerization takes place using cyclic voltammetry where we use appropriate potential ranges with a constant scan rate of 100 mV/s, and using chronoamperometry where a suitable constant potential is applied for a period of time. Then the samples are washed using acetone then ultrasonicated in acetonitrile to remove any non-covalently linked material.

2.3.11. Electrochemical Characterization of the modified films

After electrografting the coordination complexes and electropolymerization on the ITO electrodes, they are electrochemically characterized by preparing a monomer-free electrolyte solution that is usually made up of acetonitrile with 0.1 M of perchloric acid or acetonitrile with 0.1 M of lithium perchlorate. Cyclic voltammetry is used to verify the presence for example of the irreversible oxidation peak that corresponds to the oxidation of amino groups, and the presence of redox signals for iron and ruthenium that validate that this monomer/polymer is adsorbed on the electrode surface.

Furthermore, we can estimate the surface concentration of the grafted monomers and polymer films using this technique by determining the anodic and cathodic peak current from the cyclic voltammogram and then using this value to calculate the surface concentration in mol/cm^2. Also, in order to determine the type of electrochemical behavior which is either diffusion-controlled or thin film adsorption reactions for these films, the variation of the peak currents with respect to the potential scan rate is studied.

The cyclic voltammetry data shows the relationship between scan rate and peak current for a redox-active species immobilized on the electrode surface (ITO). The voltammograms were recorded at a series of scan rates ranging from 10 mV/s to 100 mV/s. If the anodic and cathodic peak currents increase proportionally with increasing scan rate, this confirms adsorption-controlled electrochemical processes. However, if the peak current varies with the square root of the scan rate, this indicates to diffusion-controlled processes.

2.3.12. Synthesis of the Vertically Oriented Mesoporous Silica Films

Mesoporous silica films were synthesized on electrode surfaces via electrochemically assisted self-assembly using a sol–gel precursor solution. The precursor sol was prepared by mixing 100 mM tetraethoxysilane (TEOS), 32 mM cetyltrimethylammonium bromide (CTAB), and 0.1 M sodium nitrate ($NaNO_3$) in a solvent mixture consisting of 20 mL deionized water and 20 mL ethanol. The pH of the solution was adjusted to approximately 3 by the dropwise addition of 1 M hydrochloric acid, followed by hydrolysis under continuous stirring for 2.5 hours at room temperature to ensure complete precursor activation.

The mesoporous silica films were then deposited onto the electrode surface using a custom-designed three-electrode electrochemical cell. Deposition was carried out by applying a fixed potential of −1.3 V for 20 seconds. Immediately after deposition, the electrodes were removed, rinsed thoroughly with ethanol and deionized water, and air-dried. The dried films were then subjected to thermal treatment by placing them in an oven at 130 °C overnight for aging.

To remove the surfactant template and generate the open mesoporous structure, the electrodes were immersed in a 0.1 M HCl solution prepared in ethanol and left for 15 minutes. This final step ensured the removal of the structure-directing agent and rendered the films ready for further functionalization or electrochemical application. Different surfactants were used to obtain the mesoporous films with different pore sizes.

Chapter III: Electropolymerization of Aminophenyl-Substituted Bis(terpyridine) Metal Complexes and Electrochromic Properties of the Obtained Metallopolymers

3. Chapter 3: Electropolymerization of Aminophenyl-Substituted Bis(terpyridine) Metal Complexes and Electrochromic Properties of the Obtained Metallopolymers

3.1. Introduction

Electropolymerization is a powerful and versatile technique for synthesizing conducting polymers directly on electrode surfaces via electrochemical oxidation [1],[2] or reduction [222], [223] of monomeric units [224], [225]. This method enables the formation of thin, uniform and adherent polymeric films, widely applicable in various fields such as (bio)sensing [226], [227], [228], energy storage [229], [230], electrochromism [231], [232], [233], smart coatings [234] and surface protection [235], [236] . The mechanism typically involves the generation of reactive intermediates, often radical cations, that undergo coupling reactions to form conjugated polymer chains [237]. The resulting materials properties are strongly influenced by the chemical structure of the monomer, the electrochemical conditions, and the nature of the supporting electrolyte [220].

The electropolymerization mechanism of organic monomers such as aniline [238], pyrrole [221], and thiophene [239] is well established, most often begining with the generation of radical cations upon anodic oxidation. Among them, polyaniline (PANI) has served as a model system due to its facile synthesis, redox activity, and environmental stability [240]. For monomers bearing aminophenyl substituents, such as aniline and its derivatives, oxidation leads to nitrogen-centered radicals that preferentially couple at the para position to form extended conjugated chains through C–N or C–C linkages [241]. These radical intermediates initiate oligomerization near the electrode surface, where successive oxidation–coupling cycles propagate polymer growth. Parameters such as monomer substituent position, solvent polarity, electrolyte composition, electrode material, and applied potential govern both the efficiency and the structural outcome of the process.

However, the scope of electropolymerization has expanded far beyond aniline-based systems [242]. In this sense, the extension of this strategy to the fabrication of metallopolymers, i.e., hybrid systems that combine the intrinsic conductivity of conjugated polymers with the redox and optical functionalities of transition metal centers [56], [243], has been explored far less, despite offering significant opportunities to develop advanced functional materials. Redox-active metallopolymers incorporate metal centers directly into polymer backbones, merging the electrical conductivity and

processability of organic polymers with the tunable electronic, optical, and catalytic properties of transition metal complexes. This hybrid nature makes them especially attractive for electrochromic applications, where multistate redox activity and precise spectral modulation are critical [243].

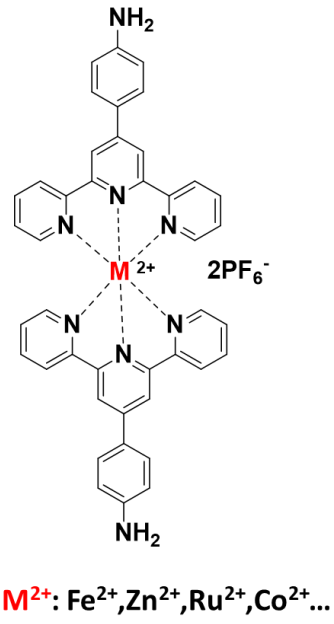

Figure 34: schematic representation of the desired metal-transition coordination complexes.

Previous studies have demonstrated the potential of electropolymerization processes to fabricate metallopolymers. For example, ruthenium(II) polypyridine complexes bearing pendant bithienyl units have been electropolymerized to yield photoredox-active films with finely controlled thickness and morphology, while preserving the intrinsic optical and redox characteristics of the metal centers [244]. Likewise, Abruña's group was a pioneer in this area demonstrating the electropolymerization of Co(II) and Ru(II) vinylterpyridine complexes, obtaining conductive films with reversible redox switching and good stability [245]. They also investigated electropolymerized bis(vinylterpyridine)cobalt complexes that showed promising electrocatalytic activity [246], [247].

More recently, Zhong et al. have made notable progress in developing electropolymerized films of ruthenium complexes for multistate electrochromism and ion sensing [248]. Zhong's group also explored reductive electropolymerization, forming polymeric networks via reduction of terpyridine ligands, significantly expanding the scope of electrochemical mechanisms that can be involved [249]. These examples highlight the versatility of electropolymerization as a bottom-up

approach for integrating transition metal complexes into electroactive films with promising applications in electrochromism [231], [232], [233], sensing [226], [250], or energy storage [229], [230].

Transition metal substituted bis(terpyridine) complexes (shown in **Figure 34**), particularly those based on Fe(II), are attractive systems for studying such effects due to their well-defined geometry, reversible Fe^{2+}/Fe^{3+} redox behavior, and strong metal-to-ligand charge transfer (MLCT) absorption in the visible. Some studies have focused on such iron-based complexes featuring bis(terpyridine) ligands functionalized with aminophenyl groups [251], [252]. In this case, one can expect an electropolymerization process starting by the oxidation of the aminophenyl moieties as for non-substituted aniline-based monomers, but the polymerization mechanism will be obviously different in case of a para-substituted position for the amine groups. Despite prior proposals suggesting azo linkages as the dominant polymerization pathway, experimental confirmation remains incomplete.

This work re-examines the electropolymerization mechanism of $[Fe(tpy\text{-}Ph\text{-}NH_2)_2]^{2+}$ to elucidate the nature of the linkages formed during electrochemical oxidation of the aminophenyl terminal group. Through this novel mechanistic investigation mainly based on new electrochemical data we aim to expand the fundamental understanding of such metallopolymer formation by electro-assisted polymerization. Through a combination of spectroscopic and electrochemical characterization, this study provides new insight into the structure and growth mechanism of electrochemically generated poly$[Fe(tpy\text{-}Ph\text{-}NH_2)_2]^{2+}$ films. This electropolymerization technique was also tested using different coordination complexes such as $[Ru(tpy\text{-}Ph\text{-}NH_2)_2]^{2+}$, $[Zn(tpy\text{-}Ph\text{-}NH_2)_2]^{2+}$, and $[Co(tpy\text{-}Ph\text{-}NH_2)_2]^{2+}$.

3.2. Results and Discussion

3.2.1. Electrochemical Behavior of $[Fe(tpy\text{-}Ph\text{-}NH_2)_2]^{2+}$ on Electrode Surfaces

3.2.1.1. Electrochemical behavior of $[Fe(tpy\text{-}Ph\text{-}NH_2)_2]^{2+}$ in the anodic region: evidence of its electropolymerization and comparison to the unsubstituted $[Fe(tpy\text{-}Ph)_2]^{2+}$ compound

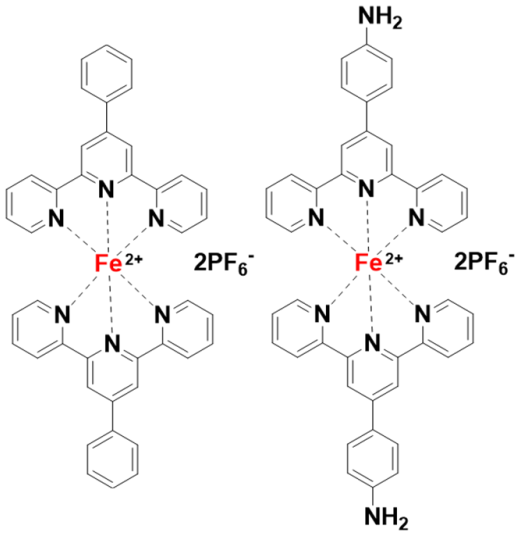

Figure 35: Structure of the compounds $[Fe(tpy\text{-}Ph)_2]^{2+}$ (1) and $[Fe(tpy\text{-}Ph\text{-}NH_2)_2]^{2+}$ (2).

The electrochemical properties of the 4-aminophenyl-functionalized bis(terpyridine) iron complex, $[Fe(tpy\text{-}Ph\text{-}NH_2)_2]^{2+}$ (compound **2**, **Figure 35**), were first investigated by multisweep CV (Figure 1) using ITO as working electrode, and compared to the behavior of the non-substituted analog $[Fe(tpy\text{-}Ph)_2]^{2+}$ (compound **1**, **Figure 35**) serving as electropolymerization-inactive control species. Typical CV curves obtained for compound **1**, recorded at a scan rate of 100 $mV \cdot s^{-1}$ in acetonitrile (+ 0.1 M $LiClO_4$), revealed a classical diffusion-controlled redox system located at a potential of 1.02 V (*vs.* Ag/AgCl) with an anodic-to-cathodic peak-to-peak separation of 160 mV, characteristic of a quasi-reversible one-electron transfer attributed to the Fe^{3+}/Fe^{2+} redox couple (see **Figure 36A**).

No changes were observed during multiple successive potential scans, indicating the absence of any polymerization process. By contrast, the electrochemical response of compound **2**, which differs structurally from compound **1** by the presence of a para-substituted aminophenyl group in the terpyridine ligand (see **Figure 35**), resulted in a shift of the metal-centered redox process to approximately 1.10 V (*vs.* Ag/AgCl), with an additional irreversible anodic pre-peak appearing at 0.94 V (see first CV scan in **Figure 36B**). This new signal is attributed to the oxidation of the aminophenyl substituents in the para position of the terpyridine ligands, forming radical cations ($-NH_2^{\bullet+}$, Eq. 1a) which can deprotonate and the resulting radicals ($-NH^{\bullet}$, Eq. 1b) to combine to form hydrazo bonds (–NH–NH–, Eq. 2), similarly to a mechanism reported for other derivatives bearing aminophenyl groups. [253] A third irreversible anodic peak with a symmetric shape appeared at

1.43 V V (*vs.* Ag/AgCl), clearly visible in this first CV scan, which can be attributed to the oxidation of the hydrazo moieties previously formed in the system into azo bonds (–N=N–, Eq. 3) when operating in an aprotic solvent such as acetonitrile. The hydrazo group is electroactive and undergoes oxidation at relatively high potentials due to the stability of the π-conjugated system.

$$tpy–Ph–NH_2 - 1\ e^- \rightarrow tpy–Ph–NH_2^{\bullet+} \quad (1a)$$

$$tpy–Ph–NH_2^{\bullet+} - 1\ H^+ \rightarrow tpy–Ph–NH^{\bullet} \quad (1b)$$

$$2\ tpy–Ph–NH_2^{\bullet} \rightarrow tpy\text{-}Ph–NH–NH–Ph–tpy \quad (2)$$

$$tpy–Ph–NH–NH–Ph–tpy - 2\ e^- - 2\ H^+ \rightarrow tpy–Ph–N=N–Ph–tpy \quad (3)$$

This electrochemical response provides a first evidence for the successful formation of azo bonds in the sample prior to any further characterization of the formed films. Upon multiple potential scanning, compound **2** displayed a progressive increase in anodic peak currents, a trend indicating the initiation of a surface-confined electropolymerization process, likely driven by the oxidation of its electron-rich aminophenyl groups. During film growth, the pre-peak at 0.96 V and the post-peak at 1.43 V tended to merge with the continuously increasing iron signal.

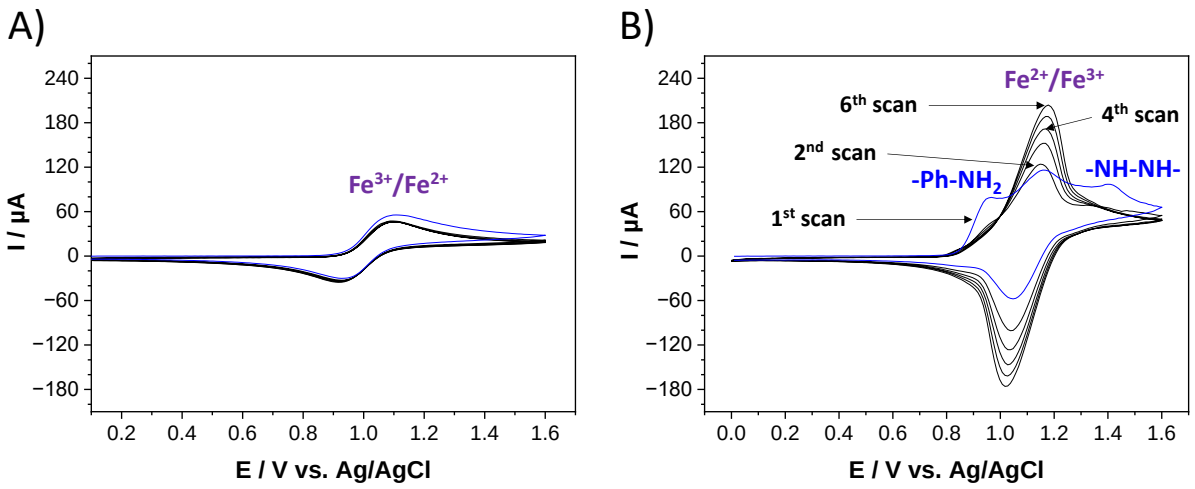

Figure 36: Comparison of the electrochemical behavior observed for compounds 1 (A) and 2 (B). Six successive CV curves (1st scan in blue) recorded at 100 mV s^{-1} in the oxidation region between 0.0 V and 1.6 V *vs.* Ag/AgCl, using ITO as working electrode in acetonitrile (+ 0.1 M $LiClO_4$) containing 1 mM of compound 1 (A) or 2 (B).

The electropolymerization of $[Fe(tpy\text{-}Ph\text{-}NH_2)_2]^{2+}$ is thus initiated by anodic oxidation of the aminophenyl terminal groups, resulting in the formation of radical cations via a one-electron

transfer process. This mechanism closely resembles the electrochemical behavior observed with aniline and other aromatic amines, such as triphenylamine and diphenylamine, where radical cation intermediates promote C–N and C–C coupling reactions, ultimately leading to the formation of conductive polymer networks. In such systems, charge delocalization extends beyond the nitrogen center to include the ortho and para positions of the aromatic ring, thereby facilitating efficient polymer growth. For instance, the electropolymerization of a complex similar to **2** but with the amino moieties in the meta position on the phenyl terminal groups proceeded by a reaction mechanism similar to that of aniline with the formation of C–N bonds (and the characteristic CV curve exhibited only two signals corresponding to the oxidation of the aminophenyl group (Eq. 1) and to the Fe^{3+}/Fe^{2+} redox couple).

In the present case (complex **2** with the amino moieties in the para position), once the radical cation is electrochemically generated, the para position is sterically or electronically blocked. This blockage prevents the usual coupling pathways and the electropolymerization occurs in another way, involving an alternative coupling reaction based on N–N or N=N bonds formation (Eqs. 2&3).

3.2.1.2. Effect of the nature of the supporting electrolyte on the electropolymerization process of 2.

The electropolymerization of 2 has been performed using different electrolytes. This was motivated by the fact that the nature of the supporting electrolyte is known to play a critical role in the electropolymerization of arylamine-based derivatives, influencing both the kinetics of electron transfer and the structure of the resulting polymer films. For instance, Patil et al. investigated the electropolymerization of poly(o-methoxyaniline) in various aqueous acidic media (HCl, H_2SO_4, HNO_3, and $HClO_4$), reporting a significant effect of the anion type and size on the rate of polymerization and the surface morphology of the resulting poly(o-methoxyaniline) films. Despite these differences, the optical absorption spectra indicated the formation of the conducting emeraldine salt phase across all electrolytes used. [252] Electrolyte composition may also affect ion-pairing, solubility of intermediates, and the stabilization of the corresponding radical cations generated during the anodic oxidation.

For example, it could be predicted that bulky, weakly coordinating anions such as ClO_4^- promote efficient delocalization of the charge on radical cation intermediates, facilitating coupling reactions and favoring polymer growth. In this sense, weakly coordinating anions such as PF_6^-, BF_4^-, ClO_4^-, could have an effect on the electropolymerization of metallopolymers by stabilizing positively charged intermediates (either metal-centered oxidation states or ligand-based radical cations) without engaging in strong coordination, which could otherwise interfere with polymer growth. In contrast, more coordinating or nucleophilic anions such as SO_4^{2-} and Cl^- may interact more strongly with reactive intermediates, leading to side reactions or reduced polymerization efficiency. Additionally, the cation of the supporting electrolyte can affect film morphology and doping level by influencing ion mobility during film formation.

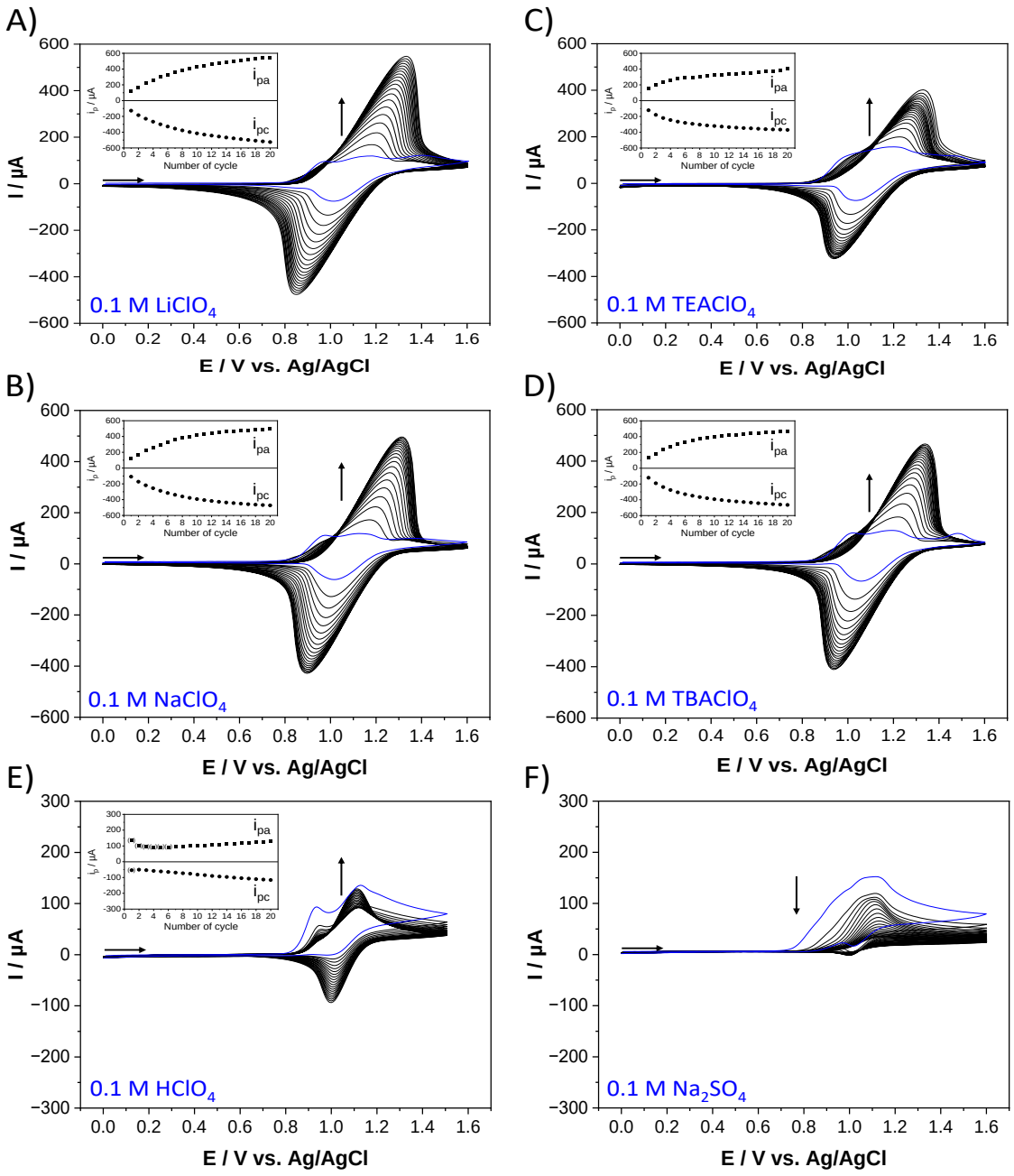

Figure 37: Effect of the supporting electrolyte on the efficiency of the electropolymerization of 2. 20 successive CV curves (1st scan in blue) recorded at 100 mV s^{-1} using ITO as working electrode in acetonitrile (ACN) containing 1 mM of compound 2 in various electrolytes: A) 0.1 M $LiClO_4$, B) 0.1 M $NaClO_4$, C) 0.1 M $TEAClO_4$, D) 0.1 M $TBAClO_4$, E) 0.2 M $HClO_4$ (in 1/1 v/v ACN/H2O), and F) 0.1 M Na_2SO_4.

Figure 37 illustrates typical CV curves (20 successive scans) recorded for the anodic electropolymerization of the iron complex (2) in the presence of various perchlorate-based

supporting electrolytes (**Figure 37**A-D), in perchloric acid (**Figure 37**E) and in sodium sulfate (**Figure 37**F). Effective electropolymerization was observed in all perchlorate-based electrolytes, as evidenced by a pronounced current increase over successive cycles, yet tending to levelling off or at least slowing down after ca. 7-8 cycles (see inserts in **Figure 37**A-D). Peak currents were slightly lower when using tetraalkylammonium counter ions, suggesting somewhat reduced film growth efficiency, which is possibly attributable to the larger size of these cations suffering from slower mobility within the growing polymer matrix; this phenomenon may also contribute to explain the slower film growth after ca. 7-8 CV cycles. The increased anodic-to-cathodic peak-to-peak separation was also found to increase with the number of CV scans (**Figure 37**A-D), indicating some increase in resistance at the electrode/solution interface due to polymer deposition.

By contrast, the CV response in $HClO_4$ was significantly different (**Figure 37**E), with less intense peak current growth upon cycling, indicating less effective electropolymerization, which can be attributed to protonation of the amino groups or destabilization of the metal–ligand complex, hindering film formation and efficient electron transfer. Furthermore, the absence of the third oxidation peak in the first CV scan (which was clearly visible in aprotic media, see **Figure 37**A-D) suggests an absence of oxidation of the hydrazo groups into azo moieties (Eq. 3). In the presence of proton donors, the deprotonation of the radical cations (generated at 0.93 V in that medium, see blue curve in **Figure 37**E) is more difficult, thus impeding the coupling reaction (Eq. 2) and preventing somehow the film growth (the evolution of the peak current as function of the number of scans is detailed in section 3.2.1.3). Protonation of (hydra)azo derivatives can also lead to the cleavage of the nitrogen-nitrogen bonds [254] or even the formation of highly reactive intermediates like nitrenium ions or aryl cations. [255]

The situation is even worse in the Na_2SO_4 electrolyte solution for which no electropolymerization can be observed (**Figure 37**F). Although redox features are present, yet with peak broadening and less well-defined signals (compare blue curve in **Figure 37**F with others in **Figure 37**), the current response rapidly decreased as the number of scans increased. This behavior suggests inefficient or inhibited electropolymerization, potentially due to the strong coordinating nature of sulfate anions (SO_4^{2-} may interact with the metal center or the ligand framework, interfering with the complex's redox processes and hindering film growth) and/or restricted electronic communication through the deposit (after 20 CV scans, the peak currents characteristic of the $Fe^{3+/2+}$ redox couple are only

33 µA for ipa and 12 µA for ipc, compared to several hundreds of µA for those corresponding to the polymeric films electrogenerated in perchlorate media).

These results highlight the crucial role of the electrolyte composition in dictating the efficiency and kinetics of the electropolymerization process. While $LiClO_4$ promoted robust film growth and electrochemical activity, $HClO_4$ and especially Na_2SO_4 appeared to impede these processes, likely due to the disruptive effects of excess protons on the polymer structure and/or affecting the coordination environment.

3.2.1.3. Effect of increasing the number of scans on the electrochemical response using 2 different electrolytes

After concluding that perchlorate-based supporting electrolytes facilitate the electropolymerization process of the iron complex and leads to the formation of electroactive films, we study the effect of changing the number of scans by performing a multisweep CV using the same conditions mentioned above where we use non-modified ITO as the working electrodes. The CV curves obtained for compound **2** (1 mM) were recorded at a scan rate of 100 $mV \cdot s^{-1}$ in acetonitrile (+ 0.1 M $LiClO_4$) and 4 different number of scans were used (6, 10, 15, and 20) on various working electrodes to follow the electropolymerization and then to characterize the films that are obtained using different techniques.

Figure 38 shows that the anodic and cathodic peak currents response as we progressively increase the number of CV scans, to confirm the accumulation of electroactive material on the electrode surface during the electropolymerization of the iron complex. In **Figure 38**A, after 6 scans, the anodic peak current corresponding to the oxidation of Fe^{2+} to Fe^{3+} increases from approximately 112 µA in the first cycle to around 260 µA, while the cathodic peak corresponding to the reduction of Fe^{3+} back to Fe^{2+} increases from –77 µA to nearly –220 µA, indicating an early but significant buildup of polymer. In **Figure 38**B, extending the scan count to 10 cycles leads to further current enhancement, with the anodic peak reaching around 375 µA and the cathodic one around -347 µA, reflecting continued polymer growth and increased redox-active surface coverage. In **Figure 38**C, after 15 scans, the currents rise more gradually, with anodic and cathodic peaks reaching 440 µA and –410 µA, respectively, suggesting a slowing growth rate possibly due to increased film thickness. Finally, in **Figure 38**D, after 20 scans, the anodic peak stabilizes around +480 µA and

the cathodic peak at –450 µA, pointing to a near-saturation state where film growth is limited by charge transfer resistance or ion diffusion through the film.

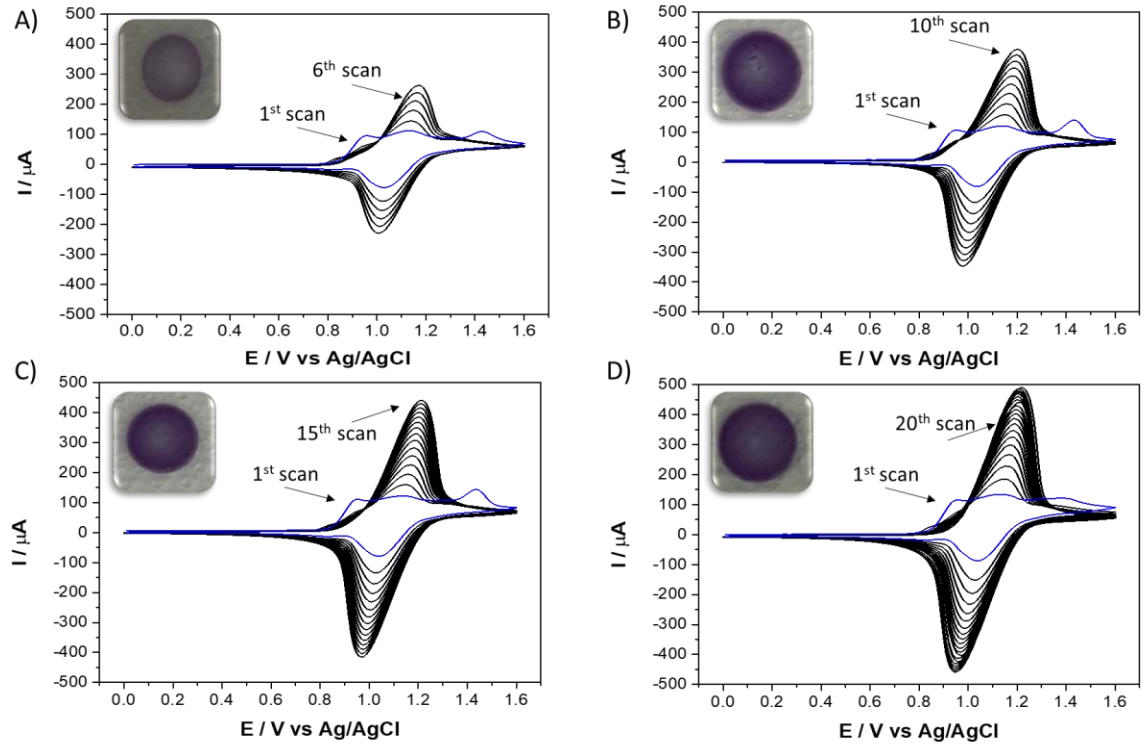

Figure 38: Effect of increasing the number of scans on the electropolymerization of 2. The CV curves were recorded at 100 mV s^{-1}using ITO as working electrode in acetonitrile (ACN) containing 1 mM of compound 2 and 0.1 M of lithium perchlorate, and apply different number of scans: A) 6 scans, B) 10 scans, C) 15 scans, and D) 20 scans.

Moreover, the anodic-to-cathodic peak-to-peak separation increases throughout the scan series, indicating rising charge-transfer resistance at the electrode interface. This effect is typically associated with the buildup of a thicker, more resistive film. The insets in each CV shows visual images of the electrode surface, where the gradual darkening and increased coloration intensity corroborate the film growth and its electrochromic behavior. The observed color change is a qualitative confirmation of the redox-active polymer deposition, providing a visual link between electrochemical performance and optical response. Altogether, these results demonstrate the controlled formation of electrochromic polymer films via multisweep CV and establish the correlation between the scan number, film thickness, and electrochemical behavior.

Then a second experiment was performed, where we use ITO as the working electrodes. The CV curves obtained for compound **2** (1 mM) were recorded at a scan rate of 100 $mV \cdot s^{-1}$ in acetonitrile (+ 0.1 M $HClO_4$) and 4 different number of scans were used (6, 10, 15, and 20). The use of this electrolyte was based on the work done by Nishihara [256], where he explained that perchloric acid ($HClO_4$) is a very good electrolyte since it protonates the aniline moiety, thereby shifting its oxidation potential positively to align closely with the oxidation potential of $M(tpy)_2$.

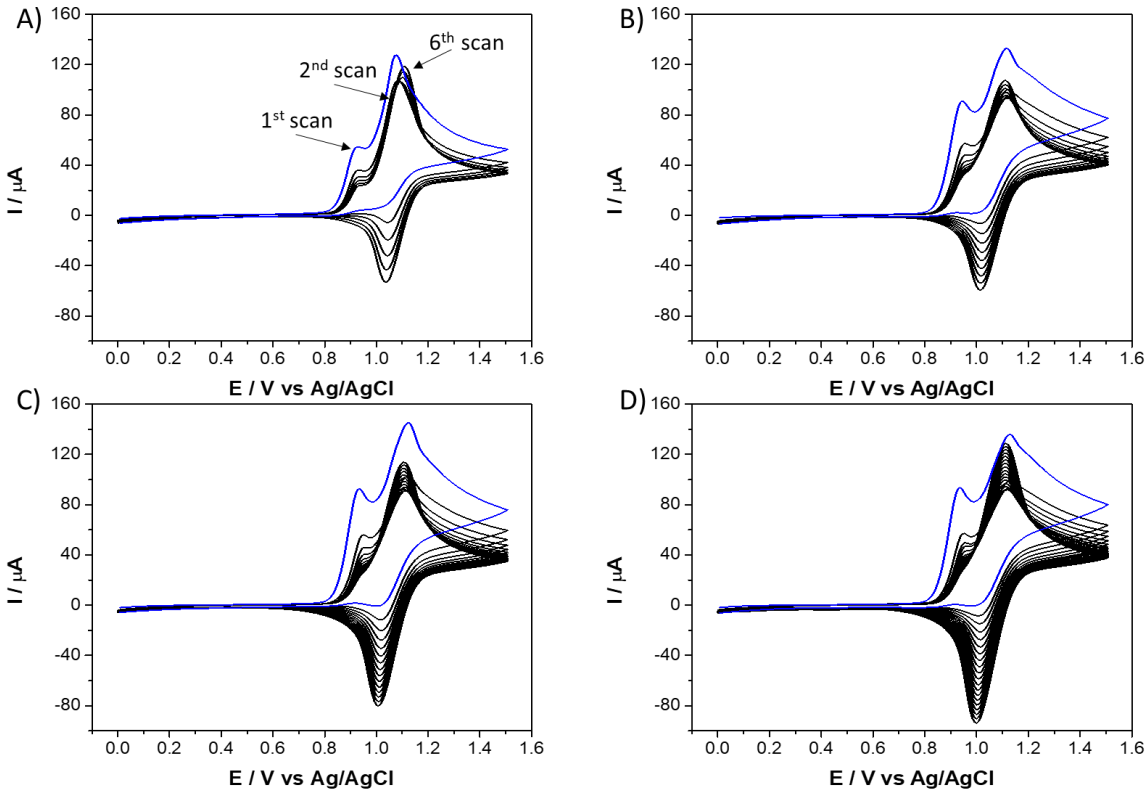

Figure 39: Effect of increasing the number of scans on the electropolymerization of 2. The CV curves were recorded at 100 mV s^{-1}using ITO as working electrode in acetonitrile (ACN) containing 1 mM of compound 2 and 0.1 M of perchloric acid, and apply different number of scans: A) 6 scans, B) 10 scans, C) 15 scans, and D) 20 scans. The blue represents the first scan.

When observing **Figure 39**A, during the first scan two peaks are found, one at 0.93 V which corresponds to the irreversible oxidation of the amino groups with a peak current of 54 µA, and another reversible at 1.07V corresponding to the Fe^{3+}/Fe^{2+} redox couple with an anodic peak with peak current of 127 µA and a small cathodic peak which is normal during the first scan in this solution due to slow kinetics and charge transfer[257]. The oxidative peak current decreases in the

second scan to 105 μA with a better-defined reduction peak. After the third scan, the anodic peak current starts to increase with a following increase in the cathodic peak current as well which indicates the start of the nucleation growth of the polymer on the ITO surface. The anodic peak current (Ipa) during the sixth scan is around 118 μA and the cathodic peak current (Ipc) is 53 μA. When comparing this to **Figure 38**A, firstly during the first scan no oxidation peak at around 1.4 V is found which is most probably due to the protonation of the hydra(azo) groups due to the change of solvent and electrolyte. As explained above, this inhibits the further oxidation to obtain the azo groups and this directly affects the polymerization kinetics. Since during the second scan the redox peak decreases to 105 μA while in the case when using lithium perchlorate, during the second peak the redox signal peak current is already increasing showing better growth of the films. Eventually, after 3 scans, using perchloric acid, the oxidative peak current starts to increase very slowly to reach at the end around 118 μA, while when using lithium perchlorate, it is around 200 μA. Even when increasing the number of scans, the rate of the increase is slower and lower and even lighter deposit is deposited on the electrode surface indicating smaller films were formed which is in alignment with the electrochemical response. Therefore, perchloric acid was not found to be the best supporting electrolyte to promote the electrompolymerization of 2 and form long metallpolymer films so lithium perchlorate was the best choice to be used below (unless mentioned otherwise).

3.2.1.4. Electrochemical response of 1 and 2 in a wider potential window on Carbon

The electrochemical behavior of compounds 1 and 2 was investigated over a potential range that included both anodic (corresponding to electropolymerization and Fe^{3+}/Fe^{2+} redox system) and cathodic (reduction of terpyridine moieties) processes using carbon as the working electrodes. Since the potential range covers also the cathodic region, all the solutions prepared are bubbled under nitrogen for 15 minutes to remove oxygen to prevent its reduction. In both cases, the potential scan was initiated in the cathodic direction and typical data are shown in **Figure 40**. During the first scan, two successive reversible reductions were observed for both compounds 1 (**Figure 40**B) and 2 (**Figure 40**D), corresponding to ligand-centered processes attributed to the reduction/reoxidation of the terpyridine moieties [258].

These reversible electron transfer processes in the cathodic region usually do not affect the electrochemical events occurring in the anodic region and, indeed, on scan reversal toward positive potentials, one can observe the reversible oxidation corresponding to the Fe^{3+}/Fe^{2+} redox couple for both complexes (occurring at 1.03 V and 1.13 V vs. Ag/AgCl, respectively). For the [Fe(tpy-Ph-NH_2)$_2$] complex, an additional irreversible anodic pre-peak appeared at 0.95 V, which marked the onset of the electropolymerization process, as well as the post-peak at 1.43 V corresponding to the oxidation of the formed hydrazo compound. In subsequent potential multisweeps, no change was noticed for 1 whereas continuous increases in peak currents were observed for 2 (**Figure 40**C), due to the progressive growth of the polymeric film (as expected from previous data, see **Figure 36**B and **Figure 37**A).

Interestingly, when scanning potentials toward reductive values for the second time (and in the following cycles as well), a new cathodic peak appeared around –1.20 to –1.25 V vs. Ag/AgCl (depending on the cycle number, see **Figure 40**C). This signal can be assigned to the reduction of azo functionalities formed during the oxidative polymerization process (Eq. 3). The involvement of azo bond formation is consistent with literature reports describing the oxidative coupling of arylamines, where N=N linkages can emerge under highly oxidative conditions and as a function of the nature of the electrolyte [259], [260], [261], or the direct oxidation of hydrazophenyl groups [56], as formed here after oxidation of the [Fe(tpy-Ph-NH_2)$_2$] complex [256]. This interpretation is further supported by the irreversible nature of the preceding anodic peak and the observed shift in the electrochemical profile, indicative of structural and electronic modifications within the polymeric film. It is also supported by the CV data recorded for azobenzene in the same medium (**Figure 40**A), exhibiting a cathodic peak located at –1.33 V vs. Ag/AgCl on forward scan (corresponding to the reduction of the azo bond).

In summary, in contrast to compound 1, which exhibits stable and unchanged electrochemical behavior over successive scans, compound 2 displayed a markedly different response. Repeated CV of compound 2 revealed not only a continuous increase in anodic and cathodic peak currents, indicative of surface-confined electropolymerization, but also the emergence of a new cathodic peak at negative potentials (a feature missing from the CV of compound 1) and likely to correspond to the formation of azo-bridging ligands resulting from oxidative coupling of the electron-rich aminophenyl groups. Such azo linkages are known to introduce additional redox-active sites,

supporting the hypothesis of a growing polymeric network with enhanced electrochemical complexity.

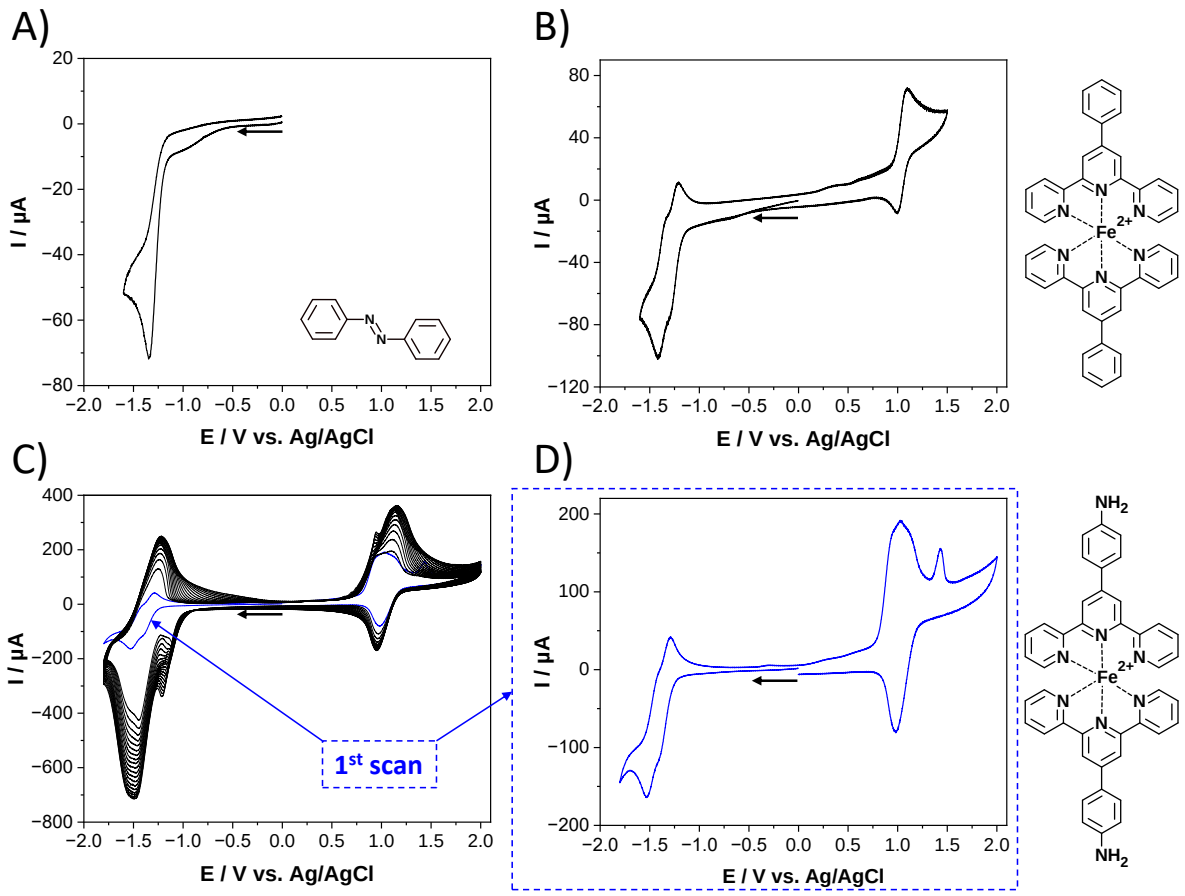

Figure 40: Comparison of the cyclic voltammograms of solutions containing 0.5 mM of azobenzene (A), 0.5 M of $[Fe(tpy\text{-}Ph)_2]^{2+}$ (C) and $[Fe(tpy\text{-}Ph\text{-}NH_2)_2]^{2+}$ (B and D) in $CH_3CN/LiClO_4$ 0.1 M. Scan rate: 100 mV s^{-1}.

3.2.1.5. Electrochemical response of 2 in a wider potential window on ITO

Since the electropolymerization was successful on the Carbon electrodes and, the same solution was prepared again which consisted of acetonitrile with 0.1 M $LiClO_4$ and 1 mM of complex 2, and in this case ITO was used as the working electrode and the CV is presented in **Figure 41**. As in the previous case, the solution was bubbled under nitrogen for 15 minutes before starting the multisweep CV to remove oxygen from the surrounding and since it doesn't react with the solution. Note that one issue that can be faced when using ITO in this case is that we are limited in the potential range used since at very low negative potentials we risk reducing the ITO itself since it

is a mixed oxide of indium and tin [262]. Then a potential range is applied between -1.6 and 1.6 V where the starting potential is at 0 V and the direction is towards the cathodic region (to -1.6 V) where the signal of the ligand is found then towards the anodic region where we should observe the redox signal of iron and the oxidation of the amino groups. During the first scan, the reversible peak corresponding to the terpyridine moiety is not present as shown in the red curve unlike that shown when using the carbon electrode, however on the scan reversal in the positive potential side, we observe the reversible oxidation corresponding to the Fe^{3+}/Fe^{2+} redox couple at 1.12 V vs. Ag/AgCl. An additional irreversible anodic pre-peak appeared at 0.93 V, as well as the post-peak at 1.42 V corresponding to the oxidation of the formed hydrazo compound.

Then during the second scan, in the reduction side a new cathodic peak appeared around –1.07 V vs. Ag/AgCl, and it is similar to the peak detected on carbon at -1.2 V signal that is assigned to the reduction of azo functionalities formed during the oxidative polymerization process. Moreover, after the second scan, the reversible redox signal designated to the terpyridine starts to more visible with the reduction at around -1.48 V and the reversible oxidation peak at -.123 V. As the number of scans increases, all of the anodic and cathodic peak currents increases and shift a bit by the increase in the peak separation that indicates the structural and electronic modifications within the polymeric film similar to the case above as shown in **Figure 41**A. Then a dark purple deposit in strongly adsorbed on the ITO surface and it is characterized electrochemically by preparing in a blank electrolyte solution (*i.e.*, 0.1 M $LiClO_4$ in acetonitrile) within the potential range corresponding to the Fe^{3+}/Fe^{2+} redox couple and the terpyridine moiety that is presented in **Figure 41**B.

Different scan rates ranging from 50 to 10 mV/s are used, where we can see clearly that the formed polymer is quite stable on the electrode and at scan rate 50 mV/s the redox peak corresponding to iron is around 1.048 V vs Ag/AgCl, and the irreversible reduction peak corresponding to azo is around -1.2 V, and finally the reversible peak corresponding to the ligand is at -1.34 V and the 2 reversible peaks on ITO are merged into 1 broad reversible signal. As the scan rate decreased, the peak current decreased accordingly and the peak to peak separation also decreased as well which was expected. Therefore, this indicates that the polymer is quite stable on the ITO even after characterization and the signals were similar to that on carbon electrode except that on the carbon

electrode starting from the first peak, the signals were clear and evident to show the reduction of azo groups in the polymer films.

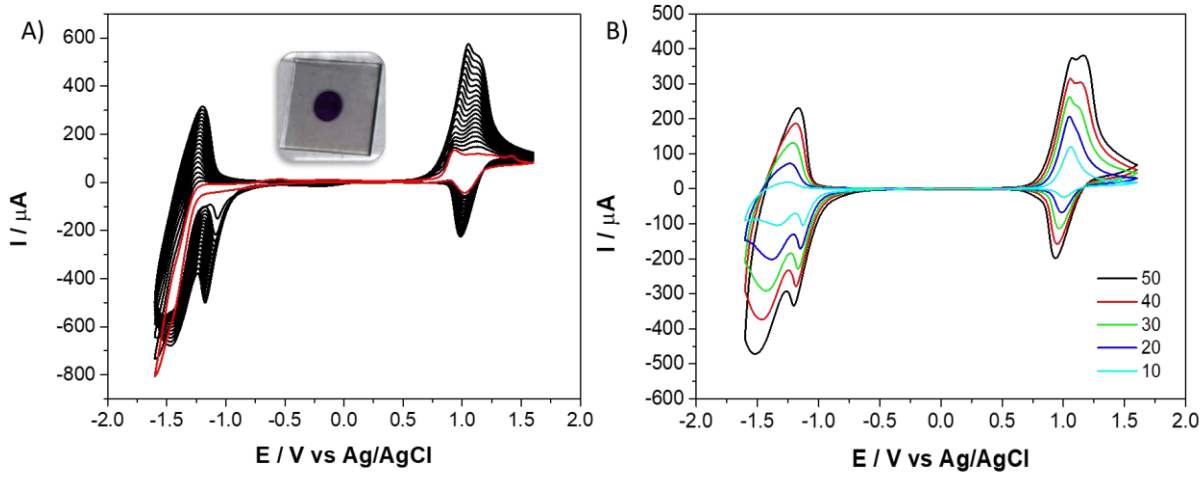

Figure 41: Electrochemical behavior observed for 2. twenty successive CV curves (1st scan in red) recorded at 100 mV/s in the region between -1.6 V and 1.6 V vs. Ag/AgCl, using ITO as working electrode in acetonitrile (+ 0.1 M $LiClO_4$) containing 1 mM of compound 2 (A). Electrochemical characterization of polymer film obtained on ITO using electrolyte solution (ACN + 0.1 M $LiClO_4$) using varying scan rate between 10-50 mV/s and potential range between -1.6 V and 1.6 V vs Ag/AgCl (B).

3.2.2. Comparison to the electropolymerization of aniline-based monomers.

The radical cation intermediates formed during the electrochemical oxidation of aminophenyl groups are resonance-stabilized, with charge delocalization involving the nitrogen atom and the ortho and para positions of the phenyl ring, resulting in three primary radical isomers as shown in **Figure 42**. In typical anilines, the para-centered radical is favored thermodynamically unless steric or electronic factors intervene. [263], [264], [265], [266]

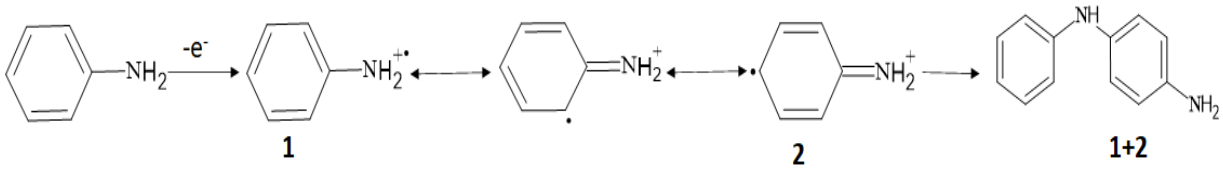

Figure 42: Schematic representation of oxidative aniline electropolymerization.

In compound 2, however, the para position is already occupied by the terpyridine substituent, effectively blocking such conventional coupling route as shown in **Figure 43**. Consequently,

alternative pathways such as ortho–ortho (C–C), NH–NH, or N=N couplings may dominate, leading to the formation of conjugated, cross-linked polymeric films. These structural features are consistent with the CV data observed here via an increase in peak current and the irreversible nature of the electropolymerization process.

This contributes to explain the different mechanism and the formation of an azobond between the $[Fe(tpy\text{-}Ph\text{-}NH_2)_2]^{2+}$ moieties in the electrodeposited films (with an additional redox process visible on the CV (blue curve in Fig. 1B) corresponding to the oxidation of NH–NH moieties, Eq. 3). The characterization of these films using various physicochemical techniques is described later.

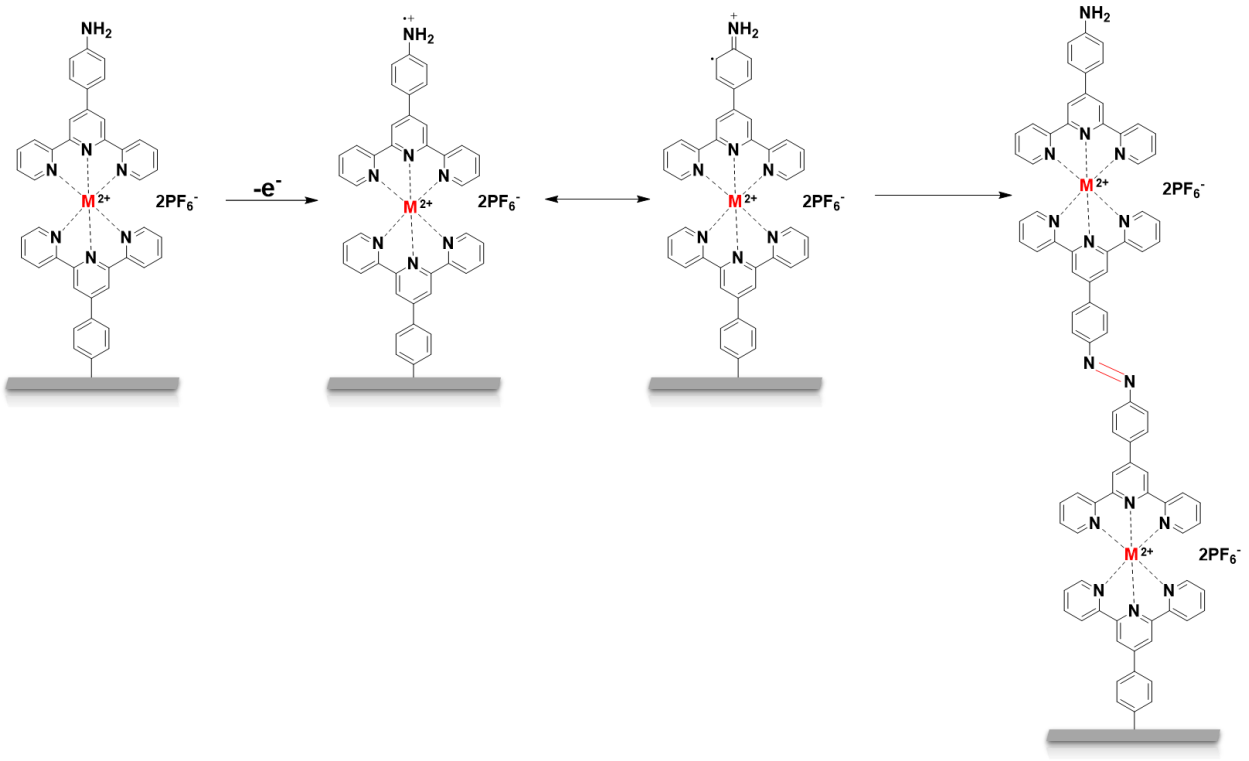

Figure 43: Schematic representation of oxidative polymerization of the coordination complexes on ITO.

3.2.3. Electrografting of the in situ monodiazonium cation of the complexes:

3.2.3.1. Principle of the method:

The main goal is to obtain stable metallopolymers on the electrode surface as mentioned in the introduction. However, these complexes specifically upon oxidation, don't form covalent links with the working electrode (ITO), and thereby will not be very stable on the electrode surface due to the lack of covalent bonds and instead the compound will be only adsorbed on the surface. Therefore, a suitable solution was performing a pre-step before polymerization which includes the

in situ formation of monodiazonium cation of the complexes followed by an electrochemical reduction of the cations. A monodiazonium cation is generated chemically by reaction of the desired coordination complex with one equivalent of sodium nitrite ($NaNO_2$) in 0.5 M HCl solution. This solution was stirred for 15 minutes yielding the formation of the monodiazonium cation N2+, then this solution is used subsequently in the electrografting step [208], [267], [268].

In electrografting, after the in situ formation of the monodiazonium cation the solution is subjected to a suitable reducing potential. This potential reduces the cation and releases a nitrogen molecule and forms very reactive aryl molecules that form a bond with the working electrode (ITO) as shown in **Figure 44**. Therefore, it is only suitable for complexes having an amine functional group.

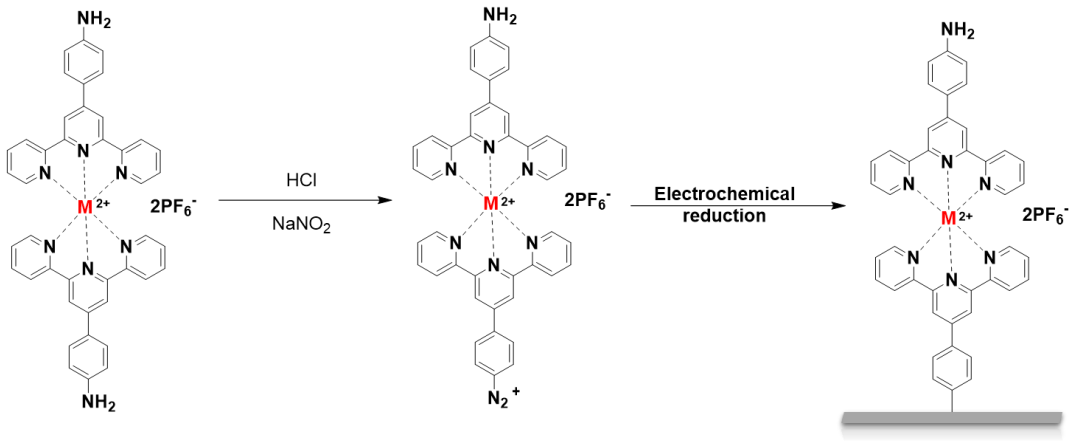

Figure 44: Schematic representation of diazonium formation and electrochemical grafting of the coordination complex.

3.2.3.2. Electrografting of 2 on ITO:

The solution prepared contains an equimolar amount (1mM) of the coordination complex (2) with sodium nitrite in a 0.5M HCl solution and the CV is performed to graft the complex using a scan rate of 100 mV/s (see **Figure 45**). The cyclic voltammogram of the solution using a potential range of 0.5 V to -0.25 V vs Ag/AgCl, shows an irreversible cathodic peak at -0.11 V with a peak current of 22 µA during the first scan which indicates the successful reduction of the monodiazonium cation and the formation of a reactive aryl radical that is likely to attach to the ITO surface. Furthermore, the decrease in the peak current during the second scan to less than 5

µA that is shown in **Figure 45**A with a continues decrease upon cycling indicates that the electrode surface is passivated after one scan only.

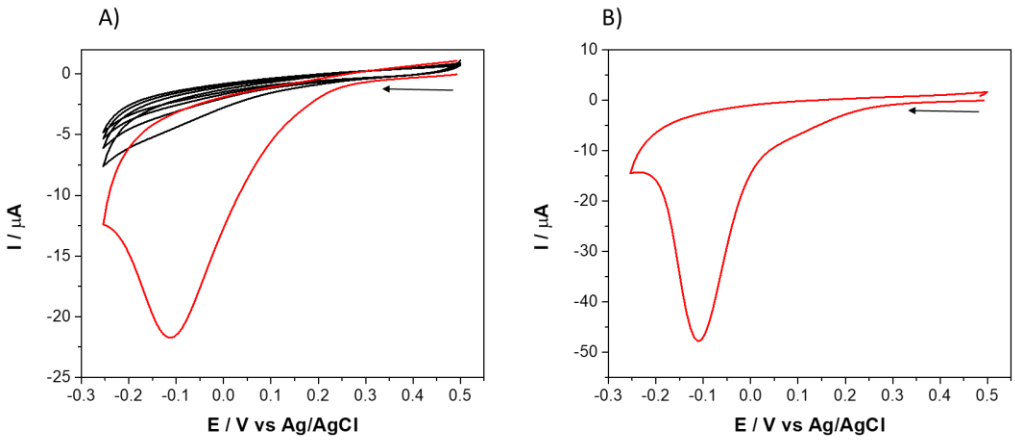

Figure 45: CVs recorded for the electrochemical reduction of in situ generated diazonium cation of complex 2, in 1 mM of 2 + 1 mM $NaNO_2$ (in 0.5 M HCl), using (A) 5 scans on bare ITO at 100 mV/s (B) 1 scan on bare ITO at 100 mV/s.

After grafting, the expected result is to have a monolayer of the electroactive complex 2 with a free amino group that can be oxidized during the electropolymerization process to form radical cations ($NH_2^{\bullet+}$), that combines with other radical cations formed in solution to form hydrazo bonds. Then further oxidation as explained above can lead to the formation of azo bonds between each monomer unit that is deposited as thin films on ITO. The major advantage in this case when comparing to direct electropolyemrization without grafting is that in this case a pre-step is involved which ensures a covalent link and therefore better stability of the resulting polymer. The electrochemical characterization of the modified electrodes would validate the success of this method since the grafted monomer is electroactive, therefore an electrochemical response corresponding to the Fe^{3+}/Fe^{2+} redox couple is sufficient to prove the effectiveness of this method. In order to ideally achieve a monolayer on the ITO that are then used in the electropolymerization process, only one scan is done to electrograft the compound as seen in **Figure 45**B.

3.2.4. Electropolymerization of 2 after grafting:

The same strategy that was explained in section 3.2.1.3 was implemented here, where the only difference is that the ITO electrodes were modified before undergoing the electropolymerization process. In this case 4 ITO electrodes undergoe the pre-step of electrografting the iron monomer

using the method explained above by preparing the solution to electrograft and use 1 scan only during the electrochemical reduction of the diazonium salt to ideally form a monolayer on the ITO. Then the second step is to perform the electropolymerization where the CV curves obtained for compound **2** (1 mM) were recorded at a scan rate of 100 $mV \cdot s^{-1}$ in acetonitrile (+ 0.1 M $LiClO_4$) and 4 different number of scans were used (6, 10, 15, and 20) that are the same condition as on bare ITO to compare the electrochemical response obtained.

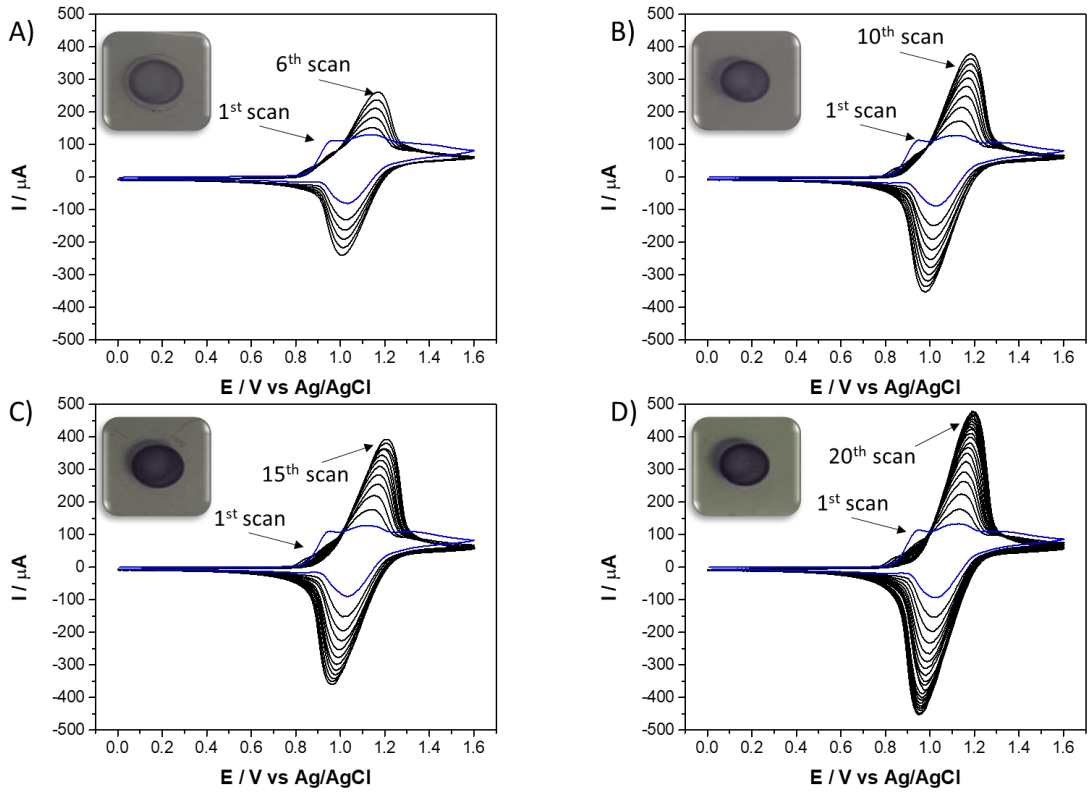

Figure 46: Effect of increasing the number of scans on the electropolymerization of 2 after electrografting. The CV curves were recorded at 100 mV/s using ITO as working electrode in acetonitrile (ACN) containing 1 mM of compound 2 and 0.1 M of lithium perchlorate, and apply different number of scans: A) 6 scans, B) 10 scans, C) 15 scans, and D) 20 scans.

When comparing the 6 scans CV in **Figure 46**A to that in **Figure 38**A, during the first scan we have first the irreversible oxidation of the amino groups at 0.95 V vs Ag/AgCl which is similar to that on the bare ITO which was 0.94 V. Then the oxidation of iron was around 1.13 V compared to 1.14 V in the previous case, and the irreversible oxidation peak taking place usually at 1.43 V when using bare ITO that corresponds to the oxidation of azo groups is not clearly detected in the

of grafted ITO. Then in the reverse scan the reduction of Fe^{3+} takes place at 1.02 V which is the same in the previous case as well. Now with respect to the peak current achieved at the end of the sixth scan the oxidative peak current was around 261 µA which is quite close to that on bare ITO which was 263 µA. Therefore, we can deduce that there is no major difference in the electrochemical response when directly electropolymerizing 2 on ITO electrodes vs grafting the monomer first then electropolymerizing. Therefore, in order to determine if the grafting helps in the stability of the polymerized films on the electrodes, they modified electrodes are characterized electrochemically to study the behavior and stability after multiple cycles.

3.2.5. Characterization of the Electropolymerized Films

3.2.5.1. Electrochemical response of the poly[Fe(tpy-Ph-NH_2)$_2$]$^{2+}$ films

The modified electrodes are electrochemically characterized using monomer free electrolyte solution to study the stability of polymer films on ITO upon multisweep CV and to quantify the amount of material deposited as a function of changing the number of scans used during electropolymerization and also to see if grafting before polymerization has any significant effects in terms of the stability of the films. The solution prepared consists of a blank electrolyte solution which is 0.1 M $HClO_4$ in acetonitrile and a potential range between 0.3 to 1.6 V vs Ag/AgCl which shows apart from the first scan for which an additional prewave corresponding to the irreversible oxidation of the terminal aminophenyl groups was observed, the reversible signal corresponding to the Fe^{3+}/Fe^{2+} redox couple remained in the same position (around 38% decrease in the anodic currents after 10 cycles for bare ITO, and 49% decrease for the grafted sample, while the cathodic peak current almost remains constant).

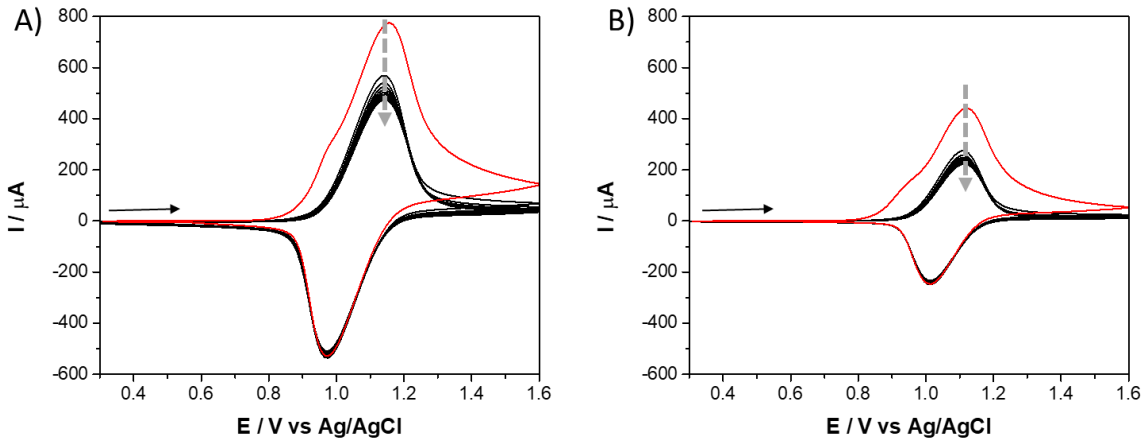

Figure 47: Multisweep CV curves recorded at a potential scan rate of 100 mV s^{-1} in monomer-free acetonitrile solution containing 0.1 M $HClO_4$ as supporting electrolyte, using poly[$Fe(tpy\text{-}Ph\text{-}NH_2)_2]^{2+}$ films electropolymerized either on bare ITO (A) or on ITO electrode previously electrografted with $[Fe(tpy\text{-}Ph\text{-}NH_2)_2]^{2+}$ moieties (B).

Figure 48A illustrates typical voltammograms recorded at various potential scan rates (from 10 to 100 mV s^{-1}) for poly$[Fe(tpy\text{-}Ph\text{-}NH_2)_2]^{2+}$ thin films previously electrogenerated on ITO for 20 CV scans. They have been obtained in a blank electrolyte solution (*i.e.*, 0.1 M $HClO_4$ in acetonitrile) within the potential range corresponding to the Fe^{3+}/Fe^{2+} redox couple. As shown, all curves consistently displayed a reversible redox signal centered around 1.05 V *vs.* Ag/AgCl, which aligns well with the electrochemical behaviour of the monomeric precursor, $[Fe(tpy\text{-}Ph\text{-}NH_2)_2]^{2+}$, in the same medium (**Figure 37**E). Furthermore, several voltammograms were recorded at various potential scan rates as well for thin films that were electrogenerated on bare ITO using 6, 10,15, and 20 scans to measure the evolution of the peak current.

The anodic-to-cathodic peak-to-peak separation (ΔEp) was found to enlarge while increasing the potential scan rate (*i.e.*, ΔEp values of 41 mV at 10 mV s^{-1} and 163 mV at 100 mV s^{-1}, see bottom inset in **Figure 48**A). This suggests some restrictions in the electron transfer processes (and possibly associated mass transport to maintain electroneutrality in the material). For such thin electroactive films, an adsorption-like behaviour would be expected in cyclic voltammetry with ΔEp close to zero and peak currents growing directly proportionally to the potential scan rate, for an ideal thin layer [61]. On the contrary, if they present a diffusion-like behaviour, the ΔEp would

be around 59 mV or higher presenting a quasi-reversible system and the peak currents would follow the Randles-Ševčík equation (Eq 1) and scales with the square root of the scan rate (reference).

$$I_p = 0.4463\, n\, F\, A\, C \sqrt{\left(\frac{n\, F\, \nu\, D}{R\, T}\right)}$$

Also, one can observe a mixed diffusion-adsorption behavior as demonstrated by the slope of the plot "log(i_p)-log(v)" (see top inset in **Figure 48**A) with a value of 0.76, lying in-between an ideal thin layer behavior (slope = 1.0) and a purely diffusional response (slope = 0.5). This confirms that charge transport occurred here via electron self-exchange between adjacent redox centers (hopping), accompanied by counterion migration to compensate the charges formed upon redox transformation of iron centers in the polymer.

From CV curves recorded at low scan rate (10 mV s^{-1}), one can clearly see the progressively larger peak currents recorded for films prepared from more CV scans (see the curves superimposed in **Figure 48**B). This is indicative of an increase in the surface concentration of iron species due to the electrodeposition of thicker films. The surface concentration of the monomer, assuming monolayer coverage, was estimated to be approximately 1.4×10^{-10} mol·cm^{-2}, as determined from the CV curve recorded from an ITO electrode electrografted with the corresponding monodiazonium derivative of compound **2**, generated in situ by reaction with one equivalent of $NaNO_2$ in 0.5 M HCl (**Figure 48**C).

From integration of CV signals of the electropolymerized films, one can estimate the surface concentrations which obviously increased as a function of the number of CV scans applied to prepare the films (**Figure 48**B). These values were around two orders of magnitude larger than that of the monolayer, confirming successful polymer deposition with film thicknesses controllable by tuning the number of CV scans during electropolymerization. For instance, a poly[Fe(tpy-Ph-NH_2)$_2$]$^{2+}$ film with a coverage of ~1×10^{-8} mol·cm^{-2} exhibited a thickness of ~9 nm (as evaluated from AFM measurements), corresponding to ~125 monomolecular layers and a site concentration of 1.6 M (assuming a density of 1.35 g/cm^3), which is consistent with the two orders of magnitude difference discussed above from electrochemical data.

Moreover, poly[Fe(tpy-Ph-NH_2)$_2$]$^{2+}$ films can be also electropolymerized from [Fe(tpy-Ph-NH_2)$_2$]$^{2+}$-electrografted ITO surfaces, but their resulting CV behavior (**Figure 48**D & 4E) were quite similar to those of the films grown directly on bare ITO (**Figure 48**A & 4B), admittedly with a slightly larger diffusional contribution and slightly smaller amounts of electrogenerated materials. As these electrografted samples did not exhibit better long-term operational stability upon multisweep CV (that might have occurred as a result of covalent bonding of the electrografted groups) and no better performance, next experiments are performed on the basis of non-electrografted electrodes.

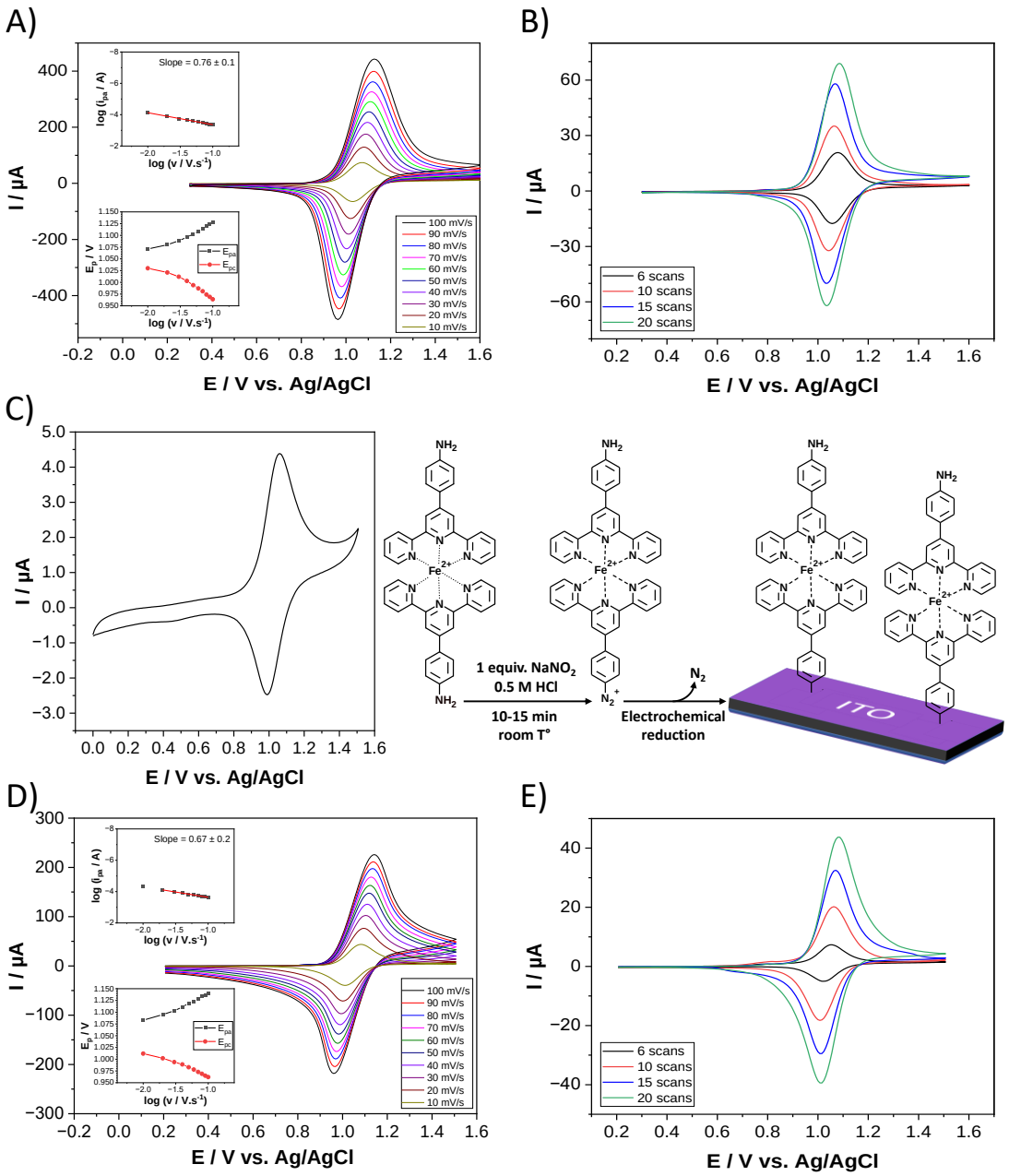

Figure 48: (A) CV curves recorded at increasing potential scan rates (from 10 to 100 mV s-1) in monomer-free acetonitrile solution containing 0.1 M $HClO_4$ as supporting electrolyte, using ITO electrodes previously covered with poly[Fe(tpy-Ph-NH_2)$_2$]$^{2+}$ films electropolymerized during 20 CV scans; the bottom insets show the corresponding variations of peak potentials (anodic Epa and cathodic Epc) with the logarithm of potential scan rate, while the top insets represent the log-log variation between the anodic peak current and scan rate (the value of the slope of the linear fitting is also given). (B) CV curves recorded at 10 mV·s^{-1} in the same medium as in (A) using poly[Fe(tpy-Ph-NH_2)$_2$]$^{2+}$ films deposited

using different numbers of oxidation scans (6, 10, 15 and 20 scans). (C) CV curve recorded at 100 mV·s⁻¹ using an ITO electrode electrografted with [Fe(tpy-Ph-NH₂)₂]²⁺ as illustrated in the right scheme. (D,E) CV curves recorded as in (A,B) but for poly[Fe(tpy-Ph-NH₂)₂]²⁺ films electrogenerated onto ITO electrodes electrografted with [Fe(tpy-Ph-NH₂)₂]²⁺ as in (C).

3.2.5.2. Raman Spectroscopy

Figure 49 presents the Raman spectra of complex 2 in its monomeric form (blue trace) and its corresponding electropolymerized film (red trace), normalized and offset for clarity and comparison. In the spectral range from 1000 to 1650 cm^{-1}, which corresponds to internal vibrational modes of the terpyridine and azobenzene moieties, the positions of the main peaks remain unchanged. This suggests that the fundamental coordination environment of the terpyridine ligands is largely preserved upon polymer formation. The only difference observed is in the relative intensities of several bands which can be attributed to the length of the chain.

Significant structural modifications are evident at lower wavenumbers (500–850 cm^{-1}), where the polymer spectrum exhibits evident peak broadening and the appearance of new features. Notably, new or enhanced bands appear at 590 and 735 cm^{-1}, while existing bands (e.g.,800 and 847 cm^{-1}) are broadened. These changes are typically attributed to a change in the ligand's ring sequence. Such modifications are consistent with the formation of new bonds between the aniline-functionalized terpyridine ligands (replacement of pyridine-aniline fragment by a pyridine-azobenzene fragment), most likely involving azo linkages that extend conjugation within the polymer backbone.

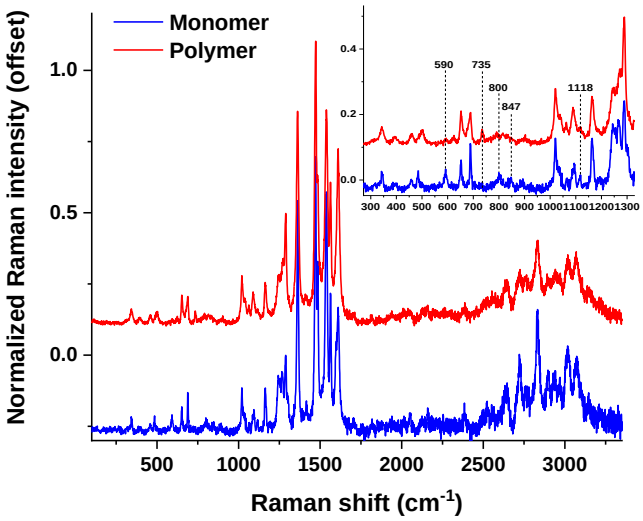

Figure 49: Comparison between Raman spectra of unpolymerized $Fe(tpy)_2$ reactant, in blue and labelled monomer, and the one of the electropolymerized film, in red and labelled polymer. Inset is a zoom in the 300 cm^{-1} – 1300 cm^{-1} region.

3.2.5.3. Infra-Red Spectroscopy

Figure 50 presents the FTIR spectra of the $[Fe(tpy\text{-}PhNH_2)_2]^{2+}$ monomer (black) and its corresponding electropolymerized film (red). In the monomer spectrum, the sharp band observed at 1611 cm^{-1} is assigned to the C=N stretching vibration of the terpyridine moiety, confirming the coordination of the ligand to the Fe(II) center. The bands at 1483 cm^{-1} and 1286 cm^{-1} are attributed to C=C aromatic ring vibrations and C–N stretching, respectively, while the signal at 1058 cm^{-1} likely corresponds to in-plane C–H bending. A prominent low-wavenumber feature at 627 cm^{-1} is associated with the Fe–N coordination bond, further validating the complex formation.

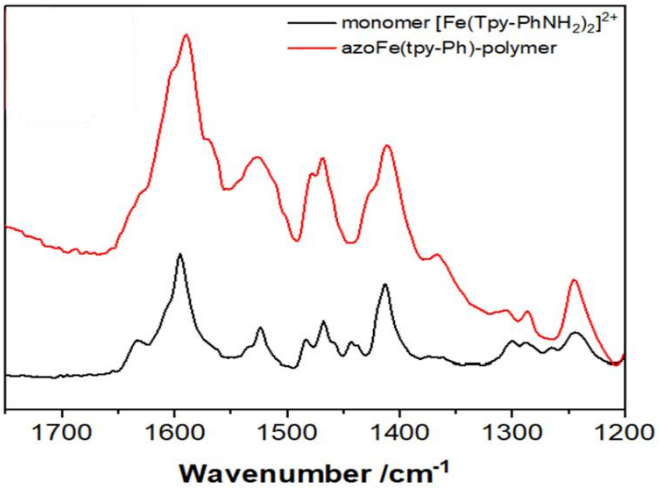

Figure 50: Comparison between IR spectra of unpolymerized reactant, in black and labelled monomer, and the one of the electropolymerized film, in red and labelled polymer.

The N–H bending vibration of the terminal $–NH_2$ group typically appears around 1620–1650 cm^{-1}, and it likely overlaps with the C=N band in the monomer. Upon electropolymerization, the intensity of this band diminishes, suggesting the participation of the amine group in the oxidative coupling reaction. Simultaneously, a broadening and increased intensity in the region between 1600 and 1400 cm^{-1} indicate enhanced conjugation and the formation of a polymeric structure, most likely through azobenzene-type N=N linkages formed between aminophenyl substituents.

The N=N stretching vibration of the newly formed azo bond is expected around 1400–1450 cm^{-1}. Although this peak in particular is not easily resolved due to overlapping with aromatic C=C vibrations, the overall spectral evolution can support its presence. The retention of the Fe–N vibration at 627 cm^{-1} in the polymer spectrum indicates that the metal–ligand framework remains intact throughout the polymerization process. Taken together, these spectral changes confirm both the successful oxidative coupling of the monomer into an extended conjugated network and the preservation of its coordination environment.

3.2.5.4. X-ray Photoelectron Spectroscopy (XPS) Analysis

Figure 51 illustrates typical XPS data comparing the spectra obtained for the monomer and the polymer. The N 1s spectrum of the $Fe(tpy\text{-}Ph\text{-}NH_2)_2^{2+}$ monomer exhibits two well-resolved components (**Figure 51**A). The primary peak at 399.0 eV is assigned to the C=N bonds of the terpyridine ligands coordinated to the Fe(II) center, [269] while a second component at 401.5 eV

corresponds to the amine groups on the phenyl substituents that can be readily protonated for electropolymerization. These assignments are consistent with the presence of both coordinated polypyridine nitrogen atoms and uncoordinated amino groups within the monomer structure. Upon electrochemical polymerization, significant changes are observed in the N 1s spectrum of the resulting poly[Fe(tpy-Ph-NH_2)$_2$]$^{2+}$ film (**Figure 51**C). The relative intensity of the amine-associated peak decreases substantially, while a slight broadening and shift in this region indicate the formation of new nitrogen species. These changes are consistent with the consumption of the primary amine groups and the formation of azo (N=N) linkages, confirming the occurrence of oxidative coupling reactions between amine-functionalized monomers during the polymerization process. Importantly, the terpyridine-associated peak at ~400.2 eV remains largely unaffected, indicating that the coordination of Fe(II) by terpyridine ligands is preserved throughout the polymerization. Note that the binding energy of the azo (N=N) moieties is reported to be around 400 eV (for azobenzene multilayers [269]), so they cannot be readily distinguished from the main signal originating from the C=N bonds of the terpyridine ligands.

The Fe 2p XPS spectra of both the monomer (electrografted on ITO) and the polymer (**Figure 51**B and **Figure 51**D, respectively) display the characteristic Fe 2p$_{3/2}$ and Fe 2p$_{1/2}$ doublet peaks at approximately 710.8 eV and 724.5 eV, respectively, with a spin–orbit splitting of 13.7 eV. This splitting, along with the observed binding energies, is consistent with Fe(II) centers in a low-spin configuration, typical of iron polypyridine coordination complexes. [270] Notably, no significant shifts or alterations in the Fe 2p peak positions are observed upon polymerization, indicating that the oxidation state and coordination environment of the iron centers remain unchanged. Minor contributions from Sn 3p (~717 eV) and In 3p (~706 eV) are also detected in the high-resolution Fe 2p spectrum of the electrografted monomer, originating from the underlying ITO substrate.

Therefore, it can be determined that the combined N 1s and Fe 2p XPS analysis provides clearly the successful electrochemical polymerization of Fe(tpy-Ph-NH_2)$_2^{2+}$ via oxidative coupling of amine groups to form azo bonds, while maintaining the integrity of the Fe(II)-terpyridine coordination environment. These findings confirm that polymerization proceeds selectively at the amino-functionalized sites without perturbing the metal-ligand core structure.

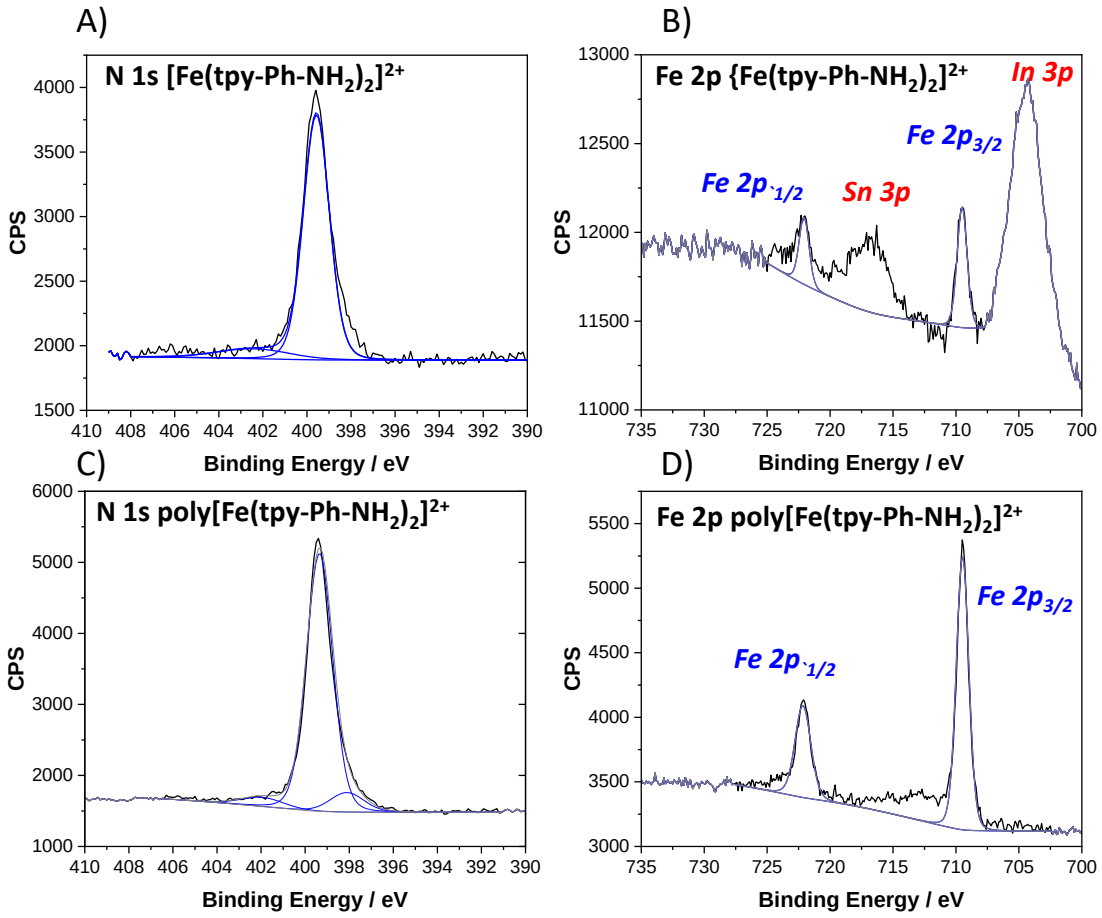

Figure 51: High-resolution XPS spectra of 2 and its electropolymerized form. (A) N 1s core-level spectrum of the monomer 2. (B) Fe 2p spectrum of 2 highlighting Fe 2p3/2 and Fe 2p1/2 components, with additional contributions from the underlying substrate (In 3p, Sn 3p). (C) N 1s spectrum of the electropolymerized film poly[Fe(tpy-Ph-NH_2)$_2$]$^{2+}$. (D) Fe 2p spectrum of the polymer film, with the characteristic Fe 2p3/2 and Fe 2p1/2 signals.

3.2.5.5. Optical Characterization using UV-VIS

The optical properties of the [Fe(tpy-Ph-NH_2)$_2$]based electropolymerized films prepared in CH_3CN containing 0.1 M $LiClO_4$ were investigated by UV-Vis spectroscopy and compared to those of the monomer **2** in solution. The UV-Vis spectrum of a solution containing 1.0×10^{-5} M of **2** in ACN (red line) displays intense bands near 300-360 nm assigned to ligand-centered (LC) π–π* transitions, along with a moderately intense band located at 570 nm and attributed to metal-to-ligand charge-transfer (MLCT) transitions [258] as shown in **Figure 52**. After electropolymerization on ITO, several changes can be noticed. First, a bathochromic shift of the

MLCT band is observed, rising from 570 up to 579 nm, consistent with enhanced π-conjugation upon polymer growth. Additionally, two new absorption bands were observed in the UV–Vis spectrum of the polymeric film. The first, centered at 378 nm, can be attributed to π–π* transitions of the azo (–N=N–) chromophore. The second, a broader and less intense band spanning the 440–520 nm region, is assigned to n–π* transitions of the azo functionality. [271] The appearance of this low-energy n–π* band is particularly significant, as such transitions are known to be sensitive to the electronic environment and are often enhanced or red-shifted in the vicinity of coordination complexes. This behavior contributes to confirm that azo groups are really formed during the electropolymerization process, and suggest that they may be involved in weak coordination or electronic interactions with metal centers, thereby modulating their optical properties. Furthermore, as the number of scans that were performed during electropolymerization increased, the absorbance bands increased as well which proves the increase in the deposited material which in other words means longer polymer chains formed.

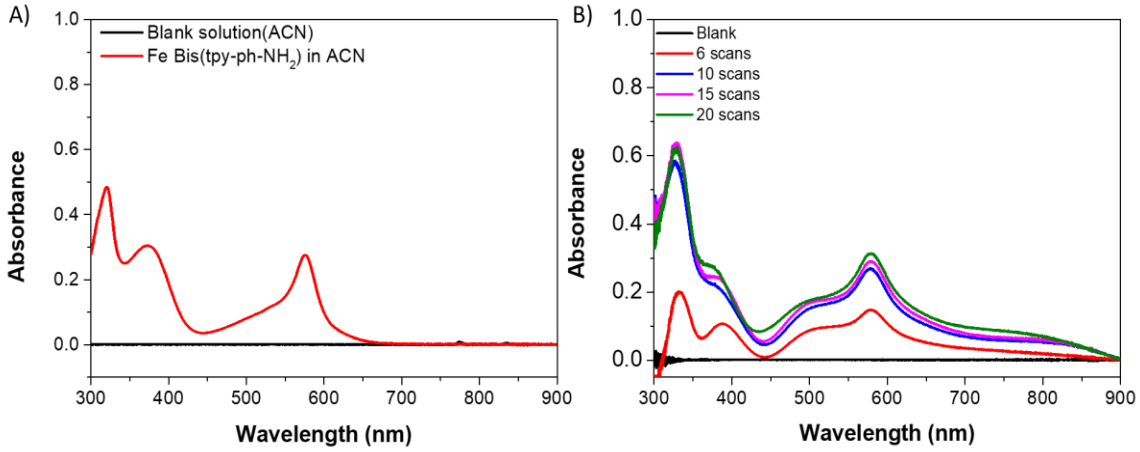

Figure 52: Comparison of the UV–Vis absorption spectra of the $[Fe(tpy\text{-}Ph\text{-}NH_2)_2]^{2+}$ in Acetonitrile (A) and the corresponding poly$[Fe(tpy\text{-}Ph\text{-}NH_2)_2]^{2+}$ film electropolymerized using different numbers of CV scans (B).

3.2.6. Electrochromic response of the films

Polypyridine ligands readily coordinate to a variety of transition metal ions, forming stable metal complexes. These complexes exhibit pronounced redox-responsive optical properties arising from

MLCT transitions. [272], [273] In low oxidation states, such as Fe^{2+}, the metal center can donate electron density to the low-lying π* orbitals of the polypyridyl ligand, giving rise to MLCT bands that manifest as intense and broad absorptions in the UV–vis region. These optical features are typically responsible for the coloration observed in such complexes. Upon one-electron oxidation ($Fe^{2+} \rightarrow Fe^{3+}$), the metal center becomes significantly electron-deficient, thereby suppressing MLCT transitions.

Based on a two-electrodes system device comprising the **poly**$[Fe(tpy\text{-}Ph\text{-}NH_2)_2]^{2+}$ film prepared here with a gel-based electrolyte, we investigated its electrochromic properties. The color of the electrochromic films was found to vary as a function of the oxidation state of the central metal, with distinct changes observed both visually and from the UV–VIS spectra upon switching between the Fe^{2+}/Fe^{3+} redox states. **Figure 53**A displays the UV-Vis spectra of the **poly**$[Fe(tpy\text{-}Ph\text{-}NH_2)_2]^{2+}$ material in the different redox states. In the normal state of the polymer film which is the reduced state, it exhibited an intense absorption band in the visible region 579 nm corresponding to metal-to-ligand charge transfer (MLCT) transitions characteristic of Fe(II) centers which is identified as the red line and is defined by the dark purple color on the electrode. In contrast, the oxidized form of this film where Fe (II) is oxidized to Fe (III) shows a significantly diminished absorption, that is presented as the disappearance of the absorbance band which is presented as the blue line and it is presented by the disappearance of the purple color and a yellowish hue is seen (see **Figure 53**B). In this two electrode system, first a reducing potential is applied to ensure that the film is in its reduced state which has a MLCT band with absorbance of 0.36, then when applying a potential of 2.5 V the MLCT band disappears and the absorbance is around zero which indicates the complete oxidation of the entire film which is identified as the bleached state where the color changes from purple to a transparent light yellowish color. To prove that the applied potential has an effect on the MLCT band, different potentials between -0.5 and 2.5 V were applied where for example when applying 2.1 V, the absorbance is around 0.14 which shows an incomplete oxidation of the polymer film as a light purple deposit is still visible on the electrode. Then when decreasing the value of the applied potential from 2.1 to 1 V, the absorbance value increased from 0.14 to 0.31 and it stabilized at this value indicating a small decrease from the initial value which was 0.36.

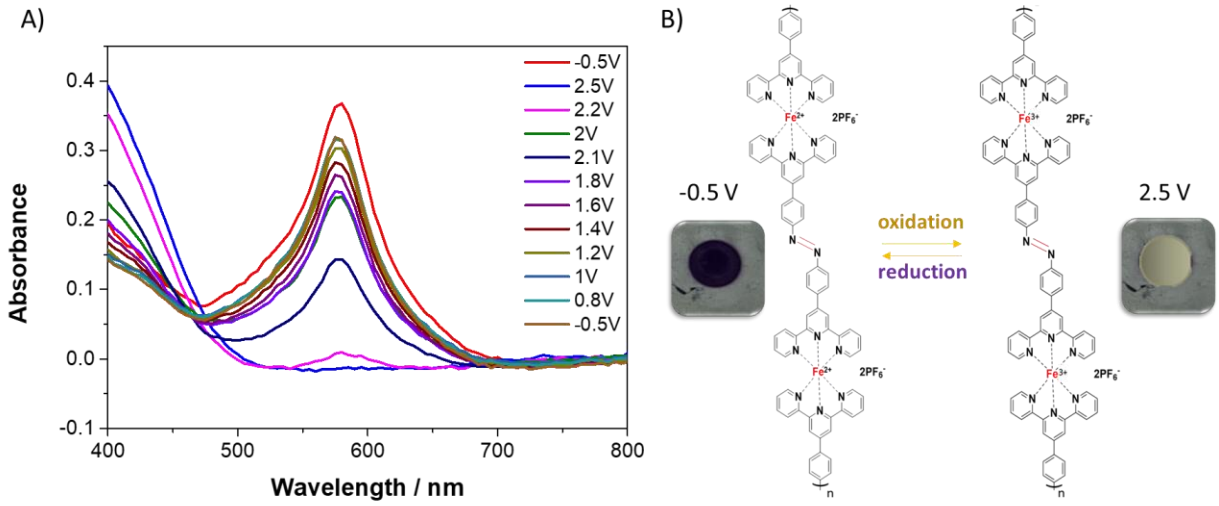

***Figure 53**: (A) UV–Vis absorption spectra of poly[Fe(tpyPhNH$_2$)$_2$]$^{2+}$ in its reduced (red trace, at –0.5 V) and oxidized (blue trace, at 2.5 V) states. (B) Photographs of the polymer film deposited on an ITO substrate at –0.5 V (left, colored state) and 2.5 V (right, bleached state).*

The polymer film exhibited a reversible color change from purple to colorless (Fig. 8B), as measured at wavelength 580 nm with the working electrode biased successively at -0.5 V (colouration step) and 2.5 V (bleaching step) for 10 or 20 s per step (**Figure 54**). The electropolymerized film demonstrated strong electrochromic performance, attributed to the high molar absorptivity of the metal-to-ligand charge transfer (MLCT) band ($\varepsilon = 3.8 \times 10^4$ M^{-1} cm^{-1}), and for the sample having been polymerized using 6 scans present a transmittance change ($\Delta T\%$) of around 22% and a high coloration efficiency of 2571 cm^2·C^{-1}. Some decrease in absorbance changes upon multiple successive redox cycling was however observed, especially at short switching times (5% decrease after 10 cycles, 28% after 40 cycles, see Fig. 8C), which are consistent with the multiweep CV data that were shown in **Figure 47** and might be due to some structural changes in the polymer during consecutive doping and dedoping processes (ingress and output of charge compensating ions during switching between the Fe^{2+}/Fe^{3+} redox states), or to incomplete reversibility of the redox switching, or to both phenomena. Indeed, by extending the duration of redox switching, some improvement can be obtained (5% decrease after 10 cycles, see **Figure 54**B). The response time was satisfactorily fast (0.7 s for colouration and 1.8 s for bleaching), as measured at 95% of the maximum absorbance variations observed after application of +2.5 V and -0.5 V, respectively. Furthermore, the optical memory is good where it takes less than 2 minutes without any potential applied to retain the colored state after oxidation. Then when

studying the modified electrode after 20 scans of electropolymerization using the 2 electrode system, it shows a transmittance change of around 45% and a high coloration efficiency. Some decrease in the absorbance was also detected in this case which was around 32% after 40 cycles and 5% after 10 cycles which is due to the same reason mentioned above. Furthermore, the response time was also good in this case 0.9 s for coloring and around 2 s for bleaching that is measured at 95% of the maximum absorbance variations. Finally, the optical memory was also good in this case with a value a bit larger than the previous case as the absorbance is higher in this case and it takes more than 2.5 minutes to retain most of the color back without any potential application.

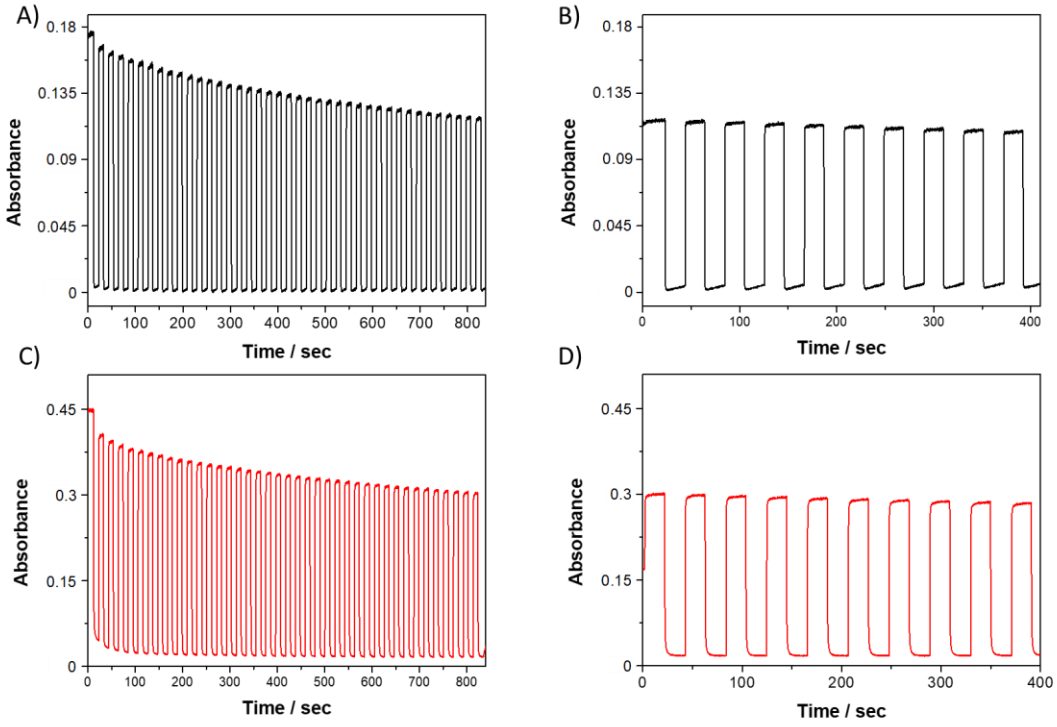

Figure 54: Chronoabsorptometry of the polymeric film over multiple redox cycles monitored at a fixed wavelength of 580 nm, respectively recorded by applying switching times of (A) 10 s and (B) 20 s for polymer formed using 6 scans, (C) 10 s and (D) s for polymer formed using 20 scans.

3.2.7. Electrochemical behavior of $[Ru(tpy\text{-}Ph\text{-}NH_2)_2]^{2+}$ on Electrode Surfaces

The transition metal plays an important role in the electrochemical and optical properties of the metallopolymers as each transition metal posses unique characteristics. As described above, the

iron based complex (2) showed successful results in electropolymerization and the formation of stable films on electrode surfaces. Therefore, in this following section the same ligand is retained and the transition metal is changed from Fe^{2+} to Ru^{2+} where both are d^6 transition metal ions and it is known that central ruthenium ions are usually harder to oxidize that the iron ion due to a more stabilized metal-centered HOMO in the 4d compared to the 3d metal complexes [274].

3.2.7.1. Electrochemical behavior of $[Ru(tpy\text{-}Ph\text{-}NH_2)_2]^{2+}$ in the anodic region: evidence of its electropolymerization and comparison to the unsubstituted $[Ru(tpy\text{-}Ph)_2]^{2+}$ compound

The electrochemical properties of the 4-aminophenyl-functionalized bis(terpyridine) ruthenium complex, $[Ru(tpy\text{-}Ph\text{-}NH_2)_2]^{2+}$ (compound 4 shown in **Figure 55**), were first investigated by multisweep CV (Figure 1) using ITO as working electrode, and compared to the behavior of the non-substituted analog $[Ru(tpy\text{-}Ph)_2]^{2+}$ (compound 3) serving as electropolymerization-inactive control species. Typical CV curves obtained for compound **3** that is presented in **Figure 56**, recorded at a scan rate of 100 mV/s in acetonitrile (+ 0.1 M $LiClO_4$), revealed a classical diffusion-controlled redox system located at a potential of 1.22 V *vs* Ag/AgCl with an anodic-to-cathodic peak-to-peak separation of 102 mV, characteristic of a quasi-reversible one-electron transfer attributed to the Ru^{3+}/Ru^{2+} redox couple. Also, there is no increase or change upon cycling which indicates that no polymerization takes place.

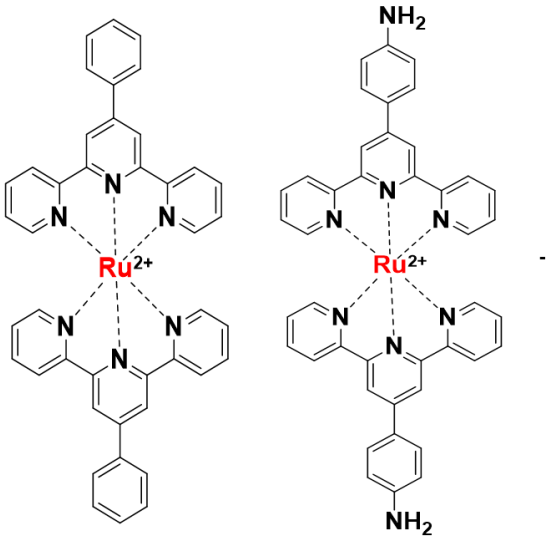

Figure 55: Structure of the compounds $[Ru(tpy\text{-}Ph)_2]^{2+}$ (3) and $[Ru(tpy\text{-}Ph\text{-}NH_2)_2]^{2+}$ (4).

This was not the case when studying the electrochemical response of compound 4, which differs structurally from compound 3 by the presence of a para-substituted aminophenyl group in the terpyridine ligand. During the first scan, two irreversible oxidation peaks are found at 0.98 V and 1.22 V vs Ag/AgCl which correspond to the oxidation of the amino groups to form radical cations ($–NH_2^{\bullet+}$, Eq. 1a) which can deprotonate and the resulting radicals ($–NH^{\bullet}$, Eq. 1b) to combine to form hydrazo bonds (–NH–NH–, Eq. 2) like in the case of iron. Then a reversible signal corresponding to the Ru^{3+}/Ru^{2+} redox couple is found at 1.36 V vs Ag/AgCl which is shifted anodically compared to the signal for compound 3. One reason for this big shift can be related to the irreversible oxidation of the hydrazo moieties previously formed in the system into azo bonds in this polymer film, where this peak could be masked by the oxidation of Ru^{2+}. This is validated during the second scan, where the oxidation peak is shifted backwards from 1.51 V during the first scan to 1.43 V vs Ag/AgCl during the second scan. Comparing to compound 2, the electropolymerization of ruthenium achieves higher peak currents where using a small number of scans already form a long polymer chain which can explain already the increase in peak to peak separation at a low number of scans.

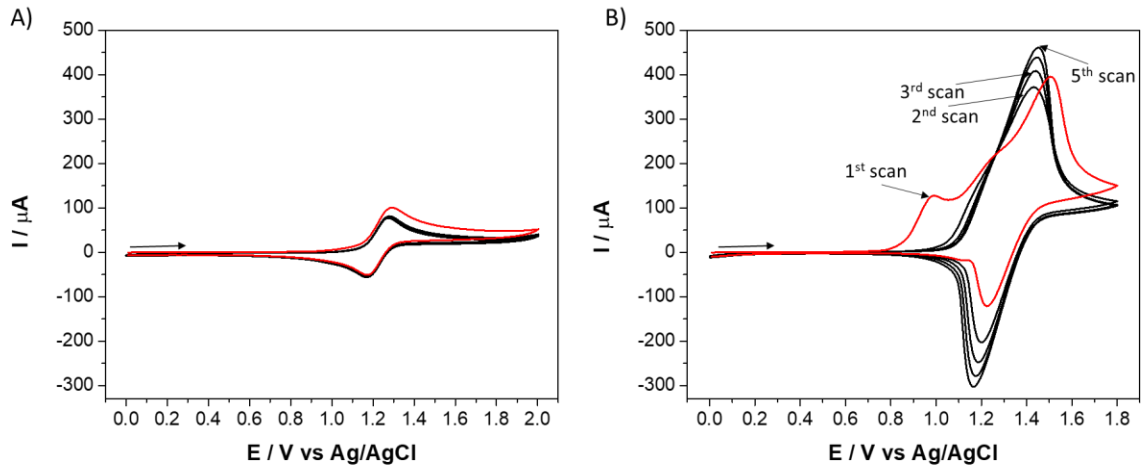

Figure 56: Comparison of the electrochemical behavior observed for compounds 3 (A) and 4 (B). Five successive CV curves (1st scan in red) recorded at 100 mV s-1 in the oxidation region between 0.0 V and 2 V* vs. *Ag/AgCl, using ITO as working electrode in acetonitrile (+ 0.1 M $LiClO_4$) containing 1 mM of compound 3 (A) or 4 (B).

3.2.7.2. Effect of the nature of the Electrolyte on the Electropolymerization process

As stated above, the electrolyte plays an important role in the electropolymerization process where it was evident that perchlorate-based electrolytes showed successful electropolymerization compared to others. In order to see if the same applies to the ruthenium complex, different solutions are prepared. **Figure 57** illustrates typical CV curves recorded for the anodic electropolymerization of the ruthenium complex (4) in the presence of various perchlorate-based supporting electrolytes (**Figure 57**A-C) and in sodium sulfate (**Figure 57**D). Effective electropolymerization was observed when using lithium perchlorate and sodium perchlorate, as evidenced by a pronounced current increase over the successive cycles. The small increase in anodic-to-cathodic peak-to-peak separation was also found to increase within the first few scans similar to the case of iron too.

While the CV response when using $HClO_4$ was different from the above, with less intense peak current growth upon cycling, indicating less effective electropolymerization, which can be explained by the protonation of the amino groups or destabilization of the metal–ligand complex. In the presence of proton donors, the deprotonation of the radical cations (generated at 0.93 V in that medium, see red curve in **Figure 57**C) is more difficult, thus impeding the coupling reaction (Eq. 2) and preventing the film growth.

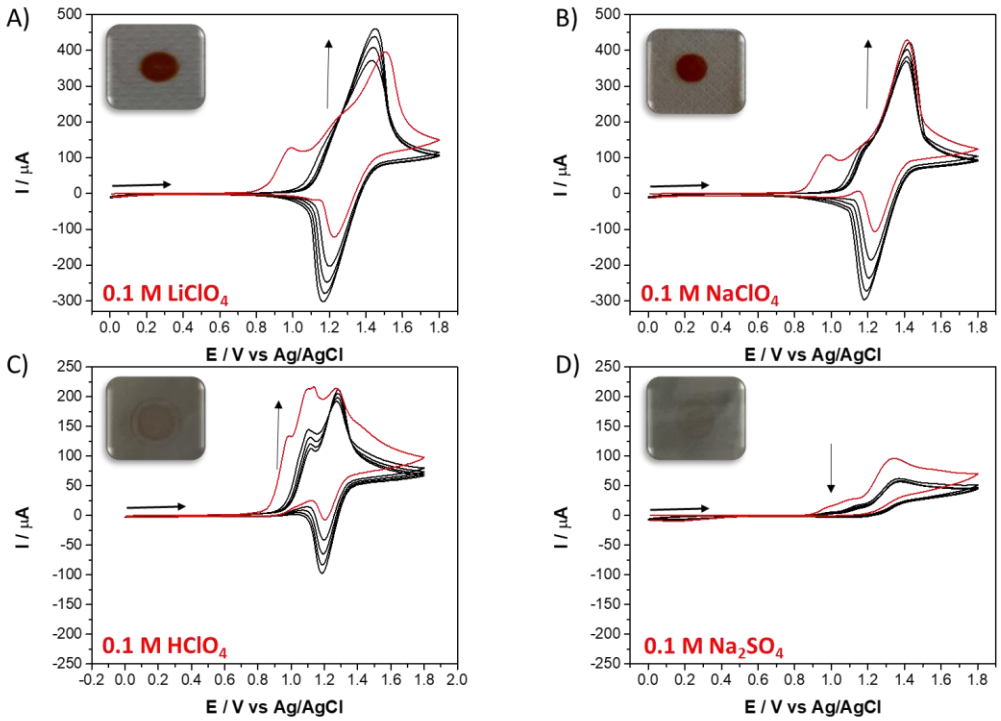

Figure 57: Effect of the supporting electrolyte on the efficiency of the electropolymerization of 4. 5 successive CV curves (1st scan in red) recorded at 100 mV s^{-1} using ITO as working electrode in acetonitrile (ACN) containing 1 mM of compound 2 in various electrolytes: A) 0.1 M $LiClO_4$, B) 0.1 M $NaClO_4$, C) 0.2 M $HClO_4$ (in 1/1 v/v ACN/H2O), and D) 0.1 M Na_2SO_4.

In the case of using Na_2SO_4 electrolyte solution, the result was still not good for which no electropolymerization can be observed. The redox signal is present, yet with peak broadening and less well-defined signals (the reduction peak is defined as the oxidation peak) and the current response rapidly decreased as the number of scans increased. This behavior suggests inefficient or inhibited electropolymerization, similar to the case of compound 2. Therefore, we can deduce that both compounds 2 and 4 are affected similarly by the nature of the electrolyte used, and for this reason lithium perchlorate was the chosen electrolyte to be used in the electropolymerization processes.

3.2.7.3. Effect of Increasing the Number of scans on the electrochemical response

We study the effect of changing the number of scans by performing a multisweep CV where we use non-modified ITO as the working electrodes. The CV curves obtained for compound **4** (1 mM)

were recorded at a scan rate of 100 $mV \cdot s^{-1}$ in acetonitrile (+ 0.1 M $LiClO_4$) and 4 different number of scans were used (2, 5, 10, and 20) on various working electrodes to follow the electropolymerization and then to characterize the films that are obtained using different techniques.

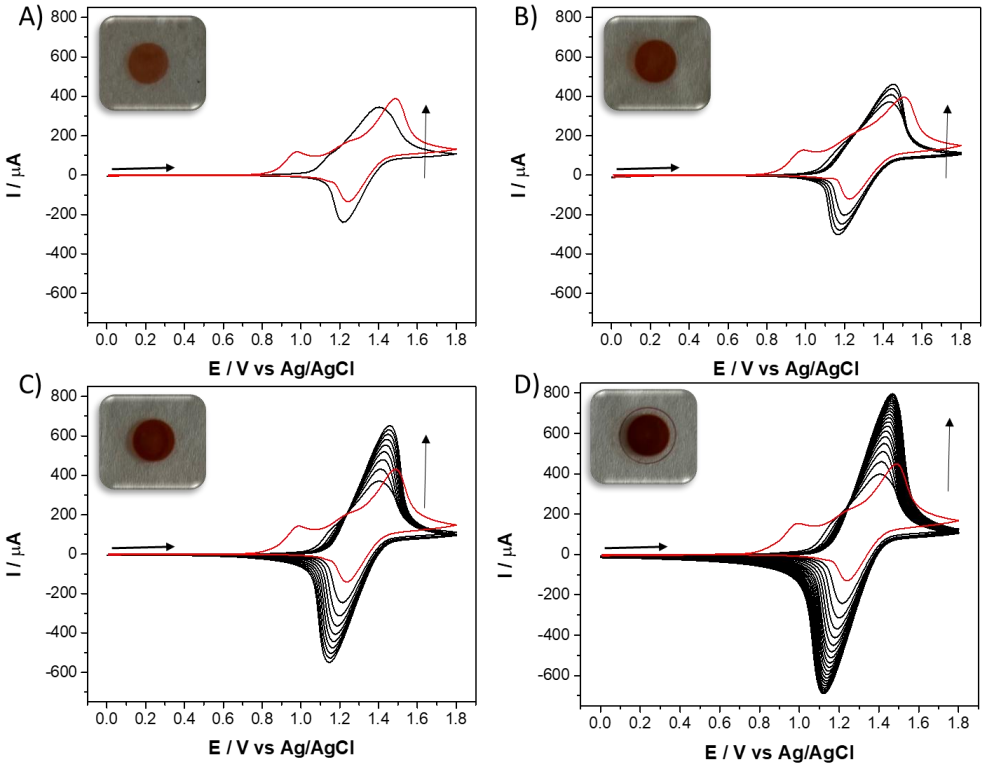

Figure 58: Effect of increasing the number of scans on the electropolymerization of 4. The CV curves were recorded at 100 mV/s using ITO as working electrode in acetonitrile (ACN) containing 1 mM of compound 4 and 0.1 M of lithium perchlorate, and apply different number of scans: A) 2 scans, B) 5 scans, C) 10 scans, and D) 20 scans.

Figure 58 shows the evolution of the cyclic voltammetry response during the successive electropolymerization of compound 4, highlighting how the anodic and cathodic peak currents progressively increase with the number of scans, reflecting the growth of the electroactive film. In **Figure 58**A, after only 2 scans, the anodic peak current corresponding to the oxidation of Ru^{2+} to Ru^{3+} decreases a bit from approximately 387 µA in the first cycle to around 345 µA and shifts from 1.5 V to 1.4 V vs Ag/AgCl, while the cathodic peak corresponding to the reduction increases from –134 µA to nearly –238 µA, which shows that using only 2 scans is already enough to obtain

a conductive metallopolymer chain. In **Figure 58**B, extending the scan count to 5 cycles leads to further current enhancement, with the anodic peak reaching around 460 µA and the cathodic one around -302 µA, reflecting continued polymer growth and increased redox-active surface coverage. In **Figure 58**C, after 10 scans, the currents rise more gradually, with anodic and cathodic peaks reaching 652 µA and –550 µA, respectively, suggesting still a relative increase and growth of polymer. Finally, in **Figure 58**D, after 20 scans, the anodic peak is around 800 µA and the cathodic peak at –690 µA, pointing to a near-saturation state, which is noticed after 10 scans the current starts to increase slowly since film growth is limited by charge transfer resistance or ion diffusion through the film.

3.2.8. Electrografting of 4 on ITO electrodes

The same principle applies here where in order to create a covalent link between the compound and the working electrode a solution is prepared that contains an equimolar amount (1mM) of the coordination complex (4) with sodium nitrite in a 0.5M HCl solution and the CV is performed to graft the complex using a scan rate of 100 mV/s. The cyclic voltammogram of the solution using a potential range of 0.5 V to -0.4 V vs Ag/AgCl, shows an irreversible cathodic peak at -0.095 V with a peak current of 25 µA during the first scan as shown in **Figure 59** which indicates the successful reduction of the monodiazonium cation and the formation of a reactive aryl radical that is likely to attach to the ITO surface. Furthermore, the decrease in the peak current during the second scan to less than 2 µA indicates that the electrode surface is passivated after one scan only similar to the case of the iron complex. The small change in the reduction peak between the two compounds is due to the change in the transition metal where ruthenium has stronger π-backbonding.

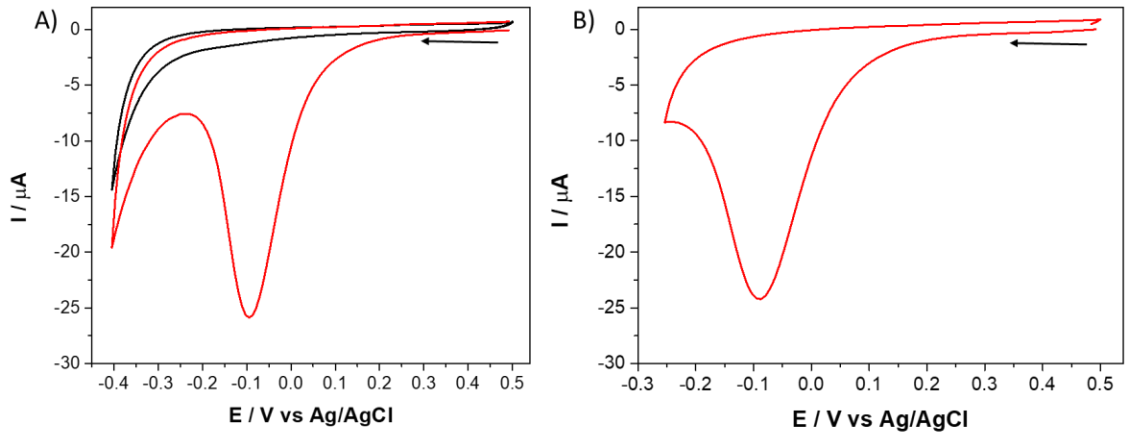

Figure 59: CVs recorded for the electrochemical reduction of in situ generated diazonium cation of complex 2, in 1 mM of 2 + 1 mM $NaNO_2$ (in 0.5 M HCl), using (A) 2 scans on bare ITO at 100 mV/s (B) 1 scan on bare ITO at 100 mV/s.

After deducing that one scan was sufficient to passivate the electrode surface, all the following grafting took place using a smaller potential window between 0.5 V and 0.25 V vs Ag/AgCl at scan rate 100 mV/s using 1 scan where the monomer is then characterized electrochemically and these modified electrodes were used for electropolymerizing 4 using $LiClO_4$.

3.2.9. ELectropolymerization of 4 after grafting

After electrografting the monomer on ITO, the second step is to perform the electropolymerization where the CV curves obtained for compound **4** (1 mM) were recorded at a scan rate of 100 $mV \cdot s^{-1}$ in acetonitrile (+ 0.1 M $LiClO_4$) and 4 different number of scans were used (2, 5, 10, and 20) that are the same condition as on bare ITO to compare the electrochemical response obtained.

When comparing the 2 scans CV in **Figure 46**A to that in **Figure 38**A, during the first scan we have first the irreversible oxidation of the amino groups at 0.96 and 1.22 V vs Ag/AgCl which is identical to that on the bare ITO which was 0.97 and 1.2 V. Then the oxidation of ruthenium was around 1.46 V similar to that in the previous case. Then in the reverse scan the reduction of Ru^{3+} takes place at 1.24 V which is the same as the reducing potential on ITO. Now with respect to the peak current achieved in this case they are a bit lower compared to the samples that were not grafted at high number of scans. Furthermore, the peak to peak separation as well increases with increasing the number of scans, so we can deduce that there is no major difference in the

electrochemical response when directly electropolymerizing 4 on ITO electrodes vs grafting the monomer first then electropolymerizing (**Figure 60**). Therefore, in order to determine if the grafting helps in the stability of the polymerized films on the electrodes, they modified electrodes are characterized electrochemically to study the behavior and stability after multiple cycles (**Figure 61**).

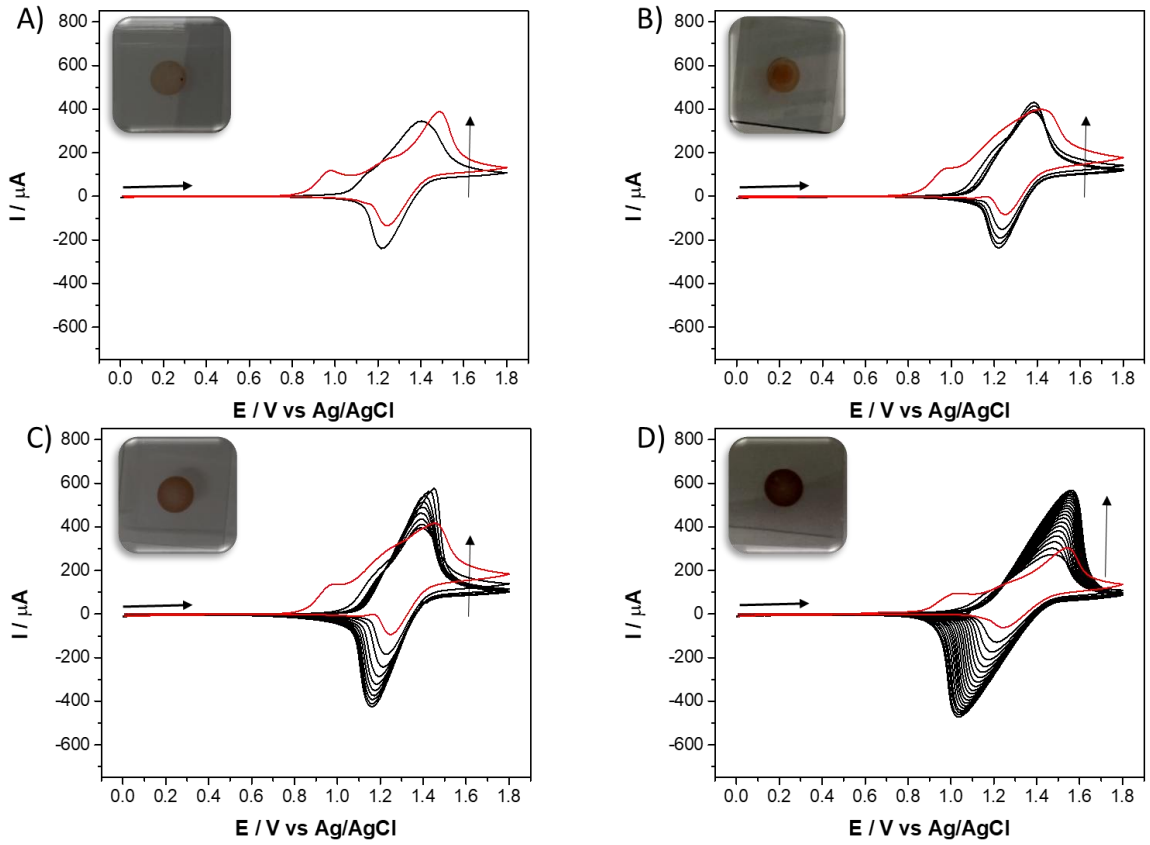

Figure 60: Effect of increasing the number of scans on the electropolymerization of 4 after electrografting. The CV curves were recorded at 100 mV/s using ITO as working electrode in acetonitrile (ACN) containing 1 mM of compound 4 and 0.1 M of lithium perchlorate, and apply different number of scans: A) 2 scans, B) 5 scans, C) 10 scans, and D) 20 scans.

3.2.10. Characterization of the Electropolymerized Films

3.2.10.1. Electrochemical response of the poly[Ru(tpy-Ph-NH_2)$_2$]$^{2+}$ films

After electropolymerization, the samples are characterized by preparing a monomer free electrolyte solution that is identical to that used to characterize the iron samples (**Figure 61**) (0.1

M $HClO_4$ in acetonitrile) and a potential range between 0 and 1.8 V vs Ag/AgCl at a scan rate of 100 mV/s. At small number of scans used (2 and 5), upon cycling the peak current especially the oxidative peak current that corresponds to the redox signal of Ru^{3+}/Ru^{2+} decreases slightly from around 130 µA to 100 µA while the reductive current remains almost constant for the 2 scans sample, while for the 5 scan sample the Ip_a decreases from 250 µA to 205µA and the Ip_c decreases from -202 µA to -183 µA.

This shows that polymer films are stable even without grafting on the electrodes, on the contrary when increasing the number of scans to 10 and 20, the current actually decreases with a percentage of more than 50 % loss which can be explained by the fact that at these higher number of scans, the ruthenium polymer chain increases in a faster rate than the iron so for the same number of scans, compound 4 gives longer chains than compound 2. This can contribute to the formation of aggregates or the deposition of oligomers on top and then by cycling, these loosely bounded material is removed from the surface of the electrode and this is evidenced by the change of color of the electrolyte solution from colorless to light red.

Even grafting before polymerization doesn't influence a big change in the stability or the electrochemical response as the peak current decreases as well for the sample electropolymerized using 20 scans from around 950 µA to around 300 µA in the anodic region and from -420 µA to -200 µA. Furthermore, the color of the deposit on the electrode becomes lighter after characterization which is in accordance to the decrease in the peak current that indicates loss of material in this case. Then in this case, similar to that of iron, the grafting didn't play an important role in the stability of the polymer films on the electrode surface.

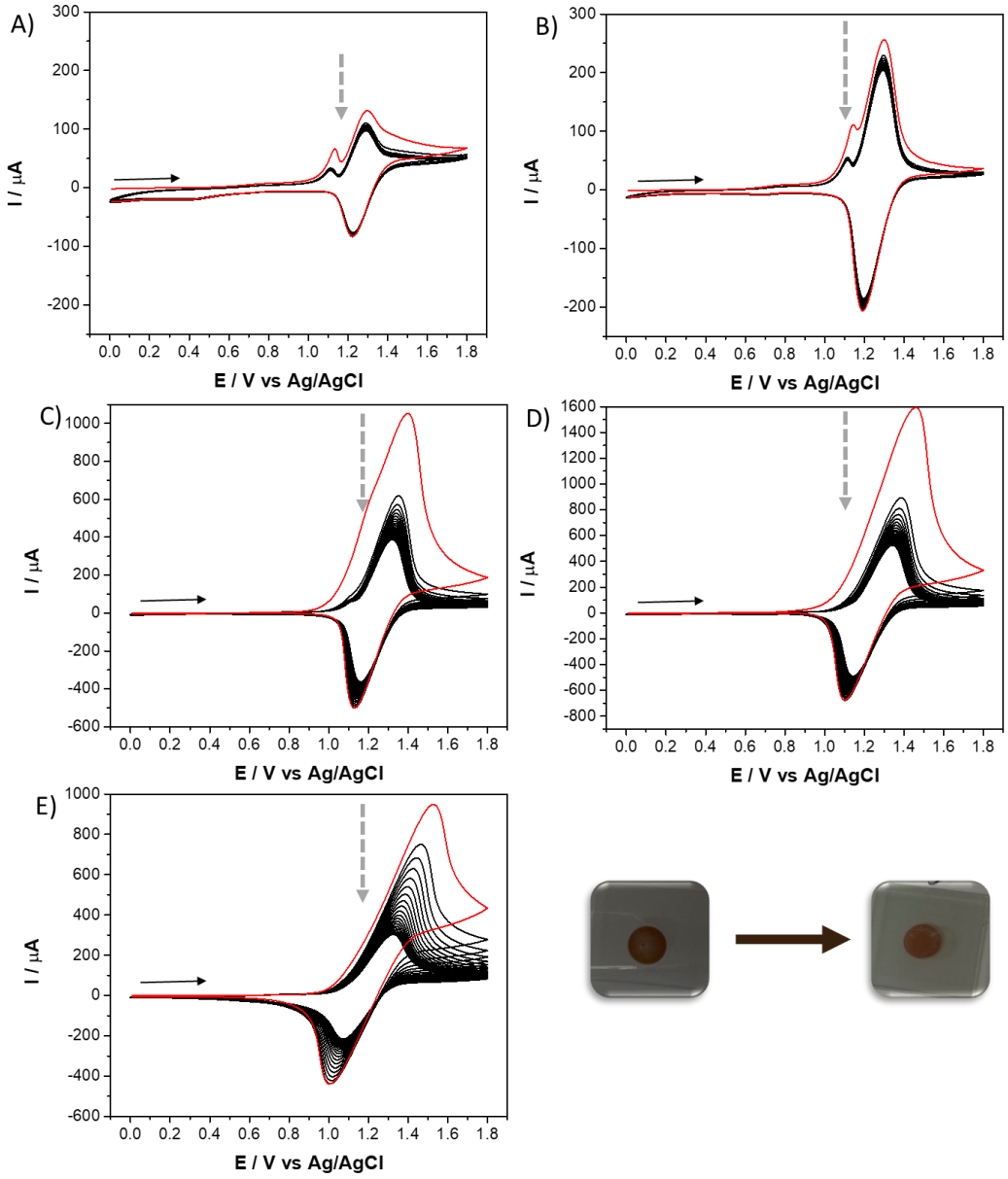

Figure 61: Multisweep CV curves recorded at a potential scan rate of 100 mV s^{-1} in monomer-free acetonitrile solution containing 0.1 M $HClO_4$ as supporting electrolyte, using poly[$Ru(tpy\text{-}Ph\text{-}NH_2)_2$]$^{2+}$ films electropolymerized either on bare ITO using different number of scans (A)2 scans, (B) 5 scans, (C) 10 scans, (D) 20 scans, and on ITO electrode previously electrografted with [$Ru(tpy\text{-}Ph\text{-}NH_2)_2$]$^{2+}$ moieties then polymerized using 10 scans (E) with an image illustrating the change in the color of the deposition.

3.2.10.2. Optical Characterization using UV-VIS

The optical properties of the [Ru(tpy-Ph-NH_2)$_2$] based electropolymerized films prepared in CH_3CN containing 0.1 M $LiClO_4$ were investigated by UV-Vis spectroscopy and compared to those of the monomer **4** in solution, as illustrated in **Figure 62**. The UV-Vis spectrum of a solution containing 1.0×10^{-5} M of **4** in ACN (red line) displays intense bands near 300-360 nm assigned to ligand-centered (LC) π–π* transitions, along with a moderately intense band located at 502 nm and attributed to metal-to-ligand charge-transfer (MLCT) transitions. The molar absorptivity of the MLCT is quite higher than that of the iron complex **2** which was already shown in literature and the reason for the blue shift of the MLCT band of the ruthenium complex is the stronger ligand field of the second-row transition metal compared to the iron complexes [274].

After electropolymerization on ITO, several changes can be noticed. The shoulder peak is not clearly identified around the 380-400 region as there is a broad and less intense band that appears upon electropolymerization. The second, broader and less intense band spanning the 440–520 nm region, which is assigned to n–π* transitions of the azo functionality. Moreover, the band corresponding to the ligand increases significantly along with the MLCT band as the number of scans used during electropolymerization increases which suggests an increase in the conjugation The appearance of this low-energy n–π* band is particularly significant, as such transitions are known to be sensitive to the electronic environment and are often enhanced or red-shifted in the vicinity of coordination complexes and in this case it is similar to the case of the iron polymer presented above. This behavior contributes to confirm that azo groups are really formed during the electropolymerization process, and suggest that they may be involved in weak coordination or electronic interactions with metal centers, thereby modulating their optical properties. Furthermore, as the number of scans that were performed during electropolymerization increased, the absorbance bands increased as well which proves the increase in the deposited material which in other words means longer polymer chains formed.

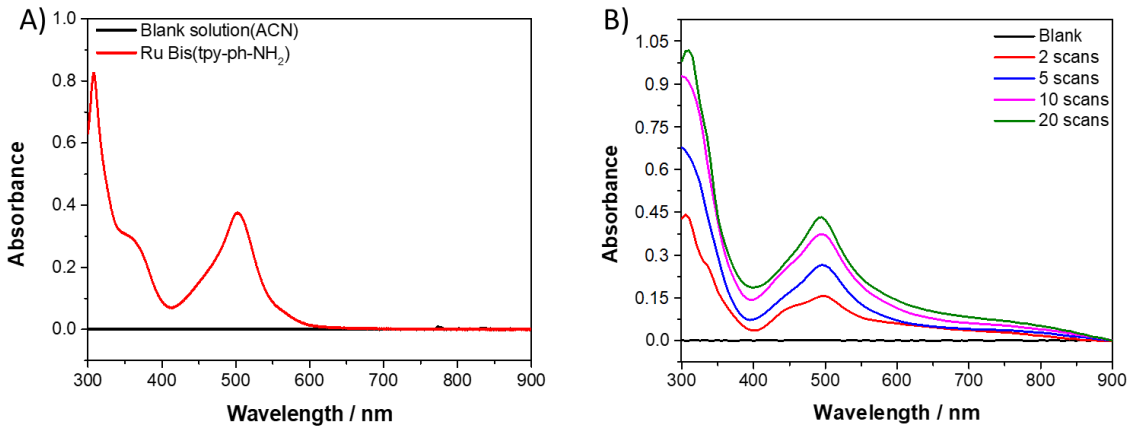

Figure 62: Comparison of the UV–Vis absorption spectra of the [Ru(tpy-Ph-NH₂)₂]²⁺ in Acetonitrile (A) and the corresponding poly[Ru(tpy-Ph-NH₂)₂]²⁺ film electropolymerized using different numbers of CV scans (B).

3.2.11. Electrochromic response of the films

As mentioned above, polypyridine ligands can coordinate to a variety of transition metal ions, that in return forms stable metal complexes. These complexes posses pronounced redox-responsive optical properties arising from MLCT transitions based on the transition metal used. Upon one-electron oxidation ($Ru^{2+} \rightarrow Ru^{3+}$), the metal center becomes significantly electron-deficient, thereby suppressing MLCT transitions. Based on a two-electrodes system device comprising the **poly**[Ru(tpy-Ph-NH₂)₂]²⁺ film prepared here with a gel-based electrolyte, we investigated its electrochromic properties. The color of the electrochromic films was found to vary as a function of the oxidation state of the central metal, with distinct changes observed both visually and from the UV–vis spectra upon switching between the Ru^{2+}/Ru^{3+} redox states. **Figure 63** displays the UV-Vis spectra of the **poly**[Ru(tpy-Ph-NH₂)₂]²⁺ material in the different redox states. In the normal state of the polymer film which is the reduced state, it exhibited an intense absorption band in the visible region 490 nm corresponding to metal-to-ligand charge transfer (MLCT) transitions characteristic of Ru(II) centers which is identified as the red line and is defined by the dark red color on the electrode. In contrast, the oxidized form of this film where Ru (II) is oxidized to Ru (III) shows a significantly diminished absorption, that is presented as the disappearance of the absorbance band which is presented as the blue line and it is presented by the disappearance of the purple color and a yellowish hue is also seen as illustrated below .In this two electrode system,

first a reducing potential is applied to ensure that the film is in its reduced state which has a MLCT band with absorbance of 0.175, then when applying a potential of 2.5 V the MLCT band disappears and the absorbance is around 0.02 which indicates the complete oxidation of the entire film which is identified as the bleached state where the color changes from red to a transparent light yellowish color. To prove that the applied potential has an effect on the MLCT band, different potentials between -0.5 and 2.5 V were applied where for example when applying 1.7 V, the absorbance is around 0.04 which shows that when decreasing the value of the applied potential from 1.7 to 1 V, the absorbance value increased indicating the reduction of the polymer and the value of the absorbance reached equilibrium when applying 0.9 V where the absorbance was 0.167 which is quite close to the original value so this indicates no major loss occurred during this process.

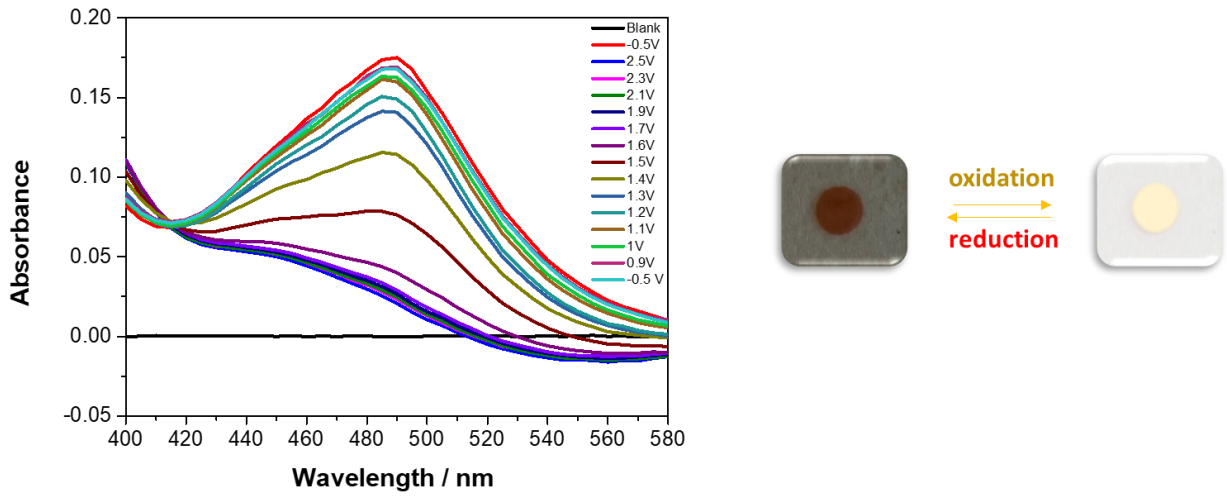

Figure 63: UV–Vis absorption spectra of poly[Ru(tpyPhNH$_2$)$_2$]$^{2+}$ in its reduced (red trace, at –0.5 V) and oxidized (blue trace, at 2.5 V) states along with the corresponding color of the deposit according to each potential applied.

The polymer film exhibited a reversible color change from red to colorless, as measured at wavelength 490 nm with the working electrode biased successively at -0.5 V (colouration step) and 2.5 V (bleaching step) for 10 or 20 s per step (**Figure 64**). The electropolymerized film demonstrated strong electrochromic performance, attributed to the high molar absorptivity of the metal-to-ligand charge transfer (MLCT) band ($\varepsilon = 4.9 \times 10^4$ M^{-1} cm^{-1}), resulting in a transmittance change (ΔT%) of around 30% and a high coloration efficiency of 3264 cm^2·C^{-1}. Some decrease in

absorbance changes upon multiple successive redox cycling was however observed, especially at short switching times, which is consistent with the multiweep CV data and might be due to some structural changes in the polymer during consecutive doping and dedoping processes (ingress and output of charge compensating ions during switching between the Ru^{2+}/Ru^{3+} redox states), or to incomplete reversibility of the redox switching, or to both phenomena. However, by extending the duration of redox switching, some improvement can be obtained. The response time was satisfactorily fast (*i.e.*, 1 s for colouration and 2.2 s for bleaching), as measured at 95% of the maximum absorbance variations observed after application of +2.5 V and -0.5 V, respectively.

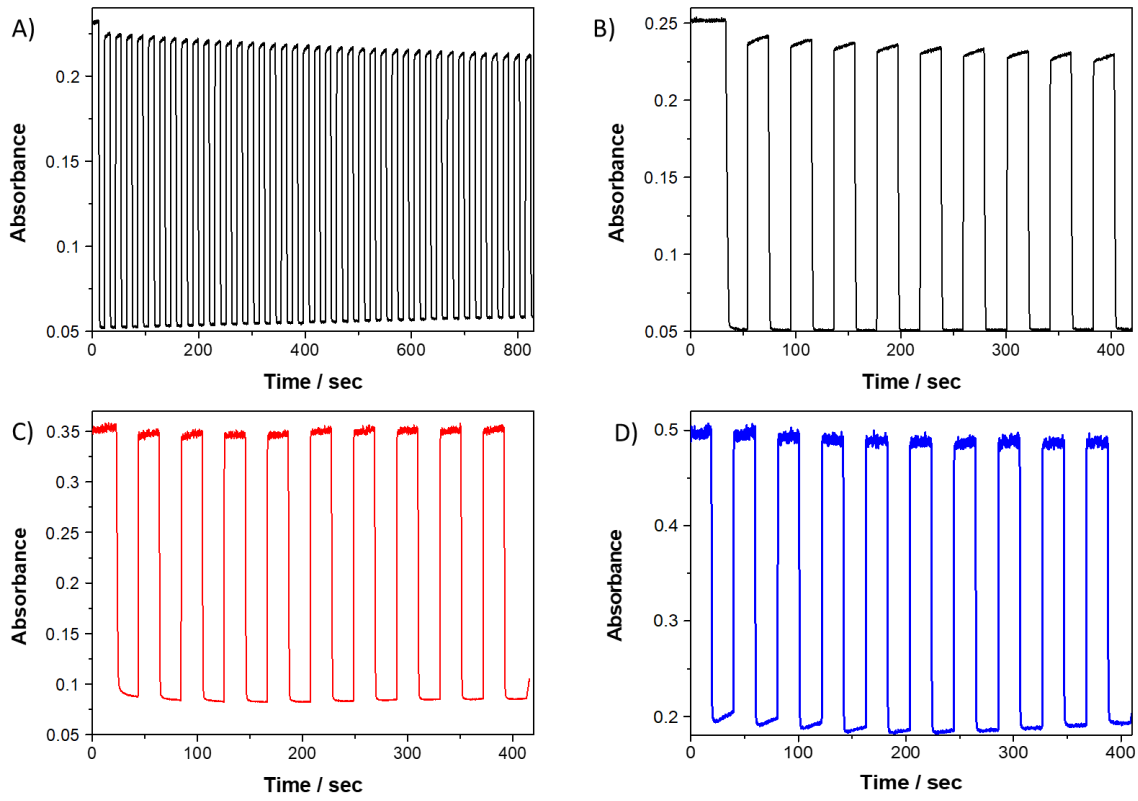

Figure 64: Chronoabsorptometry of the polymeric film over multiple redox cycles monitored at a fixed wavelength of 490 nm, respectively recorded by applying switching times of (A) 10 s and (B) 20 s for polymer formed using 2 scans, (C) 20 s for polymer formed using 5 scans and (D) 20 s for polymer formed using 10 scans.

3.2.12. Effect of Changing the Concentration of the Electroactive species on the Electropolymerization of the metallopolymers

Controlling the concentration of electroactive species during electropolymerization is a critical parameter that directly influences the nucleation, growth kinetics, and quality of the resulting polymer film. In studies of conductive polymers such as PEDOT and PANI increasing monomer concentration (from 1 to 10 mM) has been shown to enhance current density during potentiostatic deposition and promote more continuous film formation through progressive nucleation mechanisms. Analogously, for redox-active metal complexes bearing functional groups (e.g., amino-, vinyl- ligands), the availability of active species at the electrode surface governs radical coupling and film cross-linking during electropolymerization as well [275], [276].

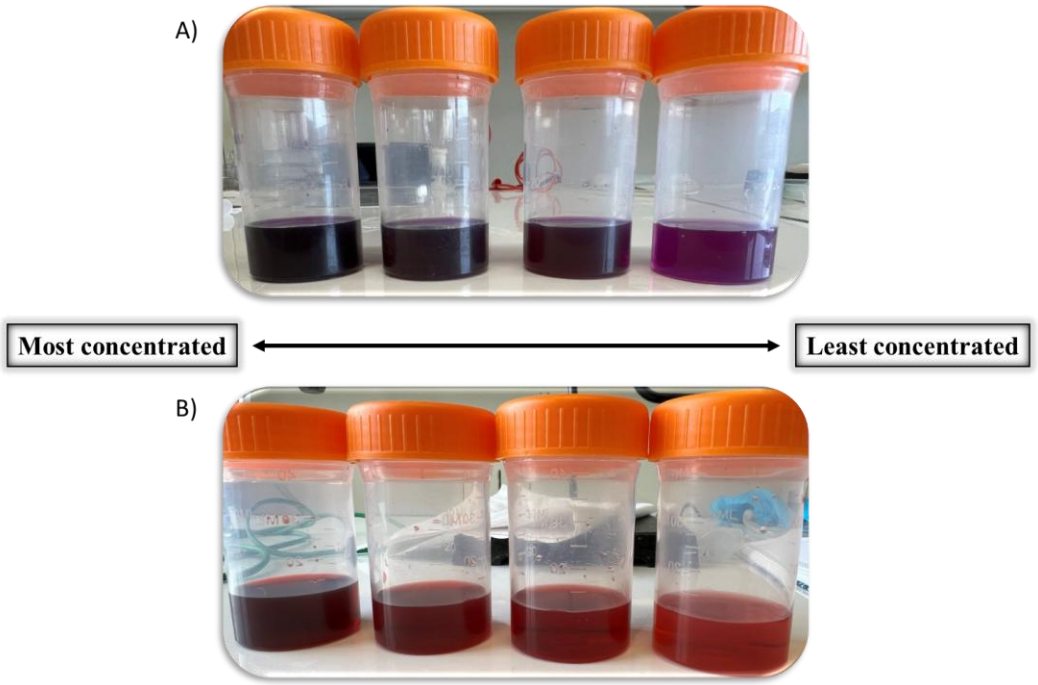

Figure 65: Formulation of solutions used to electropolymerize compounds 2 (A) and 4 (B) based on acetonitrile and 0.1 M $LiClO_4$ using different concentrations of the electroactive species from most to least concentrated: 1, 0.5, 0.3, 0.1 mM of 2 (A) and 4 (B).

Electropolymerization of compound 2 was perfomed using an acetonitrile solution containing 0.1 M $LiClO_4$ was performed over 20 cyclic voltammetry scans and using a potential range between 0 and 1.6 V vs Ag/AgCl at concentrations ranging from 1.0 to 0.1 mM as shown in **Figure 65**. As shown in **Figure 66** the concentration had a pronounced effect on both the electrochemical

response and the morphology of the resulting films on the electrode surfaces. At 1.0 mM, the cyclic voltammogram after 20 scans exhibited the highest peak currents, with an anodic value of 490 µA and a cathodic value of −458.9 µA, indicating a high surface density of electroactive species and efficient electron transfer. This condition produced a uniform, intensely purple film, characteristic of rapid nucleation and continuous polymer growth. Reducing the concentration to 0.5 mM lowered the peak currents to 246 µA and −239 µA, while at 0.3 mM the currents further decreased to 178 µA and −180 µA, respectively. These reductions are consistent with the Randles–Ševčík relationship, which shows that peak current decreases with the decrease of the analyte concentration. At the lowest concentration of 0.1 mM, the anodic and cathodic peak currents fell sharply to 42 µA and −36.6 µA, with only faint coloration of the electrode visible, indicating minimal polymer coverage.

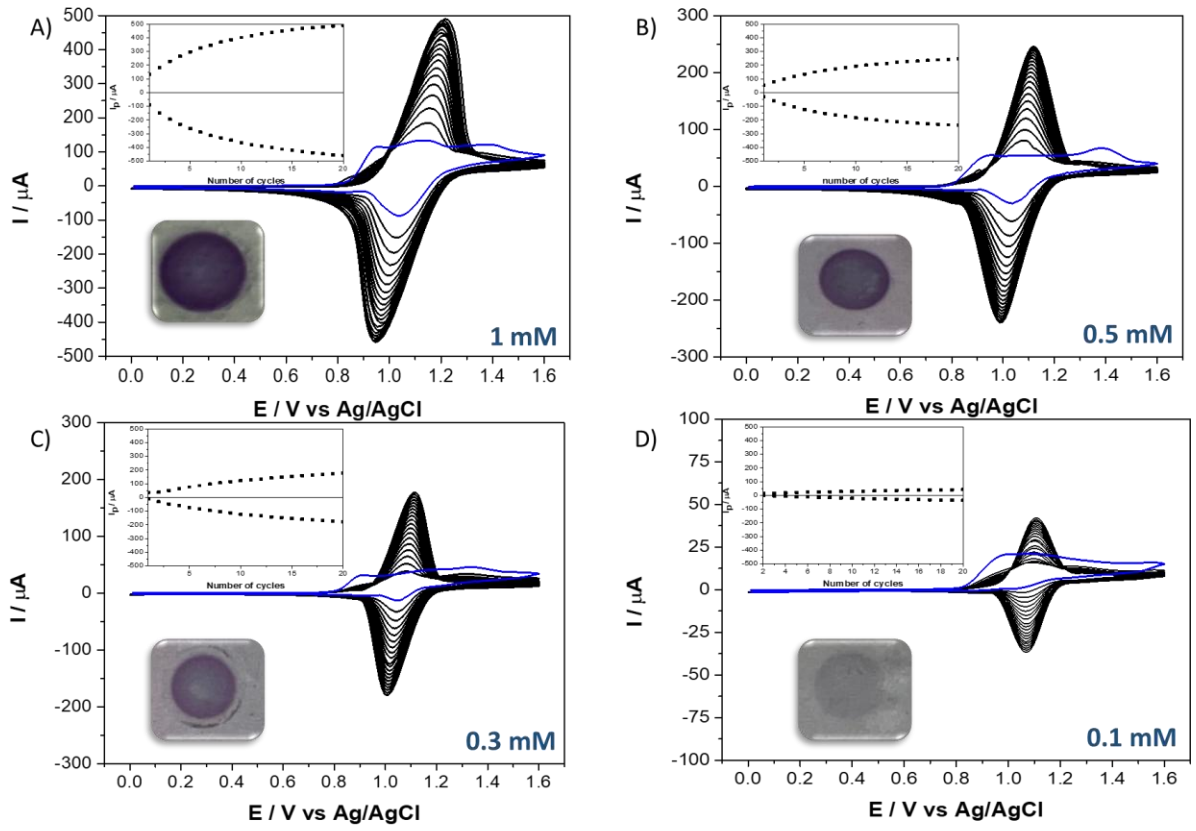

Figure 66: Effect of changing the concentration of the electroactive species on the efficiency of the electropolymerization of 2. 20 successive CV curves (1st scan in blue) recorded at 100 mV s^{-1} using ITO

as working electrode in acetonitrile (ACN) containing 0.1 M of $LiClO_4$ and compound 2 in various concentrations: (A) 1 mM, (B) 0.5 mM, (C) 0.3 mM, (D) 0.1 mM.

While higher monomer concentrations favor faster growth and more complete coverage, excessively high concentrations can lead to uncontrolled growth, rough surface morphology, and weaker adhesion which leads to the removal of the polymer when cleaning the electrode. Conversely, very low concentrations result in sparse nucleation and poor electroactivity. Thus, selecting an intermediate concentration offers a balance between growth rate, film uniformity, and adhesion, enabling optimized electropolymerization performance which was shown when using two concentrations which are 1 mM and 0.5 mM.

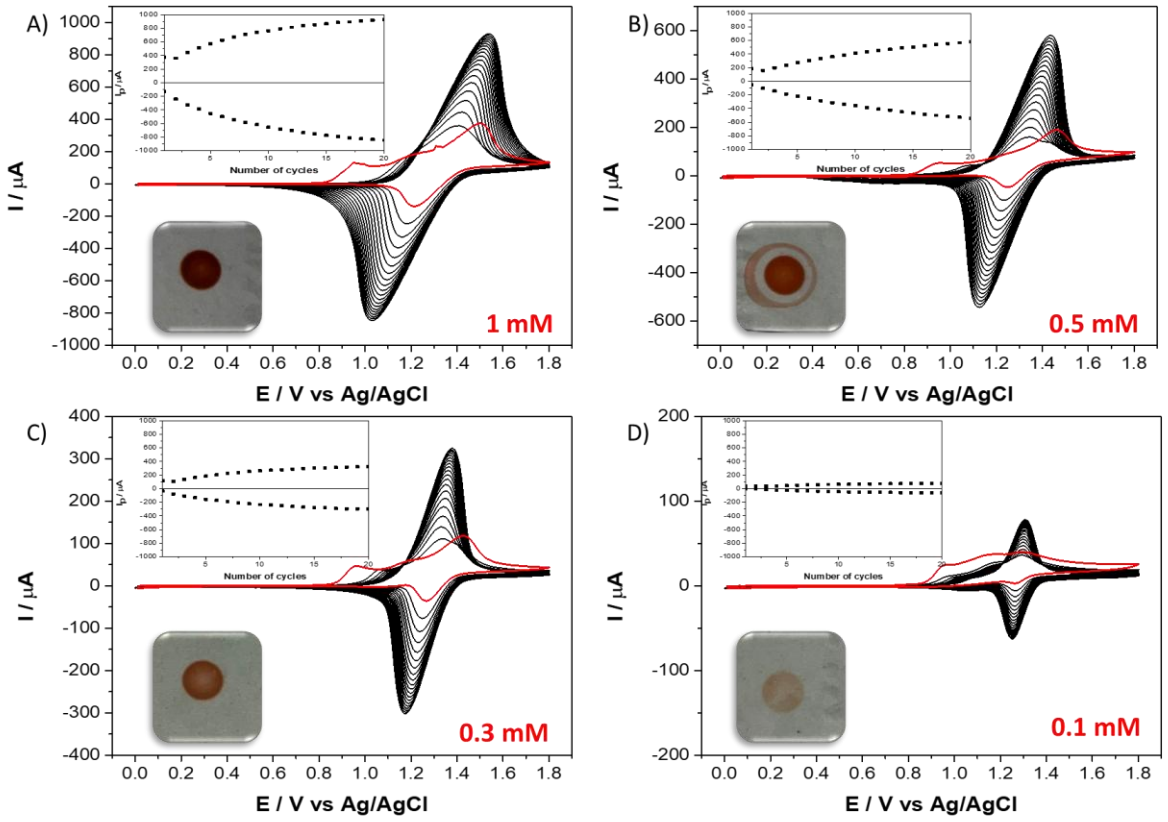

Figure 67: Effect of changing the concentration of the electroactive species on the efficiency of the electropolymerization of 4. 20 successive CV curves (1st scan in red) recorded at 100 mV s^{-1} using ITO as working electrode in acetonitrile (ACN) containing 0.1 M of $LiClO_4$ and compound 4 in various concentrations: (A) 1 mM, (B) 0.5 mM, (C) 0.3 mM, (D) 0.1 mM.

The same experiment was performed using the ruthenium complex as well, where 20 scans were performed using a potential range between 0 and 1.8 V vs Ag/AgCl for four different solutions having different concentrations for the electroactive species as shown in **Figure 67**. The concentration-dependent behavior closely mirrored that observed for the Fe(tpy-ph-NH_2) system. At 1.0 mM (Figure 34A), the cyclic voltammogram after 20 scans displayed the largest anodic and cathodic peak currents, indicative of a high density of electroactive species and efficient charge transfer, and yielded a uniform, darkly colored polymer film on the electrode surface. Reducing the concentration to 0.5 mM (Figure 34B) and 0.3 mM (Figure 34C) progressively lowered the peak currents and produced lighter films, consistent with reduced nucleation site density and slower growth rates. At the lowest concentration tested, 0.1 mM (Figure 34D), the voltammetric features were significantly attenuated and the electrode coloration was faint, signifying minimal polymer coverage. This trend is consistent with the **equation mentioned above too**, where peak current scales with the concentration of the electroactive species. The similar concentration-dependent behavior for both Ru- and Fe-based systems indicates that the governing mechanism; oxidative generation of reactive species followed by surface-confined polymer growth is common to both metal complexes. In each case, higher concentrations promote rapid nucleation and more complete coverage, whereas low concentrations result in patchy films and diminished electroactivity. Optimal film quality therefore requires a balance between sufficient monomer availability for continuous growth and avoidance of excessively rapid deposition that may compromise film morphology or adhesion.

3.2.13. Optical and Profilometric Analysis of Electropolymerized Films

Optical microscopy and surface profilometry are good tools for characterizing conducting polymer films deposited on electrodes. Optical microscopy offers a quick and non-destructive visual assessment of surface morphology revealing features such as film uniformity, color heterogeneity, cracks, and defects. This technique is widely applied as it is easy and quick to qualitatively evaluate thin-film continuity and morphology. Surface profilometry quantitatively measures film thickness and surface roughness with micrometer to nanometer precision. It has been successfully used to characterize soft organic films thicker than ~40 nm and provides reliable thickness and roughness data without damaging delicate films important when working with conducting and soft polymer coatings. Therefore, these two, optical microscopy and profilometry offer a complementary combination of qualitative and quantitative surface analysis. This dual-characterization approach

enables comprehensive understanding of how deposition parameters (such as number of electrochemical cycling) affect both the visual appearance and topographical properties of the films as shown in **Figure 68**.

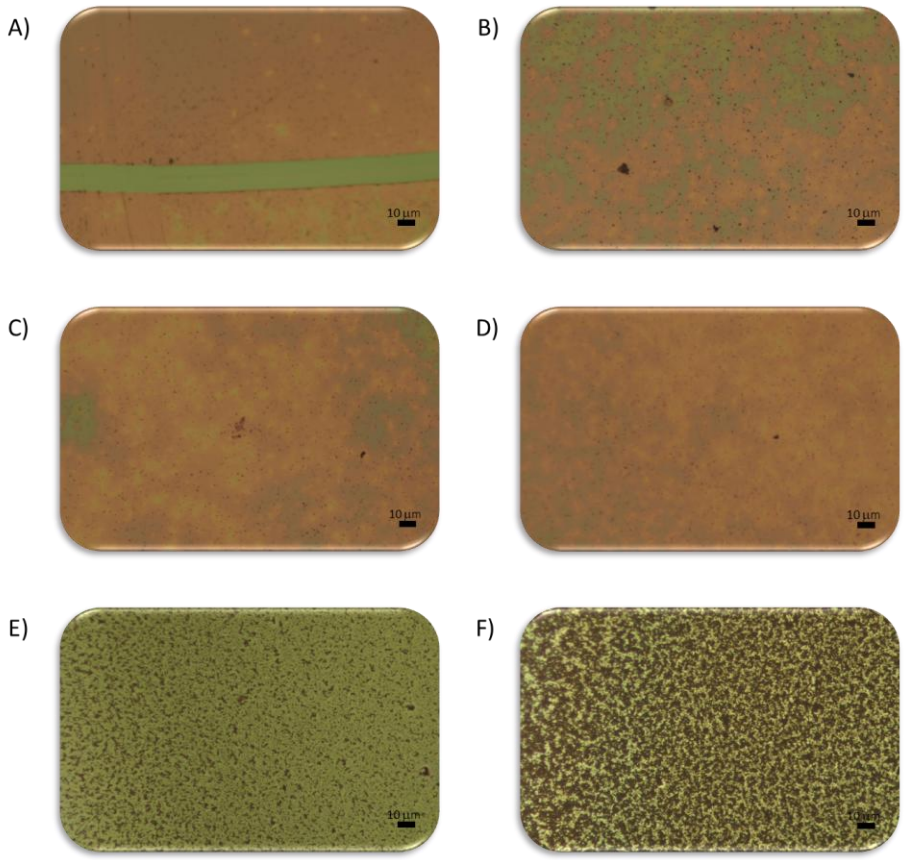

Figure 68: Optical images of modified electrode surfaces: iron samples A) 6 scans sample (edge) where the green indicates the bare electrode and the purple/pink color represents the polymer deposit, B) 6 scans sample middle, C) 20 scans sample (edge), D) 20 scans sample (middle). Ruthenium samples: E) 2 scans sample (middle), F) 20 scans sample (middle).

profilometric measurements reveal clear and quantifiable differences in the growth behavior of Fe(tpy-ph-NH_2) and Ru(tpy-ph-NH_2) metallopolymers deposited on ITO via electrochemical polymerization. For the Fe system, the film thickness increased gradually from **100 nm** at 6 scans to **300 nm** at 20 scans, corresponding to an overall average growth rate of approximately **14 nm per scan**, with interval-specific rates of 15 nm/scan (6→10 scans), 8 nm/scan (10→15 scans), and 20 nm/scan (15→20 scans). In contrast, the Ru films exhibited substantially faster growth, increasing from **120 nm** at just 2 scans to **600 nm** at 20 scans, with an overall average of **27 nm**

per scan and interval-specific rates of 26.7 nm/scan (2→5 scans), 36 nm/scan (5→10 scans), and 22 nm/scan (10→20 scans). This means that under identical conditions, Ru films grow approximately **1.8× faster per scan** than Fe films. These quantitative differences are consistent with the optical microscopy observations: Fe-derived films display smoother, more uniform coverage after extended cycling, while Ru-derived films appear rougher and more granular even at lower scan numbers, indicative of rapid and localized deposition. The faster growth of the Ru system results in substantial coverage (120–200 nm) within the first few scans, but also leads to increased topographical variation, whereas the slower, more controlled growth of Fe allows for better lateral coalescence before significant vertical build-up occurs. These morphological and growth rate trends align with the electrochemical data, where samples yielding thicker films exhibited higher peak currents, and attenuated CV responses corresponded to thinner films. Mechanistically, the differences likely arise from a combination of factors: Ru monomers may oxidize more readily, generating higher concentrations of radical cations per cycle; a higher nucleation rate and faster oligomer precipitation for Ru could lead to multiple growth centers and greater roughness; and differences in solubility, counter-ion incorporation, and steric/electronic structure may influence aggregation behavior, chain coupling, and film porosity. From a practical standpoint, the Ru system offers the advantage of rapid thickness build-up but at the expense of surface smoothness, while the Fe system enables smoother, more uniform films at slower deposition rates highlighting a trade-off that should be considered when optimizing these metallopolymers for applications requiring precise control over film morphology and electrochemical performance.

3.2.14. Electrochemical Behavior of $[Zn(tpy\text{-}Ph\text{-}NH_2)_2]^{2+}$ and $[Co(tpy\text{-}Ph\text{-}NH_2)_2]^{2+}$ on Electrode Surfaces

3.2.14.1. Electrochemical behavior of $[Zn(tpy\text{-}Ph\text{-}NH_2)_2]^{2+}$ and $[Co(tpy\text{-}Ph\text{-}NH_2)_2]^{2+}$ in the anodic region

After successfully forming metallopolymers using Fe (II) and Ru (II) as the d^6 transition metals with amino groups functionalized ligands that present good electrochemical and optical properties, two more coordination complexes were synthesized which have the same ligand as compounds 2 and 4 and only the transition metal is changed to Zn (II) (compound 5) and Co (II) (compound 6). Typical CV curves obtained for compounds **5 and 6**, recorded at a scan rate of 100 $mV \cdot s^{-1}$ using different potential ranges in acetonitrile (+ 0.1 M $LiClO_4$) using 50 scans (**Figure 70**). According

to **Figure 70**A, using the zinc solution which was a light yellow solution and applying a potential range between 0 and 1.5 V vs Ag/AgCl, there was only one irreversible oxidation peak which is normal since it is very difficult to oxidize Zn^{2+} since it has a d^{10} configuration and it is known as redox-inactive.

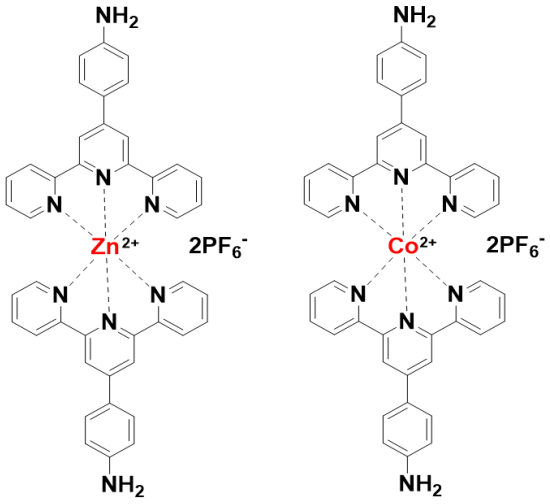

Figure 69: Structure of the compounds $[Zn(tpy\text{-}Ph\text{-}NH_2)_2]^{2+}$ (5) and $[Co(tpy\text{-}Ph\text{-}NH_2)_2]^{2+}$ (6).

The only peak present at around 1.26 V with a peak current 55 µA which corresponds to the irreversible oxidation of the amino group. The peak potential is shifted positively compared to the other complexes due to the reduced electronic delocalization since Zn^{2+} has a fully filled d-orbital. Even after scanning, no new peaks appear and the irreversible peak's current decreases to less than half during the second scan and keeps on decreasing to less than 5 µA since no polymerization is taking place. Furthermore, no deposit is seen on the working electrode after washing.

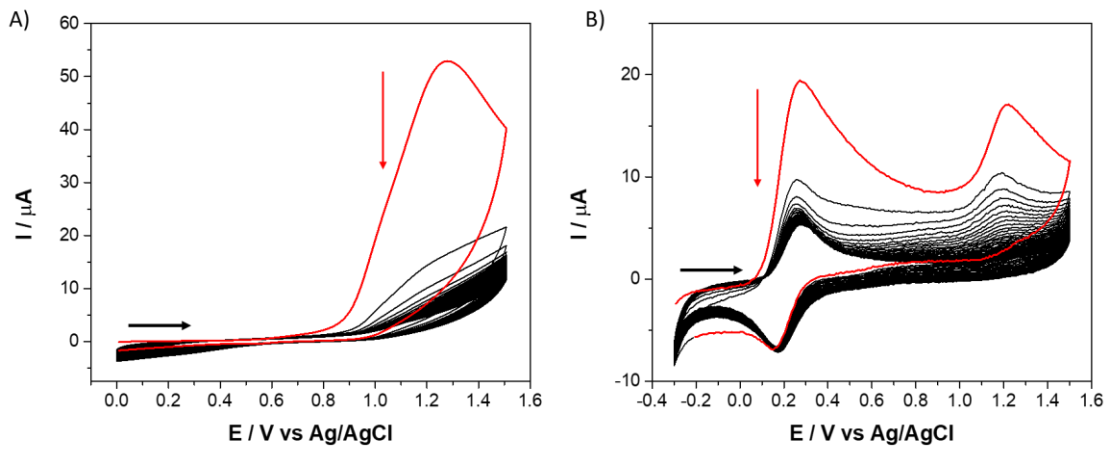

Figure 70: Electrochemical behavior observed for compounds 5 (A) and 6 (B). Fifty successive CV curves (1st scan in red) recorded at 100 mV s-1 in the oxidation region between 0 V and 1.5 V* vs. *Ag/AgCl, using ITO as working electrode in acetonitrile (+ 0.1 M $LiClO_4$) containing 1 mM of compound 5 (A), and fifty CV scans recorded at the same scan rate in the oxidation region between -0.3 V and 1.5 V vs Ag/AgCl using ITO and acetonitrile (+ 0.1 M $LiClO_4$) solution containing 1 mM of compound 6 (B).

Then when performing the same experiment using compound 6, The potential range applied was from -0.3 V to 1.5 V vs Ag/AgCl at a scan rate of 100 mV/s using 50 scans. According to the cylic voltammogram in **Figure 70**B , the first scan shows a characteristic redox signal centered at 0.19 V that is attributed to the Co^{3+}/Co^{2+} couple (ref). Additionally, the irreversible peak at 1.4 V is the irreversible oxidation of NH_2. However, after scanning neither the oxidation or reduction peak of the cobalt complex increase. On the contrary, the oxidation peak at around 0.29 V reached a peak current of 5 µA at the last scan and the reduction peak at 0.12 V reached a peak current of -7.5 µA which indicates that no electropolymerization process took place. This is validated after removing the electrode since nothing is deposited on the ITO. One explanation for such issue can be attributed to the electronic configuration of Co^{2+} since it has a d^7 electron configuration unlike Fe^{2+} and Ru^{2+} who have a d^6 electron configuration.

3.2.14.2. Electrochemical response of 5 in a wider potential window on Carbon Electrode

On ITO electrodes using the zin complex, when cycling in the anodic region only the oxidation of the amino groups was seen since there is no redox couple which is the opposite of what was seen before in the case of iron, so the working electrode is changed to carbon electrode to see the anodic

and cathodic (reduction of terpyridine moieties) processes that take place. Since the potential range covers also the cathodic region, all the solutions prepared are bubbled under nitrogen for 15 minutes to remove oxygen to prevent its reduction where the potential range is between -1.8 V and 2 V vs Ag/AgCl (**Figure 71**). During the first scan, two successive reversible reductions were observed for compound 5, corresponding to ligand-centered processes attributed to the reduction/reoxidation of the terpyridine moieties. Then when moving forward with the scan in the anodic direction, one irreversible peak is detected at around 1.14 V which corresponds to the irreversible oxidation of the amino groups. Then during the second scan, on the contrary of what was seen before, first there was no appearance of a third reduction peak which could be attributed to the reduction of azo groups that would have been formed during the electrochemical oxidation (which probably didn't as no peak was visible other than the formation of the cation radical amino groups). Second, the redox peaks that corresponds to the terpyridine ligand decreases which also further indicates that no polymerization is taking place. As the cycling continues, the reduction peak corresponding to the ligand keeps decreasing and no new signals appear so we can conclude that this process doesn't work and no metallopolymer is obtained.

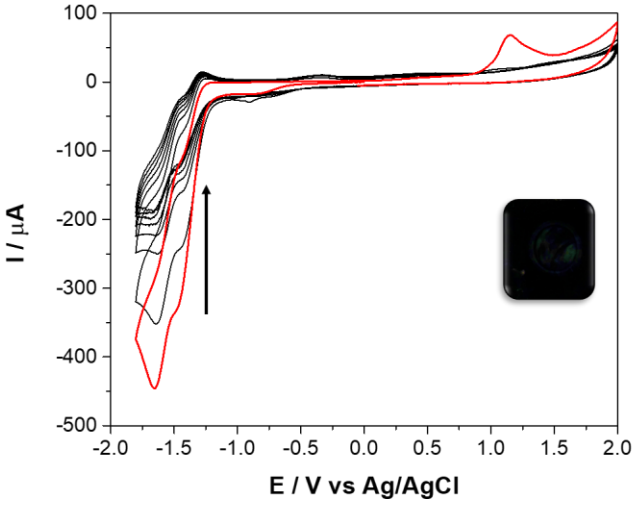

Figure 71: Electrochemical behavior observed for 5. Ten successive CV curves (1st scan in red) recorded at 100 mV/s in the region between -1.8 V and 2 V vs. Ag/AgCl, using ITO as working electrode in acetonitrile (+ 0.1 M $LiClO_4$) containing 1 mM of compound 5.

3.2.15. Electrografting of 5 and 6 on ITO followed by electropolymerization and electrochemical characterization

Since these compounds have amino groups, they can be grafted on ITO electrodes so two solutions were prepared that consist of an equimolar amount (1mM) of the coordination complexes (5 and 6) with sodium nitrite in a 0.5M HCl solution and the CV is performed to graft the complexes using a scan rate of 100 mV/s. The cyclic voltammogram of the solutions is performed using a potential range of 0.5 V to -0.4 V vs Ag/AgCl, where for the zinc complex we can see the reduction of the diazonium cation at -0.16 V vs Ag/AgCl with a peak current of 30 µA during the first scan **Figure 72**A. As expected, during the second scan, the peak current decreases significantly which indicates the passivation of the electrode surface. Then this modified electrode is electrochemically characterized using a monomer free electrolyte solution consisting of acetonitrile with 0.1 M perchloric acid to verify the effective grafting of the zinc monomer. According to **Figure 72**B, the grafting was successful as during the first scan perfomed at 100 mV/s using a potential range between 0 V and 1.5 V vs Ag/AgCl we have the oxidation of amino group found on the other side of the complex and then during the second scan, no peaks were found which is quite normal as there is no electroactive redox couple and the amino group was previously oxidized at 1 V vs Ag/AgCl with a peak current of around 2 µA which is typical value in monomer modified electrodes.

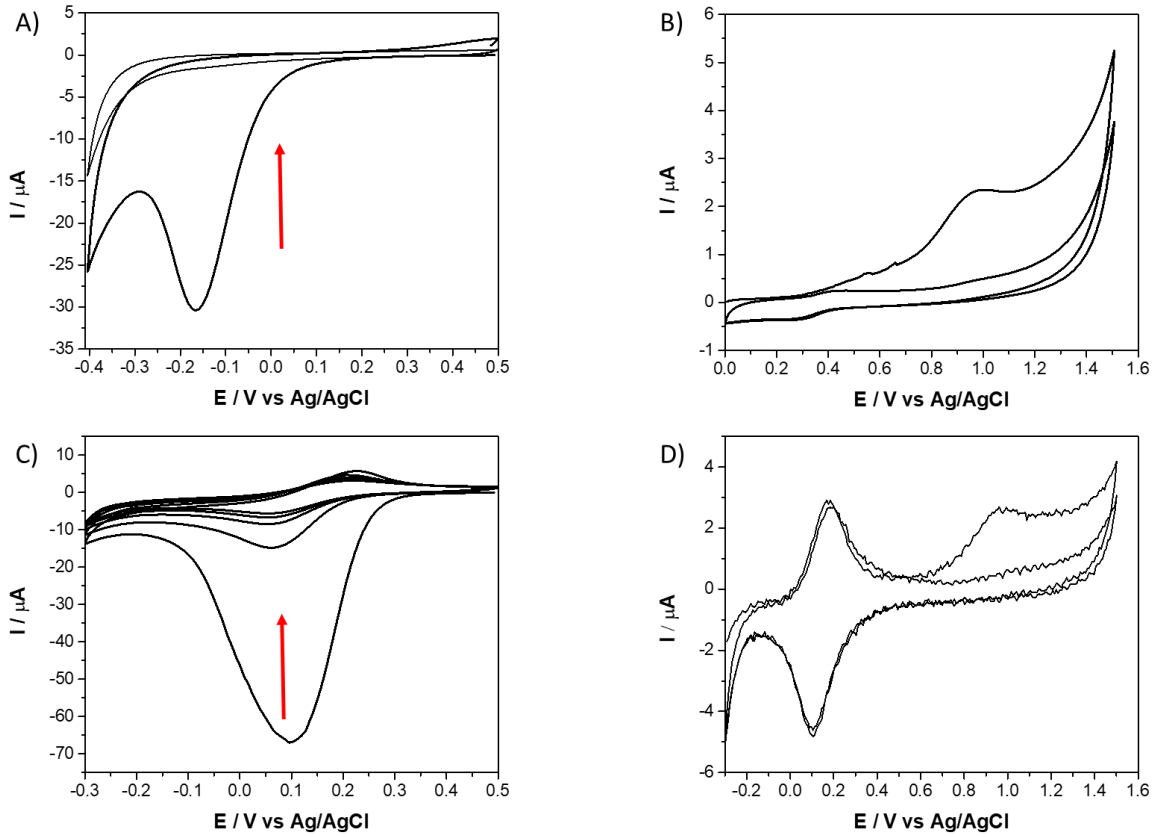

Figure 72: CVs recorded for the electrochemical reduction of in situ generated diazonium cation of complexes 5 and 6, using 1 mM of 5 and 6 + 1 mM $NaNO_2$ (in 0.5 M HCl), using (A) 2 scans on bare ITO at 100 mV/s and (C) 5 scans. Electrochemical characterization of the grafted complexes using Multisweep CV curves recorded at a potential scan rate of 100 mV s^{-1} in monomer-free acetonitrile solution containing 0.1 M $HClO_4$ as supporting electrolyte for (B) compound 5, and (D) compound 6.

The cyclic voltammogram of the solution containing the cobalt complex using a potential range of 0.5V to -0.3V vs Ag/AgCl at scan rate 100 mV/s, shows a large cathodic peak at 0.08V with a peak current of 67 µA during the first scan as shown in **Figure 72**C. However, in the reverse scan (from -0.3 to 0.5) there is a small oxidation peak at around 0.22 V with a small peak current of 5.7 µA. This peak can be related to the oxidation of the Co^{2+} to Co^{3+} which can be justified with the following scans, since during the second scan the cathodic peak at 0.06V which can correspond to the reduction of Co^{3+} to Co^{2+} and as the scanning continues both the cathodic and anodic peak decrease. Then when characterizing the electrode to see if this process was successful using the monomer free electrolyte solution shows reversible redox peak corresponding to Co^{3+}/Co^{2+} at 0.1

V with peak currents in agreement with the surrounding conditions. Furthermore, the oxidation of the amino groups was present at 1 V during the first scan which then disappears during the second scan.

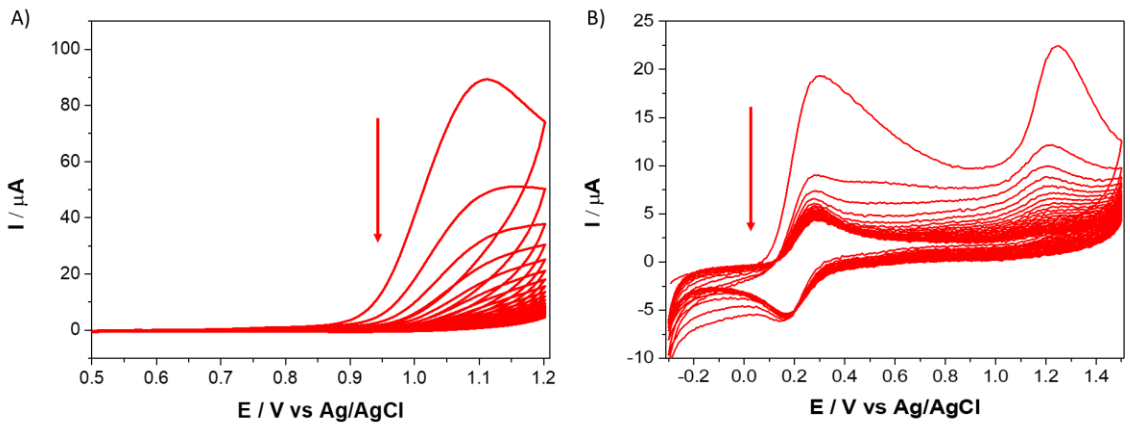

Figure 73: Electrochemical behavior observed for compounds 5 (A) and 6 (B) after grafting. Twenty fivey successive CV curves recorded at 100 mV s^{-1} in the oxidation region between 0.5 V and 1.2 V* vs. *Ag/AgCl, using ITO as working electrode in acetonitrile (+ 0.1 M $LiClO_4$) containing 1 mM of compound 5 (A), and 25 CV scans recorded at the same scan rate in the oxidation region between -0.3 V and 1.5 V vs Ag/AgCl using ITO and acetonitrile (+ 0.1 M $LiClO_4$) solution containing 1 mM of compound 6 (B).

However, as it was concluded before that electrografting does not affect the electropolymerization, in this case as well it doesn't help since none of the indicators previously seen for both iron and ruthenium compounds is found here as in the increase in the redox peak with cycling, the oxidation of hydrazo to azo groups, the appearance of a new reduction peak in the cathodic region, and absence of any deposit on the working electrode after washing as shown in **Figure 73**. In all four complexes, the first oxidative feature at ~0.8–1.0 V vs Ag/AgCl corresponds to oxidation of the pendant para-aminophenyl groups, consistent with established aniline electrochemistry. This process generates ligand-centered radical cations, but for Co(II) and Zn(II) complexes no progressive current growth is seen upon repeated cycling, and the electrode remains clean after rinsing — indicating that the oxidation does not lead to surface-confined polymer films. In terpyridine systems, Fe(II) and Ru(II) (low-spin d^6) generally support **ligand-centered** redox while maintaining their coordination sphere under oxidative cycling, enabling the radical intermediates to couple into hydrazo/azo linkages and remain anchored to the electrode surface. In contrast,

Co(II) (d^7) haves the oxidation of the metal occur before the oxidation of the amino groups which is different from the iron and ruthenium complexes that have their redox peak closer, so this might be a reason for this issue. Zn(II) (d^{10}) is redox-inactive and quite labile which could be an issue as well. Consequently, although the amine groups are oxidized in all cases, only the Fe(II) and Ru(II) complexes provide the combination of radical persistence, coupling efficiency, and coordination stability required for robust electropolymer film growth.

3.3. Conclusions and Perspectives

Controlled electropolymerization of the Fe(II) bis(terpyridine) complex bearing para-substituted terminal aniline groups, $[Fe(tpy\text{-}Ph\text{-}NH_2)_2]^{2+}$, was successfully achieved via multisweep cyclic voltammetry in aprotic perchlorate media, yielding uniform poly$[Fe(tpy\text{-}Ph\text{-}NH_2)_2]^{2+}$ films on ITO and carbon electrodes. The polymerization proceeds through oxidative coupling of the aminophenyl substituents, initially forming hydrazo linkages (–NH–NH–) that are subsequently oxidized to azo linkages (–N=N–), as confirmed by electrochemical signatures, spectroscopic analysis (Raman, FTIR, XPS), and UV-Vis evidence of new π–π* and n–π* azo transitions. This N–N coupling pathway is favored because the para position of the phenyl ring is blocked by the terpyridine unit, preventing classical aniline C–C or C–N polymerization routes. The Fe^{3+}/Fe^{2+} redox couple remains intact in the resulting metallopolymer, enabling mixed diffusion/adsorption charge transport and stable, reversible electrochromism with high coloration efficiency (up to 2571 $cm^2 \cdot C^{-1}$) and rapid switching times (<1 s for coloration). Film thickness and electrochemical performance are tunable via the number of CV scans, with $LiClO_4$ supporting electrolyte providing the most efficient growth; proton-rich ($HClO_4$) or strongly coordinating (Na_2SO_4) electrolytes inhibit polymerization by destabilizing radical intermediates or coordinating to the metal center.

Replacing Fe(II) with Ru(II) in $[Ru(tpy\text{-}Ph\text{-}NH_2)_2]^{2+}$, which also features a low-spin d^6 configuration, results in similarly efficient electropolymerization under the same conditions, but with notable differences in kinetics and film properties. The Ru(II) complex exhibits higher initial peak currents and faster growth of the electroactive film even at a small number of scans, indicating more rapid nucleation and chain propagation. This can be attributed to the more stabilized 4d metal-centered orbitals in Ru(II), which raise the ligand-to-metal charge-transfer energy and help maintain the integrity of the terpyridine coordination during ligand-centered oxidation. As with Fe(II), the polymerization proceeds via hydrazo-to-azo conversion, producing electroactive azo-

linked metallopolymer films. The resulting Ru-based films retain the reversible Ru^{3+}/Ru^{2+} redox activity, display enhanced current responses at lower scan numbers compared to Fe-based films, and are expected to offer improved long-term stability due to the inherently greater oxidative robustness of Ru(II) polypyridyl complexes. These differences suggest that Ru-based systems may be particularly advantageous for applications requiring thicker films or faster electrochromic switching without extensive cycling.

In contrast, analogous Co(II) (d^7) and Zn(II) (d^{10}) complexes undergo amine oxidation but fail to produce adherent polymer films. This is attributed to a lack of compatibility between the metal center and the ligand-radical coupling pathway. Overall, this work elucidates the electropolymerization mechanism of para-aminophenyl bis(terpyridine) metal complexes, confirms the azo-linked structure of the resulting Fe and Ru metallopolymers, and highlights the critical interplay of metal redox properties, ligand substitution pattern, and electrolyte composition in controlling film growth. These findings establish a design framework for tailoring electrochromic metallopolymers by the specific selection of metal centers and ligand functionalization, opening pathways to tunable optical responses across the visible and near-IR, and potentially photoswitchable systems exploiting azo-group photoisomerization.

Chapter 4: Confinement Effects of Vertically Oriented Mesoporous Silica Films on the Optical and Electrochemical Properties of Conducting Polymer Films

4. Chapter 4: Confinement Effects of Vertically Oriented Mesoporous Silica Films on the Optical and Electrochemical Properties of Conducting Polymer Films

4.1. Introduction

The fabrication and characterization of porous materials with precisely controlled nano-architectures has gained significant scientific attention in recent years. This growing interest is driven by their unique physical properties, enhanced chemical reactivity, and their application in various optical, electronic, magnetic, sensing, and biomedical technologies [277], [278], [279]. Nanomaterials are classified based on their dimension and shape, such as zero-, one-, two-, and three-dimensional nanostructured materials [280].

Some one-dimensional nanomaterials such as nanowires, nanotubes, and nanorods are of growing interest due to their mechanical flexibility and high aspect ratio which provide unique optical and electronic properties [281]. These 1D materials can include both hard and soft templating approaches, where the hard templates are predefined cylindrical or channel-like structures, which guide the formation of nanowires and nanotubes. And the soft templates involve self-assembled surfactant micelles, vesicles, or block copolymers that guide polymerization or material deposition into 1D shapes [282], [283]. Among these solid-state nanoporous films, mesoporous silica films have garnered significant interest due to their easy fabrication method and the presence of silanol-rich surface groups which makes these films compatible with chemical functionalization techniques [284]. With the different techniques found in literature for the preparation of these films, the interest lies in having a thin film configuration for electrochemical applications regarding rapid mass transport, surface reactivity, and the integration in electronic devices, which is achievable through depositing these thin films on a conductive solid support [285]. In such systems, the thin film architecture minimizes diffusion limitations by enabling rapid mass transport of ions and molecules through the accessible pores that is crucial for having fast electrochemical responses. For example, thiol-functionalized mesoporous silica films deposited on gold electrodes have been used for sensitive detection of Pb(II), where the short diffusion paths and direct contact with the electrode surface enhanced the voltammetric signal [286]. The inherent silanol-rich surface of these films further allows chemical functionalization with redox-active species,

nanoparticles, or enzymes, expanding their versatility across electrochemical sensors and catalytic applications.

A pretty well known method is the evaporation induced self-assembly (EISA) which is one of the earliest methods discovered to form mesoporous silica thin films [287]. However, one major drawback when using this method is the formation of parallel pore orientation to the substrate which limits the surface accessibility and hinders mass transport to the electrode surface [288]. To overcome this issue, a well-established method discovered in 2007 which is the electrochemically assisted self-assembly method was used to form mesoporous silica films with pores oriented perpendicular to the electrode surface [289]. This vertical alignment overcomes the accessibility and mass transport limitations inherent to the parallel films.

The principle of these nano-films plays an important role when coupled with conducting materials, as one-dimensional polymer films in the form of nanowires have numerous applications in various fields, including supercapacitors, electrochromic devices, and chemical sensors, due to their particular advantages over their bulk counterparts [290].Various strategies have been developed for the fabrication of one-dimensional (1D) polymer nanostructures, including electrospinning [291], chemical vapor deposition (CVD) [292], and electrodeposition [293]. These techniques help in controlling the morphology, alignment, and scalability depending on the targeted application. One pretty well-known method to form these polymer films is to use commercially available hard templates such as anodic aluminum oxide and then electrodeposit specific compounds within this template to obtain eventually after removing the template, 1D polymer nanowires such as PANI nanowires.

However, the main problem when using this kind of hard template is that the lowest diameter of the PANI nanowires that can be reached is around 10 nm [294] compared to that obtained using template free methods which gives a diameter of around 50-70 nm [295]. The diameter can be further reduced by synthesizing these nanowires in 3nm nanochannels of hexagonal mesoporous silica particles [296]. Furthermore, as mentioned above the interest lies in depositing the thin conductive films on a conductive solid support which is achievable by utilizing the vertically oriented mesoporous silica films as host films for the electropolymerization of conducting material to form thin films inside. This idea has already been reported in literature using polythiophene,

polypyrrole, and polyaniline; however, some issues were faced in these cases most notably the large diameter of the polymer wires of around 5-6 nm [297].

Recently, polyaniline wires were successfully incorporated inside vertically oriented mesoporous silica films that were deposited on ITO using EASA, where the pore size ranged between 2 and 3 nm, depending on the surfactant used [298]. Furthermore, the polymer chain was produced using electropolymerization of aniline (in an acidic solution) which is shown to be successful however some issues were faced with respect to the stability of the polymer on the electrode surface in the case of removing the template to obtain the 1D polymer films, since there is no covalent link formed. So in order to resolve that issue, a preceding step was done which is the electrografting of aminophenyl diazonium cations which generates a covalent link between the electrode surface and polymer wires. These PANI nanowires exhibit very interesting electrochromic properties due to the color switching between the oxidized and reduced states.

Inspired by the above, in the frame of this PhD work, we have adapted this approach to the generation of conducting metallopolymer films based on transition metal coordination complexes that can form metallopolymers through electropolymerization on ITO electrodes inside vertically oriented mesoporous silica films with different pore sizes (2, 3, 4.3 nm) and then characterized their optical and electrochemical properties in comparison to that obtained on bare ITO. Furthermore, some spectroelectrochemical experiments were performed in the same nature as on bare electrode to compare the bleached and colored states in response to applied voltage. This inspiration to specifically generate metallopolymers inside the films goes back to previous work performed that detailed the integration of bis (terpyridine) iron (II) complexes in the oriented mesoporous films that incorporated azide groups therefore through click chemistry to obtain covalent immobilization of monomer units inside the films [299].

The vertically oriented mesoporous silica films were prepared by EASA on ITO using a surfactant as a structure directing compound, where the surfactant was changed according to the desired pore size (cetyl- or octadecyl- or icosyl- trimethylammonium bromide), and then the electropolymerization of the coordination complex such as $[Fe(tpy\text{-}Ph\text{-}NH2)_2][PF_6]_2$ and $[Ru(tpy\text{-}Ph\text{-}NH2)_2][PF_6]_2$ is performed in the different mesochannels. The electropolymerization was monitered and performed using cyclic voltammetry and chronoamperometry, then the electrochemical characterization of the obtained modified films was done using cyclic

voltammetry. Furthermore, we study the confinement effect of these films on the optical properties of the metallopolymers formed. Finally, the spectroelectrochemical experiments for the wires inside the films were performed in the same way as for the wires obtained without films to study the effect on not only the absorbance but also the bleaching time and coloring time and the required potential to observe the change.

4.2. Results and Discussion

4.2.1. Charge selectivity for the transport of redox probes through the vertically oriented mesoporous silica films

Figure 74 shows the typical response of ITO electrodes covered with the vertically oriented mesoporous silica thin films immersed in a solution containing different redox probes before and after removing the surfactant and compared to the electrochemical response observed on bare ITO, where these charged probes demonstrate pore accessibility, ion-permselectivity, and uniformity of the vertically oriented mesoporous silica films. These films were prepared using the C_{20}TAB surfactant [300] to obtain these films with a pore size of around 4.3 nm and it is also important to mention that the ratio between TEOS and the surfactant was 0.32 (this ratio can vary between 0.16-0.96, keeping the mesostructured of the films) [301], [302]. The redox probes used in this experiment are hexaammineruthenium(III) chloride ($[Ru(NH_3)_6]Cl_3$), potassium hexacyanoferrate(II) trihydrate ($K_4[Fe(CN)_6]\cdot 3H_2O$), and 1,1′-ferrocenedimethanol ($Fc(MeOH)_2$). Three solutions were prepared which consisted of 0.1 M of sodium nitrate as supporting electrolyte and 0.5 mM of each redox probe in H_2O. The CV curves were recorded at 100 mV/s using suitable potential ranges for each redox probe. A first observation is the lack of a signal response for the two redox probes ($[Ru(NH_3)_6]Cl_3$) and ($K_4[Fe(CN)_6]\cdot 3H_2O$) (as shown for curve b in figure **Figure 74**B and C) before removing the surfactant compared to the clear reversible signal when using non-modified electrodes which suggests that we obtained films that cover the electrode surface uniformly without any cracks so neither the cations or anions would cross the surfactant-template layer. However, there is one redox probe which is the ($Fc(MeOH)_2$) that shows a good measurable signal in its neutral state, since this species is partially solubilized in the crystalline phase of the surfactant, and therefore it can diffuse through the nanopores before removing the surfactant and be oxidized. These results are in agreement to what was previously shown in the literature [300].

After removing the surfactant, the films become permeable to the solution-phase redox probes but show some differences depending on their charge. In the case of $Ru(NH_3)^{3+}_6$ and ($Fc(MeOH)_2$) species, they can easily reach the ITO electrode surface where we can see a rise of the peak current to the same order of magnitude as on the bare ITO, or even larger due to cations accumulation, where ferrocene is neutral so the accumulation is due to their oxidation to ferrocinium. On the contrary, in the case of $Fe(CN)_6^{4-}$ species the response is directly hampered and this response also can be even worsened if the concentration of the electrolyte is decreased. This perselectivity is already well presented in the literature where also mesoporous thin films with smaller pore size also present the same behavior. The main reason for this observation is the negatively charged silica over a wide range of pH range over 2 where the pH_{iso}=2, in effect this leads to the decreased currents recorded when using negatively charged probes.

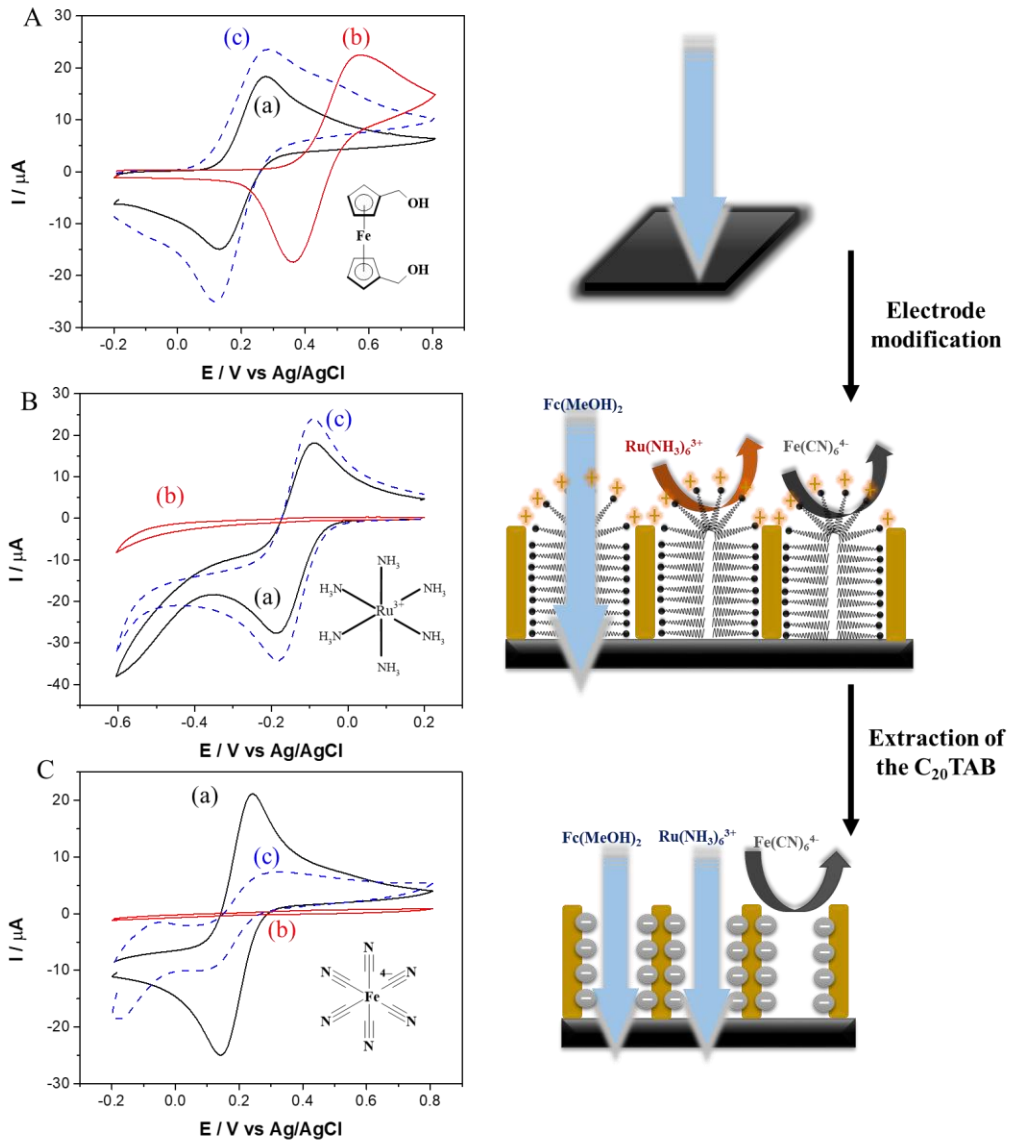

Figure 74: Cyclic Voltammograms recorded in 0.1 mM solutions of (A) $(Fc(MeOH)_2)$, (B) $Ru(NH_3)^{3+}_6$, (C) $Fe(CN)_6^{4-}$, using (a) Bare ITO and (b-c) ITO electrodes modified with vertically oriented mesoporous silica thin films (b) before and (c) after surfactant removal; the supporting electrolyte aqueous solution was 0.1 M $NaNO_3$ at potential scan rate 100 mV/s.

4.2.2. Structural Characterization of the Ordered Mesoporous Silica Films

The silica films deposited on ITO were characterized using IR spectroscopy before and after surfactant removal to detect any changes in the stretching bands that is shown in **Figure 75**. In the normal state (before removal) (curve 1), the film exhibits several vibrational features. These

include intense C–H stretching bands (asymmetric and symmetric methylene stretches near 2920 and 2850 cm^{-1}) that is characteristic of the long alkyl chains of the surfactant C_{20}TAB. The dominance of these hydrocarbon signatures confirms that the mesoporous channels are filled with surfactant micelles, which is consistent with the schematic representation showing the pore occupation. After the extraction treatment (curve 2), the disappearance of the surfactant-related C–H stretching bands confirms the efficient removal of C_{20}TAB from the silica framework. The remaining spectrum is dominated by the typical vibrational features of silica: the intense Si–O–Si asymmetric stretching vibration around 1080–1100 cm and the broad band centered around 3400 cm^{-1} attributed to surface silanol (Si–OH) groups. The enhanced intensity of the Si–OH band indicates that template removal exposes the internal silica surface, increasing the number of accessible hydroxyl groups available for further functionalization. Therefore, the FTIR analysis confirms the transition from a surfactant-filled mesostructure to an open, accessible mesoporous silica network with vertically aligned channels. This characterization demonstrates successful template extraction, which is a prerequisite for achieving selective transport, electrochemical accessibility, and functionalization of the mesoporous silica films.

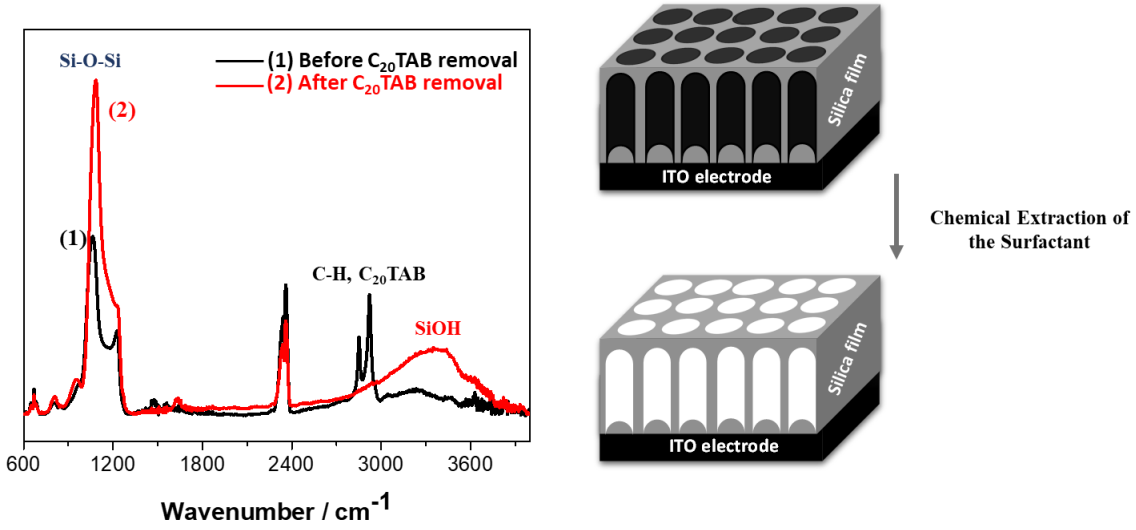

Figure 75: Infrared spectroscopy characterization of vertically aligned mesoporous silica films on ITO before (1) and after (2) surfactant extraction.

As mentioned above, the diameter of the pores of these materials depends on the length of the longest alkyl chain of the structural agent employed for the synthesis. For example, when CTAB

(C16) is used to generate these films the pore diameter was 2 nm and replacing the surfactant with ODAB (C18) shows an increase in the pore diameter to around 3 nm and finally replacing the surfactant with C_{20}TAB also shows an increase to around 4.3 nm. The orientation of the mesopores in silica thin films formed on ITO is characterized by Grazing Incidence Small Angle X-ray Scattering (GISAXS) (**Figure 76**). This film analysis shows a high level of mesostructural order over the silica membrane area, with the 2D GISAXS patterns exhibiting scattering spots in the equatorial plane, so this indicates that we obtain unique vertical orientation of these nanochannels onto the ITO surface which were generated using EASA.

The 1D scattering profile exhibits well-defined Bragg peaks, which are assigned to the (10), (11), and (20) reflections of the hexagonal mesotrucutre. The primary scattering vector, corresponding to the (10) reflection was found at (q_{10} = 1.46 nm^{-1}) so the calculated d-spacing yields a value of 4.3 nm. Then we calculate the center-to-center pore distance for the hexagonal lattice which was around 4.97 nm. This large mesostructural dimension is consistent with the use of C_{20}TAB as the structure-directing agent, as the longer alkyl chain promotes the formation of larger micellar templates compared to the other surfactants like C16 and C18 which have shorter chains. These values are scalable when comparing to the results obtained in literature when using other surfactants to form the mesoporous films such as C_{16}TAB and C_{18}TAB whereas the surfactant chain length increases the primary scattering vector decreases, the d-spacing increases, and center-to-center pore distance increases.

Table 3: Structural parameters derived from GISAXS for mesoporous silica films templated by different surfactants.

Parameter	**C_{16}TAB**	**C_{18}TAB**	**C_{20}TAB**
Surfactant chain length	C16	C18	**C20**
q_{max} (nm^{-1})	1.7 ± 0.02	1.55 ± 0.01	**1.46**
d-spacing, d_{10} (nm)	3.69	4.05	**4.30**
Pore-to-Pore (nm)	4.26	4.68	**4.97**

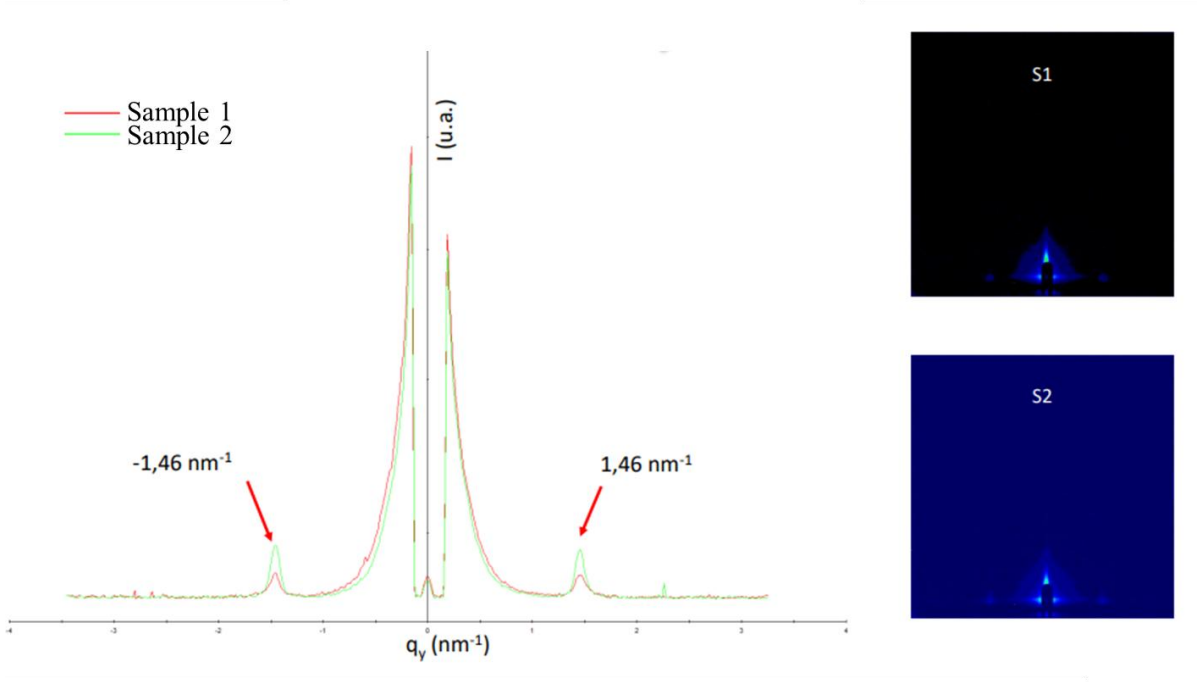

Figure 76: GISAX patterns at the incidence angle of 0.25° and corresponding fitting curves for two ITO electrodes covered with the oriented mesoporous silica films generated with C_{20}TAB.

4.2.3. Electrochemical Polymerization inside Mesoporous Silica Films with Different Pore Sizes

The main goal to be achieved in this case is to form arrays of metallopolymer nanowires on ITO electrodes through templating approaches. The first step was to form mesoporous silica films that consist of vertically aligned hexagonally-packed nanochannels which was done using the EASA method. This involves the application of a cathodic potential that induces the self-assembly of cationic surfactants onto the electrode surface and the subsequent gelification of the sol solution upon electrochemically triggered pH increase, which leads to the growth of the silica mesopore channels network that are oriented perpendicularly to the underlying support. Then after removing the surfactant, the following step is to prepare the monomer solution for electropolymerization that is either an acidic solution having perchloric acid as the supporting electrolyte, or an organic solution having lithium perchlorate as the supporting electrolyte. Then finally after polymerization, an attempt to remove the silica using a NaOH solution is performed to obtain the oriented nanoarrays.

4.2.3.1. Electropolymerization using HClO4

Three different samples are prepared, where we have 3 different ITO electrodes that have mesoporous silica films with different pore sizes that are 2, 3, and 4.3 nm to study the effect of the pore size on the electropolymerization process after removing the surfactant. We perform a multisweep CV using the deposited vertically oriented silica films on ITO as the working electrodes, and prepare a solution consisting of 1 mM of compound 2 in an acetonitrile/water mixture solution with 0.1 M $HClO_4$ using a scan rate of 100 mV/s in a potential range between 0 and 1.5 V vs Ag/AgCl.

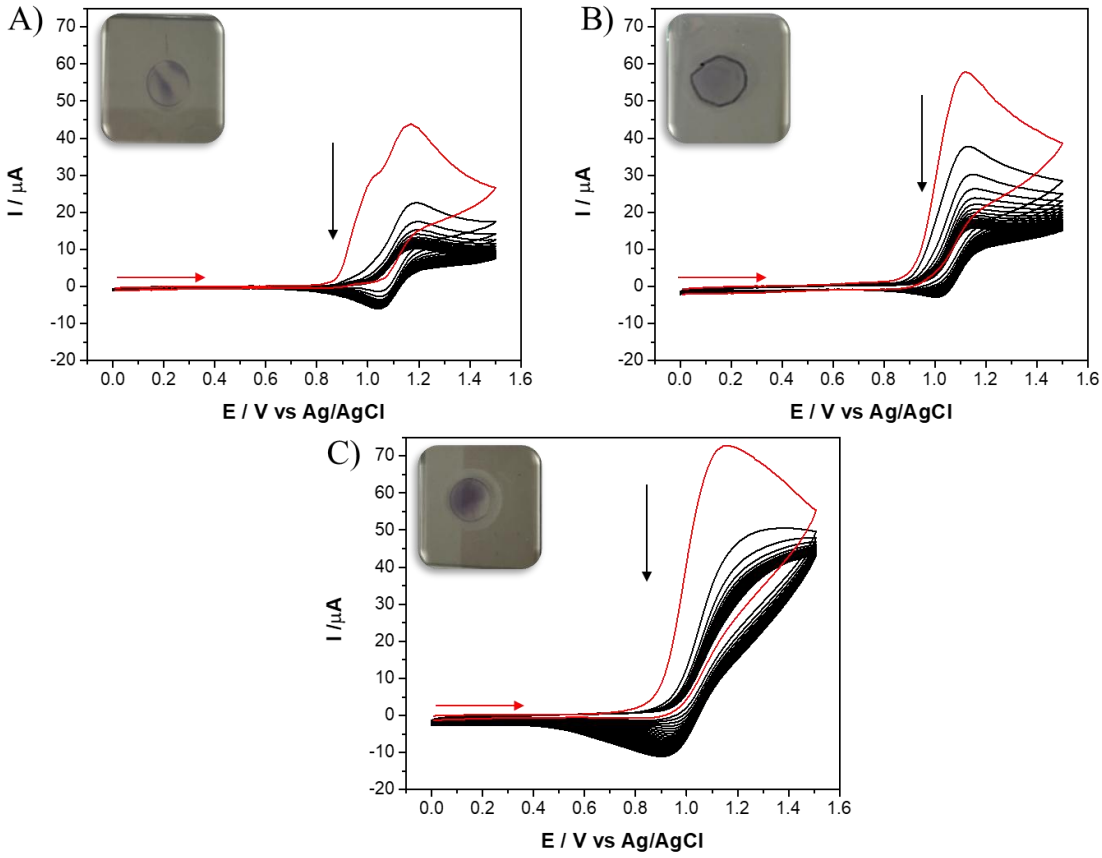

Figure 77: Effect of increasing the pore size on the electrochemical response. The CV scans were recorded at 100 mV/s using 20 scans and a solution made up of ACN/H_2O with 0.1 M $HClO_4$ and 1 mM of compound 2. The pore size of the films varied from: A) 2 nm, B) 3 nm, and C) 4.3 nm.

According to what was deduced from the previous chapter, it was shown that when perchloric acid was used as a supporting electrolyte it protonates the amino groups in the metal-ligand complex

which hinders the film formation and efficient electron transfer similar to the case that was already proved when using bare ITO electrodes. Well in this case (**Figure 77**) a new issue is also faced alongside the previous issue which is the charge of the silica walls. As we know, when the solution used has a pH lower than 2, this causes the silanol groups to become protonated and this is the case here since 0.1 M of $HClO_4$ is used. Furthermore, the monomer used to form the metallopolymer is Fe^{2+}-based complex so the charged walls can repel this complex and hinder the reaction at the electrode surface. In case A when the pore size was 2 nm during the first peak, we can observe the oxidation peak of the amino group at around 1 V vs Ag/AgCl which is shifted anodically compared to on bare ITO which is normal giving that it is harder to oxidize inside insulating films. Then a redox signal related to the Fe^{3+}/Fe^{2+} couple is recorded at 1.1 V as well shifted compared to the bare electrode. Then as the cycling is performed the anodic peak current decreases from 44 µA to 10 µA indicating that the polymerization is not successful when compared to bare electrode since even in that case it was not ideal, here it is even worse. The increase in the pore size however, showed an increase in the peak current observed during the first scan to reach 57 and 71 µA for the 3 and 4.3 nm films respectively which is related to the increase in the pore diameter that can show a less severe repulsion but overall the electropolymerization is not successful overall which is in agreement to what was shown in the previous chapter.

4.2.3.2. Electropolymerization using LiClO4

The electropolymerization is performed in ACN with 1 mM of 2 and 0.1 M of $LiClO_4$, using a potential range between 0 and 1.6 V vs Ag/AgCl at 100 mV/s (**Figure 78**). In the case of the 2 nm films, During the first scan the oxidation peak of the redox couple Fe^{3+}/Fe^{2+} took place at around 1.13 V vs Ag/AgCl and a peak current of around 150 µA which is higher than that in the case of perchloric acid which can indicate that the acidity of the solution previously played a role in the electrostatic hindrance faced. However, the reversibility is not good in this case and the peak current decreases with successive oxidation scans. After 10 scans, the sample was removed and a faint purple is seen unlike the case on bare ITO which a more intense deposit. Then when polymerizing inside mesoporous silica films with a pore size of 3 nm, a similar electrochemical response to that in the 2 nm films was visible where the anodic peak current was decreasing and the reversibility of the redox couple was poor.

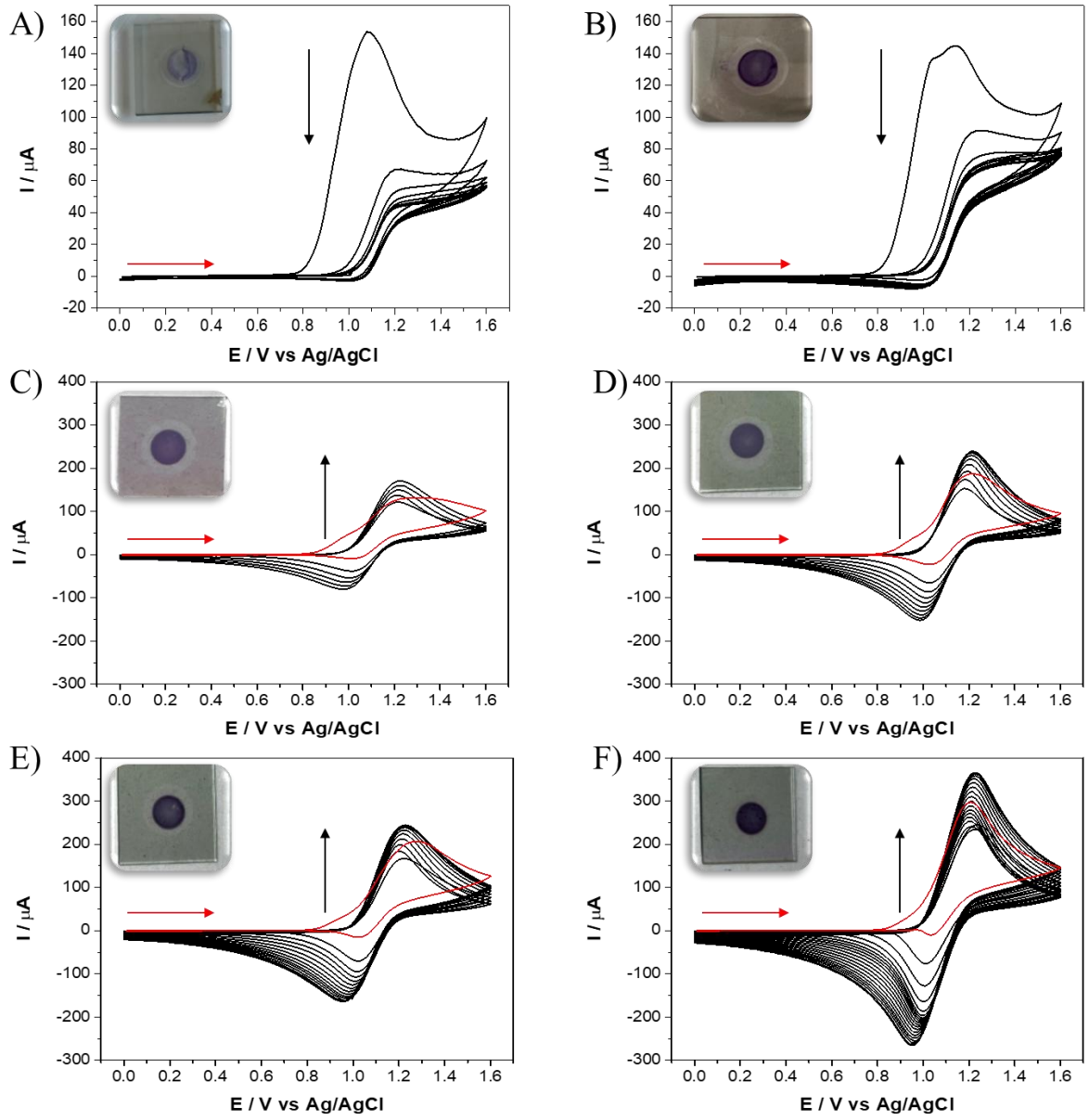

Figure 78: Effect of increasing the pore size on the electrochemical response. A solution is prepared consisting of ACN with 1 mM of 2 and 0.1 M of $LiClO_4$ at scan rate 100 mV/s using different number of cycles. 10 cycles were performed inside: A) 2 nm pore size silica films and B) 3 nm. Then we electropolymerize inside 4.3 nm mesoporous films using: C) 6 scans, D) 10 scans, E) 15 scans and F) 20 scans.

However, when we increase the pore size to 4.3 nm, the electropolymerization is shown to be successful since in the 6 scans voltammogram after the third scan the anodic and cathodic peak

current start to increase to reach 170 µA and -80 µA respectively at the end. This indicates that the electropolymerization is working and the metallopolymer is formed inside the insulating films. As the number of scans increases to the anodic peak current increased to 239, 244, and 365 µA respectively and the cathodic current increases as well to -152, -163, and -263 µA. This behavior is the closest out of the three pore sizes to that seen on bare ITO so we can deduce that the 4.3 nm mesoporous silica films are the best in this case to form the polymer films. But when comparing the kinetics of polymerization, clearly in the case of non-modified electrodes the peak current obtained is higher than that in this case and the intensity of the deposition is also different which is justifiable as we are polymerizing inside in insulating pores, also the shape of the peaks are a bit different where in this case they are a bit wider (the oxidation peak is shifted anodically and the reduction peak is shifted cathodically) and not as sharp which can justify why the irreversible oxidation peaks for the amino groups are not always clearly visible. However, the electrochemical response is in agreement with the deposited polymer inside the films as the color intensifies as the number of scans applied increases that is hindsight proves the increase in the polymer chain length.

With respect to the process of forming the polymer, The electropolymerization of $[Fe(tpy\text{-}Ph\text{-}NH_2)_2]^{2+}$ is initiated by anodic oxidation of the NH_2 terminal groups, resulting in the formation of radical cations. This mechanism closely resembles the electrochemical behavior observed with aniline and other aromatic amines, where radical cation intermediates promote C–N and C–C coupling reactions, ultimately leading to the formation of conductive polymer networks. In such systems, charge delocalization extends beyond the nitrogen center to include the ortho and para positions of the aromatic ring, thereby facilitating efficient polymer growth. For instance, the electropolymerization of a complex similar to **2** but with the amino moieties in the meta position on the phenyl terminal groups proceeded by a reaction mechanism similar to that of aniline with the formation of C–N bonds. In this case (complex **2** with the amino moieties in the para position), once the radical cation is electrochemically generated, the para position is sterically or electronically blocked. This blockage prevents the usual coupling pathways and the electropolymerization occurs in another way, involving an alternative coupling reaction based on N–N or N=N bonds formation as the case on bare electrode. After washing the samples, the polymer remains intact which indicates that it is strongly adsorbed on the electrode surface.

4.2.4. Electrochemical Characterization of the Obtained Fe Metallopolymers inside Silica Films

The modified electrodes with metallopolymers inside mesoporous films with different pore size are electrochemically characterized using monomer free electrolyte solution to study the stability of polymer films on ITO upon multisweep CV and to quantify the amount of material deposited as a function of changing the number of scans used during electropolymerization (**Figure 79**). The solution prepared contains only 0.1 M $HClO_4$ as electrolyte in acetonitrile. The potential window studied ranges from 0.5 to 1.6 V vs Ag/AgCl at a scan rate of 100 mV/s using 20 scans.

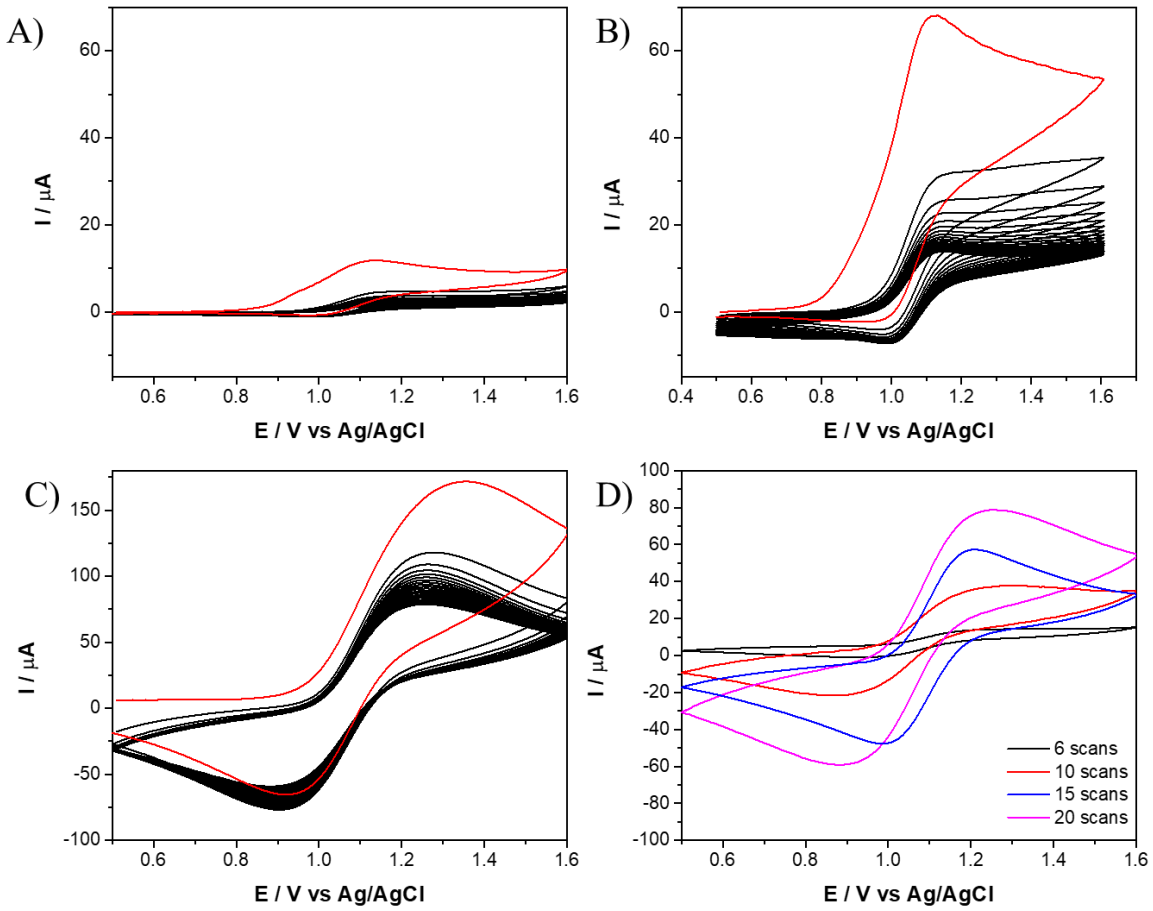

Figure 79: Multisweep CV curves recorded at a potential scan rate of 100 mV s^{-1} in monomer-free acetonitrile solution containing 0.1 M $HClO_4$ as supporting electrolyte, using poly[$Fe(tpy\text{-}Ph\text{-}NH_2)_2$]$^{2+}$ films electropolymerized (20 scans) either inside: A) 2 nm films , B) 3nm films, and C) 4.3 nm films. D) represents the overlay of the 20th cycle performed for samples polymerized with 6, 10, 15, and 20 scans inside the 4.3 nm films.

When characterizing the sample with pore size 2 nm, the electrochemical response was not good which is expected as the electropolymerization was not successful inside these pores and the measured anodic peak current was less than 10 µA. For the second sample with silica films with a pore size of 3nm, the electrochemical signal was better where during the first scan the anodic current of the redox couple reached around 65 µA and then after consecutive oxidation scans over 65 % of the current value is lost (non-strongly adsorbed molecules were removed during characterization). The electrochemical response again was shown to be clear and quantitative inside 4.3 nm films since when overlaying the last scan (20th) the peak was more defined with a higher peak current as the number of scans increased. When compared to bare ITO (see previous chapter), for samples prepared performing the same number of scans, 2 major differences are present:

1) The peak current where the peak current measured for polymers deposited on bare ITO is five times higher (for the higher nb of scans) compared to the metallopolymer formed inside the films. This could be due to ion-transport resistance of the counter-anion.
2) The peak to peak separation which increases as the number of scans increased, this results from a combination of resistance and slower ion transport in confined pores and the higher scan rate used along with the increased deposited material.

Also, usually after forming these wires, the template is removed to obtain the desired 1D material, where in this case the silica membrane can be removed using an NaOH solution that is shown in literature to be successful. However, in this case, when dipping my films in a 1 M NaOH solution after 10 minutes the polymer deposited is damaged in the sense of losing a big part of the deposit. This test was done on bare ITO with a metallopolymer deposit and another ITO with 4.3 nm films filled with the metallopolymer using the same conditions and it was evident that in both cases the film was damaged, so the issue rises from this iron-based polymer.

4.2.5. Optical Characterization of Fe-based Polymers using UV-VIS

The optical properties of the [Fe(tpy-Ph-NH_2)$_2$]based electropolymerized films inside the 4.3 nm mesoporous silica films that were prepared using CH_3CN containing 0.1 M $LiClO_4$ were investigated by UV-Vis spectroscopy and compared to those films polymerized on bare ITO (**Figure 80**). First the MLCT band is found around 579 nm similar to that found in the previous case that consistent with enhanced π-conjugation upon polymer growth. Then two bands centered

at 326 and 378 nm are detected and can be attributed to the ligand-centered (LC) π–π* transitions and π–π* transitions of the azo (–N=N–) chromophore. A broader and less intense band spanning the 440–520 nm region, is assigned to n–π* transitions of the azo functionality. These bands for the metallopolymers inside and outside silica films are very close in terms of the wavelength but differ in their absorbance values. With respect to increasing the number of scans, the absorbance of the MLCT increases indicating increase in the chain length of the polymer that is backed by the darker purple deposition. For example, the 6 and 10 scans have a similar MLCT absorbance value then when comparing to 15 and 20 the MLCT absorbance value is slightly lower inside the films versus outside which is expected since there is less space for the polymer.

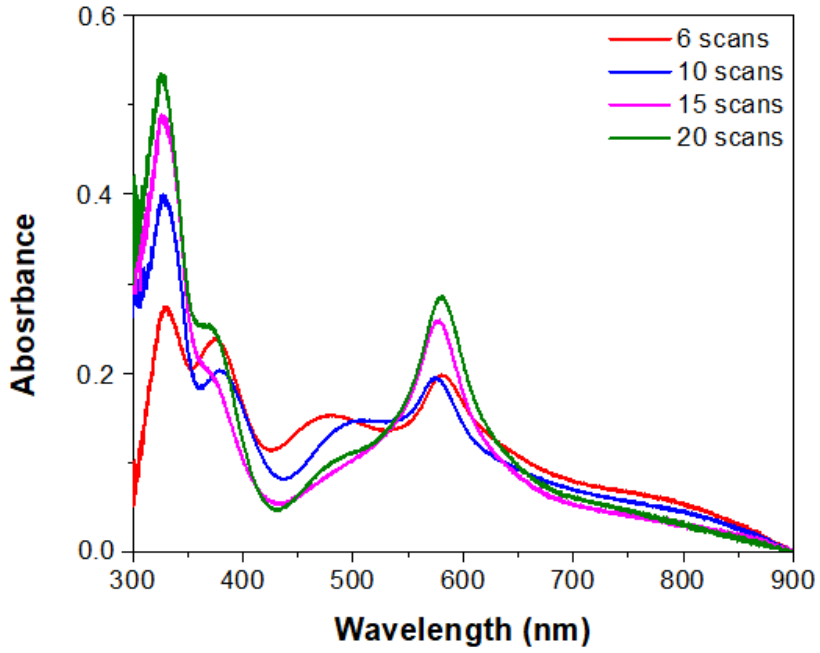

Figure 80: UV–Vis absorption spectra of poly[Fe(tpy-Ph-NH₂)₂]²⁺ film electropolymerized using different numbers of CV scans inside mesoporous silica films.

4.2.6. Electrochromic Response of the Metallopolymer inside Mesoporous Silica Films

Based on a two-electrodes system device comprising the **poly**[Fe(tpy-Ph-NH₂)₂]²⁺ film prepared inside silica films here with a gel-based electrolyte, we investigated its electrochromic properties. The color of the electrochromic films was found to vary as a function of the oxidation state of the central metal, with distinct changes observed both visually and from the UV–VIS spectra upon

switching between the Fe^{3+}/Fe^{2+} redox states. displays the UV-Vis spectra of the **poly**[Fe(tpy-Ph-NH_2)$_2$]$^{2+}$ material in the different redox states.

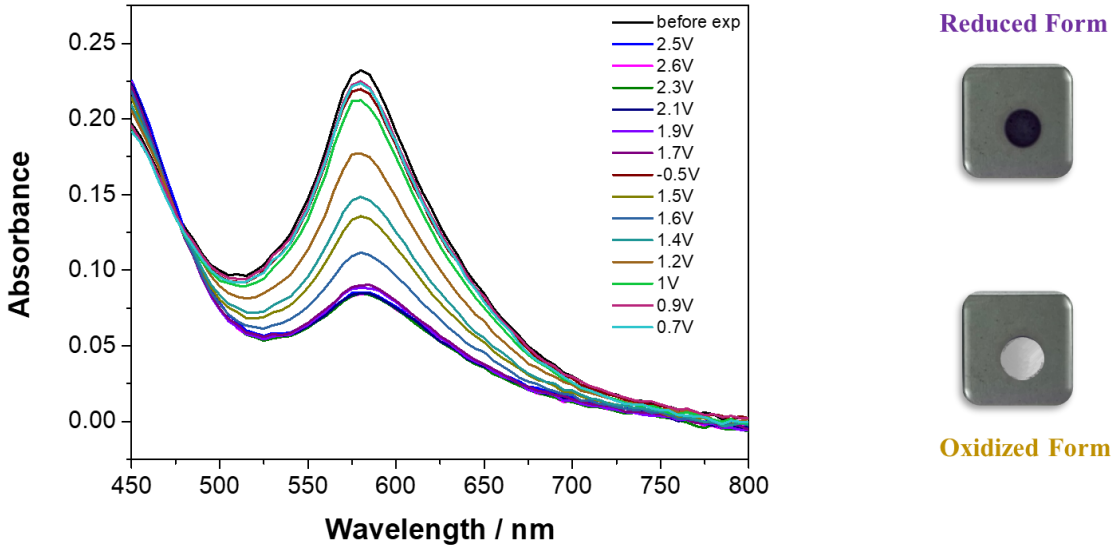

Figure 81: UV–Vis absorption spectra of poly[Fe(tpyPhNH$_2$)$_2$]$^{2+}$ inside mesoporous films in its reduced (brown trace, at –0.5 V) and oxidized (blue trace, at 2.5 V) states. Photographs of the polymer film deposited on an ITO substrate at –0.5 V (Top, colored state) and 2.5 V (Bottom, bleached state).

The polymer film which in its reduced state, exhibited an intense absorption band in the visible region 579 nm corresponding to metal-to-ligand charge transfer (MLCT) transitions characteristic of Fe(II) centers which is identified as the red line and is defined by the dark purple color on the electrode. In contrast, the oxidized form of this film where Fe (II) is oxidized to Fe (III) shows a significantly diminished absorption, translated by the disappearance of the purple color. In this two electrode system, first a reducing potential is applied to ensure that the film is in its reduced state which has a MLCT band with absorbance of 0.24, then when applying a potential of 2.5 V the MLCT band disappears and the absorbance is around 0.08 which indicates the complete oxidation of the entire film which is identified as the bleached state where the color changes from purple to a transparent light yellowish color as shown in **Figure 81**. To prove that the applied potential has an effect on the MLCT band, different potentials between -0.5 and 2.5 V are applied.

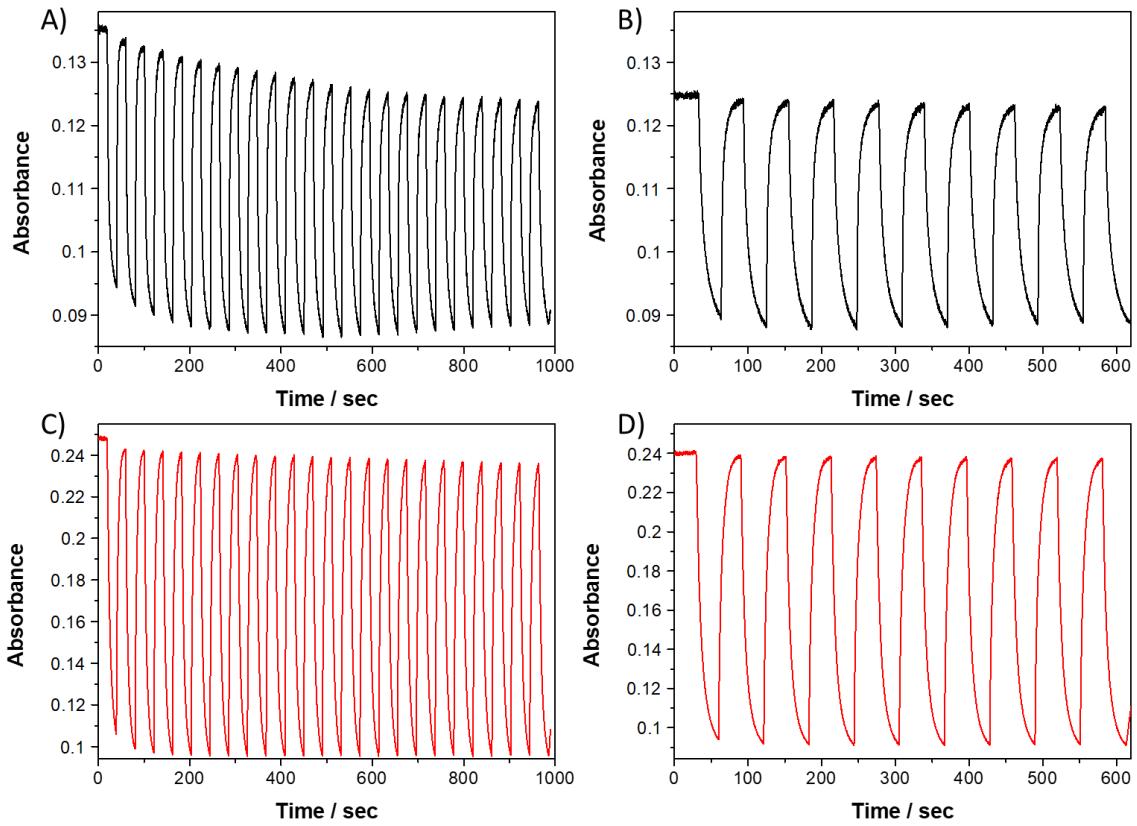

Figure 82: Chronoabsorptometry of the polymeric film over multiple redox cycles monitored at a fixed wavelength of 580 nm, respectively recorded by applying switching times of (A) 20 s and (B) 30 s for polymer formed using 6 scans, (C) 20 s and (D) 30 s for polymer formed using 20 scans inside mesoprous films.

The polymer film exhibited a reversible color change from purple to colorless, as measured at wavelength 580 nm with the working electrode biased successively at -0.5 V (colouration step) and 2.5 V (bleaching step) for 20 or 30 s per step. The electropolymerized film demonstrated good electrochromic performance, attributed to the relatively high molar absorptivity of the metal-to-ligand charge transfer (MLCT) band ($\varepsilon = 2.4 \times 10^4\ M^{-1}\ cm^{-1}$) and a goof coloration efficiency of around 2086 $cm^2.C^{-1}$ which is a bit lower than the ε obtained for the polymer on bare ITO. For the sample having been polymerized using 6 scans present a transmittance change (ΔT%) of around 10% and for the 20 scan sample the change was around 25% which is higher since more polymer is deposited. Some decrease in absorbance changes upon multiple successive redox cycling (loss around 20%) was however observed, especially at short switching times, which are consistent with

the multiweep CV data that were shown in and might be due to some structural changes in the polymer during consecutive doping and dedoping processes (ingress and output of charge compensating ions during switching between the Fe^{2+}/Fe^{3+} redox states), or to incomplete reversibility of the redox switching due to the surrounding films. Indeed, by extending the duration of redox switching, some improvement can be obtained where the absorbance is stabilized and the polymer has enough time to recover. The response time was satisfactorily fast (2.1 s for colouration and 3.2 s for bleaching), as measured at 95% of the maximum absorbance variations observed after application of +2.5 V and -0.5 V, respectively.

4.2.7. Electropolymerization of the Ruthenium Complex (4) Inside The Silica Films

After successfully proving the formation of the iron-based metallopolymer inside the 4.3 nm silica films, the same experiment is perfomed using $[Ru(tpy\text{-}Ph\text{-}NH_2)_2]$ to form a ruthenium-based metallopolymer and compare it to that of iron. In the previous part, it was shown that using perchloric acid as a supporting electrolyte was not the ideal experimental conditions unlike using lithium perchlorate. So the solution is changed in this case to ACN with 1 mM of 4 and 0.1 M of $LiClO_4$, and the experiment done above was tested in with this solution using a potential range between 0 and 1.8 V vs Ag/AgCl at a scan rate of 100 mV/s. Using 2 nm films again is shown (**Figure 83**) to be not useful in terms of forming a uniform metallopolymer, during the first scan the two irreversible oxidation peaks attributed to the amino groups are present at 0.9 and 1.1 V vs Ag/AgCl, and the oxidation of Ru^{2+} to Ru^{3+} takes place at 1.39 V that is shifted cathodically compared to the behavior on bare ITO using this solution and a continues decrease in the peak current is observed while scanning. Finally, after removing the sample it is also concluded that no deposit is formed that is in agreement with the case of iron.

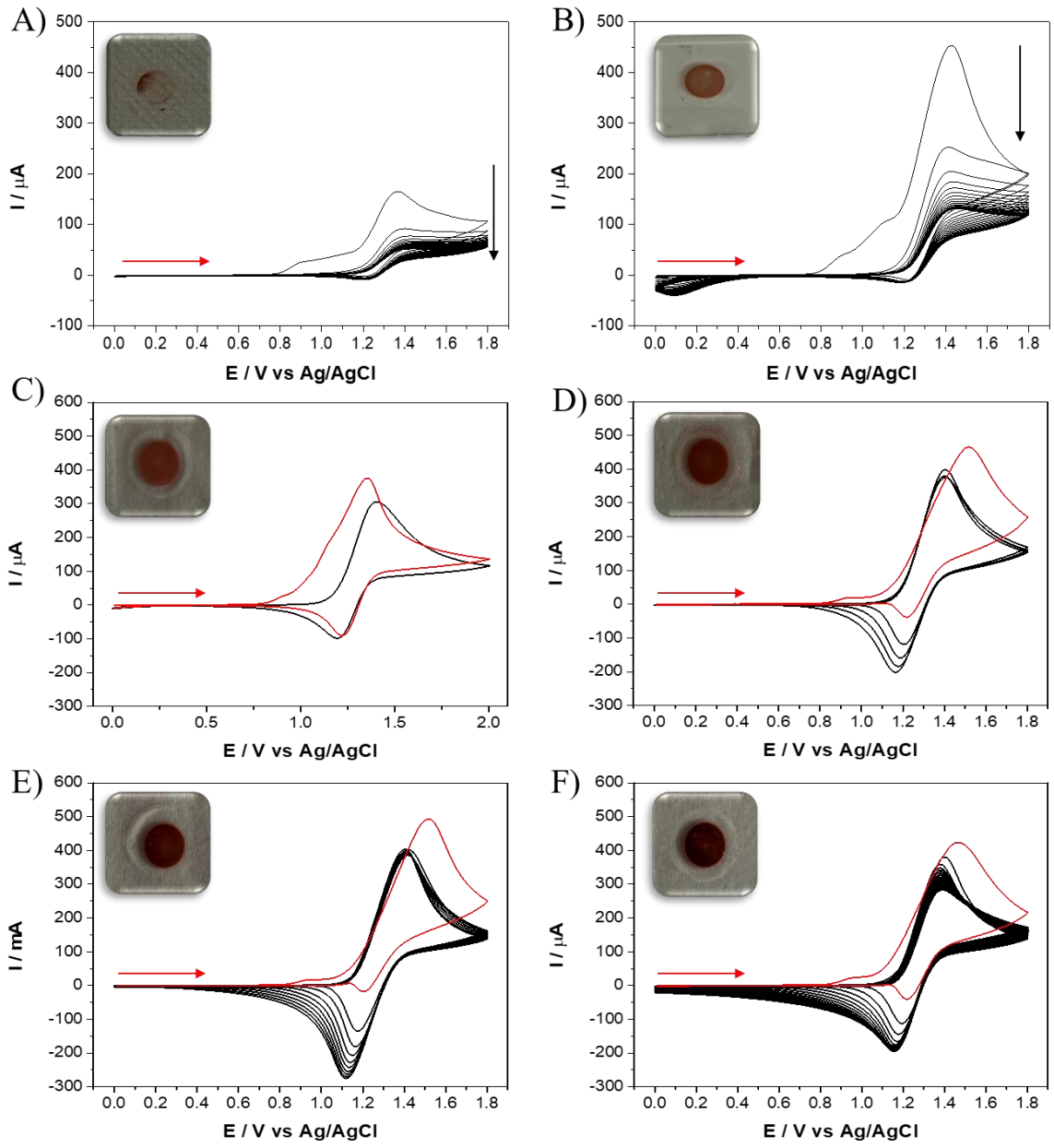

Figure 83: Effect of increasing the pore size on the electrochemical response. A solution is prepared consisting of ACN with 1 mM of 4 and 0.1 M of $LiClO_4$ at scan rate 100 mV/s using different number of cycles. 20 cycles were performed inside: A) 2 nm pore size silica films and B) 3 nm. Then we electropolymerize inside 4.3 nm mesoporous films using: C) 2 scans, D) 5 scans, E) 10 scans and F) 20 scans.

For the 3 nm films, the first difference observed is during the first scan the oxidation peak current attributed to the ruthenium species is higher than that in the 2 nm films which is normal as the pore

size increased which can allow more species to diffuse through the walls and reach the electrode surface. Then during the second scan the peak current decreases with a not very good reversible behavior for the redox couple. However, after removing the sample from the solution a red deposit is formed which is strongly adsorbed on the electrode surface even after washing and ultrasonication. Using the 4.3 nm films showed the best behavior where at least as the number of scans increased the redox signal was more clear and the reduction peak of Ru^{3+} to Ru^{2+} was better defined. As on bare ITO, during the first scan the oxidation peak of the Ru is shifted anodically at around 1.52 V vs Ag/AgCl and reduction peak at 1.21 V which close to the behavior of the precedent. However, after scanning the oxidation peak did not increase while the reduction peak did and the intensity of the deposit increased as a function of the number of scans. These films as well were shown to be stable after washing and ultrasonication where no damages to film were observed.

4.2.8. Electrochemical Characterization of the Obtained Ru Metallopolymers inside Silica Films

The modified electrodes with metallopolymers inside mesoporous films with 4.3 nm pore size are electrochemically characterized using monomer free electrolyte solution to study the stability of polymer films on ITO upon multisweep CV and to quantify the amount of material deposited as a function of changing the number of scans used during electropolymerization. The solution prepared consists of a blank electrolyte solution which is 0.1 M $HClO_4$ in acetonitrile and a potential range between 0 to 2 V vs Ag/AgCl at a scan rate of 100 mV/s using 20 scans. Similar to the case on bare ITO, the peak current decreases upon cycling until it stabilizes after a few scans where any non-strongly adsorbed material or oligomers are removed. For the 20 scans sample, we lose about 45% of the anodic peak current and 35% in the cathodic peak current which is less than the calculated loss on bare ITO which is understandable as in this case less material was deposited for the same number of scans (**Figure 84**).

The electrochemical response was shown to be clear and quantitative inside 4.3 nm films since when overlaying the last scan (20th) the peak was more defined with a higher peak current as the number of scans increased. When compared to bare ITO, for samples with the same scan 2 major differences are present, first the peak current where the peak current measured for polymers deposited on bare ITO is four times higher (for the higher nb of scans) compared to the

metallopolymer formed inside the films, where this could be due to ion-transport resistance for the counter-anion. The other issue which is also addressed in the case of electropolymerization, the peak to peak separation which increases as the number of scans increased, this results from a combination of resistance and slower ion transport in confined pores and the higher scan rate used along with the increased deposited material.

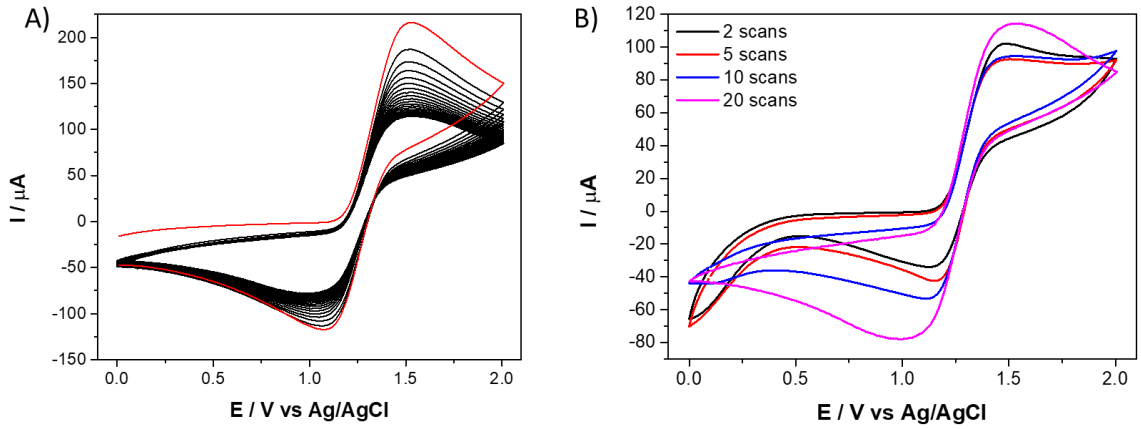

Figure 84: Multisweep CV curves recorded at a potential scan rate of 100 mV s^{-1} in monomer-free acetonitrile solution containing 0.1 M $HClO_4$ as supporting electrolyte, using poly[Ru(tpy-Ph-NH_2)$_2$]$^{2+}$ films electropolymerized (20 scans) inside: A) 2 nm films, B) represents the overlay of the 20th cycle performed for samples polymerized with 2, 5, 10, and 20 scans inside the 4.3 nm films.

4.2.9. Optical Characterization of Ru-based Polymers using UV-VIS

The optical properties of the [Ru(tpy-Ph-NH_2)$_2$] based electropolymerized films inside mesoporous silica films prepared in CH_3CN containing 0.1 M $LiClO_4$ were investigated by UV-Vis spectroscopy and compared to those prepared on bare ITO. It displays intense bands near 320 nm assigned to ligand-centered (LC) π–π* transitions that increases as the number of scans increased. Also a band centered at 380 nm, can be attributed to π–π* transitions of the azo (–N=N–) chromophore. Most importantly, a moderately intense band located at 500 nm is shown and attributed to metal-to-ligand charge-transfer (MLCT) transitions. Finally, the band corresponding to the ligand increases significantly along with the MLCT band as the number of scans used during electropolymerization increases which suggests an increase in the conjugation. The appearance of this low-energy n–π* band is particularly significant, as such transitions are known to be sensitive

to the electronic environment and are often enhanced or red-shifted in the vicinity of coordination complexes and in this case it is similar to the case on bare ITO (**Figure 85**).

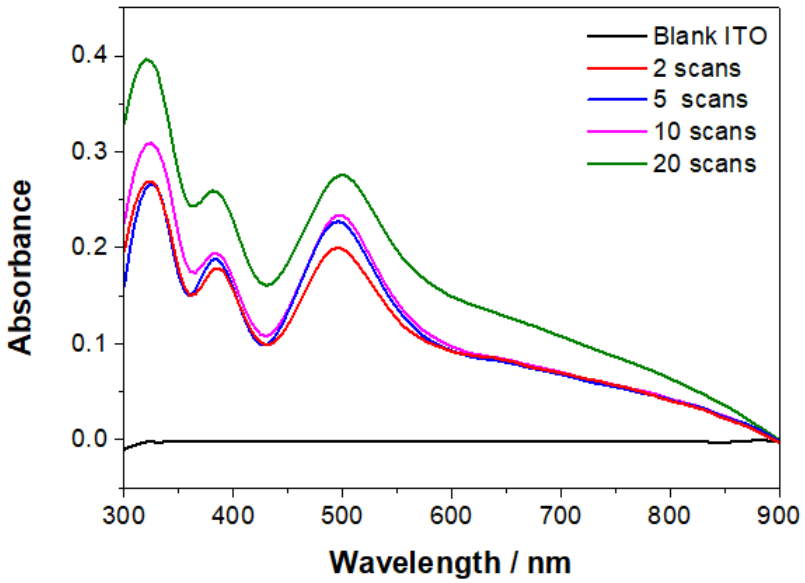

Figure 85: UV–Vis absorption spectra of poly[Ru(tpy-Ph-NH_2)$_2$]$^{2+}$ film electropolymerized using different numbers of CV scans inside mesoporous silica films.

4.2.10. Electrochromic Response of the Metallopolymer inside Mesoporous Silica Films

Based on a two-electrodes system device comprising the **poly**[Ru(tpy-Ph-NH_2)$_2$]$^{2+}$ film prepared here with a gel-based electrolyte, we investigated its electrochromic properties. The color of the electrochromic films was found to vary as a function of the oxidation state of the central metal, with distinct changes observed both visually and from the UV–vis spectra upon switching between the Ru^{2+}/Ru^{3+} redox states so the color changes from red to almost transparent. We display the UV-Vis spectra of the **poly**[Ru(tpy-Ph-NH_2)$_2$]$^{2+}$ material in the different redox states. In the normal state of the polymer film which is the reduced state, it exhibited an intense absorption band in the visible region 495 nm corresponding to metal-to-ligand charge transfer (MLCT) transitions characteristic of Ru(II) centers which is identified as the black line and is defined by the dark red color on the electrode. In contrast, the oxidized form of this film where Ru (II) is oxidized to Ru (III) shows a significantly diminished absorption, that is presented as the disappearance of the

absorbance band which is presented as the red line and it is presented by the disappearance of the purple color and a yellowish hue is also seen as illustrated below in **Figure 86**.

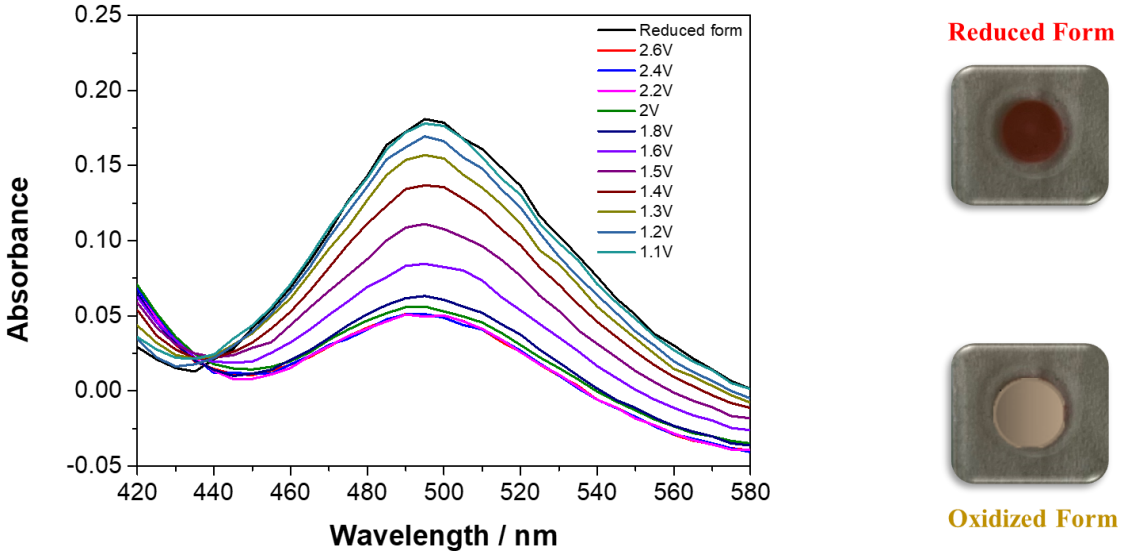

Figure 86: UV–Vis absorption spectra of poly[Ru(tpyPhNH$_2$)$_2$]$^{2+}$ inside mesoporous films in its reduced (black trace, at –0.5 V) and oxidized (red trace, at 2.6 V) states. Photographs of the polymer film deposited on an ITO substrate at –0.5 V (Top, colored state) and 2.6 V (Bottom, bleached state).

The polymer film exhibited a reversible color change from red to colorless, as measured at wavelength 490 nm with the working electrode biased successively at -0.5 V (coloration step) and 2.5 V (bleaching step) for 10 or 20 s per step (**Figure 87**). The electropolymerized film demonstrated strong electrochromic performance, attributed to the high molar absorptivity of the metal-to-ligand charge transfer (MLCT) band ($\varepsilon = 2.5 \times 10^4$ M^{-1} cm^{-1}). When switching between colored and bleached state the transmittance change varies between 19% and 35% depending on how much deposit is inside the silica films. Some decrease in absorbance changes upon multiple successive redox cycling was however observed, especially at short switching times and samples with higher amount of polymer deposited as shown previously. The response time was satisfactorily fast (2.2 s for colouration and 3.5 s for bleaching), as measured at 95% of the maximum absorbance variations observed after application of +2.5 V and -0.5 V, respectively. Furthermore, the optical memory is good where it takes around 2 minutes without any potential

applied to retain the colored state after oxidation even though it doesn't reach completely the original properties without an application of the reducing potential.

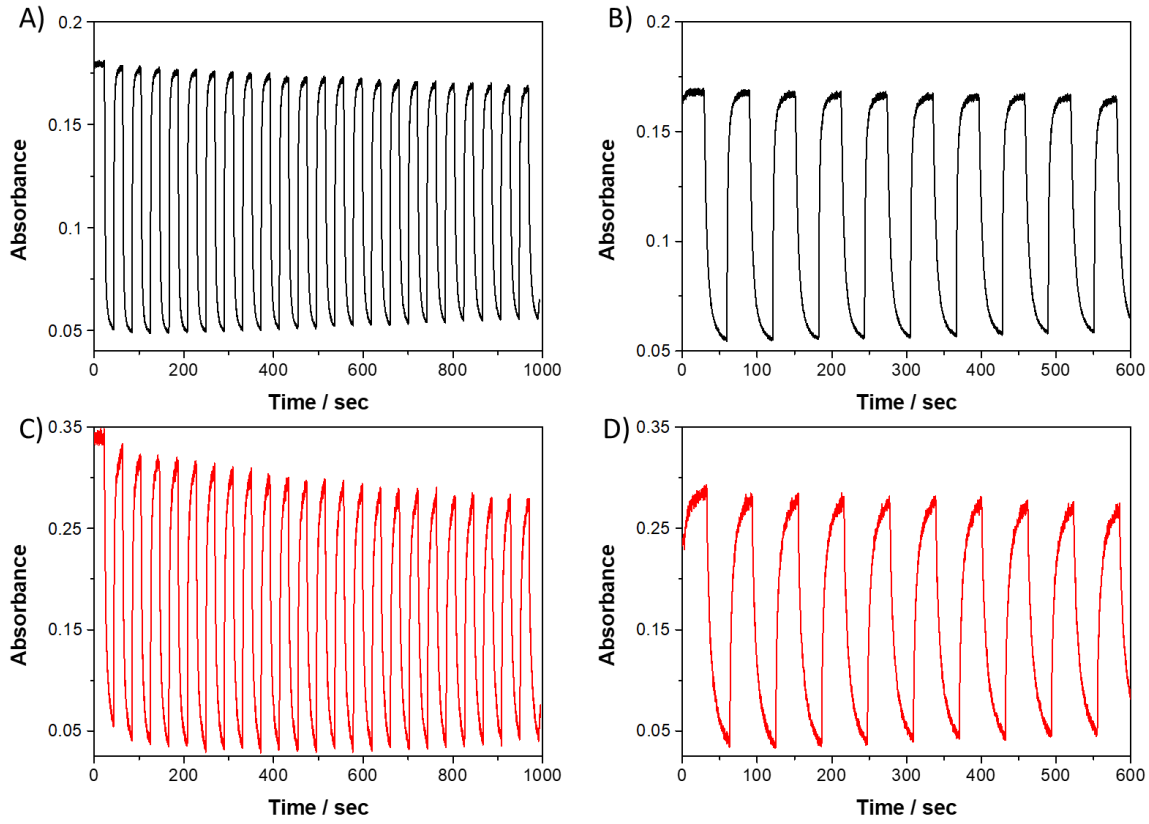

Figure 87: Chronoabsorptometry of the polymeric film over multiple redox cycles monitored at a fixed wavelength of 580 nm, respectively recorded by applying switching times of (A) 20 s and (B) 30 s for polymer formed using 6 scans, (C) 20 s and (D) 30 s for polymer formed using 20 scans inside mesoprous films.

4.3. Conclusion

This chapter established a complete framework for templating, growing, and evaluating electrochromic metallopolymer nanowires within vertically oriented mesoporous silica films on ITO. Vertically aligned, hexagonally ordered silica membranes with tunable pore diameters (~2, 3, and 4.3 nm) were obtained by EASA, as confirmed by FTIR (efficient template removal exposing silanol-rich surfaces) and GISAXS (long-range order and vertical channel orientation). Electrochemical probing with $[Ru(NH_3)_6]^{3+}$, $Fe(CN)_6^{4-/3-}$, and $Fc(MeOH)_2$ verified uniform coverage and the characteristic cation-permselective transport of silica nanochannels.

Aminophenyl-substituted bis(terpyridine) complexes, $[Fe(tpy\text{-}Ph\text{-}NH_2)_2]^{2+}$ and $[Ru(tpy\text{-}Ph\text{-}NH_2)_2]^{2+}$, were then electropolymerized by multisweep CV either directly on ITO or inside the films. Acidic media ($HClO_4$) hindered confined growth via NH_2 protonation whereas $LiClO_4$ in acetonitrile enabled effective polymerization. Confinement imposed a strong pore-size dependence: 2 nm channels yielded inefficient, unstable growth; 3 nm pores gave detectable but rapidly decaying signals; and 4.3 nm channels afforded reproducible growth with increasing peak currents over scans and robust films that withstood rinsing/ultrasonication. Confined films displayed the expected Fe^{3+}/Fe^{2+} and Ru^{3+}/Ru^{2+} couples but with lower peak currents and larger ΔE_p than on bare ITO, consistent with added ion-transport resistance and restricted diffusion. Spectroelectrochemistry confirmed clear, reversible electrochromism dominated by MLCT transitions (≈580 nm for Fe, ≈495–500 nm for Ru); within 4.3 nm pores the films retained fast switching (≈2–3.5 s at 90–95% optical change), useful contrast ($\Delta T\%$ ≈10–25% for Fe and ≈19–35% for Ru, depending on the size of the metallopolymer), and good short-term optical memory, with some amplitude attenuation under rapid cycling attributable to kinetic limitations in confinement. Furthermore, chemical removal of the silica scaffold (NaOH) damaged the Fe-based deposits, indicating the practical advantage of retaining the films as an integral support, unless polymer-compatible etching strategies are developed. Overall, these films provide effective nanostructured hosts for terpyridine-based metallopolymers when electrolyte composition and pore size are carefully chosen, with ~4.3 nm channels offering the best compromise between growth efficiency, redox stability, and electrochromic performance.

5. General Conclusion and Perspectives

This thesis has investigated the electropolymerization, structural characteristics, and electrochromic properties of metallopolymers derived from aminophenyl-functionalized bis(terpyridine) complexes of Fe(II) and Ru(II). The work was conducted both on planar electrodes and within vertically oriented mesoporous silica films, with the dual objective of elucidating the polymerization mechanism and assessing the effect of nanoconfinement on film growth and electrochemical performance. Through a combination of electrochemical and spectroscopic techniques, this research provides a comprehensive understanding of how molecular design, metal–ligand interactions, and nanoscale organization govern the formation and function of electrochromic metallopolymers.

The first part of this work focused on the controlled electropolymerization of $[M(tpy\text{-}Ph\text{-}NH_2)_2]^{2+}$ (M = Fe, Ru) complexes on indium tin oxide (ITO) and carbon electrodes. Using multisweep cyclic voltammetry in aprotic perchlorate media, uniform electroactive films of poly$[Fe(tpy\text{-}Ph\text{-}NH_2)_2]^{2+}$ and poly$[Ru(tpy\text{-}Ph\text{-}NH_2)_2]^{2+}$ were successfully generated. Mechanistic investigations combining cyclic voltammetry, UV–Vis, Raman, FTIR, and XPS analyses demonstrated that polymerization proceeds through an oxidative N–N coupling pathway rather than the conventional C–C or C–N routes observed in polyaniline. This deviation arises from steric blocking of the para position on the phenyl ring by the terpyridine substituent. As a result, the amino groups couple through hydrazo (–NH–NH–) intermediates that subsequently oxidize to azo (–N=N–) linkages, producing conjugated azo-bridged metallopolymer chains. Importantly, the Fe^{3+}/Fe^{2+} and Ru^{3+}/Ru^{2+} redox couples of the respective metal centers remain electrochemically accessible in the resulting polymers, ensuring efficient electronic communication along the polymer backbone. The metal centers thus not only preserve their intrinsic redox functionality but also serve as electronic relay points within the conjugated framework, facilitating reversible charge transport. The resulting Fe- and Ru-based metallopolymers displayed distinct electrochromic responses characterized by reversible color modulation, rapid optical switching, and high coloration efficiencies. These results confirm that subtle electronic differences between metal centers can be leveraged to tune film growth, charge transport, and optical performance, providing a rational pathway toward material optimization.

The second part of the thesis introduced nanoconfinement as a strategy to address limitations in film morphology, ion diffusion, and long-term stability. Vertically oriented mesoporous silica films with tunable pore diameters of approximately 2, 3, and 4.3 nm were fabricated on ITO electrodes by the electrochemically assisted self-assembly (EASA) method. The films were characterized by FTIR and GISAXS, confirming efficient template removal and long-range hexagonal order with channels oriented perpendicular to the substrate. Electrochemical probing using standard redox markers verified their permselective behavior and structural integrity. Electropolymerization of the aminophenyl-substituted Fe(II) and Ru(II) terpyridine complexes within these nanostructured hosts revealed a pronounced pore-size dependence. In 2 nm channels, polymer growth was strongly hindered due to steric and diffusional constraints, whereas 3 nm pores allowed partial but unstable film formation. In contrast, 4.3 nm channels enabled uniform and reproducible polymerization, yielding adherent and robust metallopolymer nanowires confined within the silica matrix. The confined films retained the characteristic Fe^{3+}/Fe^{2+} and Ru^{3+}/Ru^{2+} redox couples, although with lower peak currents and larger ΔE_p values compared to films grown on bare ITO, consistent with increased ion-transport resistance in confined geometries. Spectroelectrochemical characterization confirmed that the confined metallopolymers preserved their reversible electrochromic behavior. Films within 4.3 nm pores exhibited switching times between 2 and 3.5 s with optical contrasts of 10–35%, depending on the metal center. The confinement also enhanced film stability and prevented delamination, even under sonication, underscoring the mechanical and electrochemical benefits of templated architectures. Attempts to remove the silica scaffold chemically resulted in partial film degradation, indicating that the hybrid silica–metallopolymer architecture functions best as an integrated composite.

The results obtained in this work open several avenues for future research and technological applications. The perspectives outlined below highlight directions where the concepts developed in this thesis can be extended and deepened. The azo linkages intrinsic to these metallopolymers suggest the possibility of photoinduced cis–trans isomerization. Combining this photochemical switching with redox-controlled electrochromism could yield dual-responsive or optoelectrochromic materials. Incorporating photoactive Ru or Os complexes may also allow coupling between light absorption, charge transfer, and optical modulation, opening pathways toward smart optical devices and molecular photonics. Future studies could explore complexes

based on alternative transition metals such as Os(II), Ni(II), or Cu(II), as well as modified terpyridine or polypyridyl ligands bearing different electronic substituents. Such variations would enable tuning of redox potentials, optical gaps, and coloration wavelengths across the visible and near-infrared regions. The design of heterometallic or mixed-ligand polymers could further expand the palette of electrochromic responses and introduce multifunctionality such as luminescence or catalytic activity. Also, the combination of transparent electrodes and stable metallopolymers provides a strong foundation for the development of practical electrochromic devices such as smart windows, reflective displays, and energy-efficient optical filters. Scaling up the EASA fabrication process and integrating these hybrid films into complete device assemblies represent key next steps toward technological implementation.

6. References

[1] A. J. Bard and L. R. Faulkner, *Electrochemical methods: fundamentals and applications*, 2nd ed. New York: Wiley, 2001.

[2] *Electrochemistry for Materials Science*. Elsevier, 2008. doi: 10.1016/B978-0-444-52792-9.X5001-5.

[3] J. Mort, "Conductive Polymers," *Science*, vol. 208, no. 4446, pp. 819–825, May 1980, doi: 10.1126/science.208.4446.819.

[4] A. G. MacDiarmid, "'Synthetic metals': a novel role for organic polymers," *Current Applied Physics*, vol. 1, no. 4–5, pp. 269–279, Nov. 2001, doi: 10.1016/S1567-1739(01)00051-7.

[5] *Conducting Polymers*. in Monographs in Electrochemistry. Berlin, Heidelberg: Springer Berlin Heidelberg, 2008. doi: 10.1007/978-3-540-75930-0.

[6] M. Kraft *et al.*, "Polyanionic, Alkylthiosulfate-Based Thiol Precursors for Conjugated Polymer Self-Assembly onto Gold and Silver," *ACS Appl. Mater. Interfaces*, vol. 6, no. 14, pp. 11758–11765, Jul. 2014, doi: 10.1021/am5025148.

[7] H. Shirakawa, E. J. Louis, A. G. MacDiarmid, C. K. Chiang, and A. J. Heeger, "Synthesis of electrically conducting organic polymers: halogen derivatives of polyacetylene, (CH) x," *J. Chem. Soc., Chem. Commun.*, no. 16, p. 578, 1977, doi: 10.1039/c39770000578.

[8] T. A. Skotheim, R. L. Elsenbaumer, and J. R. Reynolds, *Handbook of conducting polymers*, 2nd ed. revised and Expanded. New York Basel: M. Dekker, 1998.

[9] A. J. Heeger, "Nobel Lecture: Semiconducting and metallic polymers: The fourth generation of polymeric materials," *Rev. Mod. Phys.*, vol. 73, no. 3, pp. 681–700, Sep. 2001, doi: 10.1103/RevModPhys.73.681.

[10] A. G. MacDiarmid, "Nobel Lecture: 'Synthetic metals': A novel role for organic polymers," *Rev. Mod. Phys.*, vol. 73, no. 3, pp. 701–712, Sep. 2001, doi: 10.1103/RevModPhys.73.701.

[11] J.-C. Chiang and A. G. MacDiarmid, "'Polyaniline': Protonic acid doping of the emeraldine form to the metallic regime," *Synthetic Metals*, vol. 13, no. 1–3, pp. 193–205, Jan. 1986, doi: 10.1016/0379-6779(86)90070-6.

[12] H. Shirakawa, "The Discovery of Polyacetylene Film: The Dawning of an Era of Conducting Polymers (Nobel Lecture)," *Angew. Chem. Int. Ed.*, vol. 40, no. 14, pp. 2574–

2580, Jul. 2001, doi: 10.1002/1521-3773(20010716)40:14<2574::AID-ANIE2574>3.0.CO;2-N.

[13] F. Garnier, G. Tourillon, J. Y. Barraud, and H. Dexpert, “First evidence of crystalline structure in conducting polythiophene,” *J Mater Sci*, vol. 20, no. 8, pp. 2687–2694, Aug. 1985, doi: 10.1007/BF00553029.

[14] S. C. Rasmussen, “Early history of polypyrrole: The first conducting organic polymer,” *Bull Hist Chem*, vol. 40, no. 1, pp. 45–55, 2015, doi: 10.70359/bhc2015v040p045.

[15] Q. Wei, M. Mukaida, K. Kirihara, Y. Naitoh, and T. Ishida, “Recent Progress on PEDOT-Based Thermoelectric Materials,” *Materials*, vol. 8, no. 2, pp. 732–750, Feb. 2015, doi: 10.3390/ma8020732.

[16] Md. B. Hasan, Md. M. Parvez, A. Y. Abir, and Md. F. Ahmad, “A review on conducting organic polymers: Concepts, applications, and potential environmental benefits,” *Heliyon*, vol. 11, no. 3, p. e42375, Feb. 2025, doi: 10.1016/j.heliyon.2025.e42375.

[17] “Conducting polymers forward,” *Nat. Mater.*, vol. 19, no. 9, pp. 921–921, Sep. 2020, doi: 10.1038/s41563-020-0792-7.

[18] A. Grimsdale and P. Dastoor, *Conjugated Polymers for Organic Electronics: Design and Synthesis*, 1st ed. Cambridge University Press, 2024. doi: 10.1017/9781139035262.

[19] P. Kar, *Doping in Conjugated Polymers*, 1st ed. Wiley, 2013. doi: 10.1002/9781118816639.

[20] A. J. Heeger, “Semiconducting polymers: the Third Generation,” *Chem. Soc. Rev.*, vol. 39, no. 7, p. 2354, 2010, doi: 10.1039/b914956m.

[21] A. F. Diaz, K. K. Kanazawa, and G. P. Gardini, “Electrochemical polymerization of pyrrole,” *J. Chem. Soc., Chem. Commun.*, no. 14, p. 635, 1979, doi: 10.1039/c39790000635.

[22] L. W. Shacklette, R. L. Elsenbaumer, R. R. Chance, H. Eckhardt, J. E. Frommer, and R. H. Baughman, “Conducting complexes of polyphenylene sulfides,” *The Journal of Chemical Physics*, vol. 75, no. 4, pp. 1919–1927, Aug. 1981, doi: 10.1063/1.442217.

[23] A. G. Macdiarmid *et al.*, “‘Polyaniline’: Interconversion of Metallic and Insulating Forms,” *Molecular Crystals and Liquid Crystals*, vol. 121, no. 1–4, pp. 173–180, Mar. 1985, doi: 10.1080/00268948508074857.

[24] J. G. Masters, Y. Sun, A. G. MacDiarmid, and A. J. Epstein, “Polyaniline: Allowed oxidation states,” *Synthetic Metals*, vol. 41, no. 1–2, pp. 715–718, Apr. 1991, doi: 10.1016/0379-6779(91)91166-8.

[25] W.-S. Huang, B. D. Humphrey, and A. G. MacDiarmid, “Polyaniline, a novel conducting polymer. Morphology and chemistry of its oxidation and reduction in aqueous electrolytes,” *J. Chem. Soc., Faraday Trans. 1*, vol. 82, no. 8, p. 2385, 1986, doi: 10.1039/f19868202385.

[26] K. G. Neoh, E. T. Kang, and T. C. Tan, “Chemical synthesis and characterization of electroactive and partially soluble polyazulene,” *Polymer Bulletin*, vol. 19, no. 4, Apr. 1988, doi: 10.1007/BF00263932.

[27] E. Contal, S. Lakard, F. Dumur, and B. Lakard, “Investigation of polycarbazoles thin films prepared by electrochemical oxidation of 3- and 9-substituted carbazoles,” *Progress in Organic Coatings*, vol. 162, p. 106563, Jan. 2022, doi: 10.1016/j.porgcoat.2021.106563.

[28] J.-E. Österholm, P. Passiniemi, H. Isotalo, and H. Stubb, “Synthesis and properties of FeCl4-doped polythiophene,” *Synthetic Metals*, vol. 18, no. 1–3, pp. 213–218, Feb. 1987, doi: 10.1016/0379-6779(87)90881-2.

[29] R. D. McCullough, S. Tristram-Nagle, S. P. Williams, R. D. Lowe, and M. Jayaraman, “Self-orienting head-to-tail poly(3-alkylthiophenes): new insights on structure-property relationships in conducting polymers,” *J. Am. Chem. Soc.*, vol. 115, no. 11, pp. 4910–4911, Jun. 1993, doi: 10.1021/ja00064a070.

[30] M. J. González-Tejera, E. S. De La Blanca, and I. Carrillo, “Polyfuran conducting polymers: Synthesis, properties, and applications,” *Synthetic Metals*, vol. 158, no. 5, pp. 165–189, Mar. 2008, doi: 10.1016/j.synthmet.2007.12.009.

[31] F. Wudl, M. Kobayashi, and A. J. Heeger, “Poly(isothianaphthene),” *J. Org. Chem.*, vol. 49, no. 18, pp. 3382–3384, Sep. 1984, doi: 10.1021/jo00192a027.

[32] A. Thadathil, H. Pradeep, D. Joshy, Y. A. Ismail, and P. Periyat, “Polyindole and polypyrrole as a sustainable platform for environmental remediation and sensor applications,” *Mater. Adv.*, vol. 3, no. 7, pp. 2990–3022, 2022, doi: 10.1039/D2MA00022A.

[33] K.-P. Strunk *et al.*, “Pristine Poly(*para* -phenylene): Relating Semiconducting Behavior to Kinetics of Precursor Conversion,” *ACS Appl. Mater. Interfaces*, vol. 11, no. 21, pp. 19481–19488, May 2019, doi: 10.1021/acsami.9b03291.

[34] D. R. Gagnon, J. D. Capistran, F. E. Karasz, R. W. Lenz, and S. Antoun, “Synthesis, doping, and electrical conductivity of high molecular weight poly(p-phenylene vinylene),” *Polymer*, vol. 28, no. 4, pp. 567–573, Jan. 1987, doi: 10.1016/0032-3861(87)90471-X.

[35] A. Elschner, S. Kirchmeyer, W. Lovenich, U. Merker, and K. Reuter, *PEDOT: Principles and Applications of an Intrinsically Conductive Polymer*, 0 ed. CRC Press, 2010. doi: 10.1201/b10318.

[36] T. M. Pappenfus *et al.*, "Regiochemistry of Poly(3-hexylthiophene): Synthesis and Investigation of a Conducting Polymer," *J. Chem. Educ.*, vol. 87, no. 5, pp. 522–525, May 2010, doi: 10.1021/ed800144p.

[37] M. Hirohata, K. Tada, T. Kawai, M. Onoda, and K. Yoshino, "Electroluminescence in conducting polymers based on poly(phenylene ethynylene)," *Synthetic Metals*, vol. 85, no. 1–3, pp. 1273–1274, Mar. 1997, doi: 10.1016/S0379-6779(97)80237-8.

[38] M. Fukuda, K. Sawada, and K. Yoshino, "Synthesis of fusible and soluble conducting polyfluorene derivatives and their characteristics," *J. Polym. Sci. A Polym. Chem.*, vol. 31, no. 10, pp. 2465–2471, Sep. 1993, doi: 10.1002/pola.1993.080311006.

[39] H. Reisch, U. Wiesler, U. Scherf, and N. Tuytuylkov, "Poly(indenofluorene) (PIF), a Novel Low Band Gap Polyhydrocarbon," *Macromolecules*, vol. 29, no. 25, pp. 8204–8210, Jan. 1996, doi: 10.1021/ma960877b.

[40] A. Malinauskas, "Chemical deposition of conducting polymers," *Polymer*, vol. 42, no. 9, pp. 3957–3972, Apr. 2001, doi: 10.1016/S0032-3861(00)00800-4.

[41] S. Jadoun and U. Riaz, "A review on the chemical and electrochemical copolymerization of conducting monomers: recent advancements and future prospects," *Polymer-Plastics Technology and Materials*, vol. 59, no. 5, pp. 484–504, Mar. 2020, doi: 10.1080/25740881.2019.1669647.

[42] G. Inzelt, "Chemical and Electrochemical Syntheses of Conducting Polymers," in *Conducting Polymers*, in Monographs in Electrochemistry. , Berlin, Heidelberg: Springer Berlin Heidelberg, 2012, pp. 149–171. doi: 10.1007/978-3-642-27621-7_4.

[43] R. D. McCullough, "The Chemistry of Conducting Polythiophenes," *Adv. Mater.*, vol. 10, no. 2, pp. 93–116, Jan. 1998, doi: 10.1002/(SICI)1521-4095(199801)10:2<93::AID-ADMA93>3.0.CO;2-F.

[44] S. K. Singh, R. Shukla, and C. Dixit, "Synthesis of polythiophene and their application," *Int. J. Phys. Math.*, vol. 4, no. 1, pp. 76–79, Jan. 2022, doi: 10.33545/26648636.2022.v4.i1a.66.

[45] L. W. Shacklette, R. R. Chance, D. M. Ivory, G. G. Miller, and R. H. Baughman, “Electrical and optical properties of highly conducting charge-transfer complexes of poly(p-phenylene),” *Synthetic Metals*, vol. 1, no. 3, pp. 307–320, Apr. 1980, doi: 10.1016/0379-6779(80)90020-X.

[46] K. Friedrich, T. Burkhart, A. A. Almajid, and F. Haupert, “Poly-Para-Phenylene-Copolymer (PPP): A High-Strength Polymer with Interesting Mechanical and Tribological Properties,” *International Journal of Polymeric Materials*, vol. 59, no. 9, pp. 680–692, Jul. 2010, doi: 10.1080/00914037.2010.483211.

[47] B. K. Moss and R. P. Burford, “A kinetic study of polypyrrole degradation,” *Polymer*, vol. 33, no. 9, pp. 1902–1908, Jan. 1992, doi: 10.1016/0032-3861(92)90490-N.

[48] A. Yussuf, M. Al-Saleh, S. Al-Enezi, and G. Abraham, “Synthesis and Characterization of Conductive Polypyrrole: The Influence of the Oxidants and Monomer on the Electrical, Thermal, and Morphological Properties,” *International Journal of Polymer Science*, vol. 2018, pp. 1–8, Jul. 2018, doi: 10.1155/2018/4191747.

[49] Y. Wang and K. Levon, “Influence of Dopant on Electroactivity of Polyaniline,” *Macromolecular Symposia*, vol. 317–318, no. 1, pp. 240–247, Aug. 2012, doi: 10.1002/masy.201200008.

[50] S. Bhandari, “Polyaniline,” in *Polyaniline Blends, Composites, and Nanocomposites*, Elsevier, 2018, pp. 23–60. doi: 10.1016/B978-0-12-809551-5.00002-3.

[51] F. Zeng, Z. Qin, B. Liang, T. Li, N. Liu, and M. Zhu, “Polyaniline nanostructures tuning with oxidants in interfacial polymerization system,” *Progress in Natural Science: Materials International*, vol. 25, no. 5, pp. 512–519, Oct. 2015, doi: 10.1016/j.pnsc.2015.10.002.

[52] J.-E. Österholm, Y. Cao, F. Klavetter, and P. Smith, “Emulsion polymerization of aniline,” *Synthetic Metals*, vol. 55, no. 2–3, pp. 1034–1039, Mar. 1993, doi: 10.1016/0379-6779(93)90195-3.

[53] Zh. A. Boeva and V. G. Sergeyev, “Polyaniline: Synthesis, properties, and application,” *Polym. Sci. Ser. C*, vol. 56, no. 1, pp. 144–153, Sep. 2014, doi: 10.1134/S1811238214010032.

[54] J.-M. Savéant, “Molecular Catalysis of Electrochemical Reactions. Mechanistic Aspects,” *Chem. Rev.*, vol. 108, no. 7, pp. 2348–2378, Jul. 2008, doi: 10.1021/cr068079z.

[55] C. Rogers, “Luminescent molecular sensors based on analyte coordination to transition-metal complexes,” *Coordination Chemistry Reviews*, vol. 233–234, pp. 341–350, Nov. 2002, doi: 10.1016/S0010-8545(02)00023-1.

[56] B. J. Holliday and T. M. Swager, “Conducting metallopolymers: the roles of molecular architecture and redox matching,” *Chem. Commun.*, no. 1, p. 23, 2005, doi: 10.1039/b408479a.

[57] K. M. Milum, Y. N. Kim, and B. J. Holliday, “Pt-[NCN] Pincer Conducting Metallopolymers That Display Redox-Attenuated Metal−Ligand Interactions,” *Chem. Mater.*, vol. 22, no. 8, pp. 2414–2416, Apr. 2010, doi: 10.1021/cm100762s.

[58] M. T. Nguyen, R. A. Jones, and B. J. Holliday, “Direct synthesis of CdSe nanocrystals within a conducting metallopolymer: toward improving charge transfer in hybrid nanomaterials,” *Chem. Commun.*, vol. 52, no. 89, pp. 13112–13115, 2016, doi: 10.1039/C6CC07193G.

[59] M. O. Wolf, “Transition-Metal-Polythiophene Hybrid Materials,” *Adv. Mater.*, vol. 13, no. 8, pp. 545–553, Apr. 2001, doi: 10.1002/1521-4095(200104)13:8<545::AID-ADMA545>3.0.CO;2-3.

[60] M. O. Wolf, “Recent Advances in Conjugated Transition Metal-containing Polymers and Materials,” *J Inorg Organomet Polym*, vol. 16, no. 3, pp. 189–199, Nov. 2006, doi: 10.1007/s10904-006-9049-4.

[61] J. M. Stanley and B. J. Holliday, “Luminescent lanthanide-containing metallopolymers,” *Coordination Chemistry Reviews*, vol. 256, no. 15–16, pp. 1520–1530, Aug. 2012, doi: 10.1016/j.ccr.2012.03.046.

[62] J. V. Sanchez, R. Diaz, P. Herrasti, and P. Ocon, “Electrogeneration and Characterization of Poly(3-methylthiophene),” *Polym J*, vol. 33, no. 7, pp. 514–521, Jul. 2001, doi: 10.1295/polymj.33.514.

[63] C. Pinheiro, A. J. Parola, F. Pina, J. Fonseca, and C. Freire, “Electrocolorimetry of electrochromic materials on flexible ITO electrodes,” *Solar Energy Materials and Solar Cells*, vol. 92, no. 8, pp. 980–985, Aug. 2008, doi: 10.1016/j.solmat.2008.03.001.

[64] G. T. Morgan and F. H. Burstall, “3. Dehydrogenation of pyridine by anhydrous ferric chloride,” *J. Chem. Soc.*, p. 20, 1932, doi: 10.1039/jr9320000020.

[65] W. R. McWhinnie and J. D. Miller, “The Chemistry of Complexes Containing 2,2′-Bipyridyl, 1, 10-Phenanthroline, or 2,2′,6′,2”-Terpyridyl as Ligands,” in *Advances in Inorganic Chemistry and Radiochemistry*, vol. 12, Elsevier, 1970, pp. 135–215. doi: 10.1016/S0065-2792(08)60049-7.

[66] K. W. Jennette, S. J. Lippard, G. A. Vassiliades, and W. R. Bauer, “Metallointercalation Reagents. 2-Hydroxyethanethiolato(2,2′,2″-terpyridine)-platinum(II) Monocation Binds Strongly to DNA By Intercalation,” *Proc. Natl. Acad. Sci. U.S.A.*, vol. 71, no. 10, pp. 3839–3843, Oct. 1974, doi: 10.1073/pnas.71.10.3839.

[67] N. Elgrishi, M. B. Chambers, V. Artero, and M. Fontecave, “Terpyridine complexes of first row transition metals and electrochemical reduction of CO_2 to CO,” *Phys. Chem. Chem. Phys.*, vol. 16, no. 27, pp. 13635–13644, 2014, doi: 10.1039/C4CP00451E.

[68] S. Aroua *et al.*, “Synthesis, Characterization, and DFT Analysis of Bis-Terpyridyl-Based Molecular Cobalt Complexes,” *Inorg. Chem.*, vol. 56, no. 10, pp. 5930–5940, May 2017, doi: 10.1021/acs.inorgchem.7b00595.

[69] R.-A. Fallahpour, “Synthesis of 4′-Substituted-2,2′:6′,2″-Terpyridines,” *Synthesis*, no. 2, pp. 0155–0184, 2003, doi: 10.1055/s-2003-36811.

[70] S. A. Sapp, C. M. Elliott, C. Contado, S. Caramori, and C. A. Bignozzi, “Substituted Polypyridine Complexes of Cobalt(II/III) as Efficient Electron-Transfer Mediators in Dye-Sensitized Solar Cells,” *J. Am. Chem. Soc.*, vol. 124, no. 37, pp. 11215–11222, Sep. 2002, doi: 10.1021/ja027355y.

[71] C. Wei, Y. He, X. Shi, and Z. Song, “Terpyridine-metal complexes: Applications in catalysis and supramolecular chemistry,” *Coordination Chemistry Reviews*, vol. 385, pp. 1–19, Apr. 2019, doi: 10.1016/j.ccr.2019.01.005.

[72] J. M. Ludlow *et al.*, “Group 8 Metallomacrocycles – Synthesis, Characterization, and Stability,” *Eur J Inorg Chem*, vol. 2015, no. 34, pp. 5662–5668, Dec. 2015, doi: 10.1002/ejic.201500971.

[73] D. B. Taylor, K. P. Callahan, and I. Shaikh, “Synthesis of a bifunctional coordination complex of osmium with curariform activity,” *J. Med. Chem.*, vol. 18, no. 11, pp. 1088–1094, Nov. 1975, doi: 10.1021/jm00245a008.

[74] G. Ciantelli, P. Legittimo, and F. Pantani, “A study of the ruthenium-2,2′,2″-terpyridine system,” *Analytica Chimica Acta*, vol. 53, no. 2, pp. 303–308, Feb. 1971, doi: 10.1016/S0003-2670(01)82089-4.

[75] M. Howe-Grant, K. C. Wu, W. R. Bauer, and S. J. Lippard, “Binding of platinum and palladium metallointercalation reagents and antitumor drugs to closed and open DNAs,” *Biochemistry*, vol. 15, no. 19, pp. 4339–4346, Sep. 1976, doi: 10.1021/bi00664a031.

[76] H. Wang *et al.*, “Synthesis, crystal structure, photophysical property and bioimaging application of a series of Zn(II) terpyridine complexes,” *Journal of Molecular Structure*, vol. 1194, pp. 157–162, Oct. 2019, doi: 10.1016/j.molstruc.2019.05.090.

[77] E. C. Constable and M. D. Ward, “Synthesis and co-ordination behaviour of 6′,6″-bis(2-pyridyl)-2,2′ : 4,4″ : 2″,2‴-quaterpyridine; ‘back-to-back’ 2,2′ : 6′,2″-terpyridine,” *J. Chem. Soc., Dalton Trans.*, no. 4, pp. 1405–1409, 1990, doi: 10.1039/DT9900001405.

[78] K. T. Potts, “α, α′-oligopyridines: A Source of New Materials,” *Bulletin des Sociétés Chimiques Belges*, vol. 99, no. 9, pp. 741–768, 1990.

[79] V. Grosshenny and R. Ziessel, “Novel ditopic terpyridine and phenylterpyridine ligands bridged by one or two ethynyl bonds: syntheses of rigid rod-like multinuclear complexes,” *Journal of organometallic chemistry*, vol. 453, no. 2, pp. C19–C22, 1993.

[80] J. England, C. C. Scarborough, T. Weyhermüller, S. Sproules, and K. Wieghardt, “Electronic Structures of the Electron Transfer Series [M (bpy) 3] n,[M (tpy) 2] n, and [Fe (tbpy) 3] n (M= Fe, Ru; n= 3+, 2+, 1+, 0, 1–): A Mössbauer Spectroscopic and DFT Study,” *European Journal of Inorganic Chemistry*, vol. 2012, no. 29, pp. 4605–4621, 2012.

[81] E. C. Constable, “2, 2′: 6′, 2 ″-Terpyridines: From chemical obscurity to common supramolecular motifs,” *Chemical Society Reviews*, vol. 36, no. 2, pp. 246–253, 2007.

[82] J. I. Bullock and P. W. Simpson, “Effect of temperature on the protonation constants of 2, 2′: 6′, 2 ″-terpyridyl and the stability constant of the bis (2, 2′: 6′, 2 ″-terpyridyl) iron (II) cation,” *Journal of the Chemical Society, Faraday Transactions 1: Physical Chemistry in Condensed Phases*, vol. 77, no. 8, pp. 1991–1997, 1981.

[83] C. García *et al.*, “Synthesis, structure and electrochemical properties of the cationic complex tris-(imidazolidine-1,10-phenanthroline)iron(II),” *Inorganic Chemistry Communications*, vol. 12, no. 5, pp. 392–395, May 2009, doi: 10.1016/j.inoche.2009.02.017.

[84] D. Qiu *et al.*, “Electropolymerization and characterization of an alternatively conjugated donor–acceptor metallopolymer: Poly-[Ru(4′-(4-(Diphenylamino)phenyl)-2,2′:6′,2″-Terpyridine)2]2+,” *Inorganic Chemistry Communications*, vol. 14, no. 1, pp. 296–299, Jan. 2011, doi: 10.1016/j.inoche.2010.11.019.

[85] J. Hjelm, R. W. Handel, A. Hagfeldt, E. C. Constable, C. E. Housecroft, and R. J. Forster, “Conducting Polymers Containing In-Chain Metal Centers: Electropolymerization of Oligothienyl-Substituted {$M(tpy)_2$ } Complexes and in Situ Conductivity Studies, M = Os(II), Ru(II),” *Inorg. Chem.*, vol. 44, no. 4, pp. 1073–1081, Feb. 2005, doi: 10.1021/ic049221m.

[86] A. Venkatanarayanan, A.-M. Spehar-Délèze, L. Dennany, Y. Pellegrin, T. E. Keyes, and R. J. Forster, “Ruthenium Aminophenanthroline Metallopolymer Films Electropolymerized from an Ionic Liquid: Deposition and Electrochemical and Photonic Properties,” *Langmuir*, vol. 24, no. 19, pp. 11233–11238, Oct. 2008, doi: 10.1021/la8011316.

[87] J. Yang, M. Sykora, and T. J. Meyer, “Electropolymerization of Vinylbipyridine Complexes of Ruthenium(II) and Osmium(II) in SiO_2 Sol−Gel Films,” *Inorg. Chem.*, vol. 44, no. 10, pp. 3396–3404, May 2005, doi: 10.1021/ic048623r.

[88] T. W. Hesterberg, X. Yang, and B. J. Holliday, “Polymerizable cationic iridium(III) complexes exhibiting color tunable light emission and their corresponding conducting metallopolymers,” *Polyhedron*, vol. 29, no. 1, pp. 110–115, Jan. 2010, doi: 10.1016/j.poly.2009.06.014.

[89] X.-Y. Chen, X. Yang, and B. J. Holliday, “Photoluminescent Europium-Containing Inner Sphere Conducting Metallopolymer,” *J. Am. Chem. Soc.*, vol. 130, no. 5, pp. 1546–1547, Feb. 2008, doi: 10.1021/ja077626a.

[90] A. Le Goff, M. Holzinger, and S. Cosnier, “Characterization of multi-walled carbon nanotube electrodes functionalized by electropolymerized tris(pyrrole-ether bipyridine) ruthenium (II),” *Electrochimica Acta*, vol. 56, no. 10, pp. 3633–3640, Apr. 2011, doi: 10.1016/j.electacta.2010.11.067.

[91] T. J. O’Sullivan, B. Djukic, P. A. Dube, and M. T. Lemaire, “A conducting metallopolymer featuring valence tautomerism,” *Chem. Commun.*, no. 14, p. 1903, 2009, doi: 10.1039/b818952h.

[92] F. Gokmese, E. Gokmese, F. Hamurcu, H. Celikkan, and M. Aksu, “Electrochemical Investigation of Zinc(II)-Furdap Amide Complex in DMSO Medium,” *CAC*, vol. 5, no. 3, pp. 244–248, Jul. 2009, doi: 10.2174/157341109788680246.

[93] M. Ito, T. Tsukatani, and H. Fujihara, “Preparation and characterization of gold nanoparticles with a ruthenium-terpyridyl complex, and electropolymerization of their pyrrole-modified metal nanocomposites,” *J. Mater. Chem.*, vol. 15, no. 9, p. 960, 2005, doi: 10.1039/b412406e.

[94] S. Myllynen and M. Wasberg, “Formation and oxidative break-up of organometallic Ru–Ru bonded polymer films in DMSO electrolyte studied using the dimer [Ru(bpy)(CO)2Cl]2 (bpy=2,2′-bipyridine),” *Journal of Electroanalytical Chemistry*, vol. 623, no. 1, pp. 93–101, Nov. 2008, doi: 10.1016/j.jelechem.2008.06.026.

[95] T. Arai, S. Sato, K. Uemura, T. Morikawa, T. Kajino, and T. Motohiro, “Photoelectrochemical reduction of CO2 in water under visible-light irradiation by a p-type InP photocathode modified with an electropolymerized ruthenium complex,” *Chem. Commun.*, vol. 46, no. 37, p. 6944, 2010, doi: 10.1039/c0cc02061c.

[96] S. Chardon-Noblat, A. Deronzier, F. Hartl, J. Van Slageren, and T. Mahabiersing, “A Novel Organometallic Polymer of Osmium(0), [Os(2,2′-bipyridine)(CO)2]n: Its Electrosynthesis and Electrocatalytic Properties Towards CO2 Reduction,” *Eur. J. Inorg. Chem.*, vol. 2001, no. 3, pp. 613–617, Mar. 2001, doi: 10.1002/1099-0682(200103)2001:3<613::AID-EJIC613>3.0.CO;2-E.

[97] S. Myllynen, M. Wasberg, and M. Haukka, “Influence of DMSO on the electroreductive Ru(bpy)(CO)2Cl2 (bpy=2,2′-bipyridine) polymer film formation,” *Journal of Electroanalytical Chemistry*, vol. 586, no. 2, pp. 217–224, Jan. 2006, doi: 10.1016/j.jelechem.2005.10.002.

[98] S. Chardon-Noblat, A. Pellissier, G. Cripps, and A. Deronzier, “Electrochemical behavior of binuclear complexes (L=2,2′-bipyridine substituted by pyrrole groups). Their reductive and oxidative electropolymerization,” *Journal of Electroanalytical Chemistry*, vol. 597, no. 1, pp. 28–38, Nov. 2006, doi: 10.1016/j.jelechem.2006.07.038.

[99] S. Myllynen and M. Wasberg, “High electrical conductivity for the partially oxidised d8 Ru–Ru bonded chain [Ru(bpy)(CO)2]n (bpy=2,2′-bipyridine) and its wide range redox

control," *Electrochemistry Communications*, vol. 11, no. 7, pp. 1453–1456, Jul. 2009, doi: 10.1016/j.elecom.2009.05.029.

[100] A. Juris, V. Balzani, F. Barigelletti, S. Campagna, P. Belser, and A. Von Zelewsky, "Ru(II) polypyridine complexes: photophysics, photochemistry, eletrochemistry, and chemiluminescence," *Coordination Chemistry Reviews*, vol. 84, pp. 85–277, Mar. 1988, doi: 10.1016/0010-8545(88)80032-8.

[101] J. P. Paris and W. W. Brandt, "CHARGE TRANSFER LUMINESCENCE OF A RUTHENIUM(II) CHELATE," *J. Am. Chem. Soc.*, vol. 81, no. 18, pp. 5001–5002, Sep. 1959, doi: 10.1021/ja01527a064.

[102] K. Kalyanasundaram, "Photophysics, photochemistry and solar energy conversion with tris(bipyridyl)ruthenium(II) and its analogues," *Coordination Chemistry Reviews*, vol. 46, pp. 159–244, Oct. 1982, doi: 10.1016/0010-8545(82)85003-0.

[103] G. E. Büchel *et al.*, "Near-Infrared Intraoperative Chemiluminescence Imaging," *ChemMedChem*, vol. 11, no. 18, pp. 1978–1982, Sep. 2016, doi: 10.1002/cmdc.201600301.

[104] M. Abrahamsson *et al.*, "Bistridentate Ruthenium(II)polypyridyl-Type Complexes with Microsecond^3 MLCT State Lifetimes: Sensitizers for Rod-Like Molecular Arrays," *J. Am. Chem. Soc.*, vol. 130, no. 46, pp. 15533–15542, Nov. 2008, doi: 10.1021/ja804890k.

[105] R. L. Mccreery, "The merger of electrochemistry and molecular electronics," *The Chemical Record*, vol. 12, no. 1, pp. 149–163, Feb. 2012, doi: 10.1002/tcr.201100006.

[106] A. Kraft, "Electrochromism: a fascinating branch of electrochemistry," *ChemTexts*, vol. 5, no. 1, p. 1, Mar. 2019, doi: 10.1007/s40828-018-0076-x.

[107] A. J. Bard, "Chemical modification of electrodes," *J. Chem. Educ.*, vol. 60, no. 4, p. 302, Apr. 1983, doi: 10.1021/ed060p302.

[108] N.-U.-A. Babar, M. N. Asghar, F. Hussain, and K. S. Joya, "Spray-assembled nanoscale cobalt-oxide as highly efficient and durable bifunctional electrocatalyst for overall water splitting," *Materials Today Energy*, vol. 17, p. 100434, Sep. 2020, doi: 10.1016/j.mtener.2020.100434.

[109] D. B. Mitzi, L. L. Kosbar, C. E. Murray, M. Copel, and A. Afzali, "High-mobility ultrathin semiconducting films prepared by spin coating," *Nature*, vol. 428, no. 6980, pp. 299–303, Mar. 2004, doi: 10.1038/nature02389.

[110] C. Zuo, A. D. Scully, and M. Gao, “Drop-Casting Method to Screen Ruddlesden–Popper Perovskite Formulations for Use in Solar Cells,” *ACS Appl. Mater. Interfaces*, vol. 13, no. 47, pp. 56217–56225, Dec. 2021, doi: 10.1021/acsami.1c17475.

[111] J. Heinze, B. A. Frontana-Uribe, and S. Ludwigs, “Electrochemistry of Conducting Polymers—Persistent Models and New Concepts,” *Chem. Rev.*, vol. 110, no. 8, pp. 4724–4771, Aug. 2010, doi: 10.1021/cr900226k.

[112] C. K. Luscombe, U. Maitra, M. Walter, and S. K. Wiedmer, “Theoretical background on semiconducting polymers and their applications to OSCs and OLEDs,” *Chemistry Teacher International*, vol. 3, no. 2, pp. 169–183, Jun. 2021, doi: 10.1515/cti-2020-0020.

[113] J. G. Ibanez, Marina. E. Rincón, S. Gutierrez-Granados, M. Chahma, O. A. Jaramillo-Quintero, and B. A. Frontana-Uribe, “Conducting Polymers in the Fields of Energy, Environmental Remediation, and Chemical–Chiral Sensors,” *Chem. Rev.*, vol. 118, no. 9, pp. 4731–4816, May 2018, doi: 10.1021/acs.chemrev.7b00482.

[114] G. Sabouraud, S. Sadki, and N. Brodie, “The mechanisms of pyrrole electropolymerization,” *Chem. Soc. Rev.*, vol. 29, no. 5, pp. 283–293, 2000, doi: 10.1039/a807124a.

[115] G. Inzelt, *Conducting Polymers*. in Monographs in Electrochemistry. Berlin, Heidelberg: Springer Berlin Heidelberg, 2012. doi: 10.1007/978-3-642-27621-7.

[116] D. Bélanger and J. Pinson, “Electrografting: a powerful method for surface modification,” *Chem. Soc. Rev.*, vol. 40, no. 7, p. 3995, 2011, doi: 10.1039/c0cs00149j.

[117] S. Gabriel, R. Jérôme, and C. Jérôme, “Cathodic electrografting of acrylics: From fundamentals to functional coatings,” *Progress in Polymer Science*, vol. 35, no. 1–2, pp. 113–140, Jan. 2010, doi: 10.1016/j.progpolymsci.2009.11.003.

[118] L. Ouyang, B. Wei, C. Kuo, S. Pathak, B. Farrell, and D. C. Martin, “Enhanced PEDOT adhesion on solid substrates with electrografted P(EDOT-NH_2),” *Sci. Adv.*, vol. 3, no. 3, p. e1600448, Mar. 2017, doi: 10.1126/sciadv.1600448.

[119] H. Zollinger, *Diazo Chemistry I: Aromatic and Heteroaromatic Compounds*, 1st ed. Wiley, 1994. doi: 10.1002/3527601724.

[120] H. Randriamahazaka and J. Ghilane, “Electrografting and Controlled Surface Functionalization of Carbon Based Surfaces for Electroanalysis,” *Electroanalysis*, vol. 28, no. 1, pp. 13–26, Jan. 2016, doi: 10.1002/elan.201500527.

[121] J. Lyskawa and D. Bélanger, “Direct Modification of a Gold Electrode with Aminophenyl Groups by Electrochemical Reduction of in Situ Generated Aminophenyl Monodiazonium Cations,” *Chem. Mater.*, vol. 18, no. 20, pp. 4755–4763, Oct. 2006, doi: 10.1021/cm060752d.

[122] P. M. S. Monk, R. J. Mortimer, and D. R. Rosseinsky, *Electrochromism and electrochromic devices*, 1. publ. Cambridge: Cambridge University Press, 2007.

[123] V. K. Thakur, G. Ding, J. Ma, P. S. Lee, and X. Lu, “Hybrid Materials and Polymer Electrolytes for Electrochromic Device Applications,” *Advanced Materials*, vol. 24, no. 30, pp. 4071–4096, Aug. 2012, doi: 10.1002/adma.201200213.

[124] J. Matsui, R. Kikuchi, and T. Miyashita, “A Trilayer Film Approach to Multicolor Electrochromism,” *J. Am. Chem. Soc.*, vol. 136, no. 3, pp. 842–845, Jan. 2014, doi: 10.1021/ja4107786.

[125] C. G. Granqvist, *Handbook of inorganic electrochromic materials*. Amsterdam: Elsevier, 1995.

[126] C. G. Granqvist, “Inorganic Non-Oxide Electrochromic Materials,” in *Handbook of Inorganic Electrochromic Materials*, Elsevier, 1995, pp. 421–430. doi: 10.1016/B978-044489930-9/50024-6.

[127] S. K. Deb, “A Novel Electrophotographic System,” *Appl. Opt.*, vol. 8, no. S1, p. 192, Jan. 1969, doi: 10.1364/AO.8.S1.000192.

[128] C. J. Schoot, J. J. Ponjee, H. T. Van Dam, R. A. Van Doorn, and P. T. Bolwijn, “New electrochromic memory display,” *Applied Physics Letters*, vol. 23, no. 2, pp. 64–65, Jul. 1973, doi: 10.1063/1.1654808.

[129] B. W. Faughnan, R. S. Crandall, and M. A. Lampert, “Model for the bleaching of WO3 electrochromic films by an electric field,” *Applied Physics Letters*, vol. 27, no. 5, pp. 275–277, Sep. 1975, doi: 10.1063/1.88464.

[130] R. S. Crandall and B. W. Faughnan, “Dynamics of coloration of amorphous electrochromic films of WO3 at low voltages,” *Applied Physics Letters*, vol. 28, no. 2, pp. 95–97, Jan. 1976, doi: 10.1063/1.88653.

[131] H. Shin, S. Seo, C. Park, J. Na, M. Han, and E. Kim, “Energy saving electrochromic windows from bistable low-HOMO level conjugated polymers,” *Energy Environ. Sci.*, vol. 9, no. 1, pp. 117–122, 2016, doi: 10.1039/C5EE03160E.

[132] J. Livage and D. Ganguli, “Sol–gel electrochromic coatings and devices: A review,” *Solar Energy Materials and Solar Cells*, vol. 68, no. 3–4, pp. 365–381, Jun. 2001, doi: 10.1016/S0927-0248(00)00369-X.

[133] C. Yan *et al.*, “Stretchable and Wearable Electrochromic Devices,” *ACS Nano*, vol. 8, no. 1, pp. 316–322, Jan. 2014, doi: 10.1021/nn404061g.

[134] D. T. Gillaspie, R. C. Tenent, and A. C. Dillon, “Metal-oxide films for electrochromic applications: present technology and future directions,” *J. Mater. Chem.*, vol. 20, no. 43, p. 9585, 2010, doi: 10.1039/c0jm00604a.

[135] P. R. Somani and S. Radhakrishnan, “Electrochromic materials and devices: present and future,” *Materials Chemistry and Physics*, vol. 77, no. 1, pp. 117–133, Jan. 2003, doi: 10.1016/S0254-0584(01)00575-2.

[136] C. Ho, I. D. Raistrick, and R. A. Huggins, “Application of A-C Techniques to the Study of Lithium Diffusion in Tungsten Trioxide Thin Films,” *J. Electrochem. Soc.*, vol. 127, no. 2, pp. 343–350, Feb. 1980, doi: 10.1149/1.2129668.

[137] R. S. Crandall and B. W. Faughnan, “Electronic Transport in Amorphous H x W O 3,” *Phys. Rev. Lett.*, vol. 39, no. 4, pp. 232–235, Jul. 1977, doi: 10.1103/PhysRevLett.39.232.

[138] I. Turyan, U. O. Krasovec, B. Orel, T. Saraidorov, R. Reisfeld, and D. Mandler, “‘Writing–Reading–Erasing’ on Tungsten Oxide Films Using the Scanning Electrochemical Microscope,” *Adv. Mater.*, vol. 12, no. 5, pp. 330–333, Mar. 2000, doi: 10.1002/(SICI)1521-4095(200003)12:5<330::AID-ADMA330>3.0.CO;2-8.

[139] V. Wittwer, O. F. Schirmer, and P. Schlotter, “Disorder dependence and optical detection of the Anderson transition in amorphous HxWO3 bronzes,” *Solid State Communications*, vol. 25, no. 12, pp. 977–980, Mar. 1978, doi: 10.1016/0038-1098(78)90887-6.

[140] F. G. K. Baucke, J. A. Duffy, and R. I. Smith, “Optical absorption of tungsten bronze thin films for electrochromic applications,” *Thin Solid Films*, vol. 186, no. 1, pp. 47–51, Apr. 1990, doi: 10.1016/0040-6090(90)90498-3.

[141] P. M. Beaujuge and J. R. Reynolds, “Color Control in π-Conjugated Organic Polymers for Use in Electrochromic Devices,” *Chem. Rev.*, vol. 110, no. 1, pp. 268–320, Jan. 2010, doi: 10.1021/cr900129a.

[142] P. M. Beaujuge, C. M. Amb, and J. R. Reynolds, “Spectral Engineering in π-Conjugated Polymers with Intramolecular Donor−Acceptor Interactions,” *Acc. Chem. Res.*, vol. 43, no. 11, pp. 1396–1407, Nov. 2010, doi: 10.1021/ar100043u.

[143] B. He *et al.*, “Low Bandgap Conjugated Polymers Based on a Nature-Inspired Bay-Annulated Indigo (BAI) Acceptor as Stable Electrochromic Materials,” *ACS Sustainable Chem. Eng.*, vol. 4, no. 5, pp. 2797–2805, May 2016, doi: 10.1021/acssuschemeng.6b00303.

[144] A. Cihaner and F. Algı, “A Novel Neutral State Green Polymeric Electrochromic with Superior n- and p-Doping Processes: Closer to Red-Blue-Green (RGB) Display Realization,” *Adv Funct Materials*, vol. 18, no. 22, pp. 3583–3589, Nov. 2008, doi: 10.1002/adfm.200801094.

[145] L. Groenendaal, F. Jonas, D. Freitag, H. Pielartzik, and J. R. Reynolds, “Poly(3,4-ethylenedioxythiophene) and Its Derivatives: Past, Present, and Future,” *Adv. Mater.*, vol. 12, no. 7, pp. 481–494, Apr. 2000, doi: 10.1002/(SICI)1521-4095(200004)12:7<481::AID-ADMA481>3.0.CO;2-C.

[146] W. Lu *et al.*, “Use of Ionic Liquids for π-Conjugated Polymer Electrochemical Devices,” *Science*, vol. 297, no. 5583, pp. 983–987, Aug. 2002, doi: 10.1126/science.1072651.

[147] C. L. Gaupp, D. M. Welsh, R. D. Rauh, and J. R. Reynolds, “Composite Coloration Efficiency Measurements of Electrochromic Polymers Based on 3,4-Alkylenedioxythiophenes,” *Chem. Mater.*, vol. 14, no. 9, pp. 3964–3970, Sep. 2002, doi: 10.1021/cm020433w.

[148] G. Zotti, S. Zecchin, G. Schiavon, and L. ‘Bert’ Groenendaal, “Electrochemical and chemical synthesis and characterization of sulfonated poly(3,4-ethylenedioxythiophene): A novel water-soluble and highly conductive conjugated oligomer,” *Macromol. Chem. Phys.*, vol. 203, no. 13, pp. 1958–1964, Sep. 2002, doi: 10.1002/1521-3935(200209)203:13<1958::AID-MACP1958>3.0.CO;2-X.

[149] S. Kirchmeyer and K. Reuter, “Scientific importance, properties and growing applications of poly(3,4-ethylenedioxythiophene),” *J. Mater. Chem.*, vol. 15, no. 21, p. 2077, 2005, doi: 10.1039/b417803n.

[150] G. Sonmez, H. B. Sonmez, C. K. F. Shen, and F. Wudl, “Red, Green, and Blue Colors in Polymeric Electrochromics,” *Advanced Materials*, vol. 16, no. 21, pp. 1905–1908, Nov. 2004, doi: 10.1002/adma.200400546.

[151] M. Moser, J. F. Ponder, A. Wadsworth, A. Giovannitti, and I. McCulloch, “Materials in Organic Electrochemical Transistors for Bioelectronic Applications: Past, Present, and Future,” *Adv Funct Materials*, vol. 29, no. 21, p. 1807033, May 2019, doi: 10.1002/adfm.201807033.

[152] S. Xiong, J. Ma, and X. Lu, “A complementary electrochromic device based on polyaniline tethered polyhedral oligomeric silsesquioxane and poly(3,4-ethylenedioxythiophene)/poly(4-styrene sulfonic acid),” *Solar Energy Materials and Solar Cells*, vol. 93, no. 12, pp. 2113–2117, Dec. 2009, doi: 10.1016/j.solmat.2009.06.006.

[153] A. F. Diaz and J. A. Logan, “Electroactive polyaniline films,” *Journal of Electroanalytical Chemistry and Interfacial Electrochemistry*, vol. 111, no. 1, pp. 111–114, Jul. 1980, doi: 10.1016/S0022-0728(80)80081-7.

[154] A. Watanabe, K. Mori, Y. Iwasaki, Y. Nakamura, and S. Niizuma, “Electrochromism of polyaniline film prepared by electrochemical polymerization,” *Macromolecules*, vol. 20, no. 8, pp. 1793–1796, Aug. 1987, doi: 10.1021/ma00174a015.

[155] S. Xiong, P. Jia, K. Y. Mya, J. Ma, F. Boey, and X. Lu, “Star-like polyaniline prepared from octa(aminophenyl) silsesquioxane: Enhanced electrochromic contrast and electrochemical stability,” *Electrochimica Acta*, vol. 53, no. 9, pp. 3523–3530, Mar. 2008, doi: 10.1016/j.electacta.2007.12.034.

[156] E. M. Girotto and M.-A. D. Paoli, “Polypyrrole Color Modulation and Electrochromic Contrast Enhancement by Doping with a Dye,” *Adv. Mater.*, vol. 10, no. 10, pp. 790–793, Jul. 1998, doi: 10.1002/(SICI)1521-4095(199807)10:10<790::AID-ADMA790>3.0.CO;2-R.

[157] P. Camurlu, “Polypyrrole derivatives for electrochromic applications,” *RSC Adv.*, vol. 4, no. 99, pp. 55832–55845, 2014, doi: 10.1039/C4RA11827H.

[158] W. W. Porter, T. P. Vaid, and A. L. Rheingold, “Synthesis and Characterization of a Highly Reducing Neutral ‘Extended Viologen’ and the Isostructural Hydrocarbon 4,4‘ ‘‘ ‘-Di- *n* -octyl- *p* -quaterphenyl,” *J. Am. Chem. Soc.*, vol. 127, no. 47, pp. 16559–16566, Nov. 2005, doi: 10.1021/ja053084q.

[159] G. Gao *et al.*, “Electrochromic Multilayer Films of Tunable Color by Combination of Copper or Iron Complex and Monolacunary Dawson-Type Polyoxometalate,” *J. Phys. Chem. B*, vol. 109, no. 18, pp. 8948–8953, May 2005, doi: 10.1021/jp044403n.

[160] S. Zhang, “Ferroin-based solid-state electrochromic display,” *Solid State Ionics*, vol. 52, no. 4, pp. 287–289, Jun. 1992, doi: 10.1016/0167-2738(92)90174-N.

[161] C. M. Elliott and J. G. Redepenning, “Stability and response studies of multicolor electrochromic polymer modified electrodes prepared from tris(5,5′-dicarboxyester-2,2′-bipyridine)ruthenium(II),” *Journal of Electroanalytical Chemistry and Interfacial Electrochemistry*, vol. 197, no. 1–2, pp. 219–232, Jan. 1986, doi: 10.1016/0022-0728(86)80151-6.

[162] C. Fan *et al.*, “Synthesis and Electrochromic Properties of New Terpyridine–Triphenylamine Hybrid Polymers,” *Macromolecules*, vol. 48, no. 18, pp. 6465–6473, Sep. 2015, doi: 10.1021/acs.macromol.5b00493.

[163] N. Vilà and A. Walcarius, “Bis(terpyridine) Iron(II) Functionalized Vertically-Oriented Nanostructured Silica Films: Toward Electrochromic Materials,” *Front. Chem.*, vol. 8, p. 830, Sep. 2020, doi: 10.3389/fchem.2020.00830.

[164] M. Scheuble, M. Goll, and S. Ludwigs, “Branched Terthiophenes in Organic Electronics: From Small Molecules to Polymers,” *Macromol. Rapid Commun.*, vol. 36, no. 2, pp. 115–137, Jan. 2015, doi: 10.1002/marc.201400525.

[165] C. M. Amb, A. L. Dyer, and J. R. Reynolds, “Navigating the Color Palette of Solution-Processable Electrochromic Polymers,” *Chem. Mater.*, vol. 23, no. 3, pp. 397–415, Feb. 2011, doi: 10.1021/cm1021245.

[166] T. Kamimori, J. Nagai, and M. Mizuhashi, “Electrochromic devices for transmissive and reflective light control,” *Solar Energy Materials*, vol. 16, no. 1–3, pp. 27–38, Aug. 1987, doi: 10.1016/0165-1633(87)90005-0.

[167] H. Diao *et al.*, “High Performance Cross-Linked Poly(2-acrylamido-2-methylpropanesulfonic acid)-Based Proton Exchange Membranes for Fuel Cells,” *Macromolecules*, vol. 43, no. 15, pp. 6398–6405, Aug. 2010, doi: 10.1021/ma1010099.

[168] J. Wang, E. Khoo, P. S. Lee, and J. Ma, “Controlled Synthesis of WO_3 Nanorods and Their Electrochromic Properties in H_2 SO_4 Electrolyte,” *J. Phys. Chem. C*, vol. 113, no. 22, pp. 9655–9658, Jun. 2009, doi: 10.1021/jp901650v.

[169] D. D. Yao, R. A. Rani, A. P. O’Mullane, K. Kalantar-zadeh, and J. Z. Ou, “Enhanced Coloration Efficiency for Electrochromic Devices based on Anodized Nb_2 O_5

/Electrodeposited MoO_3 Binary Systems," *J. Phys. Chem. C*, vol. 118, no. 20, pp. 10867–10873, May 2014, doi: 10.1021/jp5017888.

[170] P. Jia *et al.*, "Enhanced Electrochromic Switching in Multilayer Thin Films of Polyaniline-Tethered Silsesquioxane Nanocage," *Chem. Mater.*, vol. 21, no. 19, pp. 4434–4441, Oct. 2009, doi: 10.1021/cm9009817.

[171] F. S. Kim, G. Ren, and S. A. Jenekhe, "One-Dimensional Nanostructures of π-Conjugated Molecular Systems: Assembly, Properties, and Applications from Photovoltaics, Sensors, and Nanophotonics to Nanoelectronics," *Chem. Mater.*, vol. 23, no. 3, pp. 682–732, Feb. 2011, doi: 10.1021/cm102772x.

[172] G. Zhou, L. Xu, G. Hu, L. Mai, and Y. Cui, "Nanowires for Electrochemical Energy Storage," *Chem. Rev.*, vol. 119, no. 20, pp. 11042–11109, Oct. 2019, doi: 10.1021/acs.chemrev.9b00326.

[173] D. Huo, M. J. Kim, Z. Lyu, Y. Shi, B. J. Wiley, and Y. Xia, "One-Dimensional Metal Nanostructures: From Colloidal Syntheses to Applications," *Chem. Rev.*, vol. 119, no. 15, pp. 8972–9073, Aug. 2019, doi: 10.1021/acs.chemrev.8b00745.

[174] H. Liang, S. Liu, and S. Yu, "Controlled Synthesis of One-Dimensional Inorganic Nanostructures Using Pre-Existing One-Dimensional Nanostructures as Templates," *Advanced Materials*, vol. 22, no. 35, pp. 3925–3937, Sep. 2010, doi: 10.1002/adma.200904391.

[175] M. Hernández-Vélez, "Nanowires and 1D arrays fabrication: An overview," *Thin Solid Films*, vol. 495, no. 1–2, pp. 51–63, Jan. 2006, doi: 10.1016/j.tsf.2005.08.331.

[176] J. Martín, J. Maiz, J. Sacristan, and C. Mijangos, "Tailored polymer-based nanorods and nanotubes by 'template synthesis': From preparation to applications," *Polymer*, vol. 53, no. 6, pp. 1149–1166, Mar. 2012, doi: 10.1016/j.polymer.2012.01.028.

[177] S. Jarmolińska, A. Feliczak-Guzik, and I. Nowak, "Synthesis, Characterization and Use of Mesoporous Silicas of the Following Types SBA-1, SBA-2, HMM-1 and HMM-2," *Materials*, vol. 13, no. 19, p. 4385, Oct. 2020, doi: 10.3390/ma13194385.

[178] T. Nasir, G. Herzog, M. Hébrant, C. Despas, L. Liu, and A. Walcarius, "Mesoporous Silica Thin Films for Improved Electrochemical Detection of Paraquat," *ACS Sens.*, vol. 3, no. 2, pp. 484–493, Feb. 2018, doi: 10.1021/acssensors.7b00920.

[179] A. Walcarius, “Mesoporous materials and electrochemistry,” *Chem. Soc. Rev.*, vol. 42, no. 9, p. 4098, 2013, doi: 10.1039/c2cs35322a.

[180] T. M. Budnyak, I. V. Pylypchuk, V. A. Tertykh, E. S. Yanovska, and D. Kolodynska, “Synthesis and adsorption properties of chitosan-silica nanocomposite prepared by sol-gel method,” *Nanoscale Res Lett*, vol. 10, no. 1, p. 87, Dec. 2015, doi: 10.1186/s11671-014-0722-1.

[181] F. Hoffmann, M. Cornelius, J. Morell, and M. Fröba, “Silica-Based Mesoporous Organic–Inorganic Hybrid Materials,” *Angew Chem Int Ed*, vol. 45, no. 20, pp. 3216–3251, May 2006, doi: 10.1002/anie.200503075.

[182] S. Jarmolińska, A. Feliczak-Guzik, and I. Nowak, “Synthesis, Characterization and Use of Mesoporous Silicas of the Following Types SBA-1, SBA-2, HMM-1 and HMM-2,” *Materials*, vol. 13, no. 19, p. 4385, Oct. 2020, doi: 10.3390/ma13194385.

[183] S. Che, Z. Liu, T. Ohsuna, K. Sakamoto, O. Terasaki, and T. Tatsumi, “Synthesis and characterization of chiral mesoporous silica,” *Nature*, vol. 429, no. 6989, pp. 281–284, May 2004, doi: 10.1038/nature02529.

[184] R. Narayan, U. Y. Nayak, A. M. Raichur, and S. Garg, “Mesoporous Silica Nanoparticles: A Comprehensive Review on Synthesis and Recent Advances,” *Pharmaceutics*, vol. 10, no. 3, p. 118, Aug. 2018, doi: 10.3390/pharmaceutics10030118.

[185] T. Sikolenko, C. Despas, N. Vilà, and A. Walcarius, “Thickness control in electrogenerated mesoporous silica films by wet etching and electrochemical monitoring of the process,” *Electrochemistry Communications*, vol. 100, pp. 11–15, Mar. 2019, doi: 10.1016/j.elecom.2019.01.013.

[186] M. Kobayashi *et al.*, “Thickness control of 3-dimensional mesoporous silica ultrathin films by wet-etching,” *Nanoscale*, vol. 9, no. 24, pp. 8321–8329, 2017, doi: 10.1039/C7NR01560G.

[187] D. Grosso *et al.*, “Fundamentals of Mesostructuring Through Evaporation-Induced Self-Assembly,” *Adv Funct Materials*, vol. 14, no. 4, pp. 309–322, Apr. 2004, doi: 10.1002/adfm.200305036.

[188] Y. Lu *et al.*, “Continuous formation of supported cubic and hexagonal mesoporous films by sol–gel dip-coating,” *Nature*, vol. 389, no. 6649, pp. 364–368, Sep. 1997, doi: 10.1038/38699.

[189] D. Zhao, P. Yang, D. I. Margolese, and G. D. Stucky, “Synthesis of continuous mesoporous silica thin films with three-dimensional accessible pore structures,” *Chem. Commun.*, no. 22, pp. 2499–2500, 1998, doi: 10.1039/a804649b.

[190] Z. Teng *et al.*, “Highly Ordered Mesoporous Silica Films with Perpendicular Mesochannels by a Simple Stöber-Solution Growth Approach,” *Angew Chem Int Ed*, vol. 51, no. 9, pp. 2173–2177, Feb. 2012, doi: 10.1002/anie.201108748.

[191] Y. Guillemin, M. Etienne, E. Sibottier, and A. Walcarius, “Microscale Controlled Electrogeneration of Patterned Mesoporous Silica Thin Films,” *Chem. Mater.*, vol. 23, no. 24, pp. 5313–5322, Dec. 2011, doi: 10.1021/cm202668t.

[192] A. Walcarius, E. Sibottier, M. Etienne, and J. Ghanbaja, “Electrochemically assisted self-assembly of mesoporous silica thin films,” *Nature Mater*, vol. 6, no. 8, pp. 602–608, Aug. 2007, doi: 10.1038/nmat1951.

[193] T. Nasir, L. Zhang, N. Vilà, G. Herzog, and A. Walcarius, “Electrografting of 3-Aminopropyltriethoxysilane on a Glassy Carbon Electrode for the Improved Adhesion of Vertically Oriented Mesoporous Silica Thin Films,” *Langmuir*, vol. 32, no. 17, pp. 4323–4332, May 2016, doi: 10.1021/acs.langmuir.6b00798.

[194] A. Goux, M. Etienne, E. Aubert, C. Lecomte, J. Ghanbaja, and A. Walcarius, “Oriented Mesoporous Silica Films Obtained by Electro-Assisted Self-Assembly (EASA),” *Chem. Mater.*, vol. 21, no. 4, pp. 731–741, Feb. 2009, doi: 10.1021/cm8029664.

[195] G. Herzog, E. Sibottier, M. Etienne, and A. Walcarius, “Electrochemically assisted self-assembly of ordered and functionalized mesoporous silica films: impact of the electrode geometry and size on film formation and properties,” *Faraday Discuss.*, vol. 164, p. 259, 2013, doi: 10.1039/c3fd00021d.

[196] T. Nasir, N. A. Vodolazkaya, G. Herzog, and A. Walcarius, “Critical Effect of Film Thickness on Preconcentration Electroanalysis with Oriented Mesoporous Silica Modified Electrodes,” *Electroanalysis*, vol. 31, no. 2, pp. 202–207, Feb. 2019, doi: 10.1002/elan.201800533.

[197] A. Walcarius, “Silica-based electrochemical sensors and biosensors: Recent trends,” *Current Opinion in Electrochemistry*, vol. 10, pp. 88–97, Aug. 2018, doi: 10.1016/j.coelec.2018.03.017.

[198] M. Etienne, L. Zhang, N. Vilà, and A. Walcarius, “Mesoporous Materials-Based Electrochemical Enzymatic Biosensors,” *Electroanalysis*, vol. 27, no. 9, pp. 2028–2054, Sep. 2015, doi: 10.1002/elan.201500172.

[199] A. Walcarius, “Mesoporous Materials-Based Electrochemical Sensors,” *Electroanalysis*, vol. 27, no. 6, pp. 1303–1340, Jun. 2015, doi: 10.1002/elan.201400628.

[200] N. Vilà and A. Walcarius, “Electrochemical response of vertically-aligned, ferrocene-functionalized mesoporous silica films: effect of the supporting electrolyte,” *Electrochimica Acta*, vol. 179, pp. 304–314, Oct. 2015, doi: 10.1016/j.electacta.2015.02.169.

[201] S. Ahoulou, N. Vilà, S. Pillet, D. Schaniel, and A. Walcarius, “Non-covalent Immobilization of Iron-triazole ($Fe(Htrz)_3$) Molecular Mediator in Mesoporous Silica Films for the Electrochemical Detection of Hydrogen Peroxide,” *Electroanalysis*, vol. 32, no. 4, pp. 690–697, Apr. 2020, doi: 10.1002/elan.201900444.

[202] M. G. Bellino, A. E. Regazzoni, and G. J. A. A. Soler-Illia, “Amylase-Functionalized Mesoporous Silica Thin Films as Robust Biocatalyst Platforms,” *ACS Appl. Mater. Interfaces*, vol. 2, no. 2, pp. 360–365, Feb. 2010, doi: 10.1021/am900645b.

[203] J. Wang, N. Vilà, and A. Walcarius, “Redox-Active Vertically Aligned Mesoporous Silica Thin Films as Transparent Surfaces for Energy Storage Applications,” *ACS Appl. Mater. Interfaces*, vol. 12, no. 21, pp. 24262–24270, May 2020, doi: 10.1021/acsami.0c03650.

[204] A. M. R. Ramírez, M. A. Gacitúa, E. Ortega, F. R. Díaz, and M. A. Del Valle, “Electrochemical in situ synthesis of polypyrrole nanowires,” *Electrochemistry Communications*, vol. 102, pp. 94–98, May 2019, doi: 10.1016/j.elecom.2019.04.007.

[205] M. C. Fuertes, M. Marchena, M. C. Marchi, A. Wolosiuk, and G. J. A. A. Soler-Illia, “Controlled Deposition of Silver Nanoparticles in Mesoporous Single- or Multilayer Thin Films: From Tuned Pore Filling to Selective Spatial Location of Nanometric Objects,” *Small*, vol. 5, no. 2, pp. 272–280, Jan. 2009, doi: 10.1002/smll.200800894.

[206] S. M. Fonseca, T. Moreira, A. J. Parola, C. Pinheiro, and C. A. T. Laia, “PEDOT electrodeposition on oriented mesoporous silica templates for electrochromic devices,” *Solar Energy Materials and Solar Cells*, vol. 159, pp. 94–101, Jan. 2017, doi: 10.1016/j.solmat.2016.09.002.

[207] B. K. Kuila and M. Stamm, “Fabrication of oriented polyaniline nanostructures using block copolymer nanotemplates and their optical, electrochemical and electric properties,” *J. Mater. Chem.*, vol. 20, no. 29, p. 6086, 2010, doi: 10.1039/c0jm00352b.

[208] W. Ullah, G. Herzog, N. Vilà, and A. Walcarius, “Polyaniline nanowire arrays generated through oriented mesoporous silica films: effect of pore size and spectroelectrochemical response,” *Faraday Discuss.*, vol. 233, pp. 77–99, 2022, doi: 10.1039/D1FD00034A.

[209] C. Schotten, T. P. Nicholls, R. A. Bourne, N. Kapur, B. N. Nguyen, and C. E. Willans, “Making electrochemistry easily accessible to the synthetic chemist,” *Green Chem.*, vol. 22, no. 11, pp. 3358–3375, 2020, doi: 10.1039/D0GC01247E.

[210] L. L. Faulkner and A. J. Bard, *Electrochemical methods and applications*, 2nd ed. New Yor: Wiley, 2001.

[211] F. Scholz, Ed., *Electroanalytical Methods*. Berlin, Heidelberg: Springer Berlin Heidelberg, 2005. doi: 10.1007/978-3-662-04757-6.

[212] A. Escarpa, M. C. González, and M. Á. López, *Agricultural and Food Electroanalysis*, 1st ed. Wiley, 2015. doi: 10.1002/9781118684030.

[213] J. Hoyos-Arbeláez, M. Vázquez, and J. Contreras-Calderón, “Electrochemical methods as a tool for determining the antioxidant capacity of food and beverages: A review,” *Food Chemistry*, vol. 221, pp. 1371–1381, Apr. 2017, doi: 10.1016/j.foodchem.2016.11.017.

[214] N. Elgrishi, K. J. Rountree, B. D. McCarthy, E. S. Rountree, T. T. Eisenhart, and J. L. Dempsey, “A Practical Beginner’s Guide to Cyclic Voltammetry,” *J. Chem. Educ.*, vol. 95, no. 2, pp. 197–206, Feb. 2018, doi: 10.1021/acs.jchemed.7b00361.

[215] M. Rafiee, D. J. Abrams, L. Cardinale, Z. Goss, A. Romero-Arenas, and S. S. Stahl, “Cyclic voltammetry and chronoamperometry: mechanistic tools for organic electrosynthesis,” *Chem. Soc. Rev.*, vol. 53, no. 2, pp. 566–585, 2024, doi: 10.1039/D2CS00706A.

[216] A. Mandru, J. Mane, and R. Mandapati, “A Review on UV-visible spectroscopy,” Dec. 2023, doi: 10.5281/ZENODO.10232708.

[217] D. N. G. Krishna and J. Philip, “Review on surface-characterization applications of X-ray photoelectron spectroscopy (XPS): Recent developments and challenges,” *Applied Surface Science Advances*, vol. 12, p. 100332, Dec. 2022, doi: 10.1016/j.apsadv.2022.100332.

[218] A. Orlando *et al.*, “A Comprehensive Review on Raman Spectroscopy Applications,” *Chemosensors*, vol. 9, no. 9, p. 262, Sep. 2021, doi: 10.3390/chemosensors9090262.

[219] P. Müller-Buschbaum, “A Basic Introduction to Grazing Incidence Small-Angle X-Ray Scattering,” in *Applications of Synchrotron Light to Scattering and Diffraction in Materials and Life Sciences*, vol. 776, M. Gomez, A. Nogales, M. C. Garcia-Gutierrez, and T. A. Ezquerra, Eds., in Lecture Notes in Physics, vol. 776. , Berlin, Heidelberg: Springer Berlin Heidelberg, 2009, pp. 61–89. doi: 10.1007/978-3-540-95968-7_3.

[220] J. Heinze, B. A. Frontana-Uribe, and S. Ludwigs, “Electrochemistry of Conducting Polymers—Persistent Models and New Concepts,” *Chem. Rev.*, vol. 110, no. 8, pp. 4724–4771, Aug. 2010, doi: 10.1021/cr900226k.

[221] G. Sabouraud, S. Sadki, and N. Brodie, “The mechanisms of pyrrole electropolymerization,” *Chem. Soc. Rev.*, vol. 29, no. 5, pp. 283–293, 2000, doi: 10.1039/a807124a.

[222] T. McCormac and D. Farrell, “Electrochemical investigation into the interaction between various pyrrole moieties and the well-known electron acceptor, tetracyanoethylene,” *Electrochimica Acta*, vol. 46, no. 20–21, pp. 3287–3299, Jul. 2001, doi: 10.1016/S0013-4686(01)00621-1.

[223] Y. Shi, G. Wang, Q. Chen, J. Zheng, and C. Xu, “Electrochromism and electrochromic devices of new extended viologen derivatives with various substituent benzene,” *Solar Energy Materials and Solar Cells*, vol. 208, p. 110413, May 2020, doi: 10.1016/j.solmat.2020.110413.

[224] M. H. Rahman *et al.*, “Recent Progress on Electroactive Polymers: Synthesis, Properties and Applications,” *Ceramics*, vol. 4, no. 3, pp. 516–541, Sep. 2021, doi: 10.3390/ceramics4030038.

[225] T.-H. Le, Y. Kim, and H. Yoon, “Electrical and Electrochemical Properties of Conducting Polymers,” *Polymers*, vol. 9, no. 4, p. 150, Apr. 2017, doi: 10.3390/polym9040150.

[226] J. H. T. Luong, T. Narayan, S. Solanki, and B. D. Malhotra, “Recent Advances of Conducting Polymers and Their Composites for Electrochemical Biosensing Applications,” *JFB*, vol. 11, no. 4, p. 71, Sep. 2020, doi: 10.3390/jfb11040071.

[227] M. Ates, “A review study of (bio)sensor systems based on conducting polymers,” *Materials Science and Engineering: C*, vol. 33, no. 4, pp. 1853–1859, May 2013, doi: 10.1016/j.msec.2013.01.035.

[228] T. Zidarič, D. Majer, T. Maver, M. Finšgar, and U. Maver, “The development of an electropolymerized, molecularly imprinted polymer (MIP) sensor for insulin determination using single-drop analysis,” *Analyst*, vol. 148, no. 5, pp. 1102–1115, 2023, doi: 10.1039/D2AN02025D.

[229] C.-X. Zhang, S.-L. Mei, X.-H. Chen, E.-T. Liu, and C.-J. Yao, “Electrochemical construction of functional polymers and their application advances in lithium batteries,” *J. Mater. Chem. C*, vol. 9, no. 48, pp. 17182–17200, 2021, doi: 10.1039/D1TC05311F.

[230] G. Roselló-Márquez, D. M. García-García, M. Cifre-Herrando, and J. García-Antón, “Electropolymerization of PPy, PEDOT, and PANi on WO3 nanostructures for high-performance anodes in Li-ion batteries,” *Heliyon*, vol. 10, no. 24, p. e41075, Dec. 2024, doi: 10.1016/j.heliyon.2024.e41075.

[231] T. Nicolini, B. A. Frontana-Uribe, A. Kuhn, and G. Salinas, “Tuning the Electrochemical Properties of Poly-thiophenes with a 2,5-Dithienil-N-subtituted-pyrrole Bearing an Aniline Moiety for Electrochromic Devices,” *ChemElectroChem*, vol. 10, no. 24, p. e202300346, Dec. 2023, doi: 10.1002/celc.202300346.

[232] C. Gu, A.-B. Jia, Y.-M. Zhang, and S. X.-A. Zhang, “Emerging Electrochromic Materials and Devices for Future Displays,” *Chem. Rev.*, vol. 122, no. 18, pp. 14679–14721, Sep. 2022, doi: 10.1021/acs.chemrev.1c01055.

[233] V. Rai, R. S. Singh, D. J. Blackwood, and D. Zhili, “A Review on Recent Advances in Electrochromic Devices: A Material Approach,” *Adv Eng Mater*, vol. 22, no. 8, p. 2000082, Aug. 2020, doi: 10.1002/adem.202000082.

[234] T. F. Otero and J. G. Martinez, “Electro-chemo-biomimetics from conducting polymers: fundamentals, materials, properties and devices,” *J. Mater. Chem. B*, vol. 4, no. 12, pp. 2069–2085, 2016, doi: 10.1039/C6TB00060F.

[235] H. Bai, C. Li, and G. Shi, “Electrochemical Fabrication of Superhydrophobic Surfaces on Metal and Semiconductor Substrates,” *Journal of Adhesion Science and Technology*, vol. 22, no. 15, pp. 1819–1839, Jan. 2008, doi: 10.1163/156856108X319999.

[236] M. Fatahiamirdehi, M. Mahani, S. F. Mirseyed, A. Rostamian, and M. Ostadhassan, “Enhancing corrosion resistance of 316L stainless steel through electrochemical deposition of polyaniline coatings in acidic environments,” *J Mater Sci*, vol. 59, no. 31, pp. 14716–14727, Aug. 2024, doi: 10.1007/s10853-024-10047-2.

[237] M. Gvozdenovic, B. Jugovic, J. Stevanovic, and B. Grgur, “Electrochemical synthesis of electroconducting polymers,” *Hem Ind*, vol. 68, no. 6, pp. 673–684, 2014, doi: 10.2298/HEMIND131122008G.

[238] A. F. Diaz and J. A. Logan, “Electroactive polyaniline films,” *Journal of Electroanalytical Chemistry and Interfacial Electrochemistry*, vol. 111, no. 1, pp. 111–114, Jul. 1980, doi: 10.1016/S0022-0728(80)80081-7.

[239] M. Onoda, T. Iwasa, T. Kawai, K. Yoshino, J. Nakayama, and H. Nakahara, “Electrochemical polymerization of oligothiophene derivatives and their doping properties,” *Synthetic Metals*, vol. 55, no. 2–3, pp. 1632–1637, Mar. 1993, doi: 10.1016/0379-6779(93)90297-A.

[240] A.-N. Chowdhury, Ed., *Trends in polyaniline research*. in Chemistry research and applications. New York: Nova Science Publishers, Incorporated, 2013.

[241] A. F. Diaz, K. K. Kanazawa, and G. P. Gardini, “Electrochemical polymerization of pyrrole,” *J. Chem. Soc., Chem. Commun.*, no. 14, p. 635, 1979, doi: 10.1039/c39790000635.

[242] M. M., B. Z., J. S., T. Lj., and B. N., “Electrochemical Polymerization of Aniline,” in *Electropolymerization*, E. Schab-Balcerzak, Ed., InTech, 2011. doi: 10.5772/28293.

[243] P. G. Pickup, “Conjugated metallopolymers. Redox polymers with interacting metal based redox sites,” *J. Mater. Chem.*, vol. 9, no. 8, pp. 1641–1653, 1999, doi: 10.1039/a902244i.

[244] J. Hjelm, R. W. Handel, A. Hagfeldt, E. C. Constable, C. E. Housecroft, and R. J. Forster, “Conducting Polymers Containing In-Chain Metal Centers: Electropolymerization of Oligothienyl-Substituted {M(tpy)$_2$ } Complexes and in Situ Conductivity Studies, M = Os(II), Ru(II),” *Inorg. Chem.*, vol. 44, no. 4, pp. 1073–1081, Feb. 2005, doi: 10.1021/ic049221m.

[245] K. Takada, G. D. Storrier, F. Pariente, and H. D. Abruña, “EQCM Studies of the Redox Processes during and after Electropolymerization of Films of Transition-Metal Complexes of Vinylterpyridine,” *J. Phys. Chem. B*, vol. 102, no. 8, pp. 1387–1396, Feb. 1998, doi: 10.1021/jp971860d.

[246] H. C. Hurrell, A. L. Mogstad, D. A. Usifer, K. T. Potts, and H. D. Abruna, “Electrocatalytic activity of electropolymerized films of bis(vinylterpyridine)cobalt(2+) for the reduction of carbon dioxide and oxygen,” *Inorg. Chem.*, vol. 28, no. 6, pp. 1080–1084, Mar. 1989, doi: 10.1021/ic00305a016.

[247] C. Arana, M. Keshavarz, K. T. Potts, and H. D. Abruña, “Electrocatalytic reduction of CO2 and O2 with electropolymerized films of vinyl-terpyridine complexes of Fe, Ni and Co,” *Inorganica Chimica Acta*, vol. 225, no. 1–2, pp. 285–295, Oct. 1994, doi: 10.1016/0020-1693(94)04059-1.

[248] C.-J. Yao, Y.-W. Zhong, and J. Yao, “Five-Stage Near-Infrared Electrochromism in Electropolymerized Films Composed of Alternating Cyclometalated Bisruthenium and Bis-triarylamine Segments,” *Inorg. Chem.*, vol. 52, no. 17, pp. 10000–10008, Sep. 2013, doi: 10.1021/ic401288g.

[249] B.-B. Cui, H.-J. Nie, C.-J. Yao, J.-Y. Shao, S.-H. Wu, and Y.-W. Zhong, “Reductive electropolymerization of bis-tridentate ruthenium complexes with 5,5″-divinyl-4′-tolyl-2,2′:6′,2″-terpyridine,” *Dalton Trans.*, vol. 42, no. 39, p. 14125, 2013, doi: 10.1039/c3dt51627j.

[250] P. S. Sharma, A. Pietrzyk-Le, F. D’Souza, and W. Kutner, “Electrochemically synthesized polymers in molecular imprinting for chemical sensing,” *Anal Bioanal Chem*, vol. 402, no. 10, pp. 3177–3204, Apr. 2012, doi: 10.1007/s00216-011-5696-6.

[251] K.-H. Wu, R. Sakamoto, H. Maeda, E. J. H. Phua, and H. Nishihara, “Ultralong π-Conjugated Bis(terpyridine)metal Polymer Wires Covalently Bound to a Carbon Electrode: Fast Redox Conduction and Redox Diode Characteristics,” *Molecules*, vol. 26, no. 14, p. 4267, Jul. 2021, doi: 10.3390/molecules26144267.

[252] K. Hanabusa, A. Nakamura, T. Koyama, and H. Shirai, “Electropolymerization and characterization of terpyridinyl iron (II) and ruthenium (II) complexes,” *Polymer International*, vol. 35, no. 3, pp. 231–238, Nov. 1994, doi: 10.1002/pi.1994.210350303.

[253] B. R. L. Ferraz, T. Guimarães, D. Profeti, and L. P. R. Profeti, “Electrooxidation of sulfanilamide and its voltammetric determination in pharmaceutical formulation, human urine and serum on glassy carbon electrode,” *Journal of Pharmaceutical Analysis*, vol. 8, no. 1, pp. 55–59, Feb. 2018, doi: 10.1016/j.jpha.2017.10.004.

[254] Y.-Q. Wang, H.-Z. Yu, J.-Z. Cheng, J.-W. Zhao, S.-M. Cai, and Z.-F. Liu, “End-Group-Dominated Electrochemical Kinetics of Azobenzene Self-Assembled Monolayers on Gold,” *Langmuir*, vol. 12, no. 22, pp. 5466–5471, Jan. 1996, doi: 10.1021/la960270o.

[255] H. Zhu *et al.*, “An iron supramolecular compound containing terpyridine polycarboxylic acid for high performance lithium-ion batteries,” *Inorganica Chimica Acta*, vol. 535, p. 120848, May 2022, doi: 10.1016/j.ica.2022.120848.

[256] K.-H. Wu, R. Sakamoto, H. Maeda, E. J. H. Phua, and H. Nishihara, “Ultralong π-Conjugated Bis(terpyridine)metal Polymer Wires Covalently Bound to a Carbon Electrode: Fast Redox Conduction and Redox Diode Characteristics,” *Molecules*, vol. 26, no. 14, p. 4267, Jul. 2021, doi: 10.3390/molecules26144267.

[257] S. Lin, Q. Wu, and Y. Lu, “Recent Progress of the Application of Electropolymerization in Batteries and Supercapacitors: Specific Design of Functions in Electrodes,” *ChemElectroChem*, vol. 11, no. 12, p. e202300776, Jun. 2024, doi: 10.1002/celc.202300776.

[258] Y. Wang, T. Liu, L. Chen, and D. Chao, “Water-Assisted Highly Efficient Photocatalytic Reduction of CO_2 to CO with Noble Metal-Free Bis(terpyridine)iron(II) Complexes and an Organic Photosensitizer,” *Inorg. Chem.*, vol. 60, no. 8, pp. 5590–5597, Apr. 2021, doi: 10.1021/acs.inorgchem.0c03503.

[259] S. Wawzonek and T. W. McIntyre, “Electrolytic Preparation of Azobenzenes,” *J. Electrochem. Soc.*, vol. 119, no. 10, p. 1350, 1972, doi: 10.1149/1.2403994.

[260] L. R. Sharma, A. K. Manchanda, G. Singh, and R. S. Verma, “Cyclic voltammetry of aromatic amines in aqueous and non-aqueous media,” *Electrochimica Acta*, vol. 27, no. 2, pp. 223–233, Feb. 1982, doi: 10.1016/0013-4686(82)80007-8.

[261] M. Matsushita, H. Kuramitz, and S. Tanaka, “Electrochemical Oxidation for Low Concentration of Aniline in Neutral pH Medium: Application to the Removal of Aniline Based on the Electrochemical Polymerization on a Carbon Fiber,” *Environ. Sci. Technol.*, vol. 39, no. 10, pp. 3805–3810, May 2005, doi: 10.1021/es040379f.

[262] L. Liu, S. Yellinek, I. Valdinger, A. Donval, and D. Mandler, “Important Implications of the Electrochemical Reduction of ITO,” *Electrochimica Acta*, vol. 176, pp. 1374–1381, Sep. 2015, doi: 10.1016/j.electacta.2015.07.129.

[263] M. Beregoi *et al.*, “Electrochromic properties of polyaniline-coated fiber webs for tissue engineering applications,” *International Journal of Pharmaceutics*, vol. 510, no. 2, pp. 465–473, Aug. 2016, doi: 10.1016/j.ijpharm.2015.11.055.

[264] S. Mu, C. Chen, and J. Wang, “The kinetic behavior for the electrochemical polymerization of aniline in aqueous solution,” *Synthetic Metals*, vol. 88, no. 3, pp. 249–254, Jun. 1997, doi: 10.1016/S0379-6779(97)03863-0.

[265] G. A. Planes, J. L. Rodríguez, M. C. Miras, G. García, E. Pastor, and C. A. Barbero, “Spectroscopic evidence for intermediate species formed during aniline polymerization and polyaniline degradation,” *Phys. Chem. Chem. Phys.*, vol. 12, no. 35, p. 10584, 2010, doi: 10.1039/c002920c.

[266] E. M. Genies and C. Tsintavis, “Redox mechanism and electrochemical behaviour or polyaniline deposits,” *Journal of Electroanalytical Chemistry and Interfacial Electrochemistry*, vol. 195, no. 1, pp. 109–128, Nov. 1985, doi: 10.1016/0022-0728(85)80009-7.

[267] C. Gautier, “A post-functionalization toolbox for diazonium (electro)-grafted surfaces: review of the coupling methods,” 2021.

[268] “Gautier - 2021 - A post-functionalization toolbox for diazonium (el.pdf.”

[269] M. Kehrer *et al.*, “XPS investigation on the reactivity of surface imine groups with TFAA,” *Plasma Processes & Polymers*, vol. 16, no. 4, p. 1800160, Apr. 2019, doi: 10.1002/ppap.201800160.

[270] M. C. Biesinger, L. W. M. Lau, A. R. Gerson, and R. St. C. Smart, “Resolving surface chemical states in XPS analysis of first row transition metals, oxides and hydroxides: Sc, Ti, V, Cu and Zn,” *Applied Surface Science*, vol. 257, no. 3, pp. 887–898, Nov. 2010, doi: 10.1016/j.apsusc.2010.07.086.

[271] G. Bichot, X. Sallenave, R. Métivier, and S. Péralta, “Synthesis and characterization of new push-pull azobenzene. Cis → Trans isomerization kinetic study,” *Dyes and Pigments*, vol. 239, p. 112774, Aug. 2025, doi: 10.1016/j.dyepig.2025.112774.

[272] Y.-W. Zhong, N. Vila, J. C. Henderson, and H. D. Abruña, “Dithienylcyclopentenes-Containing Transition Metal Bisterpyridine Complexes Directed toward Molecular Electronic Applications,” *Inorg. Chem.*, vol. 48, no. 3, pp. 991–999, Feb. 2009, doi: 10.1021/ic801588y.

[273] N. Vilà, Y.-W. Zhong, J. C. Henderson, and H. D. Abruña, “Anthracene-Bridged Binuclear Ruthenium Complexes: Electrochemical and Spectroscopic Evidence of Electronic

Communication Through the π System," *Inorg. Chem.*, vol. 49, no. 3, pp. 796–804, Feb. 2010, doi: 10.1021/ic900100w.

[274] M. T. Gamache, B. Gehring, G. S. Hanan, and D. G. Kurth, "Spectro-electrochemical study of iron and ruthenium bis-terpyridine complexes with methyl viologen-like subunits as models for supramolecular polymers," *Dalton Trans.*, vol. 53, no. 31, pp. 13151–13159, 2024, doi: 10.1039/D4DT00974F.

[275] H. J. N. P. D. Mello and M. Mulato, "Effect of aniline monomer concentration on PANI electropolymerization process and its influence for applications in chemical sensors," *Synthetic Metals*, vol. 239, pp. 66–70, May 2018, doi: 10.1016/j.synthmet.2018.02.008.

[276] S. Kulandaivalu, Z. Zainal, and Y. Sulaiman, "Influence of Monomer Concentration on the Morphologies and Electrochemical Properties of PEDOT, PANI, and PPy Prepared from Aqueous Solution," *International Journal of Polymer Science*, vol. 2016, pp. 1–12, 2016, doi: 10.1155/2016/8518293.

[277] T. Trindade, P. O'Brien, and N. L. Pickett, "Nanocrystalline Semiconductors: Synthesis, Properties, and Perspectives," *Chem. Mater.*, vol. 13, no. 11, pp. 3843–3858, Nov. 2001, doi: 10.1021/cm000843p.

[278] J. Hu, T. W. Odom, and C. M. Lieber, "Chemistry and Physics in One Dimension: Synthesis and Properties of Nanowires and Nanotubes," *Acc. Chem. Res.*, vol. 32, no. 5, pp. 435–445, May 1999, doi: 10.1021/ar9700365.

[279] D. Van Noort and C.-F. Mandenius, "Porous gold surfaces for biosensor applications," *Biosensors and Bioelectronics*, vol. 15, no. 3–4, pp. 203–209, Jun. 2000, doi: 10.1016/S0956-5663(00)00061-0.

[280] Paras *et al.*, "A Review on Low-Dimensional Nanomaterials: Nanofabrication, Characterization and Applications," *Nanomaterials*, vol. 13, no. 1, p. 160, Dec. 2022, doi: 10.3390/nano13010160.

[281] E. Garnett, L. Mai, and P. Yang, "Introduction: 1D Nanomaterials/Nanowires," *Chem. Rev.*, vol. 119, no. 15, pp. 8955–8957, Aug. 2019, doi: 10.1021/acs.chemrev.9b00423.

[282] G. Kawamura, H. Muto, and A. Matsuda, "Hard template synthesis of metal nanowires," *Front. Chem.*, vol. 2, Nov. 2014, doi: 10.3389/fchem.2014.00104.

[283] N. Gangwar, C. Gangwar, and J. Sarkar, “A review on template-assisted approaches & self assembly of nanomaterials at liquid/liquid interface,” *Heliyon*, vol. 10, no. 17, p. e36810, Sep. 2024, doi: 10.1016/j.heliyon.2024.e36810.

[284] H. S. Varol *et al.*, “Electropolymerization of Polydopamine at Electrode-Supported Insulating Mesoporous Films,” *Chem. Mater.*, vol. 35, no. 21, pp. 9192–9207, Nov. 2023, doi: 10.1021/acs.chemmater.3c01890.

[285] S. Pevzner, O. Regev, and R. Yerushalmi-Rozen, “Thin films of mesoporous silica: preparation and characterization,” *Current Opinion in Colloid & Interface Science*, vol. 4, no. 6, pp. 420–427, Dec. 1999, doi: 10.1016/S1359-0294(00)00018-2.

[286] W. Yantasee, Y. Lin, X. Li, G. E. Fryxell, T. S. Zemanian, and V. V. Viswanathan, “Nanoengineered electrochemical sensor based on mesoporous silica thin-film functionalized with thiol-terminated monolayer,” *Analyst*, vol. 128, no. 7, p. 899, 2003, doi: 10.1039/b303973k.

[287] D. Grosso *et al.*, “Fundamentals of Mesostructuring Through Evaporation-Induced Self-Assembly,” *Adv Funct Materials*, vol. 14, no. 4, pp. 309–322, Apr. 2004, doi: 10.1002/adfm.200305036.

[288] N. A. N. Mohamed *et al.*, “Effects of surfactant head group modification on vertically oriented mesoporous silica produced by the electrochemically assisted surfactant assembly method,” *Nanoscale Adv.*, vol. 5, no. 12, pp. 3316–3325, 2023, doi: 10.1039/D3NA00031A.

[289] A. Walcarius, E. Sibottier, M. Etienne, and J. Ghanbaja, “Electrochemically assisted self-assembly of mesoporous silica thin films,” *Nature Mater*, vol. 6, no. 8, pp. 602–608, Aug. 2007, doi: 10.1038/nmat1951.

[290] Y. Zhou, N. Shida, Y. Koizumi, K. Endo, I. Tomita, and S. Inagi, “Fabrication of One-Dimensional Polymer Nanowires by Templated Bipolar Electropolymerization Promoted by Electrophoretic Effect,” *Macromolecules*, vol. 53, no. 18, pp. 8123–8130, Sep. 2020, doi: 10.1021/acs.macromol.0c00873.

[291] J. Xue, T. Wu, Y. Dai, and Y. Xia, “Electrospinning and Electrospun Nanofibers: Methods, Materials, and Applications,” *Chem. Rev.*, vol. 119, no. 8, pp. 5298–5415, Apr. 2019, doi: 10.1021/acs.chemrev.8b00593.

[292] W. Smok and T. Tański, “A Short Review on Various Engineering Applications of Electrospun One-Dimensional Metal Oxides,” *Materials*, vol. 14, no. 18, p. 5139, Sep. 2021, doi: 10.3390/ma14185139.

[293] G. She, L. Mu, and W. Shi, “Electrodeposition of One-Dimensional Nanostructures,” *NANOTEC*, vol. 3, no. 3, pp. 182–191, Nov. 2009, doi: 10.2174/187221009789177777.

[294] D. Huo, M. J. Kim, Z. Lyu, Y. Shi, B. J. Wiley, and Y. Xia, “One-Dimensional Metal Nanostructures: From Colloidal Syntheses to Applications,” *Chem. Rev.*, vol. 119, no. 15, pp. 8972–9073, Aug. 2019, doi: 10.1021/acs.chemrev.8b00745.

[295] L. Liang, J. Liu, C. F. Windisch, Jr., G. J. Exarhos, and Y. Lin, “Direct Assembly of Large Arrays of Oriented Conducting Polymer Nanowires,” *Angew. Chem. Int. Ed.*, vol. 41, no. 19, pp. 3665–3668, Oct. 2002, doi: 10.1002/1521-3773(20021004)41:19<3665::AID-ANIE3665>3.0.CO;2-B.

[296] C.-G. Wu and T. Bein, “Conducting Carbon Wires in Ordered, Nanometer-Sized Channels,” *Science*, vol. 266, no. 5187, pp. 1013–1015, Nov. 1994, doi: 10.1126/science.266.5187.1013.

[297] M. A. Del Valle, M. Gacitúa, F. R. Díaz, F. Armijo, and R. D. Río, “Electrosynthesis of polythiophene nanowires via mesoporous silica thin film templates,” *Electrochemistry Communications*, vol. 11, no. 11, pp. 2117–2120, Nov. 2009, doi: 10.1016/j.elecom.2009.09.009.

[298] W. Ullah, G. Herzog, N. Vilà, and A. Walcarius, “Electrografting and electropolymerization of nanoarrays of PANI filaments through silica mesochannels,” *Electrochemistry Communications*, vol. 122, p. 106896, Jan. 2021, doi: 10.1016/j.elecom.2020.106896.

[299] N. Vilà and A. Walcarius, “Bis(terpyridine) Iron(II) Functionalized Vertically-Oriented Nanostructured Silica Films: Toward Electrochromic Materials,” *Front. Chem.*, vol. 8, p. 830, Sep. 2020, doi: 10.3389/fchem.2020.00830.

[300] N. A. N. Mohamed *et al.*, “Increasing the Diameter of Vertically Aligned, Hexagonally Ordered Pores in Mesoporous Silica Thin Films,” *Langmuir*, vol. 38, no. 7, pp. 2257–2266, Feb. 2022, doi: 10.1021/acs.langmuir.1c02854.

[301] P. Kuang, X. Zhang, C. He, X. Cao, and B. Wang, “Positronium time-of-flight Measurements of Mesoporous Silica Films,” *Acta Phys. Pol. A*, vol. 133, no. 1, pp. 3–6, Jan. 2018, doi: 10.12693/APhysPolA.133.3.

[302] A. Goux, M. Etienne, E. Aubert, C. Lecomte, J. Ghanbaja, and A. Walcarius, “Oriented Mesoporous Silica Films Obtained by Electro-Assisted Self-Assembly (EASA),” *Chem. Mater.*, vol. 21, no. 4, pp. 731–741, Feb. 2009, doi: 10.1021/cm8029664.

Abstract:

This thesis explores the electropolymerization and electrochromic properties of metallopolymers derived from aminophenyl-functionalized bis(terpyridine) complexes of Fe(II) and Ru(II), investigating both their fundamental behavior on planar electrodes and study the confinement effect of these metallopolymers inside vertically oriented mesoporous silica films. The initial study focused on the oxidative electropolymerization of $[M(tpy\text{-}Ph\text{-}NH_2)_2]^{2+}$ (M = Fe, Ru) complexes on indium-tin oxide (ITO) electrodes. A detailed mechanistic investigation, using cyclic voltammetry complemented by UV-Vis, IR, Raman, and XPS spectroscopy, revealed that polymerization proceeds via the formation of azo bonds, a pathway distinct from conventional polyaniline due to steric hindrance from the terpyridine units. The resulting poly$[Fe(tpy\text{-}Ph\text{-}NH_2)_2]^{2+}$ films exhibited a reversible Fe^{3+}/Fe^{2+} redox couple and served as efficient electrochromic materials. To overcome limitations related to film morphology and ion transport, a nanoconfinement strategy was employed. Vertically oriented mesoporous silica films with tunable pore sizes (2–4.3 nm) were synthesized on ITO via electrochemically assisted self-assembly (EASA) to act as structured templates. Electropolymerization within these nanochannels revealed a critical pore-size dependence, with 4.3 nm pores proving optimal for the formation of well-defined, stable metallopolymer nanowires. The confined systems retained their electrochromic activity while benefiting from the ordered nanoarchitecture, which facilitated mass transport and interfacial stability. In conclusion, this work provides fundamental insights into the unique electropolymerization mechanism of sterically hindered terpyridine complexes and demonstrates that nanoconfinement is a powerful approach for fabricating structured metallopolymer hybrids with good electrochromic performance. The findings establish a versatile platform for developing advanced materials for optoelectronic applications.

KEYWORDS: Conducting metallopolymer, electrochemical polymerization, bis(terpyridine) complexes, electrochromism, mesoporous silica, nanoconfinement.

Cette thèse explore l'électropolymérisation et les propriétés électrochromes de métallopolymères dérivés de complexes bis(terpyridine) aminophénylés de Fe(II) et Ru(II), en étudiant à la fois leur comportement fondamental sur électrodes planaires et l'effet de confinement de ces métallopolymères au sein de films de silice mésoporeuse à canaux verticaux.L'étude initiale s'est focalisée sur l'électropolymérisation oxydante des complexes $[M(tpy\text{-}Ph\text{-}NH_2)_2]^{2+}$ (M = Fe, Ru) sur des électrodes en oxyde d'indium-étain (ITO). Une enquête mécanistique détaillée, combinant voltammétrie cyclique et spectroscopies UV-Visible, IR, Raman et XPS, a révélé que la polymérisation progresse via la formation de liaisons azo, une voie distincte de la polyaniline conventionnelle du fait de l'encombrement stérique imposé par les unités terpyridine. Les films de poly$[Fe(tpy\text{-}Ph\text{-}NH_2)_2]^{2+}$ obtenus présentent un couple redox réversible Fe^{3+}/Fe^{2+} et se comportent comme d'excellents matériaux électrochromes. Pour dépasser les limitations liées à la morphologie des films et au transport ionique, une stratégie de nanoconfinement a été mise en œuvre. Des films de silice mésoporeuse à orientation verticale, de tailles de pores ajustables (2–4,3 nm), ont été synthétisés sur ITO par auto-assemblage assisté électrochimiquement (EASA) afin de servir de gabarits structurés. L'électropolymérisation au sein de ces nano-canaux a mis en évidence une dépendance critique à la taille de pore: les pores de 4,3 nm se sont avérés optimaux pour former des nanofils de métallopolymère bien définis et stables. Les systèmes confinés conservent leur activité électrochrome tout en bénéficiant de l'architecture nano-ordonnée, qui facilite le transport de masse et la stabilité interfaciale. En conclusion, ce travail apporte des éclairages fondamentaux sur le mécanisme d'électropolymérisation de complexes terpyridine stériquement contraints et démontre que le nanoconfinement constitue une approche puissante pour fabriquer des hybrides métallopolymères structurés aux bonnes performances électrochromes. Ces résultats établissent une plateforme polyvalente pour le développement de matériaux avancés destinés aux applications optoélectroniques.

Mots-clés: métallopolymère conducteur, polymérisation électrochimique, complexes bis(terpyridine), électrochromisme, silice mésoporeuse, nanoconfinement.